A Study of Electrochemically Induced Lattice Distortions in Layered Perovskites

by

Alexander W.H. Whittingham

A thesis

presented to the University of Waterloo

in fulfillment of the

thesis requirement for the degree of

Doctor of Philosophy

in

Chemistry

Waterloo, Ontario, Canada, 2022

Examining Committee Membership

The following individuals are members of the examining committee for this thesis. The decision of the examining committee is by majority vote.

External examiner:	Daniel Guay Professor Institut National de la Recherche Scientifique (INRS)
Supervisor:	Rodney Smith Assistant Professor Department of Chemistry, University of Waterloo
Internal Member:	Holger Kleinke Professor Department of Chemistry, University of Waterloo
Internal Member:	Anna Klinkova Assistant Professor Department of Chemistry, University of Waterloo
Internal-External Member:	Jeff Gostick Associate Professor Department of Chemical Engineering, University of Waterloo

Author’s Declaration

I hereby declare that I am the sole author of this thesis. This is a true copy of the thesis, including any required final revisions, as accepted by my examiners.

I understand that my thesis may be made electronically available to the public.

Abstract

The intermittency of renewable electricity necessitates the development of energy storage solutions that are rapidly deployable. Solid state devices such as fuel cells, electrolyzers and batteries have could potentially address the energy storage problem, but additional advances in material science are required for wide scale adoption. Ruddlesden-Popper oxides are materials with a unique structural layout that enables electronic and ionic conductivity. Numerous compositions of Ruddlesden-Popper oxides have been reported, and several research groups have proposed bulk descriptors towards the goal of controlling their properties in a predictable manner. While many of these descriptors are useful, the electrochemical behaviour of these materials is complex and can result in nuanced changes to their properties. This manuscript seeks to develop a detailed electrochemical map of the processes within these phases to gain insights into their electrocatalytic performance.

In Chapter 3, a rigorous structural and electrochemical study of La_2CuO_4 is presented. Voltammetric characterization was used to identify relevant Cu-based redox processes in the material under inert conditions. The application of potential bias for extended periods at oxidizing and reduction voltages yielded systematic distortions relative to the parent structure. These conditions showed signs of charge compensation through the formation of charge carriers and defects, but also resulted in amorphization of the material. Both effects altered the electrocatalytic reduction of O_2 and CO_2.

In Chapter 4, the surface interactions between CO_2 and $La_{2-x}Sr_xCuO_4$ are elucidated. Utilization of voltametric techniques revealed that the stability of $La_{2-x}Sr_xCuO_4$ is dependent on Sr content and the presence of CO_2. Alternating current techniques revealed that bubbling CO_2 into the electrolyte increases the concentration of redox active surface species. *In-situ* FTIR experiments identified surface bound carbonates as primary carbonaceous surface species. The binding mode of the carbonates exhibit a structural dependency, resulting in bidentate carbonate for La_2CuO_4 and monodentate carbonates for $La_{2-x}Sr_xCuO_4$. These findings suggest that the bidentate mode resulted in increased surface strain and drove amorphization in La_2CuO_4.

Chapter 5 explored the dependence of cation substitution on the oxygen reduction activity of $La_{2-x}Sr_xNi_{1-y}Fe_yO_4$. Substitution of La for Sr, or Ni for Fe caused systematic changes to the structure and electrocatalytic activity of the Ruddlesden-Popper oxide. Structural characterization techniques revealed that Sr-substitution resulted in expansion the *a*/*b* plane and simultaneously elongated the unit

cell along the *c*-axis. Fe-substitution elongated the *c*-axis without expanding the *a*/*b* plane and simultaneously introduced oxygen defects into the material. Hydrodynamic voltammetry revealed that incorporation of Fe into the lattice directly controlled the onset, Tafel slope and selectivity of the oxygen reduction reaction. Correlational analysis concluded that Fe-induced structural distortions are responsible for the observed changes in electrocatalytic behaviour.

Chapter 6 expanded on Chapter 5 by examining the effect of Co-substitution on the structure and electrochemistry of $La_{2-x}Sr_xNi_{1-y}Co_yO_4$. A combination of PXRD and Raman spectroscopy provided evidence that substitution of Ni for Co caused a progressive contraction of the unit-cell along the *c*-axis. Correlation analysis revealed that the contraction of the unit cell is directly related to the Tafel slope of ORR.

Chapter 7 provides a summary of the thesis and some concluding remarks.

Acknowledgements

My transformation from an undergraduate student to a competent researcher was a long and difficult process. Even though this dissertation has my name on it, I believe that this accomplishment would not have been possible without the dedication and support provided by those around me. Here, I would like to thank the individuals who contributed to this accomplishment. First, I would like to thank my supervisor, Dr. Rodney D.L. Smith, for the guidance, insights, and time he has provided me. Starting a lab from scratch and remaining committed to my development through one of the worst pandemics in recent memory is a significant task worth recognition. I would also like to thank my committee, who made the time to attend my meetings and provided valuable feedback that contributed to my professional development. I would like to extend this thanks to my external examiner, who took the time to critic my work and attend my defense.

Thank you to my lab mates, especially Elif Pinar Alsaç and Yutong Liu. Thank you for your company, discussions, and consistent support since joining the group in 2018. Your expertise in electrochemistry, structural analysis, Raman spectroscopy was invaluable to my growth as a chemist. Through your friendship and comradery, I truly felt a sense of belonging in this research group. Both of you were key factors to my success in this group and I will remember our time together during all my future endeavors.

Finally, none of this would be possible without my family, to whom this thesis is dedicated.

Dedication

This dissertation is dedicated to my family, which includes my parents, grandparents, and sister. My parents, Nicole and Anthony Whittingham, have demonstrated a deep commitment to my education for over 28 years. This thesis is a direct product of their love, nurturing, persistence, and financial support over almost three decades. I am grateful for the opportunities you have provided me. To my grandparents, Beryl and Cecil Tulloch, who contributed to my professional development by helping me secure a Co-op position, allowed me to live with them, and took care of me after I contracted the chikungunya virus, thank you. It was one of the most memorable moments of my life, and your words of encouragement pushed me through difficult times in my university career. Finally, to my sister, Elizabeth Lauren Whittingham, who makes time for me even during her busiest moments. Thank you for talking me through the rough patches and being the best big sister, I could ask for. I love you all, this one is for you.

Table of Contents

List of Figures

List of Tables

List of Equations

$n_d = 4 * \left(\frac{i_d}{i_d + \frac{i_r}{N}} \right)$ 85

List of Schemes

List of Abbreviations

adsorbate based mechanism
ABM, 19
alternating current
AC, 33
attenuated total reflection
ATR, 58
cyclic voltammogram
CV, 33
density functional theory
DFT, 20
direct current
DC, 33
Electrochemical CO_2 reduction
ECR, 10
Electrochemical impedance spectroscopy
EIS, 33
ethylene diamine
EN, 22
ethylene diamine tetraacetic acid
EDTA, 22
Fourier-transform infrared spectroscopy
FTIR, 29
free induction decay
FID, 32
full width at half maximum
FWHM, 62
gadolinium doped ceria
GDC, 10
gas diffusion electrodes
GDE, 14
hydrogen evolution reaction
HER, 10
La_2CuO_4
LCO, 38
$La_{2-x}Sr_xCuO_4$
LSCO, 59
lattice oxygen mediated mechanism
LOM, 19
neodymium-doped yttrium aluminium garnet
Nd:YAG, 30
Nuclear magnetic resonance spectroscopy
NMR, 32
oxygen evolution reaction
OER, 11
oxygen reduction reaction
ORR, 9
Powder X-ray diffraction
PXRD, 23
proton NMR
^{1}H:NMR, 32
radio frequency
RF, 32
resistor-capacitor
RC, 34
reversible hydrogen electrode
RHE, 20
Rotating disc electrode
RDE, 35
rotating ring disc electrode
RRDE, 37
Ruddlesden Popper oxides
RPO, 1
scanning electron microscope
SEM, 27
solid oxide fuel cell
SOFC, 9
transmission electron microscopy
TEM, 26
X-ray photoelectron spectroscopy
XPS, 13
yttrium stabilized Zr
YSZ, 10

Chapter 1: Introduction

1.1 Preamble

There is a growing demand for renewable electricity to power all facets of society to address our energy appetite and environmental concerns. The drive for electrification necessitates that we continue to develop technology such as fuel cells, batteries, and electrolyzers to enable this future. Great strides have been made to realize such systems, however, their development is fundamentally linked to the properties of the electrode materials and the reactions they catalyze. From a chemical standpoint, the electrode must be able to catalyze chemical reactions at appreciable rates with high efficiency. Reaction selectivity must also be considered, as undesired products can be detrimental to the long-term performance of electrochemical cells. A fundamental problem is the stability of electrodes, which are expected to operate under harsh conditions for prolonged periods. Long-term stability is required for electrochemical devices to be economic viability.

Ruddlesden-Popper oxides (RPOs) are a class of electrode materials that possess properties with the potential to enable a low-carbon future, such as electrical conductivity, ion mobility, layered structure, and the ability to accommodate structural distortions. These qualities make RPOs a popular choice for electrode materials in research groups seeking to develop solid-state devices, electrolyzers, fuel cells and batteries. However, RPOs are structurally complex with nuanced changes to their structure and composition, which impact the qualities that make them useful for energy storage. An additional layer of complexity is encountered when considering the reactions catalyzed on the surface, as they can proceed through mechanisms that are seldom encountered in other metal oxide materials. While descriptors relating bulk structural parameters to their catalytic performance have been developed, detailed characterization of these phases is still needed. This dissertation seeks to perform in-depth characterization using a variety of methods to better understand and develop RPOs.

1.2 The Ruddlesden-Popper Oxide Structure and Its Polymorphs

The original Ruddlesden-Popper phase was first described by the scientists S.N Ruddlesden and P. Popper,[1] who discovered an entire family of oxides with the K_2NiF_4 structure. The number of these "Ruddlesden-Popper" phases has expanded considerably since 1957 and many have been used as electrocatalysts.[2] Ruddlesden-Popper oxides are a class of metal oxide with the general formula

A_2BO_4, where A is a hard often inert ion and B is a transition metal or metalloid.[3] The crystal structure depicted in Figure 1.1 is characterized by alternating layers of perovskite (ABO_3) and pseudo-rocksalt (AO) motifs which extend infinitely in the *a*-*b* plane. The perovskite layer is distinguished by a B-site cation with 6-fold coordination that is surrounded by 8 edge-sharing AO_9 sites. BO_6 octahedra are often tetragonally distorted[4], resulting in B-O bonds that are longer in the axial positions than in the equatorial plane. Tetragonal distortions are frequently observed in nickelates[5], cobaltites[6], and especially cuprates[7] because of Jahn-Teller distortions. The pseudo-rocksalt layer, bound to the perovskite layer via the B-O axial bonds, is a distorted variant of the halite unit cell. The coordination number of the A-site cations in this layer is 9 compared to 6-fold environment expected in other rocksalt materials such as NaCl. While the structure described here is the standard structure for RPOs, it is worth noting that various polymorphs of these structures have also been synthesized such as higher order RPOs with the formula $A_{n+1}B_nO_{3n+1}$ shown in Figure 1.1.[8,9] These compositions can be obtained using similar synthetic protocols as n = 1 RPOs and can be obtained by tuning the stoichiometry of the A and B site to the desired target. La_2NiO_4, $La_3Ni_2O_7$ and $La_4Ni_3O_{10}$ RPOs with the *I*4/mmm space group were prepared in this way by using a modified Pechini method.[9]

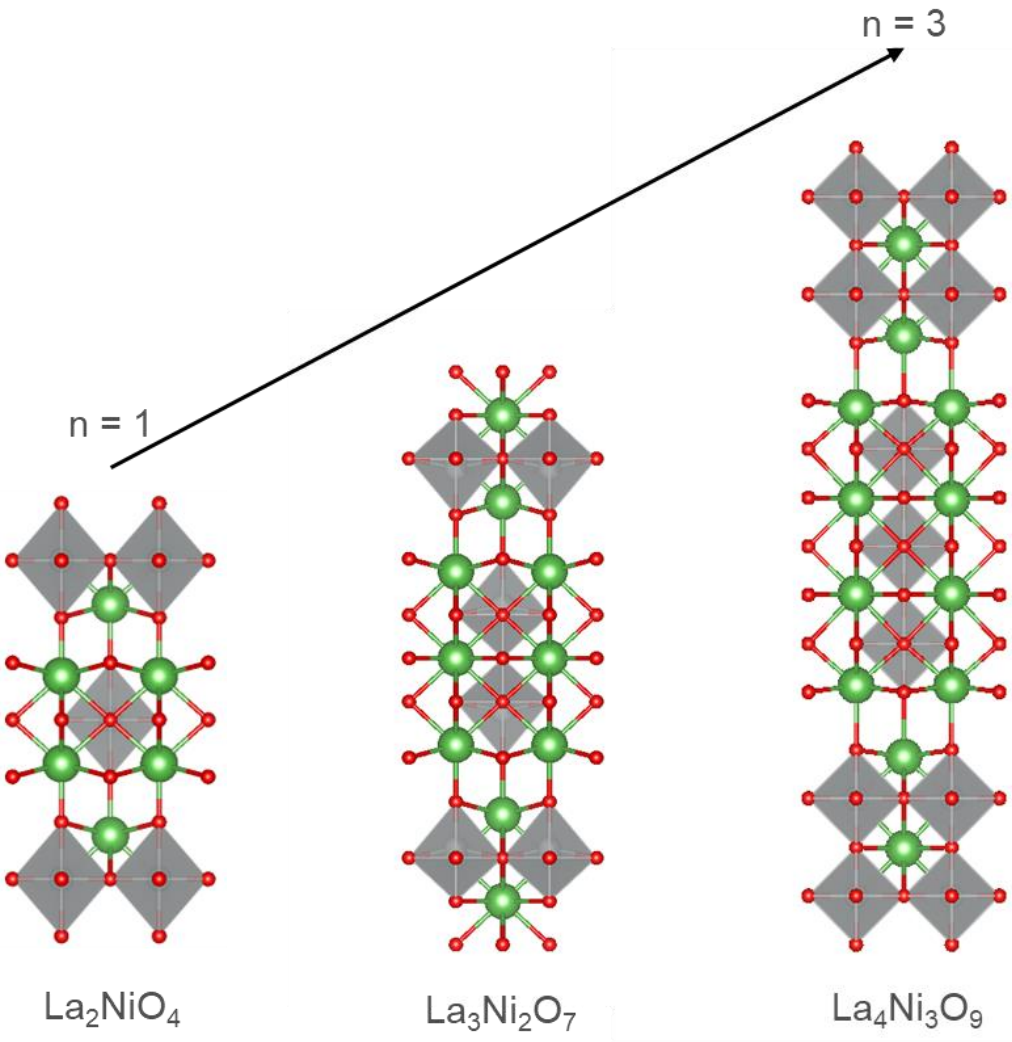

Figure 1.1: The unit cell of first, second and third order $La_{n+1}Ni_nO_{3n+1}$ RPOs with the *I4/mmm* space group. The green spheres represent La, grey octahedral sites represent Ni and red is oxygen.

The determining factor of whether a RPOs will form is a combination of ion size compatibility and the maintenance of charge neutrality. In the former, a useful predictor for whether an RPO will form is the Goldschmidt tolerance factor, a structural descriptor that was originally conceived to describe the structural diversity of ABO_3-type perovskite materials through variations in their unit cell geometry.[10] The Goldschmidt tolerance factor (t-factor) relates the atomic radii of the A, B and

chalcogen (X) sites to assess structural stability of perovskites and the degree of lattice distortion (Equation 1.1).

$$t = \frac{r_A + r_O}{\sqrt{2}(r_B + r_O)} \quad (1.1)$$

Application of the t-factor to perovskites has produced an effective descriptor for predicting the crystal structure that will be adopted. A standard perovskite adopts a cubic unit cell with the space group *Pm-3m*, but are also known to adopt hexagonal, tetragonal, orthorhombic, and rhombohedral sub-types (Figure 1.2).[11] There is significant overlap between tolerance factors of these sub-types, but it is generally accepted that perovskites with a t-factors of 1 tend to form the cubic structure. A perovskite that exemplifies this situation is $SrTiO_3$ (Figure 1.2A).[12] A decrease of the atomic radii of the A-site cation will cause the t-factor to decrease inducing a tilt in the BO_6 octahedrons and the formation of an orthorhombic or rhombohedral unit cell. Tolerance factors below 0.89 generally induce such a distortion resulting in distorted perovskites such as $CaTiO_3$ (*Pnma*[13]; Figure 1.2B) or rhombohedral $LaAlO_3$ (*R-3c*; Figure 1.2C).[14] At t-factors around 0.7 and lower perovskites hit a stability limit where other phases form. A t-factor greater than 1 can favor hexagonal perovskites such as $BaNiO_3$ which possess 1D chains of face sharing octahedra in place of corner sharing motifs (Figure 1.2D).[15]

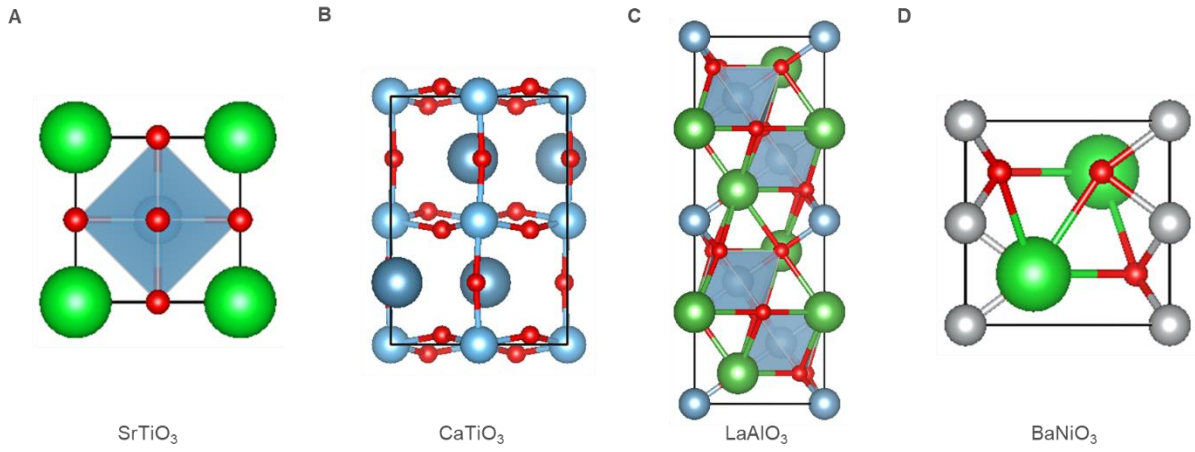

Figure 1.2: An overview of perovskite structures predicted based on their Goldschmidt tolerance factor. A tolerance factor of 1 yields the cubic structure $SrTiO_3$ (A), while lower

tolerance factors result in orthorhombic (B) or rhombohedral unit cells (C). Tolerance factors greater than 1 tend to form the hexagonal $BaNiO_3$ structure (D).

The concept of the t-factor has also been extended from perovskites to use in other systems including RPOs, where they have become useful to predict the formation of other polymorphs.[3] In general, RPOs with the standard K_2NiF_4 structure are stable for t-factors between of 0.99 to 0.87[3], and compositions outside this range can induce lattice distortion, the formation of polymorphs, or phase segregation into A and B-site oxides. Known polymorphs of RPOs are described by the shorthand notation T, O, S, T* or T' and are depicted in Figure 1.3. O structures are simple orthorhombic distortions of the K_2NiF_4 structure (Figure 1.3A) that cause the unit cell to expand relative to the tetragonal structure. Orthorhombic structures are observed for La_2CuO_4 (Figure 1.3B), which has a *Cmce* space group[16] and La_2CoO_4 (Figure 1.3C) which has a *Fmmm* space group.[17] The T' structure is essentially an RPO except with the apical oxygen of the B-site octahedra displaced into the interstitial sites of the AO layer. These structures belong to the Nd_2CuO_4 (Figure 1.3D) family of perovskite oxides that are characterized by square planar, corner-sharing BO_4 motifs alternating by fluorite type NdO layers.[18] T* structures are like K_2NiF_4 except one of the apical oxygens is missing from the octahedral sites, leaving a square pyramidal B-site. The AO layers alternate between rocksalt and fluorite type structures. The $Pr_{2-x}Sr_xCuO_4$ transitions from the T' to the T* (Figure 1.3E) state after the Sr concentration is adjusted to $x = 0.4$.[19] S-phase structures contrast with previous unit cells because the equatorial sites, rather than the axial oxygen sites, are gone. An example of the S-phase is Sr_2CuO_3 (Figure 1.3F) which has 1 less oxygen in its chemical formula than RPOs.[20] In a similar way to the perovskite examples presented above, phase segregation into A-O, B-O, perovskite oxides and other phases will occur at extreme t-factors. These polymorphs T, O, T*, T' and S are observed for the cuprate family of RPOs and are rare to find for other transition metal polymorphs.

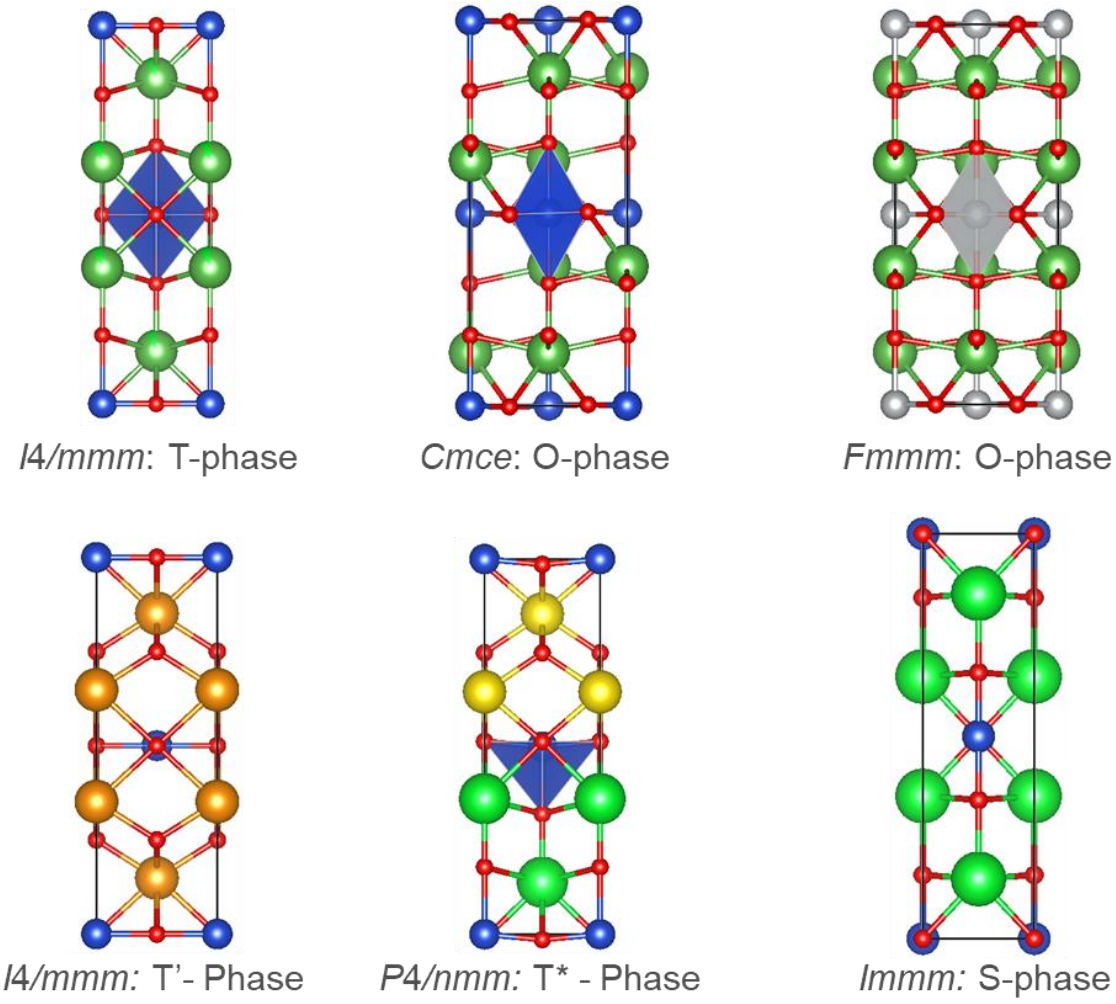

Figure 1.3: Crystal structures of the T, O, O, T', T* and S polymorphs of the RPO structure. (A) The T phase is represented by the $La_{2-x}Sr_xCuO_4$ crystal structure with the *I4/mmm* space group, (B) The O structure, La_2CuO_4 with *Cmce* and (C) La_2NiO_4 with *Fmmm* space group symmetry. (D) The T' structure of Nd_2CuO_4 with *I4/mmm* symmetry, (E) The T* phase of $Pr_{2-x}Sr_xCuO_4$ with *P4/nmm* symmetry and (F) The S-phase Sr_2CuO_3 with *Immm* symmetry.

The Goldschmidt tolerance factor is a convenient descriptor that accounts for the effects of ionic radii on the stability of structures and is useful for comparisons of isovalent cations, although electrostatic contributions also play a major role on the formation of RPOs. Substitution with atoms of a different valence forces the RPO structure to compensation electronically, and ionically to maintain neutrality. This charge compensation mechanism, first through the formation of charge carriers and then through

the formation of anion vacancies, is a common theme across the RPO literature.[21] Studies on nickelates and cuprates demonstrate this concept quite clearly, where oxygen defect concentration has been measured chemical titration, thermogravimetric analysis,[21,22] and surface sensitive techniques[23]where substitution of trivalent La^{3+} with divalent Sr^{2+} results in the formation of holes according to the Kröger-Vink notation shown in Equation 1.2.[8] Accommodation of Sr^{2+} into $La_{2-x}Sr_xCuO_4$ is accomplished at low concentrations of *x*, typically less than $x = 0.2$. At low dopant concentrations the increase in carrier concentration improves the conductivity of the semiconductor (Equation 1.2).[24] Above this concentration, ionic compensation is accomplished through the formation of oxygen vacancies depicted in Equation 1.3. This is clear from studies on $La_{2-x}Sr_xCuO_4$,[25,26] $La_{2-x}Sr_xNiO_4$[27] and $La_{2-x}Sr_xCoO_4$[28,29] that the oxygen δ can range from $x = +0.1/-0.4$, +0.14/-0.05, and +0.15/-0.1 for each phase, respectively. Computational studies have provided insight into the charge compensation mechanism by calculating the formation energy oxygen interstitials and vacancies.[30] The formation energy of interstitial defects is much lower for cobalt, nickel and copper RPOs at Sr concentrations lower than $x = 0.25$, but vacancies are energetically favored at Sr concentrations between $x = 0.3$ and 1. The driving force to change the concentration of point defects in RPOs appears to track the O 2p band center, a concept that will be explained later in section 1.4.[30]

$$\boldsymbol{Sr'_{La} + M^{x}_{M} = M_{\dot{M}} + Sr'_{La} + e^{-}} \qquad (\mathbf{1.2})$$

$$\boldsymbol{2Sr'_{La} + V_{\ddot{o}} = \{2Sr'_{La}V_{\ddot{o}}\}^{x}} \qquad (\mathbf{1.3})$$

Regardless of the polymorph described, the key feature of all RPOs is their mixed ionic and electronic conductivity that arises from the layered structure. The perovskite layer is responsible for electronic conductivity and works by facilitating electron transfer along the B-site planes. The rocksalt layer is responsible for ionic conductivity, and several reports have demonstrated that the ionic conductivity occurs primarily in the *a*-*b* plane and is often over an order of magnitude higher than along the *c*-axis.[31–33] Computational studies have provided evidence for a plausible mechanism, whereby the apical oxygen is inserted into the interstitial sites of the rocksalt layer where oxygen ions can diffuse laterally (Figure 1.4).[34–36] The movement of apical oxygens has been directly observed in nickelate systems through neutron diffraction studies, however, it is not necessarily the sole ionic conductivity mechanism as ionic conduction via vacancy mechanisms have been proposed as well.[37]

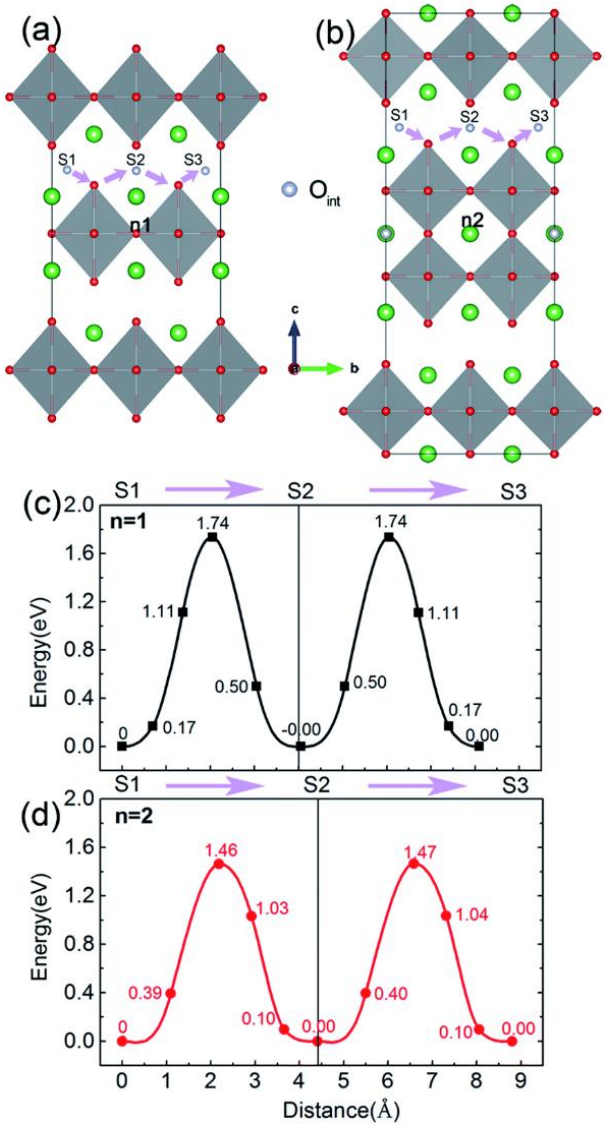

Figure 1.4: Oxygen diffusion via an interstitial mechanism for (A) La_2NiO_4 and (B) $La_3Ni_2O_7$. S_1 to S_3 denotes the pathway that O_{int} migrates through the lattice in both crystal structures. The corresponding energy barriers are depicted for each structure in (C) and (D). Copied with permission from Ref 34.

Understanding mixed ionic and electronic conductivity is an important component of electrocatalysis in RPOs because oxide mobility can be a rate-limiting process. This is the case in several types of electrode assemblies including electrolyzers and solid oxide fuel cells. In several cases, oxygen vacancies lead to the direct enhancement of electrocatalytic reactions, such as the

oxygen reduction reaction (ORR) in RPOs.[38] Theoretical calculations on the La_2NiO_4 show that the binding energy for oxygen on a vacancy laden (001) surface is 0.81 eV lower than the same pristine surface, highlighting the significance of this effect.[39] The impact of oxygen vacancies on ORR and other electrocatalytic reactions will be discussed further in Section 1.4.

Tuning mixed conductivity of RPOs is frequently accomplished through modifications to synthetic protocol or by changing the chemical composition. $La_{2-x}A_xCuO_{4+\delta}$ is the archetypal example of how new properties arise from oxygen non-stoichiometry. Several studies have found that the interstitial oxygen concentration can be tuned electrochemically[40,41] or thermally by heating under oxygen,[42] resulting in high-temperature superconductivity. Electrochemical oxidation of La_2CuO_4 in alkaline media successfully inserted excess oxygen into the lattice. Introduction of oxygen interstitials is a slow process at room temperature with oxide having a diffusion coefficient of $D_0 = 10^{-16}$ cm^2 s^{-1}, but hours of oxidation elongates the *c* unit cell parameter from 13.16 to 13.22 Å .[40] Using this method, La_2CuO_4 was converted to a high-temperature superconductor at 45 K (tunable). In other RPO systems, conventional electrical conductivity is a function of dopant or defect concentration.[43] Most RPOs are semiconductors, but the reported bandgaps ranging from *ca.* 1 eV for $La_{2-x}Sr_xCuO_4$[44] to 4 eV for $LaSrAlO_4$.[45] Introduction of dopants increases the amount of charge carriers that can migrate through the lattice with the identity of the defect controlling the conductivity. Introduction of divalent cations such as Sr to the A site results in holes according to the Kröger-Vink notation shown previously creating a *p*-type semiconductor. Likewise, substitution of the A-site with a tetravalent cation such as Ce will yield an *n*-type semiconductor. The conductivity of RPOs varies widely across ranges of temperature and composition with systems like $La_{0.6}Sr_{1.4}MnO_4$ having 5 S cm^{-1} and $Nd_{1.7}Ca_{0.3}NiO_4$ having 153 S cm^{-1}.[43]

1.3 Utilization of Ruddlesden-Popper Oxides as Electrodes

1.3.1 Key Reactions

RPO electrodes are increasingly utilized as anodes and cathodes to drive electrocatalytic reactions.[46] The promise of using RPOs for electrocatalysis is that they could accelerate slow, multi-electron transfer reactions while simultaneously transporting oxide-ion equivalents through the crystal lattice. The mixed ionic-electronic conductivity is a sought after property that enables the construction of solid state devices and is central to the concept of solid oxide fuel cell (SOFC) technology.[47] SOFCs come in many configurations, but standard designs introduce fuels such as H_2 or hydrocarbons to the

anode where they are oxidized at by oxide equivalences originating from the electrochemical oxygen reduction reaction (ORR) taking place at the cathode. Transport of oxide from the cathode to the anode is accomplished by a solid electrolyte such as yttrium stabilized Zr (YSZ) or gadolinium doped ceria (GDC). Much of the literature examining oxygen transport in RPOs is performed at high temperature to increase mobility through the cell but is also possible at low temperatures as well. The mechanism of ORR is the focus of intense study for RPOs and is dependent on the compositions, temperature, and electrolyte conditions. For simplicity's sake, the overall reactions in alkaline and acidic media are shown in Scheme 1.

$$O_2 + 4e^- + 2H_2O \longrightarrow 4\,^-OH \text{ (alkaline)}$$
$$O_2 + 2e^- + H_2O \longrightarrow H_2O^- + {}^-OH \text{ (alkaline)}$$
$$O_2 + 4e^- + 4H^+ \longrightarrow 2H_2O \text{ (acidic)}$$
$$O_2 + 2e^- + 2H^+ \longrightarrow H_2O_2 \text{ (acidic)}$$

Scheme 1: Overall oxygen reduction reactions in alkaline and acidic electrolytes

Scheme 1 depicts that oxygen reduction follows either two or four proton coupled electron pathways. Electrochemical reduction of oxygen using metal oxides is typically performed in alkaline media due to electrode corrosion in the presence of acidic electrolyte solutions.

RPOs are also used as cathodes in the electrolyzer configuration where the hydrogen evolution reaction (HER) and electrochemical CO_2 reduction (ECR) are reported. The hydrogen evolution reaction involves a two-electron transfer to protons following the reaction overall reactions shown in Scheme 2 for alkaline and acidic conditions respectively.[48]

$$2H^+ + 2e^- \rightleftharpoons H_2\,(g)$$
$$2H_2O + 2e^- \rightleftharpoons H_2\,(g) + {}^-2OH$$

Scheme 2: Hydrogen evolution overall mechanism in acidic and alkaline media

CO_2 reduction is of considerable interest because of the possibility of displacing fossil fuels and petrochemical precursors with renewable hydrocarbons derived from carbon neutral sources.[49–51] In aqueous media CO_2R involves multiple proton and electron transfer steps resulting in a diverse assortment of products including, but not limited to, formic acid, carbon monoxide, methane, C_2 and C_3 carbon-oxygenates.[51] A major challenge for CO_2R on heterogenous electrocatalysis is to control

the product distribution of the products obtained in addition to increasing rates of reaction.[52] The selectivity problem is intrinsically linked to linear scaling relations between CO_2R intermediates on the surface that are all similarly stabilized by an electric field due to similar bonding configurations.[53] In this endeavor, the heterogeneous electrocatalyst community can overcome scaling relationships by introducing secondary interactions that selectively stabilize intermediates in the reaction pathway. These strategies include compositional tuning of electrocatalysts, modifications to morphology, utilization of different substrates, tethering of monolayers to the surface and use of external forces.[54]

Studies that use RPOs as anodes typically explore the oxygen evolution reaction (OER) first. Oxygen evolution involves the oxidation of water through a four-electron transfer process that is coupled to proton transfer. It is frequently described as "sluggish" in the context of electrolyzers and is a major reaction increases the overpotential of water-splitting electrolyzers. OER can proceed through either $2e^-$ or $4e^-$ transfer pathway resulting in peroxide or oxygen respectively. In the context of RPOs and related perovskite oxides the mechanism for this reaction can proceed through either a adsorbate mediated pathway or a lattice oxygen mediated pathway.[55]

Regardless of the reaction being studied, the effect of the reaction conditions and substrate-surface interactions must be studied. The common themes that arise are temperature control, compositional control, morphology, and their impact on the long-term stability of these catalysts.

1.3.2 Electrocatalysis at High and Low Temperatures

The high-temperature behavior of RPOs is frequently discussed in the context (SOFC) due to the enhancement of electronic conductivity and ionic diffusion. The basic design of a solid oxide fuel cell is the cathode deposited on top of a solid electrolyte such as yttria-stabilized zirconium (YSZ) or gadolinium doped ceria (GDC) followed by an anode that catalyzes an oxidation reaction. In some cases, a single material can act as all three components, however, only the triple layered set-up will be mentioned here. The basic operation of a SOFC is as follows and often requires temperatures between 600 to 1000 °C to ensure O^{2-} mobility. High operating temperatures of SOFCs have beneficial and detrimental consequences for the kinetics, conductivity, and stability of electrode materials.

A benefit of high operating temperatures is an overall increase in reaction rate according to the Arrhenius relationship (Equation 1.4), where k is the rate constant, A is the pre-exponential factor, E_a is the activation barrier for the reaction, R is the ideal gas constant and T is the temperature. Increasing the temperature improves the kinetics of slow processes such as OER and ORR that are

widely considered to be sluggish reactions resulting from the breaking/formation of the O-O bond.[56] Ionic conductivity is also governed by the Arrhenius equation meaning that bond surface catalysis and transportation of O^{2-} into the bulk of the lattice is enhanced.

$$\boldsymbol{k = Ae^{-E_a/RT}} \qquad (\mathbf{1.4})$$

The RPOs that are applied to OER, and ORR are often cuprates, nickelates, ferrates and cobaltatesare *p* or *n* type semiconductors depending on the substituents or defects in the crystal lattice.[57] Unlike metallic alloys, a semiconductor's electrical conductivity is directly proportional to the number of charge carriers, their charge, and their mobility. Because the number of charge carriers inside semiconducting materials is small[24] increasing the temperature is more practical to increase charge carrier mobility and by extension conductivity.[24] Depending on whether the charge carrier for the electrode electrons or holes, two different overall mechanisms exist for the consumption of fuel at electrodes (Equation 1.5 and 1.6).[58] It is generally accepted that the mechanism of ORR on high temperature electrodes governed by the formation of surface vacancies on the surface of the electrode and transport properties of oxides through the solid electrolyte.[58,59] ORR on RPOs is governed by the following elementary steps: adsorption of oxygen onto a vacancy, disassociation of the O-O bond, and incorporation of the O^{2-} ions into the lattice.[58]

$$\boldsymbol{O_2^{gas} + 2V_{\ddot{o}} = 2O_o^x + 4\dot{h}} \qquad (\mathbf{1.5})$$

$$\boldsymbol{O_2^{gas} + 2V_{\ddot{o}} + 4e^- = 2O_o^x} \qquad (\mathbf{1.6})$$

In general, the properties of RPOs at elevated temperatures have been linked to observable bulk parameters such as oxygen exchange kinetics. Surface oxygen exchange kinetics generally refers to the process whereby gaseous O_2 is activated on a mixed ionic-electronic conductor and transported across the surface interface into the bulk of the material.[60] In RPOs the surface oxygen exchange kinetics are dependent on several factors, including the crystal facet exposed, morphology of the particle and the chemical composition of the electrode material. The oxygen exchange kinetics of epitaxially grown $La_{2-x}Sr_xCuO_4$ films with (001), (103), and (114) planes exposed was measured using electrochemical impedance spectroscopy at 550°C. Comparison of the Nyquist plots for each plane shows clear differences in resistance and translate into *k* values for oxygen exchanges that are two-orders of magnitude higher on (114) than (001).[61] Similar experiments have been conducted for La_2NiO_4, Pr_2NiO_4 and Nd_2NiO_4 epitaxially grown films finding similar orientation dependent surface

oxygen exchange coefficients.[33,62] Production of RPO nanorods using a microemulsion sol-gel method highlights the effect of particle shape and reinforces findings for crystal facet orientation. RPOs fabricated via conventional sol-gel or solid-state synthesis routes often result in spherical polycrystalline particles with no control over facet exposure whereas La_2NiO_4 nanorod were found to be dense with (001) planes.[63] The compositional effects on surface oxygen exchange have been explained in detail by other research groups. Generally, B-site substitution has a large effect on this parameter at high temperatures. B-site substitution controls bond B-O bond length, electrical conductivity, and population of oxygen defects. The identity of the A or B site cations does not provide clean trends in oxygen exchange kinetics and can more accurately be described by the descriptors discussing in Section 1.4.[35]

High operating temperatures can have beneficial effects for the operation of a fuel cell, but can be deleterious to the long-term stability of the electrode. One of the primary issues is due to a parameter called the thermal expansion coefficient that measures the degree to which a material expands with increasing temperature. Often, the thermal expansion coefficients of the cells are incompatible with each other, resulting in increased localized strain at the electrode-electrolyte interface.[64] If this property is not considered, it could result in premature degradation of the cell on a microscopic scale or greater problems such as cracking or flaking of the electrode material from the electrolyte.[43,65] Migration of atoms through the cathode is also possible, resulting inside reactions which often passivate the electrodes. This phenomenon has been observed in other perovskite oxides as well and is attributed to a combination of electrostatic and strain driven processes. Migration of A-site atoms at intermediate and high temperatures is a substantial problem as it could cause the accumulation of AO_x on the surface, which is not only an insulator, but blocks the catalytically active sites of RPOs. This phenomenon has been observed on several members of the $n = 1$ RPO family, such as the $La_{2-x}Sr_xNiO_4$ system where SrO_x was detected by a combination of low energy ion scattering and X-ray photoelectron spectroscopy (XPS) and $La_{2-x}Sr_xCoO_4$ where segregation was detected by specialized X-ray diffraction techniques.[66] The driving force for phase segregation has been described in $LaMnO_3$ perovskite oxides as a combination of electrostatic effects arising from defects and strain effects from cation size mismatch.[67] The authors detected phase segregation by electron microscopy and found that larger cations, such as Ba, deteriorate at a faster rate relative to smaller cations such as Sr and Ca. This phenomenon is temperature-dependent with segregation being observed primarily between 430-830°C on Sr and Ba substituted $LaMnO_3$. Electrostatic effects were analyzed by systematically

changing the partial pressure of O_2 used to anneal these phases. Higher phase segregation is observed under annealing in 760 Torr of air versus 1 x 10^{-9} Torr because the space-charge region at the surface is minimized by the introduction of oxygen defects under near vacuum conditions. Similar effects were also observed for Manganate perovskites under electrochemical conditions as well, where reduction yields a reduced concentration of surface Sr, but oxidations produces SrO_x.[68]

Mismatch of the thermal expansion coefficients of the cathode and solid electrolyte can also result in exsolution of the B-site cations that can have consequences for the observed catalytic activity.[69] Exsolution is frequently observed for perovskite-type oxides and results in phase segregation of B-site metal into a secondary phase under reducing conditions.[70] At high temperature conditions this phenomenon often results in the formation of metallic nanoparticles and is often exploited to produce highly active electrocatalysts. These nanoparticles have been directly observed through electron microscopic techniques for, Fe[71], Ni[72], Co,[73], Cu[74] and alloys of mixed B-site cations.[75,76] The presence of these nanoparticles have been cited as being directly involved in the activation of CO_2[73] and hydrogen gas.[77]

Operation of electrodes at low temperatures generally simplifies studies and avoids high temperature instability; however, a new set of problems arises. Unlike high-temperature conditions, analysis of electrocatalysts at low temperatures do not follow a standardized cell design or fabrication protocols. While a pure pellet of material is ideal, it is not always practical for low temperature cells. Ionically conducting polymers are often used as a binder for powdered catalysts and are mixed with additives such as carbon black to improve the electrical conductivity. While additives are useful, they can change the local environment for the electrocatalyst through mass transfer effects and secondary hydrophobic interactions.[78] Mass transfer effects are also affected by the geometry of the cell used, where results obtained using an H-cell are not directly comparable in gas diffusion electrodes (GDE) or forced convection experiments. Part of this discrepancy arises from increased concentrations of analyte found at the triple-phase boundaries of GDE and increased current densities.[79] Compounding the basic reporting issues, there is no universally agreed upon mechanism for oxygen reduction at low temperature, while at high temperature there is some consensus that a vacancy mechanism dominates.[59] In addition, the mechanism of OER and ORR has been reported to change depending on subtle changes to the composition of the material.

1.4 The Effect of Heteroatom Substitution on Electrocatalytic Performance

Heteroatom substitution is a facile way for researchers to modify the electronic, optical, thermal and electrocatalytic properties of RPOs. An RPO phases has been reported for most alkali earth metals, and transition metals on the periodic table. While the breath of compositions is useful for developing structure-function relationships, two primary considerations must be made. The major concern is the valence of the heteroatom and the size, which could result in a lower solubility limit in the lattice if not appropriately considered. This would complicate analysis for electrocatalysis where pure phases are required to enhance the certainty of an active site.

1.4.1 Effect on Electrocatalytic Activity

In the previous section, A and B site substitution was discussed in the context of oxygen exchange kinetics as being critical to electrocatalytic reactions at high temperatures. A-site substitution acts as a mechanism to directly control the charge compensation mechanisms and thus oxygen exchange kinetics. In the literature general observations have been made about the effect of A/B site substitution on the properties of RPOs and their catalytic activity pertaining to OER/ORR.[35,46] Generally, the effect of A-site substitution with an ion of lower valence causes the electronic conductivity to increase while the ionic conductivity decreases. This is depicted in the $La_{2-x}Sr_xNiO_4$[80,81] and $La_{2-x}Sr_xCuO_4$[82] where oxygen diffusion through the lattice can be attenuated by an order of magnitude. B-site substitution impacts both the ORR[83] and OER[57] activity by modifying the bond length of the M-O which is critical to both diffusion and oxygen exchange kinetics. The effects are often nuanced, showing unexpected changes and compositional changes are not always clear over a wide range of compositions.[46] Because of this, several electrochemical descriptors have been developed to describe the electrochemical activity in relation to the electronic configuration and geometric factors. The occupancy of molecular orbitals in perovskites[84,85] and RPOs[86] has been correlated to key electrochemical performance indicators such as onset potential and current density. In a similar fashion the band position and density of states of transition metals relative to oxygen band centers has been used as a first principle descriptor to predict oxygen exchange kinetics.[87] Geometric distortions have also been reported with bulk strain influencing the system.[88] Oxygen vacancies formed through heteroatom substation also has an impact on the electrocatalytic activities for a variety of systems.[89] Effects of higher dimensional defects[90] has also been examined, but in the context of this dissertation all phases have been fabricated in a similar fashion so it is anticipated that

the morphology and defect populations should be similar. The discussion is therefore limited to electronic, geometric, and defect related descriptors.

When substituting strain is often introduced, a concept that is seldom brought up and appears to have a remarkable impact on electrocatalytic activity. A study of the effect of strain on pulsed laser deposited Nd_2NiO_4 demonstrated unambiguously the effect of strain on reaction kinetics of ORR in RPOs. The authors deposited thin films of Nd_2NiO_4 onto $SrTiO_3$ and $NdGaO_3$ substrates to induce tensile and compressive strain respectively while monitoring the oxygen exchange kinetics with electrochemical impedance spectroscopy between 360 and 420 °C (Figure 1.5).[91]

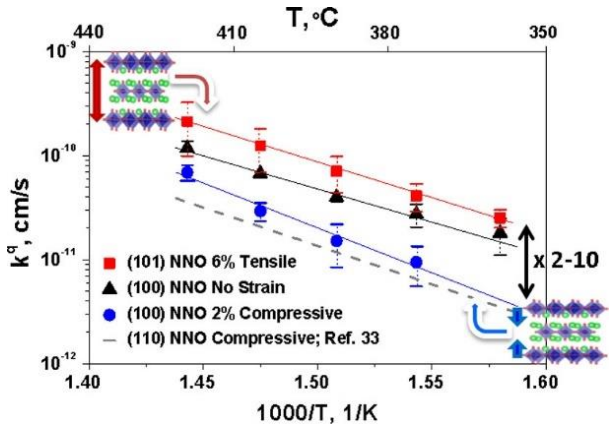

Figure 1.5: The effect of strain applied along the *c*-axis of Nd_2NiO_4. Arrhenius plots for unstrained Nd_2NiO_4 (black), is depicted alongside 6% tensile (red) and 2% compressively strained Nd_2NiO_4 (blue). Another compressively strained sample from the literature is also provided (dashed line). Copied with permission from Ref 91.

The Arrhenius plot (Figure 1.5) shows that Nd_2NiO_4 films with tensile strain enhances oxygen exchange kinetics slightly in comparison to the unstrained sample, however, there is a 2-to-10-fold enhancement for tensile strained films relative to the compressively strained films. The effect of tensile strain on RPOs extends to other nickelate systems such as La_2NiO_4. Sequentially decreasing the thickness of epitaxially grown La_2NiO_4 (100) films from 370 to 14 nm was used to increase the volumetric tensile strain.[92] A film with 7.68% in the *a*/*b* plane and 5.32% along the c-axis increased the surface exchange coefficient by 2 orders of magnitude. The authors of the report hypothesize that the reason for strain related enhancements originates from lowering the formation energy of the interstitial oxide defects, thereby increasing oxygen incorporation into the film. For perovskite oxides molecular orbital and band structure descriptors have been employed to establish trends in catalytic

activity observed between different compositions of the A and B site. The most relevant measures of electrocatalytic activity are electronic in nature, such as the e_g filling of B-site cations, and O 2p band location. In perovskite oxides the number of e_g electrons plotted against the overpotential for ORR results in a volcano plot of activity with perovskites having a singly occupied e_g orbital at the apex (Figure 1.6A).[93] The phases $LaMnO_3$ and $LaNiO_3$ have the maximum activity with the authors hypothesizing that this descriptor arises from modification of M-O bond covalency that controls $O_2^{2-}/^-OH$ intermediate turnover rates (Figure 1.6B). Such findings are in line with the Sabatier principle that asserts that a catalyst should not bind intermediates too weakly or too strongly. A description of activity of e_g filling is an indirect descriptor of adsorption energy descriptors that have been developed on perovskites to elucidate OER mechanisms.[55] Similarly, the location of the O 2p band position relative to the Fermi level was found to linearly correlate to the area specific resistance and oxygen exchange kinetics. Such relationships again arise from the O_{vac} formation energy and the B-O binding energy.[94] Such phenomena extend to RPOs as well, suggesting that perovskites and RPOs are similar enough in this respect.

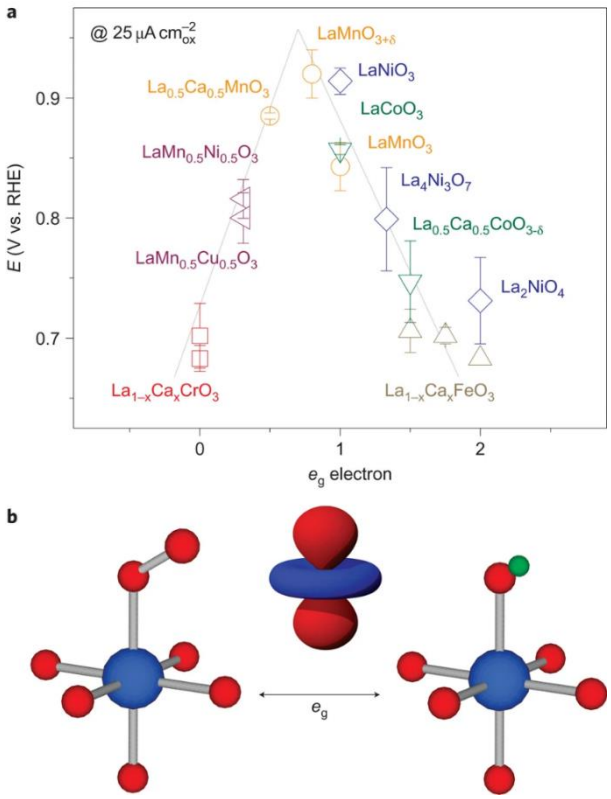

Figure 1.6: The utilization of E_g filling as a descriptor for electrocatalytic ORR performance. (A) A volcano plot of the onset potential for ORR *E*, plotted against the e_g electron count of perovskite oxides. (B) The impact of e_g electrons within the d_z^2 orbital on $O_2^{2-}/^{-}OH$ exchange kinetics Copied with permission from Ref 93.

Introduction of defects to the lattice can have a profound impact on electrocatalysis. Unsaturated metal sites provided by oxygen defects are often described as having an electronic structure that differs from the bulk material and therefore has different adsorption properties for intermediates in the reaction pathway.[95] The density of coordinatively unsaturated metal cations was found to directly correlate with OER overpotential of transition metal oxides with diverse coordination environments such as NiO, Co_3O_4, MnO_2, Fe_2O_3 and TiO_2 (Figure 1.7).[95] The authors concluded that metal oxides that bind OER intermediates weakly benefit from more undercoordinated sites, while the opposite is true for electrocatalysts that adsorb them strongly. The electronic origin of this effect is thought to arise from filling the antibonding states of oxygen adsorbates, which can be tuned by adjusting the Fermi-level of transition metal oxides. Other coordination environment-based descriptors have been developed to generalize the effect of unsaturated coordination environments on transition metals and

their oxides.[95,96] An example is the generalized coordination number, a weighted average of an atom's coordination number and that of its nearest neighbors that correlates with the d-band center of an atomic site and therefore the adsorption energies of key intermediates.[97] The coordination number concept has been extended to include factor in the effect of orbital overlap.[98,99] Catalytic enhancements observed from oxygen defects could be interpreted as the modification of oxygen adsorption by altering the d-band position and Fermi level.

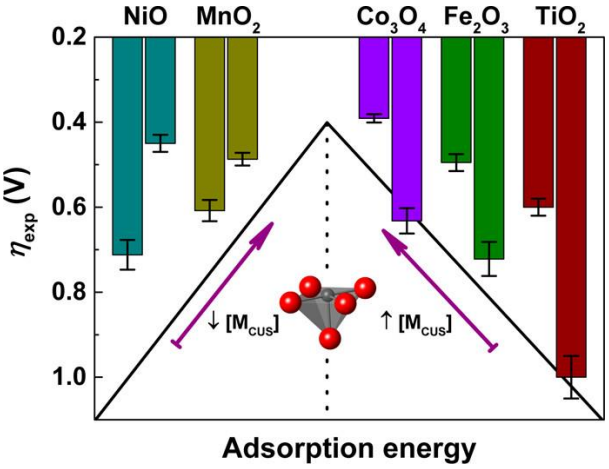

Figure 1.7: The relationship between OER overpotential and the density of coordinatively unsaturated environments [M_{cus}]. Copied with permission from Ref 95.

An important implication of defect formation is their impact on the mechanism of electrocatalytic reactions. In RPOs the formation of oxygen defects is observed primarily in the perovskite layer on B-site octahedra. According to neutron diffraction measurements, oxygen vacancies can form at either B-$O_{equatorial}$ or B-O_{apical} sites, which could potentially behave as an active site.[37] The intentional incorporation of oxygen defects into perovskite-type oxides can increase reaction rates and change mechanistic pathways. For example, the application of the $La_{0.5}Sr_{1.5}Ni_{1-y}Fe_yO_4$ family of RPOs to drive OER demonstrated that incorporation of oxygen vacancies changes the reaction mechanism from an adsorbate based (ABM) to a lattice oxygen mediated mechanism (LOM). The change in mechanism is thought to arise from a process of cross hybridization of the 3d Fe, Ni and O 2p which increases covalency of the Ni-O bond. Such properties were accompanied by lowering of the O_{vac} formation energy in combination with enhanced oxide diffusion necessary for a LOM mechanism. Another study claims that the LOM has also been observed in other RPOs such as $Sr_3(Co_{0.8}Fe_{0.1}Nb_{0.1})_2O_7$.[100] In this study they authors combined X-ray absorption spectroscopy of

transition metal and oxygen edge positions together with density functional theory (DFT) to support their LOM hypothesis. A thermochemical map constructed from DFT simulations supports that a LOM is energetical preferable relative to the ABM mechanistic pathway with predicted overpotentials of 0.22 V and 0.71 V vs reversible hydrogen electrode (RHE) for the LOM and ABM mechanisms respectively. These calculations together with a shift in the Co L_3 and O K-edge positions suggests a high degree of Co-O covalency that is often a requirement for the LOM. Their linear sweep voltammetry yields an overpotential of 0.334 V vs RHE which is closely aligned with their predicted overpotential. While lattice oxygen mediated mechanisms appear to be kinetically fast mechanistic pathways the structural principles that dictate when this pathway is taken in RPOs is needed.

1.5 Challenges, Strategy and Objectives

The fundamental challenges for the study of RPOs arise from their structure, electrocatalytic reactions, and descriptions of electrocatalytic activity. In previous sections the stability of RPOs as a function of temperature, substrate, and electrolyte compositions was discussed. The formation of passivating films from the A-site segregation, exsolution of the redox active perovskite layer and loss of long-range order affect the ability transfer electron at the rates necessary for catalysis.

In Section 1.4, the fundamental challenges governing electrocatalytic interactions was introduced. Apart from optimization of reaction rates through compositional tuning scaling relationships need to be targeted in electrocatalysis to achieve higher current densities and control over reaction activities. RPOs offer a potential opportunity to break scaling relationships due to the proximity of two dissimilar structures close to each other. A proposed strategy to break scaling relationship is the use of support or promoter effects that offer new coordination environment for molecules to bind. In this way, the rocksalt and perovskite layer could offer a means for bifunctional activation of small molecules and to selectively target intermediates that control the reaction pathway taken.

Beyond development of potential catalytic enhancements, the ability to describe small molecule interactions and observing relevant structural changes is critical for RPOs. Monitoring structural changes in RPOs is especially important because mixed conductivity can introduce defects, distortions and potentially drive phase changes that offer novel active sites. The use of bulk structural and electrochemical parameters is useful, but neglecting phenomenon at the surface could result in oversights that oversimplify interactions taking place at the surface. A detailed analysis of structural

changes before, during and after catalysis with an array of characterization techniques should allow for greater insights for the electrochemical properties of RPOs.

This dissertation attempts to address some of these challenges through a detailed structural, spectroscopic, and electrochemical analysis of several RPO compositions. X-ray diffraction will be the primary method used to assign the crystal structure of RPOs and measure unit cell dimensions. Tracking lattice parameters as the composition of the RPOs is varied should provide insight into the bonding of the structure. The acquisition of Raman spectra will be used to ascertain localized changes to the symmetry of the environment, lattice distortions, and direct observation of changes to bond strength to relevant species. Electrochemical experiments will be performed to map the changes to the redox active components, mechanisms and structural stability using standard performance benchmarks such as Tafel slope and overpotential.

1.6 Thesis Overview

The principal goals of this work are to systematically study the effects of heteroatom substitution and electrochemical pretreatments on defects, phase changes and distortions on key electrocatalytic reactions. Using a combination of electrocatalytic, spectroscopic and structural characterization techniques, this dissertation seeks to build structure function relationships for the n = 1 family of RPOs. In this endeavor the following chapters are presented:

Chapter 2: Will go over a detailed explanation of all instrumentation, characterization techniques and synthetic protocols used.

Chapter 3: Is a study on defect formation and phase changes relevant to the study of the La_2CuO_4 system.

Chapter 4: Studies CO_2-surface interactions using an electrochemical and *in-situ* techniques to establish reaction mechanisms.

Chapter 5: Elucidations of the effect of Fe substitution on the ORR kinetics and selectivity for $La_{2-x}Sr_xNi_{1-y}Fe_yO_4$

Chapter 6: Expands upon the work of Chapter 5 by assessing the effect of Co substitution on ORR mechanisms in $La_{2-x}Sr_xNi_{1-y}Co_yO_4$ phases.

Chapter 7: Summary and concluding remarks.

Chapter 2: Experimental

2.1 Citrate-Nitrate Gel Synthesis

Synthesis of a citrate-nitrate gel is a common method for preparation of metal oxide powders. In particular, it is frequently used to synthesize perovskite-type materials with diverse elemental compositions.[101] Synthesis typically occurs in the aqueous phase, where the nitrate salts of transition, alkali, and alkali-earth metal are dissolved in solution. In the absence of nitrate salts, metal nitrates can be formed through the reaction of oxide or carbonate precursors with nitric acid. Citric acid is introduced into the nitrate solution, typically in equimolar amounts, to act as a chelating agent via carboxylate groups. Chelation ensures that the metal ions remain soluble and become immobilized in a gel framework after dehydration of solution using heat or vacuum distillation. There are several variations of the citrate-nitrate gel method, where additional chelating agents can be added if citrate is insufficient for the task, including but not limited to ethylene diamine tetraacetic acid (EDTA) and ethylene diamine (EN). These chelating agents can bind metal cations through ligation with nitrogen lone pairs, in addition to the citrate carboxyl groups. The organic components of the gel are removed through heat-induced auto-combustion of the gel assisted, which is assisted by the oxidizing power of the nitrate salts. The process takes place at temperatures greater than 350°C, leaving behind an ash precursor with metal oxides uniformly dispersed throughout. All the phases made in this paper are formed by heating the ash precursors at temperatures between 980 and 1000°C. A schematic

summary for the synthesis of $La_{2-x}Sr_xCuO_4$ RPO phase is shown in Figure 2.1. This sequence of reactions is a general summary of the nitrate-gel process.

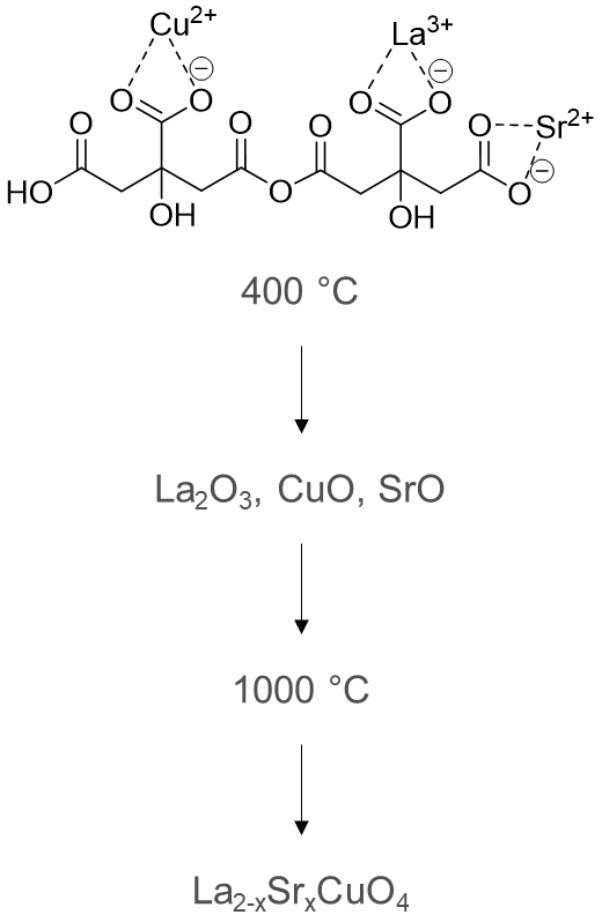

Figure 2.1: Citrate nitrate gel synthesis of $La_{2-x}Sr_xCuO_4$.

2.2 Powder X-ray Diffraction

Powder X-ray diffraction (PXRD) is a characterization method that can determine the crystal structure of solids with long-range order. The operating principle of PXRD is frequently compared to the diffraction of visible light through an optical grating.[24] The spacing of planes in crystal lattices have a similar size to the wavelength of X-rays (Å), allowing them to behave as diffraction grating in three dimensions. This phenomenon was originally described by Laue and modelled according to a 1-dimensional array of atoms; however, Braggs law is much more convenient to use.[24] Constructive

interference arising from diffraction of X-rays by a crystal lattice is described by Braggs law (Equation 2.1):[24]

$$\boldsymbol{2dSin\theta = n\lambda} \qquad (\mathbf{2.1})$$

Where *d* is the lattice spacing, θ is the angle of the incident X-ray relative to the plane of the sample, *n* is the order of diffraction, which is typically 1, and λ is the wavelength of the incident light. Satisfaction of Braggs law causes constructive interference of the diffracted light (Figure 2.2A), which is then detected as a peak in a powder diffraction pattern. When Braggs law is not satisfied, diffracted X-rays destructively interfere with each other, and no peak is observed in the diffraction pattern (Figure 2.2B). A useful powder pattern is obtained by examining diffraction patterns through a range of 2θ values, with values of 0 to 120 being sufficient most crystal systems. The position of the 2θ values is directly dependent on the unit cell dimensions and the number of peaks on the symmetry. In general, high symmetry crystal structures have fewer peaks in their diffraction pattern, while low symmetry crystals have more peaks.

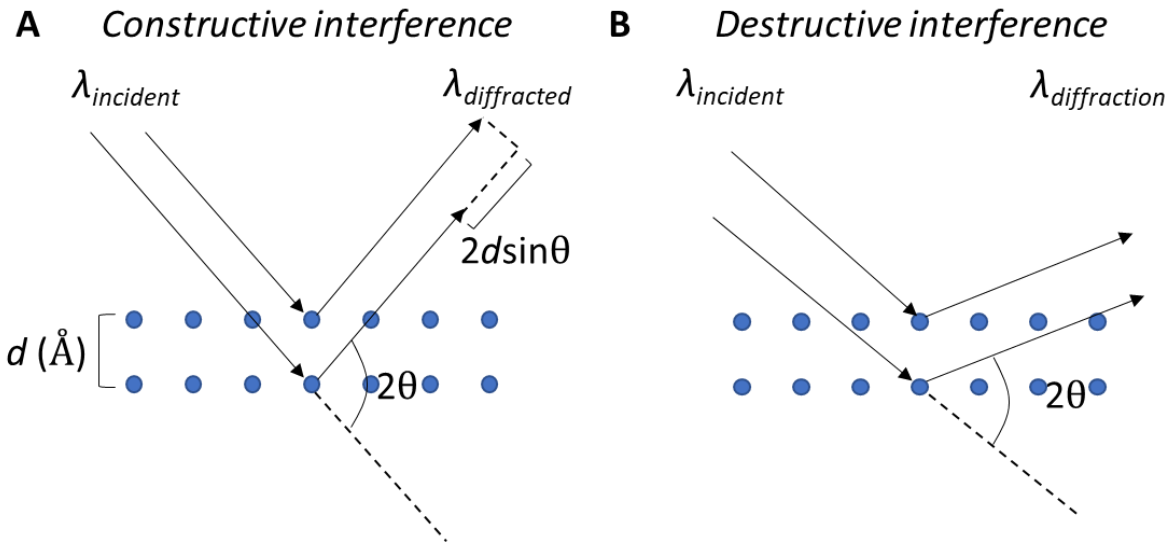

Figure 2.2: A depiction of Braggs law. (A) When Braggs law is satisfied diffracted X-rays constructively interfere. (B) When Braggs law is not satisfied destructive interference occurs.

The intensity of diffraction peaks is a product of the type of atom that interacts with incident X-rays. Scattering of X-rays is dependent on the number of electrons that atoms possess. Therefore,

larger the atomic number of the atom, the more electrons it must diffract the incident X-rays. The intensity of a particular lattice plane is proportional to the structure factor F_{hkl} for a plane:[24]

$$\boldsymbol{F_{hkl} = f_{hkl}\sin(\omega t - \delta_{jkl})} \quad (\mathbf{2.2})$$

$$\boldsymbol{F_j = f_j * e^{2\pi i(hx_j + jy_j + iz_j)}} \quad (\mathbf{2.3})$$

$$\boldsymbol{F_j = \sum f_j * e^{(i\delta_j)}} \quad (\mathbf{2.4})$$

$$\boldsymbol{I_{hkl} \propto F_{hkl}^2} \quad (\mathbf{2.5})$$

Where f_j is the amplitude of the wave, i is the square root of -1, hkl represents the miller indices, and xyz is the coordinates of the atom. These are summed in all crystallographic orientations to yield the peak intensity of a diffraction pattern.

Diffractometers are available in several geometries. In Chapter 3, a Panalytical diffractometer is used, but data presented in Chapters 4, 5, and 6 is exclusively acquired on an Inel diffractometer in the Bragg-Brentano configuration. The basic setup for a PXRD in the Bragg Brentano configuration is shown in Figure 2.3,[102] and reflects the setup of the Panalytical diffractometer. Powder samples are mounted onto an aluminum flat stage equipped with a silicon (001) crystal that lies directly in the path of the X-ray beam emanating from the source. This machine utilizes a Cu K_a source that is filtered with Ni to remove the Cu $K_{\alpha 2}$ component. The Inel diffractometer is different with respect to its source, sample stage and detector. In addition to a Ni filter, the Inel device uses a Ge crystal to create monochromatic X-rays with a wavelength of 1.5406 Å. The sample holder is an aluminium dish, which is mounted on a rotating stage. Rotation of the sample stage removes interference from the preferred orientation effect. Unlike the Panalytical instrument, the detector is a static array of Geiger counters oriented to detect X-rays and acquires signals from $2\theta = 0$ to 120 simultaneously. This removes the need to sweep the detector through predefined values of 2θ as shown in Figure 2.3. After the acquisition, a Rietveld refinement[103] is performed using the appropriate unit cell of the crystal.

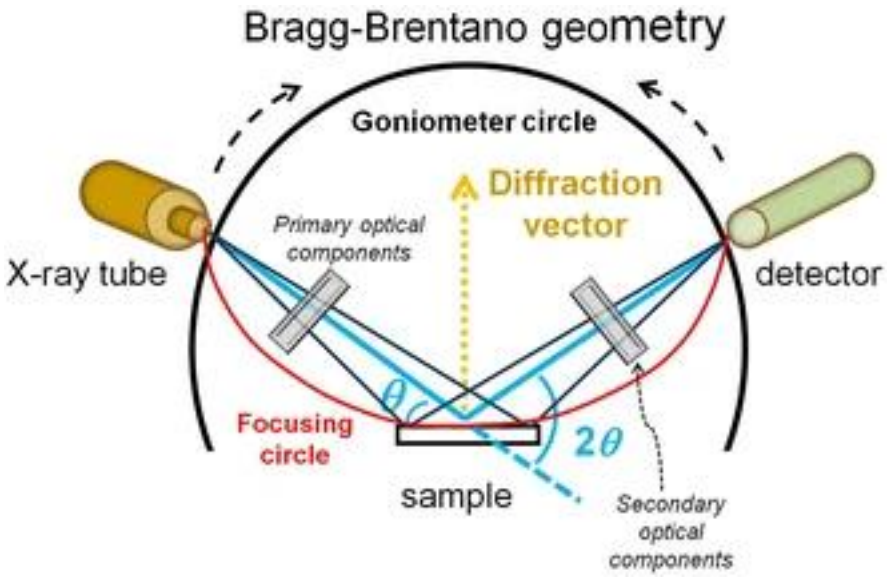

Figure 2.3: A depiction of a basic PXRD apparatus consisting of an X-ray source, a flat stage sample holder with rotation an analyzer crystal and a detector. Copied with permission from Ref 102.

2.3 Electron Microscopy

Modern electron microscopy can provide detailed structural information for solid-state materials. This technique can provide morphological, crystallographic, structural, compositional and elemental information.[104] Electron microscopy allows for the visualization of particles from micrometer to the nanometer scale because it is not constrained by the resolution limits of optical microscopy. Magnification down the nanometer scale also allows for the identification of lattice planes. Electron diffraction allows for the identification of the bulk diffraction data that can be used to characterize the space group and unit cell dimensions.

The fundamental components of an electron microscope are shown in Figure 2.4.[105] Creation of a transmission electron microscopy (TEM) image begins at the source, which creates monochromatic electrons. The electrons from the source are focused into a coherent beam by the first and second condenser lens. The first lens controls the area of the spot probed by the microscope, while the second lens is responsible for controlling intensity. Focused electrons then pass through an aperture that selectively rejects high-energy electrons before they strike the sample. Electrons transmitted through the sample pass through a series of lenses, ultimately arriving at the projector lens that focuses the

image onto a screen or camera. Electron microscopes can also be configured into a scanning electron microscope (SEM) configuration. This form of microscopy detects electrons that are backscattered rather than transmitted through the sample. In this configuration, detailed information about the surface and particle morphology can be obtained.

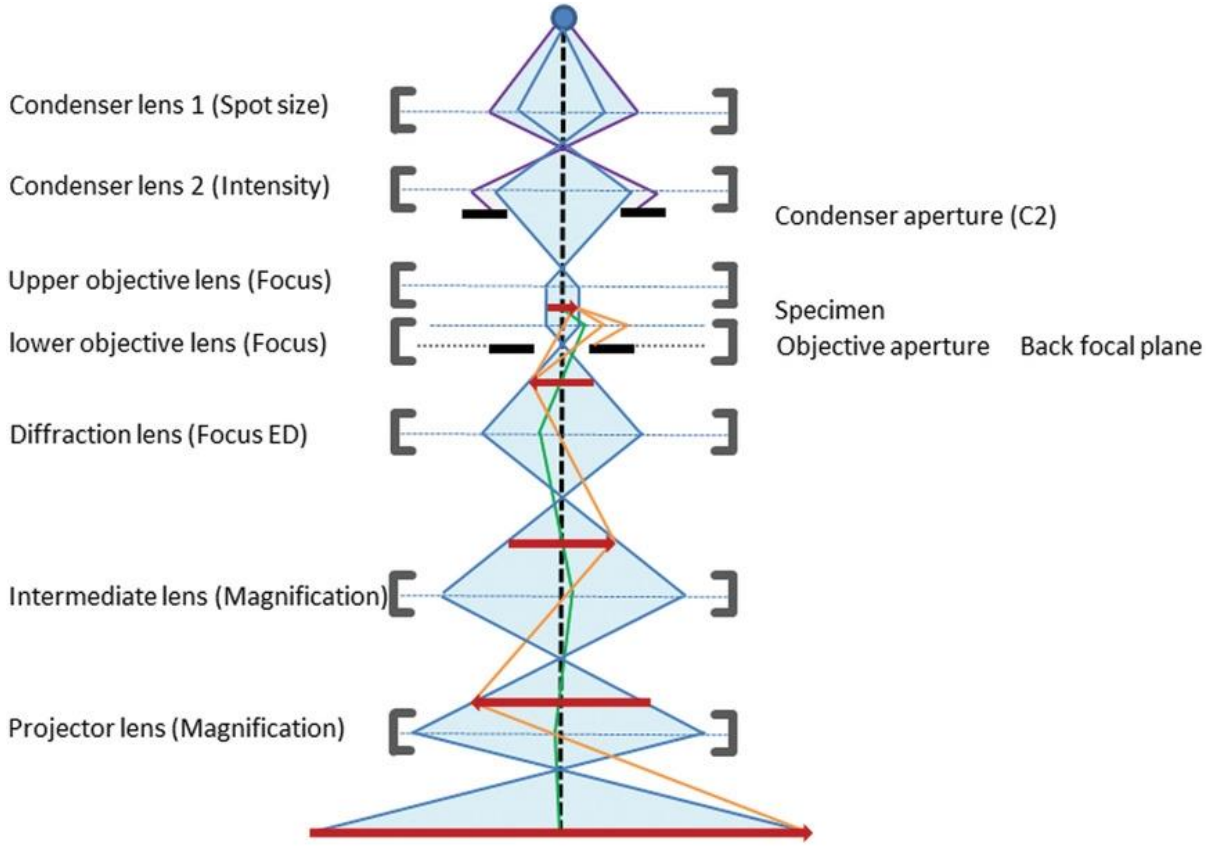

Figure 2.4: A schematic of an electron microscope. Copied with permission from Ref 105.

2.4 X-ray Photoelectron Spectroscopy

X-ray photoelectron spectroscopy (XPS) is a surface sensitive characterization method that relies on the photoelectric effect to yield elemental, chemical and local chemical information of samples. This technique necessitates the use of metallic and semiconducting samples.[106] The basic apparatus consists of an X-ray source, an ultrahigh vacuum chamber and a detector to measure the kinetic energy of electrons. X-ray sources typically use the Mg K_α (1253.6 eV) or Al K_α (1486.6 eV) light to generate photoelectrons and are selected because they have narrow line widths. This property is favorable because it enhances the resolution of the XPS spectrum.[106] Ultrahigh vacuum conditions

ensure that electrons can be detected without any energy losses due to interactions or charge transfer to gases in the surrounding environment. The kinetic energy of these electrons is measured at an electron energy analyzer and the current detected yielding peaks that provide insight into the local chemical environment. A typical hemispherical electron analyzer is shown in Figure 2.5.[107]

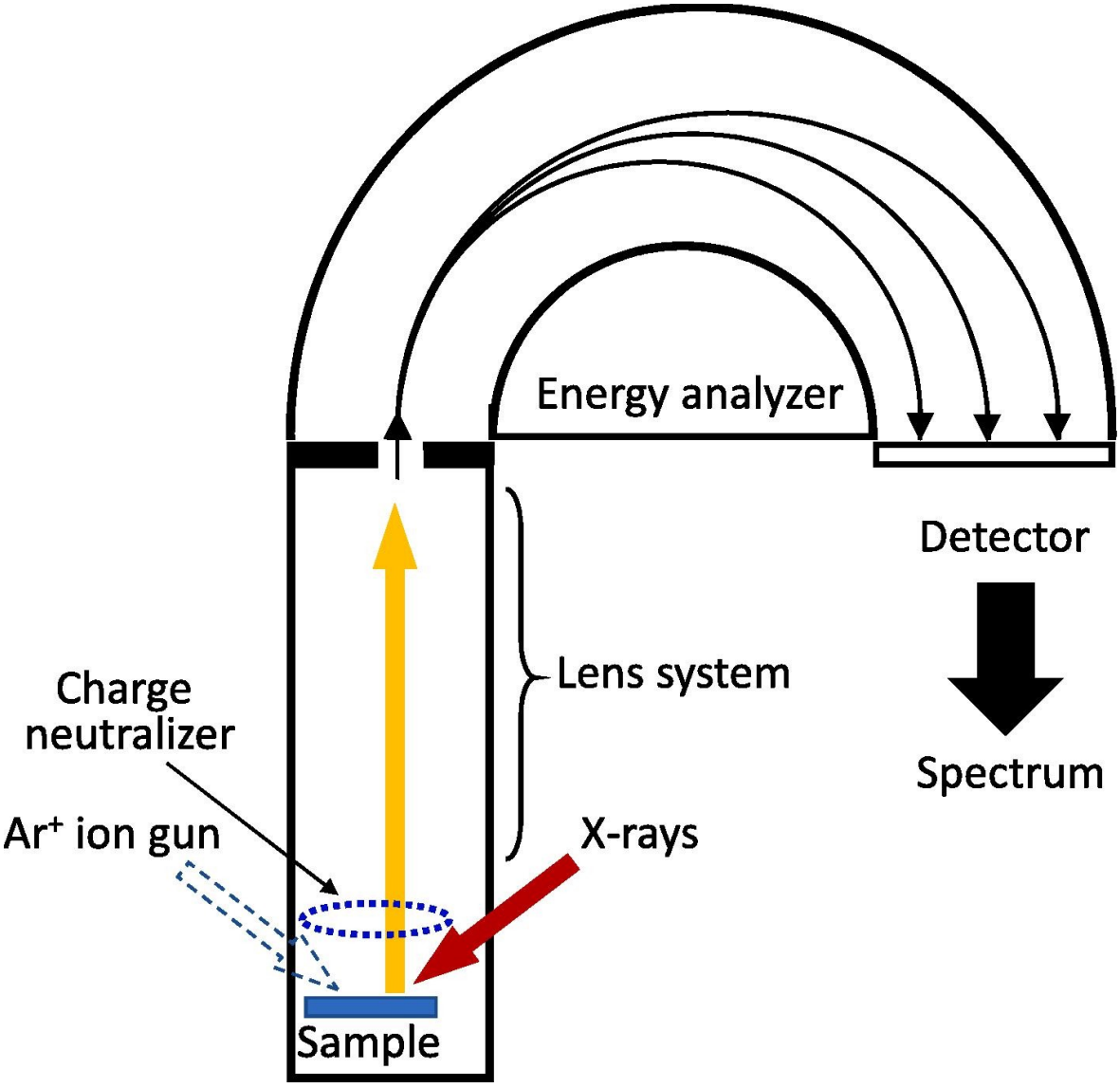

Figure 2.5: An overview of a standard XPS apparatus consisting of a source of focused X-rays, a sample, and a detector with an electron collection lens, electron energy analyzer and an electron detector that transduces the signal into an XPS spectrum. Copied with permission from Ref 107.

The elemental information at the surface obtained by calculating the binding energy (E_B) of the element according to Equation 2.6, where KE_e^- is the kinetic energy of the ejected electron and the incident energy of the X-ray source is given by hν. The E_B is unique to each individual element and there are documented binding energies for at least 92 elements, however, there is sometimes overlap between the energies of certain elements.[106]

$$\boldsymbol{KE_{e-} = h\nu - E_B} \qquad (\mathbf{2.6})$$

Peak intensities can be used to quantify the amount of surface species on the catalyst surface. The intensity of an element given by their peak area may be used to help quantify the amount of each element on the surface after analysis according to Equation 2.7:[106]

$$\boldsymbol{C_x = \left(\frac{I_x}{S_x}\right) \Big/ \sum\left(\frac{I_i}{S_i}\right)} \qquad (\mathbf{2.7})$$

Where I_x is the area or intensity and S_x is the sensitivity factor of the element x.

Apart from element information and their relative concentrations, information about the local environment can be obtained through the morphology of peaks and shifts in BE. Generally, metal oxides are found at higher bond energies than pure metals because of the electronegativity of oxygen.[106] The more electronegative the element, the larger this shift. Information about the valence band and special resolution are outside of the scope of this paper as they require specialized apparatus. Purely elemental and chemical information is presented in this dissertation.

2.5 Vibrational Spectroscopic Techniques: Raman and Infrared Spectroscopy

Fourier-transform infrared spectroscopy (FTIR) is ubiquitous for studying functional groups in molecules and solids. The working principle of FTIR begins with the irradiation of chemical bonds with infrared light. If the frequency of infrared light matches the vibrational frequency of a molecule's functional groups, the light is absorbed, promoting the molecule to a vibrationally excited state.[108] Plotting the absorption profile as a function of infrared frequency (cm^{-1}) yields the FTIR spectrum of a molecule, which provides a fingerprint of all vibrational modes within a material.

Changes to these spectra provide a useful handle to study changes to bonding within materials. Raman spectroscopy is another form of vibrational spectroscopy. Light is made up of two components, an electric field and magnetic field components. The electric field interacts with the electron clouds of atoms and temporarily polarizes the system resulting in a dipole. This polarized state results in the scattering of light at wavelength different from the incident. The induced dipole moment *u* is directly proportional to the external electric field, provide by the incident light, *E* and the molecular polarizability α.[109]

$$\vec{u} = \tilde{\alpha}\vec{E} \qquad (2.8)$$

The scattering of light is frequency dependent. This equation has been expanded upon in reference 106 and describes the secondary electromagnetic radiation resulting from polarization as the product of three components[109]:

$$u(t) = \alpha_0 E_0 \cos(\omega_0 t) + \frac{1}{2}\left(\frac{\partial \alpha}{\partial q}\right) q_0 E_0 \cos(\omega_0 - \omega_q)t + \frac{1}{2}\left(\frac{\partial \alpha}{\partial q}\right) q_0 E_0 \cos(\omega_0 + \omega_q)t \quad (2.9)$$

Where the first component describes light that is elastically scattered, the second term inelastically scattered and red-shifted relative to the incident light, while the third term is inelastically scattered and blue-shifted relative to the incident light. Each of these terms is referred to as Rayleigh, Stokes Raman scattering and anti-stokes Raman scattering, respectively. The Stokes and anti-Stokes components contain information about the vibrationally exited states because they are shifted. In theory, both can be used but the Stokes lines are generally greater in intensity because the other relies on the population of thermally excited states described by a Boltzmann distribution. A lower population of vibration in the thermally excited state is the reason why anti-Stokes spectra are usually orders of magnitude weaker than the Stokes spectra.[24]

Relative to adsorption, the scattering of light provides a relatively weak signal, and the resolution is limited by the bandwidth of light. In Raman spectroscopy both issues are remedied with the use of a laser which is both monochromatic and intense. Several laser sources are available commercially, including He-Ne laser (633 nm) and neodymium-doped yttrium aluminium garnet (Nd:YAG) laser (532 nm). The choice of laser can be used to enhance the signal acquired from Raman, however; some lasers can introduce fluorescence to the spectra or cause phase change to the material that complicates the analysis of phases. This manuscript uses 532 nm exclusively because it was determined to be an optimal tradeoff between sensitivity and fluorescence.

The selection rule for Raman spectroscopy is that the polarizability of a molecule changes. This rule is demonstrated in Figure 2.6:

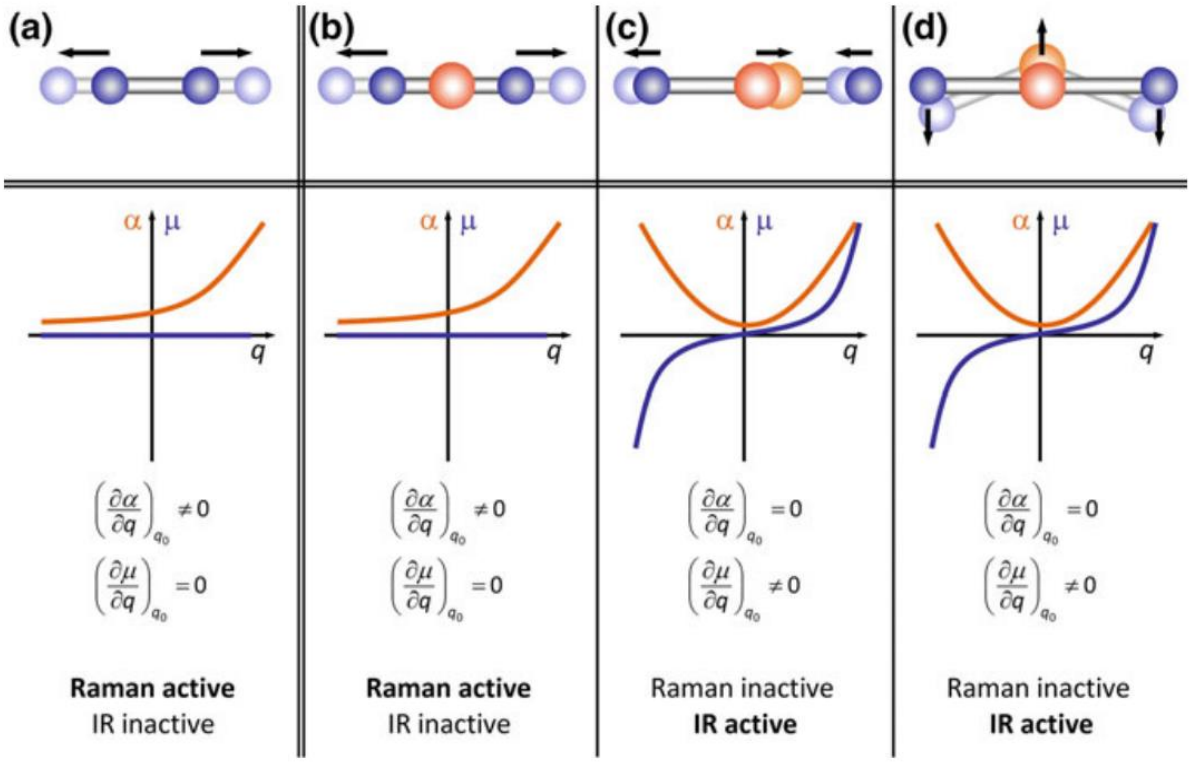

Figure 2.6: The selection rules for Raman and IR spectroscopy. For (A) a homonuclear diatomic the polarizability α (orange) changes during the vibration while the net dipole μ (blue) remains constant causing it to be Raman active by IR inactive. The selection rules for a (B-D) linear three atom are shown for a (B) symmetric, (C) antisymmetric, and (D) waging vibrations. Copied with permission from Ref 109.

A Raman spectrum, like the infrared, is typically thought of as a fingerprint of vibrational modes within a solid, however, when vibrational modes are assigned either through single crystal studies or computation of vibrational energies, specific conclusions about the structure can be drawn.[110] Several studies have shown how Raman spectroscopy can be employed to study phenomena such as strain,[111] defects,[112] and heteroatom substitution[113] in a variety of materials. In this dissertation, trends in the

position of the vibrations, the number of peaks, and their relative intensities will be examined to study structure of RPOs in depth.

2.6 Nuclear Magnetic Resonance

Nuclear magnetic resonance spectroscopy (NMR) is routinely used to determine the structure of organic molecules. This technique relies on the magnetic properties of atomic nuclei, their spin, and their interactions with neighboring nuclei to produce an NMR spectrum. Effective study of these interactions requires strong magnetics fields on the order of multiple Teslas that are produced by superconducting magnets inside the apparatus. Nuclear spins in a field of this magnitude will align parallel or anti-parallel to the magnetic field, removing the energetic degeneracy between the two states in a process referred to as Zeeman splitting. A radio frequency (RF) pulse on the order of MHz is absorbed by the low energy state promoting it an excited antiparallel state. The excited state then relaxes back down to its ground state yielding a weak RF signal referred to as free induction decay (FID).[114] Fourier transform of the FID data (time domain) yields an NMR spectrum that is characteristic of the functional groups in a compound. Any spin active nuclei can be detected by NMR, but the focus of this work concerns proton NMR (^{1}H:NMR).

Interpretation of ^{1}H:NMR spectra for organic molecules focuses on three major features, chemical shift, peak multiplicity, and intensity. Chemical shift refers to the location of a peak on the spectrum which can be located upfield (shielded) or downfield (deshielded). Electron withdrawing groups located adjacent to protons are often responsible for a deshielding affect resulting in a downfield shift of protons, while the inverse is true for electron donating groups. The chemical shifts for a variety of functional groups are well documented and tabulated.[115] J-coupling is capable of splitting peaks into multiplets and originates from the spin-spin coupling of nuclei through bonds. Coupling of n equivalent protons on adjacent carbons results in a splitting pattern of n + 1 which is described by a Pascal's triangle distribution. The intensity of NMR peaks is directly proportional to the number of nuclei in the sample. Utilization of an internal standard of known concentration allows for the determination of the concentration of the unknown provided that the molecular formula is known. Determination of the molar concentration of *x* is shown below, where *M* is the concentration of the substance, *I* is the intensity and *N* is the number of nuclei.[116]

$$\frac{\boldsymbol{M_x}}{\boldsymbol{M_{std}}} = \frac{\boldsymbol{I_x}}{\boldsymbol{I_{std}}} \times \frac{\boldsymbol{N_{std}}}{\boldsymbol{N_x}} \qquad (\mathbf{2.10})$$

2.7 Electrochemical Techniques

2.7.1 Cyclic voltammetry

Cyclic voltammetry provides a wealth of information on the thermodynamics and kinetics of redox processes. Using a potentiostat the electrochemical potential is swept, usually with a staircase or linear waveform from open circuit potential towards two predefined vertex potentials. The current is measured as the potential is swept resulting in a cyclic voltammogram (CV) plot with potential on the x-axis and current on the y-axis. Commonly, information about redox processes is made by interpreting the distance between redox peaks and their intensity. For a freely diffusing species, the reversibility of the redox couple is given by the separation of these redox peaks, with a separation of 59 mV indicating a completely reversible electron transfer reaction. Redox peaks with a separation than 59 mV are quasi-reversible or irreversible processes. Current of peaks is related to the amount of redox active species in solution, and in the context of solids, the concentration of species on the surface. Applications of cyclic voltammetry and their interpretations are too numerous to cover in this manuscript alone, but several of their most frequent uses include the study of reaction mechanisms, adsorption processes, determination of electrochemically active surface area and electrocatalysis.[117]

2.7.2 Electrochemical Impedance Spectroscopy

Electrochemical impedance spectroscopy (EIS) is a technique used to measure the total complex resistance of an electrochemical systems (impedance) to an alternating current (AC). The impedance measured is the product of processes taking place at the electrode surface that can be modelled by analogous circuit elements such as resistors, capacitors, and inductors.[118] Impedance is reflected as a similar concept to Ohm's law when a system is perturbed by a direct current (DC; Figure 2.7A) voltage, but in the AC voltage case the voltage and current are dependent on the angular frequency of the applied potential (Figure 2.7B). In an electrochemical system the total impedance felt is a combination of double layer capacitance and the resistance to charge transfer.[118] Combined

capacitance and resistance will have a phase dependence that rationalizes this model.[117]

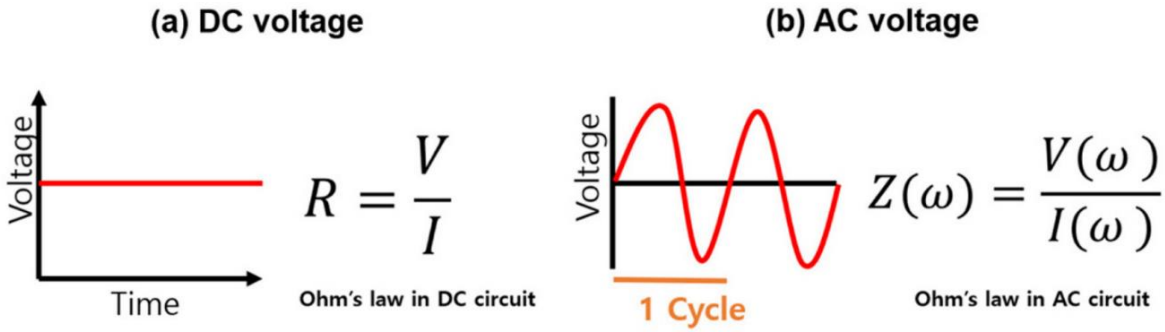

Figure 2.7: Comparing contrasting DC and AC voltammetry. (A) DC voltage is constant with time and is described by Ohm's law. (B) AC voltammetry the voltage is dependent on the frequency of the AC current and so Ohm's law is rewritten as impedance with the voltage and current having dependance on the angular frequency. Copied with permission from Ref 118.

The two common ways to represent data obtained from EIS are through Nyquist and Bode plots. A Nyquist plot consists of "real" impedance (Z_r) plotted along the x-axis with "imaginary" impedance (Z_i) along the y-axis. The distinction between real and imaginary impedance originates from the phase dependance of circuit elements on the AC disturbance, where the imaginary component behaves as a phase dependent capacitor and the real component is independent like a resistor. A Nyquist plot can be fit according to an equivalent circuit of appropriate circuit components; usually a resistor-capacitor (RC) circuit that reflects the fundamental processes at the electrode. Nyquist plots obtained from real electrochemical systems, such as fuel cells or lithium-ion batteries will depict a semicircular plot between high to medium frequencies, followed by a linear region at lower frequencies.[118] A Randle's circuit is typically enough to model most electrochemical systems. This circuit consists of a resistor, representing solution resistance, in series with an RC circuit representing charge transfer resistance and double layer capacitance (Figure 2.8A). A Warburg element accounts for the low frequency linear region that makes a 45° angle relative to the x-axis. This region is typically observed when the system is under mass transfer-controlled conditions. A well fit model will allow for the accurate determination of electrolyte resistance, charge transfer resistance and diffusion parameters. Bode plots show the magnitude and phase changes of the system as a function of the applied frequency. While it is useful for circuit analysis, the Nyquist plot is typically more common (Figure 2.8B).

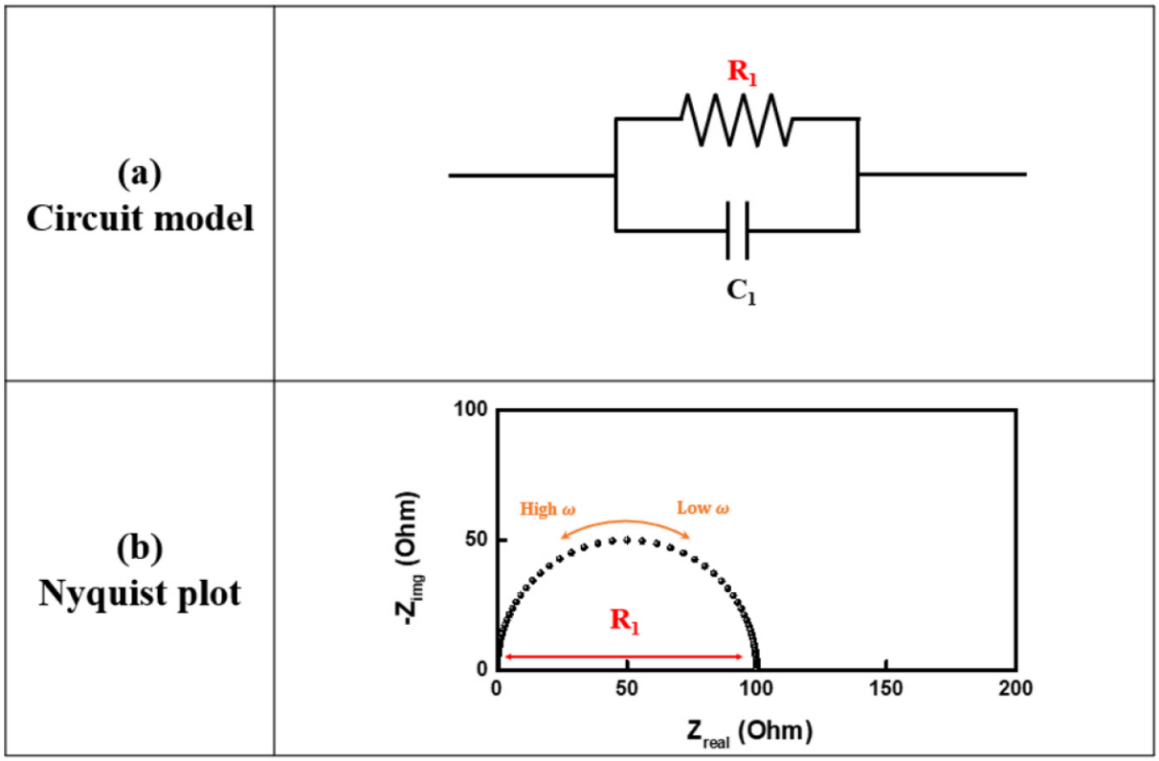

Figure 2.8: A depiction of an (A) RC circuit model consisting of a resistor in parallel with a capacitor and the corresponding (B) Nyquist plot. Copied with permission from Ref 118.

EIS spectra can be applied at multiple potentials for a detailed analysis of catalyst properties and kinetics at different potentials. Mott Schottky analysis is frequently done to characterize semiconducting materials, such as RPOs. This plot is the reciprocal of the capacitance squared against potential that allows for the extraction of flat band potential and doping density. Flatband potential is the voltage where the depletion layer does not exist, giving a relative location of the Fermi-level of the semiconductor. The slope of this plot can be used to acquire the dopant density of a semiconductor.[119]

2.7.3 Rotating (Ring) Disc Electrode Analysis

Rotating disc electrode (RDE) analysis differs from conventional electrochemistry because it occurs under forced convection of electrolyte to the electrode surface. Hydrodynamic conditions offer several advantages over standard configurations, allowing for rapid steady state conditions, decreased importance of double layer charging and increased mass transfer of redox active analytes to the

surface.[120] RDE facilitate the study of electron transfer processes at the electrode surface without significant contribution to mass transfer currents. The basic rotating disc apparatus is shown in Figure 2.9A,[121] where the electrode is housed inside an insulating wall and mounted onto a motor shaft with the disc exposed the electrolyte solution. The motor spins the electrode with an angular velocity of ω that is usually between a few hundred to thousands of RPM that forces the electrolyte solution along the face of the face of the electrode surface (Figure 2.9B).[121]

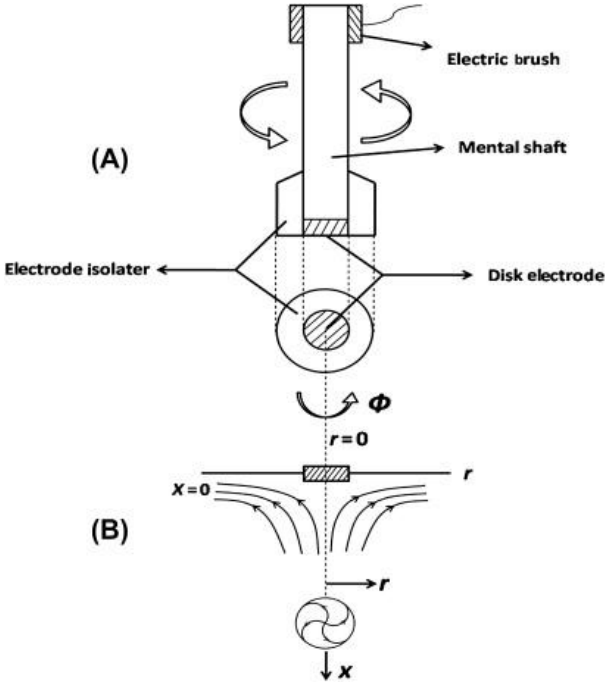

Figure 2.9: Rotating disc electrode consisting of an (A) electric brush motor, a motor shaft, an insulating housing, and electrode disc. The forced convection of the solution is shown in panel (B). Copied with permission from Ref 121.

The theoretical framework behind the operating principle of RDEs was first described by Levich who pioneered the use of RDE towards the study of electrochemical systems.[122] His primary contribution to electrochemical research was the solution to the convection diffusion-equation for a planar RDE cumulating in the description of the mass transfer limiting current ($I_{l,c}$). The equation below now referred to as the Levich equation (Equation 2.11) describes this process.

$$i_{l,c} = 0.62nFAD_0^{\frac{2}{3}}\omega^{\frac{1}{2}}\nu^{-\frac{1}{6}}C_0^* \qquad (2.11)$$

The limiting current is the product of the number of electrons transferred (n), Faraday's constant (F), the geometric area of the electrode (A), the diffusion coefficient D_0, the angular rotation rate ω, the kinematic viscosity ν, and the concentration of the analyte C_0. In a scenario where slow electron transfer kinetics is convoluted with mass transfer it is better to use the Koutecký-Levich equation (Equation 2.12), which is essentially the reciprocal of the equation above.[120]

$$\frac{\mathbf{1}}{\boldsymbol{i_{l,c}}} = \frac{\mathbf{1}}{\boldsymbol{I_k}} + \frac{\mathbf{1}}{\mathbf{0.62}\boldsymbol{nFAD_0^{\frac{2}{3}}\nu^{-\frac{1}{6}}C_0^*}}\omega^{-\frac{\mathbf{1}}{\mathbf{2}}} \qquad (\mathbf{2.12})$$

Plotting the $1/i_{lc}$ against $\omega^{-1/2}$ produces a Koutecký-Levich plot that has an x intercept of $1/I_k$. Determination of I_k for multiple regions on a linear sweep voltammogram allows for the determination of the kinetics of the electrode in non-ideal conditions.[123] The slope of the line for both Levich and Koutecký-Levich can be used to solve for n the number of electrons transferred during the reaction.

RDE studies are of critical importance for screening potential catalyst materials for ORR.[124] As mentioned in Chapter 1, reduction of oxygen can proceed through two different electrochemical pathways, a four electron-transfer process yielding H_2O and a two-electron process yielding peroxide. When all other terms are accounted for the Levich and Koutecký-Levich equations can be used to determine the number of electrons transferred (n). This parameter should lie somewhere between two and four with intermediate values suggesting a mixture of the two pathways. Essentially, n provides direct insight into competing reaction pathways during ORR. Direct measurement of n is also possible by using a rotating ring disc electrode (RRDE) instead. The operating principle of an RRDE is the same as RDE, but with a Pt ring that acts as a second working electrode to oxidize peroxide generated at the disc. Comparison the ring and disc current provides a direct measurement of n without interference from other parameters.

Chapter 3: Electrochemically Induced Phase Changes in La_2CuO_4 during Cathodic Electrocatalysis

This chapter is reproduced in part with permission from John Wiley and Sons: A. W. H. Whittingham, R. D. L. Smith, *ChemElectroChem* **2019**, *6*, 5116. (DOI:10.1002/celc.201901412)

Contribution statements: Synthesis, experimental measurements and data interpretation was performed by A. W. H. Whittingham. Additional data analysis and proofing was done by R. D. L. Smith.

3.1 Introduction

The field of solid-state electrocatalysis is key technology with the potential to facilitate long-term storage of renewable energy in chemical bonds.[125–127] Development of electrocatalytically active materials is accelerating-rapidly to facilitate the transition to a sustainable and low-carbon economy. While high-throughput screening of electrocatalysts for OER, ORR and ECR is desirable, it increases the possibility that contribution of *in-situ* changes will be overlooked in discussion surrounding the origins of catalytic activity.[128–130] Such phase changes, which are often undetected or unanalyzed, are reported to contribute significantly to the observed catalytic activity of many metal oxides.[131,132] Therefore, structural characterization of these phases, and a deep understanding of the reaction mechanism is necessary for rational catalyst development, especially when activity is variable in the literature. Such information should provide the foundation to introduce targeted changes to catalyst behavior, such as control over reaction trajectory and increased current densities.

La_2CuO_4 (LCO) is one of the most intensely studied compositions with the RPO structure because of its superconducting properties at relatively high temperatures.[133] Structural analysis on the origins of superconductivity in LCO discovered that this phenomenon is highly sensitive to oxygen content, resulting in the fabrication of hypo and hyper-stoichiometric LCO. Often, oxygen hyper-stoichiometric LCO is fabricated by heating at high temperatures and pressures in an oxygen atmosphere that incorporates oxide anions into the interstitial sites of the LaO layer.[134–136] To synthesize hypostoichiometric phase LCO is subjected to similar environments under inert atmosphere or vacuum. To circumvent the high temperatures and pressures necessary for defect formation, milder methods defect incorporation have been developed. Electrochemical oxidation and relatively low voltages was shown to easily incorporate excess oxygen into the lattice over hour-long

time spans[133,137,138] The processes for inserting oxygen into LCO and its subsequent redox processes are well documented, with voltages of redox processes reports and structural nuances discussed. Incorporation of oxygen follows a three step process the first is the electrochemical oxidation of Cu^{3+}. Absorption and insertion of oxygen into the lattice follows which in alkaline media comes from hydroxide ions.[138] Once inside the lattice the oxide ion equivalents diffuse through the bulk of the lattice through the interstitial sites of the rocksalt layer as discussed in Chapter 1. While oxygen deficient phases of LCO have been reported, a detailed account of cathodic processes and their associated phase changes are not available. Regardless, A and B-site substituted phases have been utilized as cathodes for photocatalytic HER[139], ORR[140] and ECR.[141,142] Sr-doped phases ($La_{2-x}Sr_xCuO_4$) are of particular interest because of the discrepancies in selectivity observed when applying these phases for ECR. The original account of $La_{2-x}Sr_xCuO_4$ phases being used to drive electrocatalytic CO_2 reduction observed the formation of C_2 and C_3 alcohols after electrolysis in a gas diffusion setup in alkaline media.[141] Obtaining multi-carbon oxygenates within such a narrow range of selectivity is a rare phenomenon in ECR. Replication of this experiment by another group using a similar gas diffusion electrode found that mainly hydrocarbons were obtained after prolonged electrolysis.[142] No clear explanation for the discrepancy between the reaction pathways is provided which underscores the need to characterize the catalyst structure and surface intermediates in more detail. Gaining insight into surface interactions that govern the reaction pathway taken will require *in-situ* and *ex-situ* analysis of cuprate based RPOs applied to ECR. The objective of this chapter is not to replicate previous studies, but to provide an in-depth analysis of the electrochemical processes in LCO. This will provide a deeper understanding of relevant structural features that are present during catalysis. Here, a map of electrochemical processes and phase stability during cathodization of LCO is provided to gain insight into its interactions with small molecules and generate a framework to study LCO in alkaline conditions.

In this chapter, a detailed analysis of the electrochemical behaviour and associated phases changes of LCO in alkaline conditions is presented. The results shown confirm that the layered structure of RPOs can be altered electrochemically via the introduction of oxygen defects, which distort the unit cell. The distortions result in new electrocatalytic properties, but cause structural instability at cathodic voltages. LCO decomposes to an amorphous metal hydroxide at voltages relevant to HER and ECR. These phases changes appear to be present in recent reports and demonstrate their utility is achieving the desired catalytic activity.

3.2 Results

3.2.1 Electrochemical Behaviour and Cu Redox Processes of La_2CuO_4

The redox chemistry of La_2CuO_4 is stable, albeit, in a narrow span of voltages under alkaline conditions. Cyclic voltammograms acquired between -0.4 and 1.1 V vs RHE reveal two anodic peaks at 0.57 ($E_{p,a1}$) and 0.82 V ($E_{p,a2}$) (Figure 3.1A). These processes are accompanied by additional set of broad cathodic peaks at 0.29 ($E_{p,c1}$) and 0.01 ($E_{p,c2}$) V respectively. When the upper potential of the CV is adjusted to 0.7 V $E_{p,a2}$ and $E_{p,c2}$ disappear, while $E_{p,c1}$ is more pronounced. When the upper potential is shifted to 0.4 V the CV shows near ideal capacitive behaviour, but with cathodic current displaced from the zero current axis. The magnitude of the observed capacitance and the cathodic offset appears to increase with slower scan rates and is accompanied by a slow cathodic phase change at 0.8 V (Figure 3.1B).

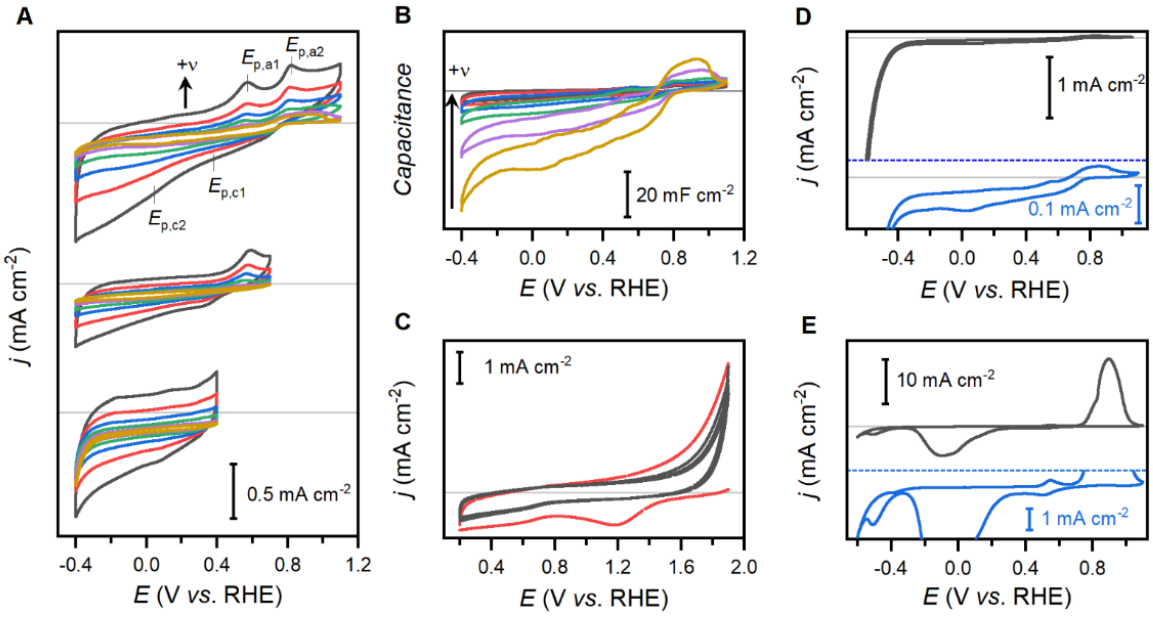

Figure 3.1: Cyclic voltammetry of La_2CuO_4 within variable voltage windows. (A) Stable and reproducible redox behaviour is observed between 1.1 and -0.4 V vs RHE. (B) Cyclic voltammetry data between 1.1 and -0.4 V vs RHE was displayed with capacitance instead of current to highlight irreversible phases changes. (C) Expansion of the voltage region to 1.9 V and (D) expansion of the cathodic window to -0.8 V vs RHE. (E) Data obtained on a polycrystalline copper foil standard. Panels D and E have magnified regions shown in blue to

highlight small redox processes. The scan rate was varied between 5 to 200 mV s^{-1} in panels (A) and (B) 500 mV s^{-1} in panel (C) and 5 mV s^{-1} in (D) and (E). Grey lines highlight the region of zero current.

Cyclic voltammograms acquired between 1.9 and 0.2 V vs RHE show two main features: the onset of oxygen evolution at ca. 1.5 V and a small cathodic peak at 1.2 V that appears during the first cycle (Figure 3.1C). Anodization at 1.9 V for 3 three hours increases the size of the cathodic peak, which disappears after the first cathodic sweep. The electrochemically driven oxidation of Cu^{2+} to Cu^{3+},followed by oxygen intercalation into interstitial sites; is well-documented process.[41,133,137,138,143] The oxygen intercalation process is quite slow and takes place over the span of several hours or sometimes days.[138] The irreversible cathodic process must therefore be assigned to the reduction of Cu^{3+} to Cu^{2+} on the catalyst surface.

When the cathodic potential is swept to -0.8 V exponential increases in current densities are observed, indicating the onset of HER beyond -0.4 V (Figure 3.1D). The onset of hydrogen evolution simultaneously increases the cathodic offset currents at potentials negative of 0.5 V and broadens $E_{p,a2}$ substantially. Cathodization of LCO at -0.8 V for three hours introduces an additional anodic process near 0.9 V that distorts $E_{p,a2}$ and increases cathodic current between 0.8 and -0.4 V. Introduction of an additional redox process suggests that a phase change has occurred, but the voltametric characterization of Cu foil suggests that metallic Cu is absent after electrolysis (Figure 3.1E).

3.2.2 Electrochemically Induced Modification to The La_2CuO_4 Structure

PXRD experiments reveals that prolonged electrochemical conditioning of LCO results in unit cell distortions. The pristine material is an orthorhombic polymorph of the standard K_2NiF_4 structure and Rietveld refinement indicates that *a, b, and c* have the dimensions of 5.3818, 5.4285 and 13.2095 Å respectively (Figure 3.2A; Appendix A.1). LCO can accommodate significant oxygen non-stoichiometry and is often reported as $La_2CuO_{4+\delta}$. The value of δ is reported as a range of positive and negative values in the literature which is summarized in Appendix Table A.1.[139,143–155] The weak scattering power of oxygen increases the uncertainty of δ when determined by Rietveld refinement of PXRD patterns. To increase the accuracy of determining δ in $La_2CuO_{4+\delta}$ a calibration curve correlating the unit cell parameter *c* to δ was constructed by pulling upon available data reported in the literature (Figure 3.2C; Appendix Table A.1). The calibration curve yields a strong positive correlation of *c* to δ reflecting that increased oxygen incorporation into the lattice expands this

parameter. This calibration curve enables the estimation of δ with high confidence by using the lattice parameter obtained from a Rietveld refinement of the powder diffraction measurements. Rietveld refinements of the PXRD measurements suggest that electrochemical conditioning of LCO at 1.9, 1.3, -0.2 and -0.4 V for three hours causes the unit cell dimensions to distort (Figure 3.2B; Table 3.1). Conditioning the sample at 1.3 V appears to have a negligible impact on the dimensions of the *c*-axis relative to the pristine material. Oxidation of LCO electrodes at 1.9 V elongates the *c*-axis, a result consistent with previous reports of oxide intercalation into LaO interstitial sites.[41,133,137,143,144] This change also accompanied by changes to overlapping peaks at a 2θ of ca. 34 that indicate the beginning of a transition to the *I*4*/mmm* phase, a result that is also consistent with literature.[40] Samples reduced at -0.2 and -0.4 V causes the same unit cell parameter to contract a result that is in line with the removal of oxygen from the structure (Figure 3.2C). At the most cathodic potential, -0.8 V, a complete loss of long-range order is apparent by absence of the orthorhombic structure in PXRD. The RPO structure is maintained at voltages spanning 1.9 to -0.4 V, but electrochemical conditioning results in oxygen non-stoichiometry that can be observed indirectly by the modification unit cell parameters. Application of extreme negative potentials necessary for the reduction of H_2O or CO_2 will ultimately drive an irreversible transformation into an amorphous and poorly defined phase.

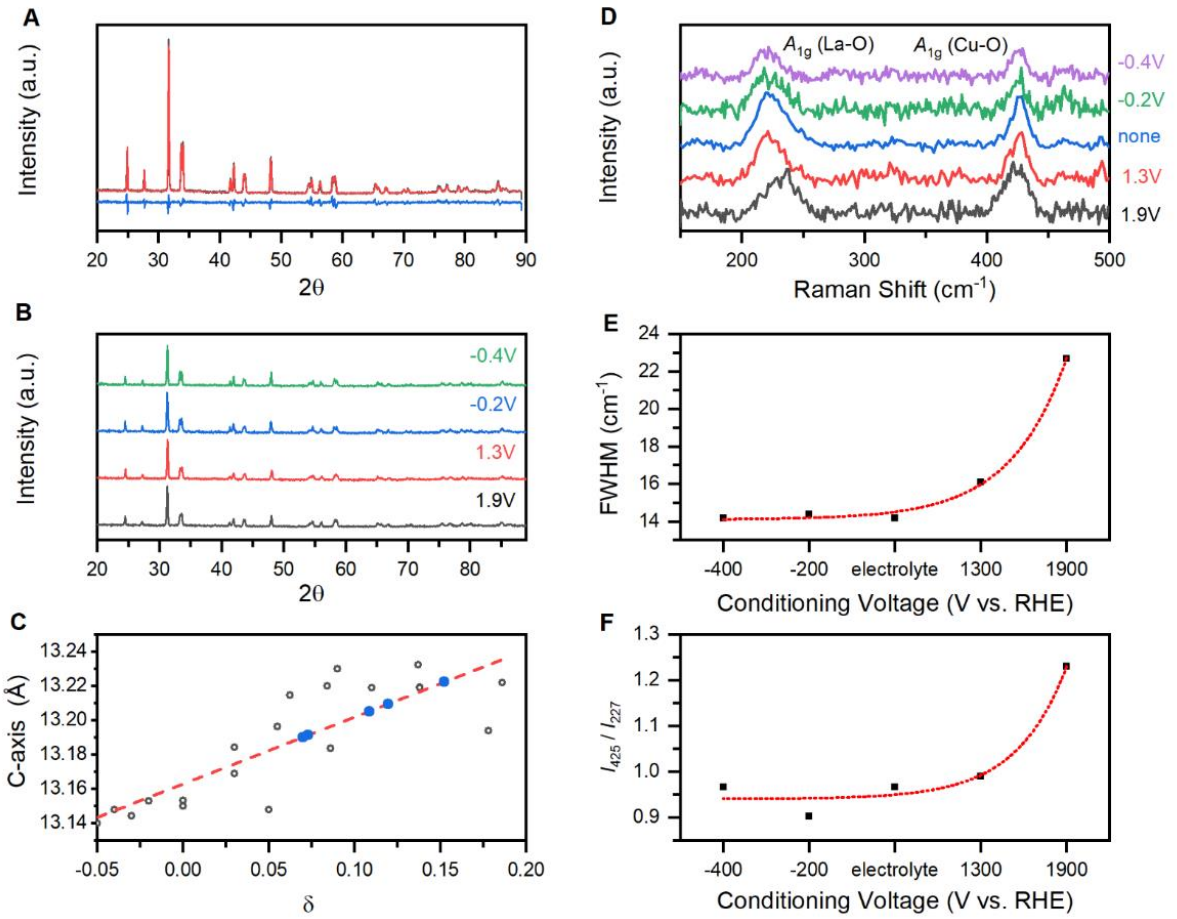

Figure 3.2: PXRD and Raman spectroscopic analysis for $La_2CuO_{4+\delta}$. (A) XRD pattern for pristine $La_2CuO_{4+\delta}$ and the Rietveld refinement fit using the *Cmce* space group. (B) PXRD patterns for the electrochemically conditioned $La_2CuO_{4+\delta}$ phase after chronoamperometry at -0.4, -0.2, 1.3 and 1.9 V vs RHE for three hours. (C) The calibration curve of δ against *c* derived from literature values (open black circles) used to estimate oxygen non-stoichiometry from Rietveld refinement. The samples analyzed in this chapter are plotted as blue circles. (D) Raman spectra acquire of pristine and electrochemically conditioned samples. (E) The full width half mass for the A_g stretching vibration involving the Cu-O bond and the intensity ratio (F) of the Cu-O stretch against the La-O stretch. The trendlines in (E) and (F) are shown in red to guide the reader.

Table 3.1: Unit cell parameters of electrochemically conditioned samples.

Treatment	*a* (Å)	*b* (Å)	*c* (Å)	ΔV (Å^3)	δ [a]
1.9 V	5.383 (0.001)	5.423 (0.001)	13.222 (0.001)	0.0104	0.15
1.3 V	5.374 (0.001)	5.419 (0.001)	13.205 (0.001)	-0.3569	0.11
as-prep	5.382 (0.001)	5.429 (0.001)	13.210 (0.001)	-	0.12
-0.2 V	5.378 (0.001)	5.424 (0.001)	13.190 (0.002)	-0.3112	0.07
-0.4 V	5.378 (0.001)	5.428 (0.001)	13.191 (0.001)	-0.2231	0.07
-0.8 V	-	-	-	-	-

[a] estimated through comparison with literature; see Figure 3.2C

Raman spectra of electrochemically conditioned LCO reveals systematic changes to the location, width, and relative intensity of Cu-O vibrations. Four Raman active vibrations are predicted for RPO structure, but only two have been experimentally observed and consistently assigned.[149,156] The first vibration, located at 225 cm^{-1}, arises from the symmetric movement of La ions along the c-axis with A_g symmetry.[149,156] The second vibration at 420 cm^{-1} is a symmetric stretch of Cu-O_{ax} along the c-axis with A_g symmetry.[149,156] Both vibrations are present for the pristine and electrochemically conditioned samples (Figure 3.2D). More vibrations are observed between 500-1000 cm^{-1} (Appendix A.2) but will not be discussed because their assignments vary amongst literature reports. The Cu-O_{ax} vibration broadens as the sample is oxidized and decreases in intensity relative to the La-based vibration (Figure 3.2E and 3.2F). In comparison, the width of the La-based vibration remains static (Table 3.2).

Table 3.2: Peak parameters used for the curves employed during the peak fitting process. Samples fit include pristine La_2CuO_4, in addition to oxidized and reduced phases.

	A_g (La-based)			A_g (O-based)		
Treatment	Center	FWHM	Height	Center	FWHM	Height
1.9 V	232.34	29.35	1094	423.25	22.71	1346
1.3 V	222.79	25.25	1077	425.58	16.10	1066
as-prep	224.42	29.00	1468	426.46	14.17	1418
-0.2 V	221.66	29.38	419	425.12	14.37	378
-0.4 V	224.42	29.00	1468	426.46	14.17	1418

XPS shows that electrochemical conditioning of LCO increases the content of hydroxides and changes the Cu oxidation state on the surface. The XPS spectra for pristine LCO is like those previously reported for $La_{2-x}Sr_xCuO_4$, with Cu $2p_{3/2}$ and $2p_{1/2}$ peaks located at 932.9 and 952.7 eV

(Figure 3.3A).[26] Two shake-shakeup satellites, a feature associated with Cu^{2+}, are also visible at 941.7 and 962.2 eV. The shake-up satellite associated with Cu $2p_{3/2}$ has two components at 940.61 and 942.81 eV which have been previously reported.[157] Because these shake-up satellites are associated with paramagnetic Cu, a decrease of intensity would indicate the accumulation of diamagnetic Cu^{+}/ Cu^{3+}. The main Cu $2p_{3/2}$ peak undergoes a shift from 932.9 eV to 934.1 eV when anodized. Reduction of LCO causes the same peak to shift 932.8 eV. Due to significant overlap of Cu 2p peaks for Cu^{0} and Cu^{+}, analysis of the LMM region is needed to increase confidence in assignment of surface species. The LMM spectra for the pristine sample has a peak with a kinetic energy of 918.2 eV with a low energy shoulder similar to CuO (Figure 3.3B).[157] The main peak shifts to 916.1 eV following reduction and 914.6 eV after oxidation. The reduction-induced shift of the main peak indicates the formation of Cu^{+}, the accumulation of surface hydroxide or both. Absence of a strong peak at 918.6 eV indicates that Cu^{0} is not present after cathodic conditioning. Pristine LCO has a O1s spectra with three visible components with binding energies of 528.5, 530.2 and 531.9 eV respectively (Figure 3.3C). These features have been reported as lattice oxygen[158], surface-bound carbonates[159], and oxides of adventitious carbon species respectively in other RPO phases. Prevalence of 531.3 and 531.4 eV components in the O 1s spectra for electrochemically conditioned samples is consistent with the complete conversion of surface oxides to hydroxides.

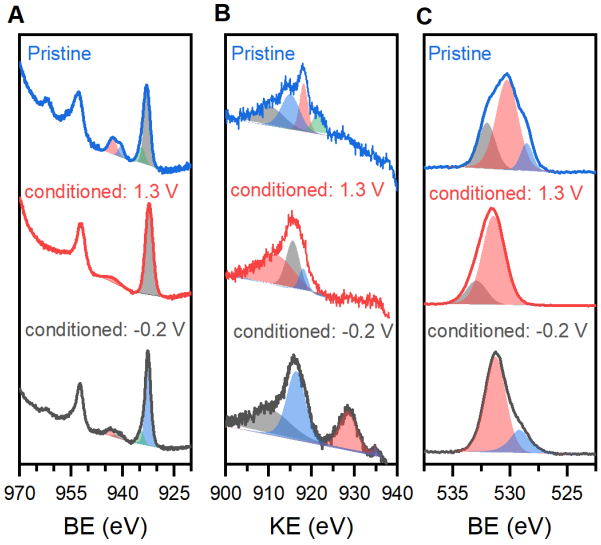

Figure 3.3: X-ray photoelectron spectroscopy of the pristine, anodized and cathodized forms of La_2CuO_4. The (A) Cu 2p, (B) Cu LMM and (C) O 1s regions are shown.

3.2.3 Modifications of the Surface and Small Molecule Interactions

Modification to the morphology of LCO particles is visible by electron-microscopy following electrochemical conditioning. The pristine sample shows sintered clusters of smaller crystallites that range from ca. 100 to 500 nm in size (Figure 3.4). Oxidation of the sample at 1.3 V appears to preserve the original morphology of these particles, however, reduction at -0.8 V results in the formation of platelet-like structures. Analysis of LCO lattice planes using electron-microscopy is not possible because of electron-induced damage to the material (Appendix A.3). This is evident by the formation of large nodules on particle under higher magnification. This prevented further analysis of amorphous shells and other nano-sized features because of the electron beam induced phase changes.

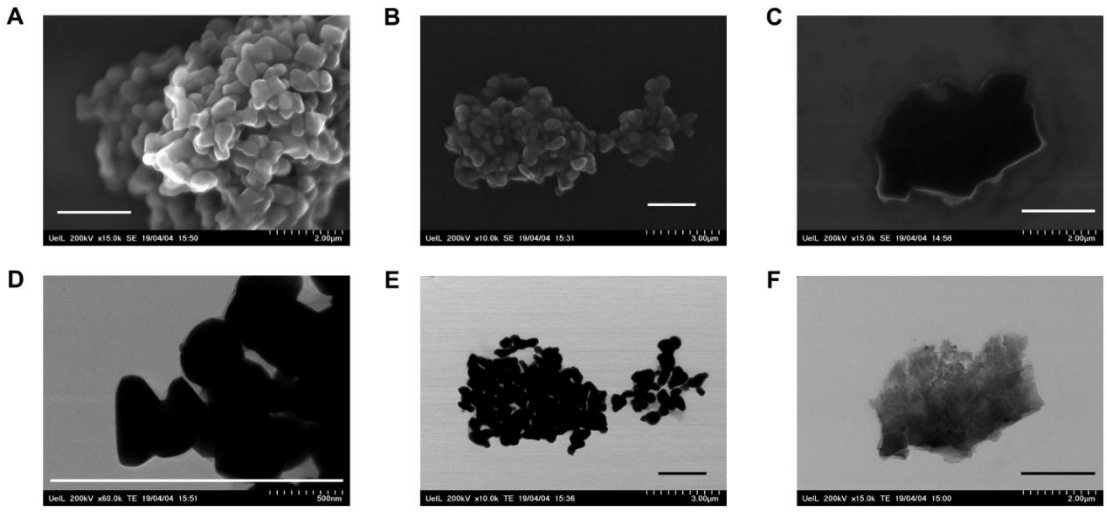

Figure 3.4: Electron micrographs obtained in (A-C) SEM and (D-F) TEM configurations on pristine (A, D) La_2CuO_4, (B, E) anodized and (C, F) cathodized forms of La_2CuO_4. The lines drawn on each sample represent 2 µm.

Voltammetric characterization of pristine, oxidized, and reduced LCO phases under N_2, O_2 and CO_2 purged environments shows that electrochemically induced structural changes have consequences for the observed electrocatalytic activity. Purging the solution with N_2 gas shows an exponential increase of current at ca -0.4 V that is consistent with the onset of HER. Switching the purge gas to CO_2 indicates a strong interaction between CO_2 and the surface of LCO (Figure 3.5A). The onset of exponential current shifts anodically to -0.3 V with the appearance of new anodic

process at 0.65 V and two cathodic peaks at 0.53 and -0.18 V. The irreversible current offset observed under N_2 purged conditions are intensified when O_2 gas is introduced to the electrolyte solution, a finding that supports electrocatalytic ORR activity (Figure 3.5B). The number and current density of redox processes under O_2 purged conditions are nearly identical to those under N_2. Introduction of CO_2 to the electrolyte solution completely suppresses the cathodic current offset observed under N_2 and O_2 purged conditions. These findings appear to support a that reaction between CO_2 and the surface of oxidized LCO occurs. The fundamental redox processes observed on the oxidized sample are very similar to the pristine sample. All three peaks observed on the pristine material persist after oxidation, but the onset of catalytic current near -0.5 V shifts anodically by *ca*. 100 mV. When the oxidized sample is cycled under O_2 purged electrolyte an increase in current density beyond 0.8 V suggests that it retains ORR activity. The magnitude of the current density is attenuated relative to the pristine sample. Samples reduced at -0.4 V show the same three peaks observed under CO_2 for pristine and oxidized samples. The cathodized sample is different, however, because the current offset observed for other samples is much smaller under O_2 and CO_2 purged conditions. The different voltametric behaviours observed for pristine and electrochemically treated LCO confirms that electrochemically induced phase changes affect interactions between the surface and electrocatalytically relevant small molecules.

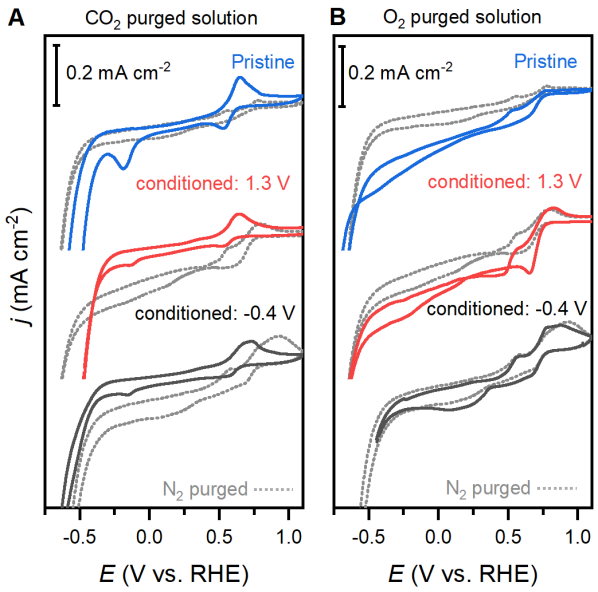

Figure 3.5: Cyclic voltammetry of La_2CuO_4 under CO_2 purged conditions (A) and O_2 purged conditions (B) after electrochemical conditioning. The dashed lines represent cyclic voltammograms acquired under N_2 purged conditions.

Table 3.3: Yields and faradaic efficiency after CO_2 reduction for 3 hrs ^{1}H:NMR

	Formate		Acetate		Product ratio
Treatment	mmoles	Efficiency	mmoles	Efficiency	Formate:Acetate
-0.4 V	6.77	20.9%	0.239	2.95%	7.1
None	1.20	18.8%	0.201	12.6%	1.5
+1.3 V	2.53	15.4%	0.087	2.13%	7.2

Differences in product distribution between the pristine and conditioned phases provides additional evidence that electrochemically induced phase changes can alter the reaction pathway taken for ECR. ^{1}H:NMR spectra (Figure 3.6; Table 3.3) of the electrolyte following electrolysis shows an up-field singlet located at 8.326 ppm and a downfield singlet located at 1.785 ppm. The lack of peak splitting indicates that there are no protons on adjacent carbons. The singlet with significant up-field chemical shift is characteristic of formate due to the proximity of an electron withdrawing carboxyl group. The singlet located downfield is characteristic of a methyl-group adjacent to an electron-withdrawing group. Comparison of this peak to a sodium acetate standard confirms that this peak belongs to acetate. The relative ratio of formate:acetate Faradaic efficiencies provides direct evidence that the

electrochemically induced phase change alters the reaction pathway taken (Table 3.3). This ratio changes from 1.5 for the pristine sample to 7.1 and 7.2 for the reduced and oxidized phase, respectively. The cathodically-induced phase change is expected to continually alter the electrocatalytic properties of pristine and oxidized samples during electrolysis, although it prevents more nuanced analysis of electron-transfer kinetics and product analysis.

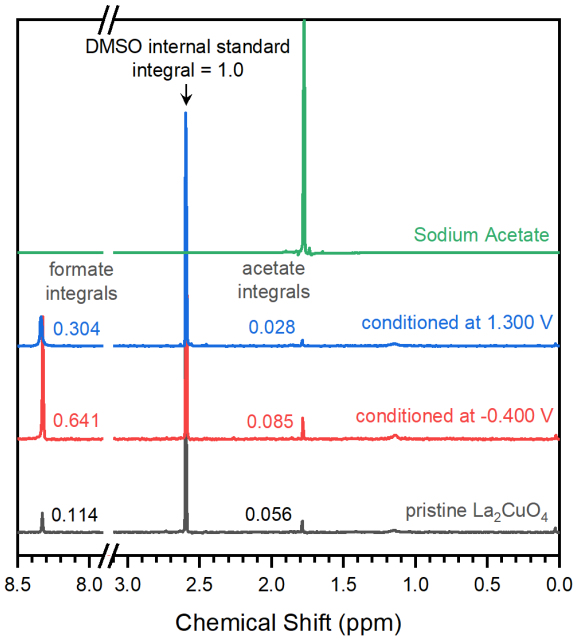

Figure 3.6: ^{1}H:NMR of electrolyte solutions taken after after 3 hrs of chronoamperometry for anodized (Blue), cathodized (Red) and pristine (Black) La_2CuO_4 samples. A sodium acetate standard is shown in green.

3.3 Discussion

The ability to change the composition and oxygen stoichiometry in cuprate-based RPOs provides a handle to control both ionic and electronic conductivity in the lattice. Such properties provide a means to manipulate the electrocatalytic behaviour of RPO to achieve optimal cathode properties. While mixed conductivity is desirable, it also introduces significant disorder that can be detrimental during long-term electrolysis. In this chapter, three key electrochemically induced structural modifications in LCO are identified, each which have subtle impacts on the electrocatalytic reduction of H_2O, CO_2 and O_2.

3.3.1 Key Electrochemically Induced Phase Changes

The first process is an irreversible oxidation located at 1.2 V, which has previously been assigned to the oxidation of Cu^{2+} to Cu^{3+}, followed by incorporation of adsorbed oxygen into the bulk of the structure.[41,133,143,144] A cathodic peak that is also located at 1.2 V accompanies the oxidation process, but is undetectable upon subsequent cycles. The disappearance of this cathodic peak even after prolonged chronoamperometry at 1.3 V allows us to assign the process to the reduction of Cu^{3+} accumulated on the surface. The expansion of unit cell volume following oxidation and the simultaneous loss of paramagnetic Cu^{2+} indicates that oxygen was incorporated into the interstitial sites of the rocksalt (LaO) layer. By utilizing the calibration curve made in Figure 3.2C, we assign δ = 0.12 for the pristine phase, δ = 0.11 for the sample conditioned at 1.3 V and δ = 0.15 for the sample conditioned at 1.9 V. These values appear to reinforce what is expected for 1.3 V which is a surface driven process which has a comparable δ to the pristine phase, and 1.9 V which follows the anticipated expansion of the unit cell.

Characterization of cathodic redox processes in LCO is not well documented, however; limiting to -0.4 V to 1.1 V vs RHE seems to yield stable, reproducible redox behavior for LCO (Figure 3.1A). Four Cu-based redox processes are observed in this region: $E_{p,a2}$, $E_{p,a1}$, $E_{p,c2}$ and $E_{p,c1}$. To assign these processes peak capacitance (Figure 3.7 A and C) and current (Figure 3.7 B and D) was examined as a function of scan rate (ν). Analysis of the peak current for $E_{p,a1}$ and $E_{p,a2}$ shows that they show linear dependence on ν and $\nu^{1/2}$ respectively. Modelling $E_{p,a2}$ according to the Randles-Ševčík equation (Equation 3.1) indicates that it is a bulk process following semi-infinite diffusion regime Figure 3.7D.

$$i_p = 0.4633\left(\frac{nF\upsilon D}{RT}\right)^{\frac{1}{2}} \qquad (3.1)$$

In contrast, $E_{p,a1}$ varies linearly with ν, in accordance with a surface bound process with finite diffusion (Figure 3.7C). Based on these findings, we assign $E_{p,a1}$ and $E_{p,a2}$ to the oxidation surface and bulk Cu^{+} respectively. The constant peak capacitance $E_{p,a1}$ (Figure 3.7A) indicates that this is a surface process. Analysis of the cathodic peaks using method is not possible because of significant overlap between an irreversible cathodic current and the broadness peak, both that decrease confidence in results obtained by peak fitting. Changing the voltage window of the CVs allows for the analysis of these peaks by probing their relationship to the anodic processes. Limiting the voltage window to -0.4 to 0.7 V causes both $E_{p,a2}$ and $E_{p,c2}$ to disappear allowing for the assignment of these

peaks to the $Cu^{2+/+}$ redox process within the bulk of the catalyst (Figure 3.1A). Using similar reasoning the $E_{p,a1}$ and $E_{p,c1}$ peaks are also linked and can be assigned to the $Cu^{2+/+}$ process on the surface. The offset of the CVs at 0.8 V (Figure 3.1C) indicate a in irreversible reduction of Cu that causing the unit cell to contract. Oxygen vacancies cause LCO to contract[41,133,137,143,144] and it is unlikely that electrolyte components K^+ and ^-OH will intercalate into the structure. The change in oxygen stoichiometry is small and no signs of structural degradation was observed following cathodization. Therefore, the crystal structure is maintained in this region.

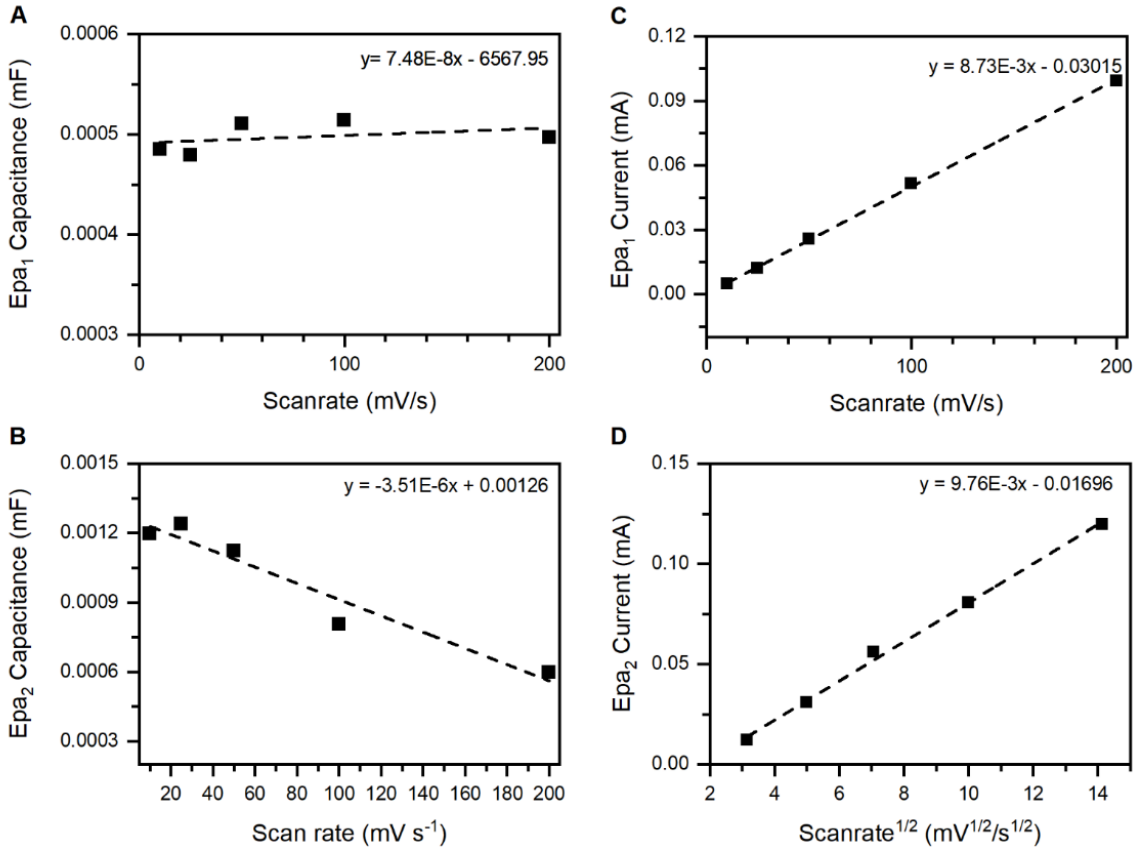

Figure 3.7: The peak capacitance (A, B) and peaks current (C, D) behaviour that arises from variable scan rate experiments for $E_{p,\,a1}$ (A, C) and $E_{p,\,a1}$ (B, C).

Utilization of voltages more cathodic than -0.4 V destroys the crystal structure of LCO. Complete amorphization of LCO is apparent from the complete disappearance of all Bragg peaks in the diffraction pattern, and TEM where the morphology changes to a platelet-like structure (Figure 3.4F).

Voltammetric characterization of this phase does not match the redox processes of metallic Cu and XPS does not support the formation of Cu^0 in the Cu 2p or Cu LMM region.

3.3.2 Consequences of Electrochemical Conditioning on Small Molecule Interactions

Cathodic amorphization of LCO impedes the long-term analysis of the structural changes and electrochemically induced-defects, but transient voltammetric analysis of the pristine material provides useful insights into surface-small molecule interactions. ORR cathodic current at 0.8 V vs RHE is related to the decrease in oxygen stoichiometry within the material. Changes to unit cell parameters suggests that vacancy formation involves the reduction of Cu^{2+} which decreases the oxygen stoichiometry in the bulk of the material. The identical currents between N_2 and O_2 for LCO after cathodic conditioning demonstrates that cathodically-induced amorphization completely inhibits ORR. The CVs are essentially superimposable suggesting that the complete amorphization inhibits ORRs and the process that introduces oxygen vacancies into the material. This suggests the ordered crystalline phase is therefore necessary to facilitate ORR at appreciable rates and electrochemical conditioning. Further, this suggests that oxygen vacancies are likely formed simultaneously during ORR. The maintenance of the RPO structure for ORR appears to follow conventional theory for oxygen-exchange kinetics described in Chapter 1, whereby oxygen migrates through the lattice in well-defined pathways.[35]

Introduction of CO_2 is concurrent with a well-defined reduction process near the onset of an irreversible phase changes, implying an interaction between CO_2 and defects. A new peak observed at -0.2 V and an anodic shift of the electrocatalytic current demonstrates a significant interaction between CO_2 and the LCO phases. Oxidation of LCO at 1.3 V yields similar current densities under CO_2 and ORR purged conditions. The oxidized phase has a larger current offset under O_2 due to a decrease in oxygen stoichiometry on cathodic scans; inhibition cathodic currents with CO_2 provide additional support for binding of CO_2-surface after reduction at 0.8 V. Cathodic amorphization is especially relevant because it occurs at voltages near the onset of ECR.

Similar redox processes to those previously discussed are observed in the presence of CO_2, suggesting that amorphization does not interfere with the initial binding of CO_2 to the surface of LCO. Cathodic shifts of catalytic currents relative to those observed in N_2 purged conditions, but the continued production of formate and acetate indicates that this shift arises from attenuation of electron-transfer kinetics rather than a complete loss of ECR capabilities. Modification of ECR

selectivity and electrochemical properties after conditioning underscores the importance of structural stability as a critical factor in the development of RPO cathodes. Compositional tuning is sometimes employed to address stability concerns for RPO cathodes, but inconsistency of reported ECR products on polycrystalline $La_{2-x}Sr_xCuO_4$ implies that structural modification and amorphization impact other members of cuprate RPOs. Rigorous structural and electrochemical characterization should be done when discussing catalysis RPO electrocatalysts.

3.3.3 Amorphization and Defects in the Literature.

The amorphization observed in this chapter extends to data reported on $La_{2-x}Sr_xCuO_4$ (*I4/*mmm) cathodes for ECR, however, analysis on electrochemically induced phase changes is seldom discussed. In one instance, the authors reported that that $La_{1.8}Sr_{0.2}CuO_4$ yields C_2 and C_3 alcohols with a combined faradaic efficiency of 20%; such rare and narrow selectivity is highly valued for ECR.[141] *Ex-situ* analysis of these phases by PXRD reveals a simultaneous shift of (113) and (200) planes with moderate peak broadening. A shift of lattice plane position suggests that the loss of lattice oxygen from the bulk structure that coincides with the results presented in this chapter. A decrease of long-range order, indicated by peak broadening also agrees with voltametric characterization. It also appears that the introduction of disorder is synonymous with a decrease C_2 and C_3 products. These findings are similar to our observation that the formate:acetate ratio is altered by significant amorphization implying that the RPO structure may assist the facilitation of C-C coupling (Table 3.3). A similar set of experiments was repeated in 2014[142] yielding hydrocarbons instead of alcohols, but *ex-situ* characterization is unavailable, highlighting the importance of phase change analysis. Recent reports utilizing La_2CuO_4 for ECR indicates that the breadth of selectivity is much broader than previously thought, and that product distributions obtained from these phases are highly sensitive to nano-structuring,[160] defects[161] and *in-situ* phase changes.[162] Interestingly, nanostructures and grain boundaries tend to form CO, CH_4, C_2H_4 as products. In neutral electrolytes, Cu nanoparticles were shown to form on the surface of LCO with high selectivity for CH_4. Alkaline electrolysis with defect-laden LCO compositions replicates the selectivity for C_2/C_3 alcohols previously reported on $La_{2-x}Sr_xCuO_4$, providing convincing evidence that oxygen vacancies are critical for controlling reaction trajectory. While ECR is a complex process, being influenced by factors such as the electrolyte, pH, partial pressure of CO_2 and potential applied, careful study of structural modifications is critical for guiding RPOs cathode development.[50]

Few reports are available that assess ORR performance at low temperature in aqueous electrolytes, however, SOFC and oxygen mobility studies provides context to compare our findings against.[140] Analysis of ORR kinetics for $La_{2-x}Sr_xCuO_4$ at intermediate temperatures (500-700 °C) shows that phase remains stable after prolonged ORR and the high temperature formation oxygen vacancies enhance catalyst kinetics.[140] ORR on pristine LCO appears to reflect this finding as evident by the increased offset of cathodic current observed under these conditions. Complete inhibition of ORR after amorphization is consistent with the conventional understanding of oxygen exchange kinetics on RPOs. Such findings reinforce that ORR relies on bulk mobility of oxygen through well-defined pathways in the crystal lattice, leaving behind oxygen vacancies that can further react with oxygen.[35] Preventing such phases changes should be a key consideration when developing RPO cathodes that rely on oxygen mobility.

3.4 Conclusion

In this chapter, the cathodic electrochemical behaviour of LCO under conditions pertinent to HER, ORR and ECR was thoroughly analyzed. The oxygen stoichiometry of pristine LCO increased when anodized at voltages beyond 1.2 V for prolonged durations. Expansion of the unit cell following electrochemical oxidation maintains the RPO crystal structure in accordance with previous reports. Novel structural changes were observed in a stable region between 0.8 and -0.4 V, increasing the oxygen deficiency of LCO and induced a contraction of the unit cell along the *c*-axis. Potentials more cathodic of this stable region cause complete amorphization of structure, yielding plate-like structures without long range order. XPS indicates an abundance of surface-bound hydroxides and a loss of paramagnetic Cu^{2+}, however; no Cu metal is observed. Voltammetry under N_2, O_2 and CO_2 purged conditions after electrochemical pre-treatment indicates that cathodic amorphization has consequences for ORR and ECR. Sr-substituted LCO materials have reported interesting activity for ECR, but with differing product distributions. Results of this study indicate that oxygen mobility in LCO phases can introduce structural instability in the cathodic voltage regime where ECR takes place and should be a key consideration for the development of cuprate-based RPOs.

3.5 Experimental Details

3.5.1 Synthesis

La_2CuO_4 was synthesized from a citrate-nitrate gel precursor using a modified literature report. Citric acid was added to an aqueous solution containing stoichiometric amounts of $La(NO_3)_3$ (99 % purity, Alfa Aesar) and $Cu(NO_3)_2$ (ACS grade, Fischer Scientific) in milli-Q water (18.2 MΩ) and was mixed vigorously until dissolved. This solution was heated to 90 °C under vacuum yielding a viscous dark blue liquid that was dried overnight at 120 °C. A bright blue solid was obtained and ground with an agate mortar and pestle to reduce the particle size. The ground solid was loaded into porcelain crucible and transferred to a muffle furnace that was ramped to 980 °C for 12 hours. The resulting product yielded a black solid.

3.5.2 Electrochemistry

The electrodes used in this study were prepared by drop casting 200 μL of an ethanol-based suspension containing La_2CuO_4 (50 mg ml^{-1}) and 0.125 % Nafion (from 5 % suspension in 1-propanol and H_2O, Alfa Aesar) onto freshly polished (50 nm Al_2O_3, Metlab Corporation) wafers of glassy carbon (Hochtemperatur Werkstoffe GmbH, Germany). Electrodes were then mounted into a custom electrochemical cell made of high-density polyethylene, where a silicone O-ring masks the active surface area to 1.894 cm^2. The working electrode was connected to the potentiostat via an electrical contact made by affixing copper tape to the rear of the glassy electrode. Electrochemical measurements were acquired using a BioLogic SP300 potentiostat. The modified glassy carbon electrode served as the working electrode, a Hydroflex Reversible hydrogen electrode (RHE; Gaskatel GmbH, Germany) was used as the reference electrode and a platinum mesh as the counter electrode. Measurements used 1 M KOH (aq) deaerated with N_2. Voltammetry was performed at 5 mV s^{-1} unless otherwise stated.

3.5.3 Structural Characterization

Electron microscopy was performed on a Hitachi HV2000 STEM with a 200-kV acceleration voltage and a 30 μA current. X-ray diffraction experiments were performed on a Panalytical diffractometer equipped with a flat sample stage using a 2θ range of 10 to 90°. Ex-situ experiments on electrochemically conditioned samples were performed by scraping material from glassy carbon electrodes into acetone using a polypropylene spatula. The suspension was then drop cast onto a

silicon (001) crystal mounted atop an aluminum stage for XRD analysis. Unit cell parameters were extracted through Rietveld refinement of the diffraction data using the GSAS-2 software package.[103] Fitted parameters include particle size, La and Cu thermal parameters, and fractional oxygen occupancy.

3.5.4 Raman Spectroscopy

Raman spectroscopy was carried out with a Renishaw inVia Raman microscope. Spectra were acquired using a 532 nm laser filtered to 1 % laser power with neutral density filters. Each spectrum was acquired over a period of 480 seconds. Spectra were analyzed in Renisaw WiRE V5.2 software, where baselines were subtracted using a polynomial function.

3.5.5 Electrolysis and ^{1}H:NMR Product Analysis

Electrolysis was carried out in a custom-made high-density polyethylene cell where two-compartments are separated by a Nafion 117 membrane. A constant CO_2 purge into the electrolyte was maintained during the electrolysis. The potential was held at −0.3 V for 3 hours. An 800 µl aliquot of the electrolyte solution from the working electrode compartment was combined with 100 µl of D_2O and 100 µl of DMSO as an internal standard. ^{1}H:NMR experiments were run on a Bruker 500 MHz NMR.

Chapter 4: Mechanistic Insights into the Spontaneous Reaction Between CO_2 and $La_{2-x}Sr_xCuO_4$

This chapter is reproduced in part with permission from Canadian Science Publishing: A. W. H. Whittingham, J. Lau, R. D. L. Smith, *Can. J. Chem*. **2021**, 99, 773-779 (DOI:10.1139/cjc-2021-0059)

Contribution statements: Synthesis, structural characterization, and most electrochemical experiments was performed by A. W. H. Whittingham. J. Lau acquired some electrochemical and *in-situ* spectroelectrochemical measurements. Additional data analysis and proofing was done by R. D. L. Smith.

4.1 Introduction

In Chapter 1, electrochemical CO_2 reduction was identified as a promising solution to convert renewable electricity into carbon neutral fuels and petrochemicals.[49–51] Realization of ECR at appreciable scales necessitates a deep understanding of the interactions that guide multiple proton and electron transfers towards a desired product. At the scale of the catalytic system, the feasibility of ECR is contingent on a variety of factors including surface-CO_2 interactions, selection of electrolyte[163], solvent[164], temperature[165], and the composition of the material. A key mechanism for controlling and enhancing the ECR is CO_2-surface interaction. CO_2-surface interactions are directly influenced by the adsorption thermodynamics of transition-metal and p-block elements. The transition metals Ag[166], Au[167], Zn[168], and Pd[169] bind CO_2 strongly and tend to form carbon monoxide as their primary product. Metalloids such as Sn[170], Pb[171] and Bi[172] often yield formic acid because they bind CO_2 quite weakly.[173] Cu is often cited as having optimal CO_2-surface interactions that facilitates further reduction to multi-carbon products such as ethane, ethylene and ethanol that increases its appeal as a ECR catalyst.[174] While the formation of multi-carbon products is desirable the application of Cu-based electrocatalysts often yields a broad range of products that introduce energetic penalties to separate. Evidence suggests that the distribution of products is related to the binding mode of CO_2 after the initial electron transfer.[175] CO_2 has been reported to bind in a variety of configurations, but carbon or oxygen down configurations are most common. Computation studies provide evidence that carbon down adsorption modes form CO and more reduced products while oxygen down configurations favor COOH.[175] Surface-sensitive spectroscopic techniques such as operando-Raman

have detected these intermediates on Au[176] and Ag alloys.[177] These studies provide valuable insights about the interactions of CO_2 on the surface and can guide the development of mechanistic pathways.

An additional layer of complexity is added to ECR when the catalyst material is altered by CO_2 during electrolysis. In Chapter 3, La_2CuO_4 was subject to prolonged electrochemical conditioning that impacted the stability of the catalyst and the product selectivity of ECR.[178] Electrochemical conditioning under anodic and cathodic potentials caused the La_2CuO_4 catalyst to amorphize. Structural degradation of La_2CuO_4 simultaneously switched ECR selectivity away from acetate for the pristine phase, and towards formate, highlighting the need for surface characterization after electrolysis. Such findings suggests that this phenomenon will occur in $La_{2-x}Sr_xCuO_4$ phases that have been applied to ECR, and the impact of amorphization will need to be studied in relation to the selectivity of ECR. Beyond ECR, other studies have also demonstrated that CO_2 surface interaction can have detrimental effects on the performance on electrocatalytic devices. The introduction of CO_2 into the electrolyte of alkaline fuel cells acts as a poison on the membrane and electrode materials that increases electrical resistance in the system.[179] For perovskites specifically, there is the tendency for the A-site atoms, such as Sr, to migrate from their ideal lattice positions and form electrochemically inert carbonates that passivates the electrode.[180,181] Carbonates, however, have also been identified as participants in the reaction pathway for ECR. *In-situ* analysis of Sn/SnO_x electrodes using FTIR with attenuated total reflection (ATR) showed the formation of these carbonates unambiguously and proposed that surface adsorbed carbonates is an intermediate that precedes the formation of formate.[182] The ability to assign CO_2 surface interactions and assess their impacts on electrochemical processes could provide valuable insight for those seeking to enhance electrocatalysis.

This chapter will explore the interactions between CO_2 and polycrystalline RPOs with the composition $La_{2-x}Sr_xCuO_4$ in neutral, aqueous bicarbonate buffer solutions while evaluating catalyst stability. PXRD diffraction patterns and Raman spectroscopy reveal a phase transition from orthorhombic to tetragonal unit cells upon substitution of La(III) with Sr(II). Cyclic voltammograms acquired over a range of scan rates indicates that that reduction of the RPOs results in amorphization via multistep mechanism involving an irreversible chemical step. Voltammetric and impedance experiments under N_2 and CO_2 purged conditions identify a Cu(II) surface species that reacts spontaneously with CO_2 after reduction to Cu(I). *In-situ* infrared spectroscopy shows that surface bound carbonates with variable absorption modes are the only species observed on the surface after reduction. The bidentate carbonate mode of adsorption is primarily associated with LCO and results

in rapid structural degradation, but the conversion to the tetragonal structure disfavors this bidentate mode which stabilizes the material.

4.2 Results

4.2.1 Structural Characterization

PXRD patterns clearly show a transition from an orthorhombic to a tetragonal crystal system when Sr is substituted for La in the $La_{2-x}Sr_xCuO_4$ (LSCO) family of materials. Rietveld refinement of the La_2CuO_4 ($x = 0$) phase (Figure 4.1A) using the *Cmce* space group yields lattice parameters of 5.354, 5.400 and 13.138 Å, respectively (Table 4.1). These results agree with the previous results provided in Chapter 3.[183] These unit cell dimensions indicates that the closest Cu-Cu distances are 3.785 and 3.818 Å respectively, allowing for the direct comparison to Cu-Cu distances in $La_{2-x}Sr_xCuO_4$ crystals using *a* or *b* unit cell parameter. The orthorhombic unit cell of La_2CuO_4 is apparent from the multiplicity of Bragg peaks shown in the diffraction patterns. Peaks belonging to the planes (202) and (022) near 2θ of 33°, (204) and (024) near 43°, (133) and (313) near 58° are doublets for La_2CuO_4 (Figure 4.1B), but they merge into singlets for Sr-doped phases (Figure 4.1D). The orthorhombic structure, and thus the inequivalence in *a* and *b* unit cell parameters, arises from the tilting of corner sharing Cu-O octahedral away from the *c*-axis (Figure 4.1C). This results in asymmetric expansion of *b* relative to *a*. Alignment of the octahedral sites along the *c*-axis (Figure 4.1F) removes the inequivalence between the *a* and *b* parameters which manifests in the diffraction pattern as the absence of Bragg peak splitting (Figure 4.1D). This requires changing the space group used for Rietveld refinements from the orthorhombic *Cmce* to a tetragonal *I4/mmm* unit cell for $La_{1.9}Sr_{0.1}CuO_4$,

$La_{1.8}Sr_{0.2}CuO_4$, $La_{1.7}Sr_{0.3}CuO_4$, $La_{1.6}Sr_{0.4}CuO_4$, and $La_{1.5}Sr_{0.5}CuO_4$ (Figure 4.2).

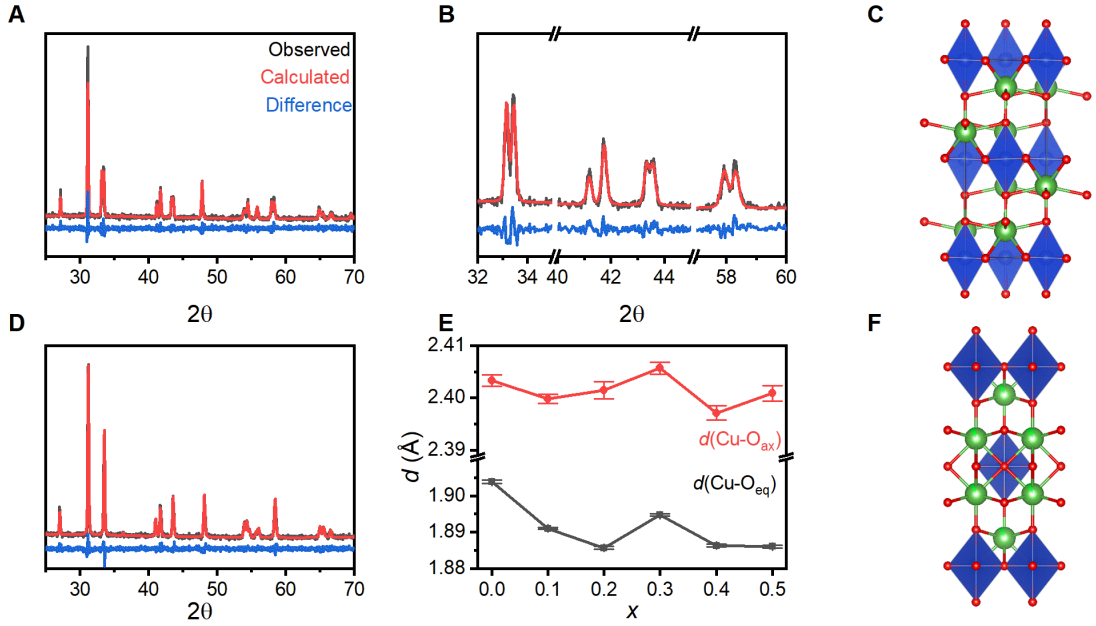

Figure 4.1: Structural analysis of $La_{2-x}Sr_xCuO_4$ phases using PXRD. (A) Rietveld refinement of La_2CuO_4 with the orthorhombic *Cmce* unit cell with (B) the peak multiplicity magnified for between 2θ 32-60 and (C) the unit cell of La_2CuO_4 with the *Cmce* space group. (D) The Rietveld refinement of $La_{1.8}Sr_{0.2}CuO_4$ using the *I4/mmm* unit cell displayed alongside (E) the effect of Sr substitution on the length of axial and equatorial Cu-O bonds. (F) The *I4/mmm* unit cell for $La_{2-x}Sr_xCuO_4$ phases.

Rietveld refinements of $La_{2-x}Sr_xCuO_4$ (x = 0 to 0.5) reveal a gradual contraction of axial and equatorial Cu-O bonds until x = 0.2, after which bond lengths are relatively static (Table 4.1, Figure 4.1E). An electronic charge compensation mechanism is known to take place at Sr concentrations below x = 0.2 where holes are introduced due to the charge mismatch between La(III) and Sr(II).[87,184–187] Concentrations of Sr beyond x = 0.2 result in the formation of oxide vacancies instead of holes as a form of ionic charge compensation.[87,184–187] Therefore, the initial bond contraction between x = 0 - 0.2 can be attributed to the oxidation of Cu(II) to Cu(III) , while the formation of oxygen vacancies is more prevalent for x = 0.3 – 0.5.

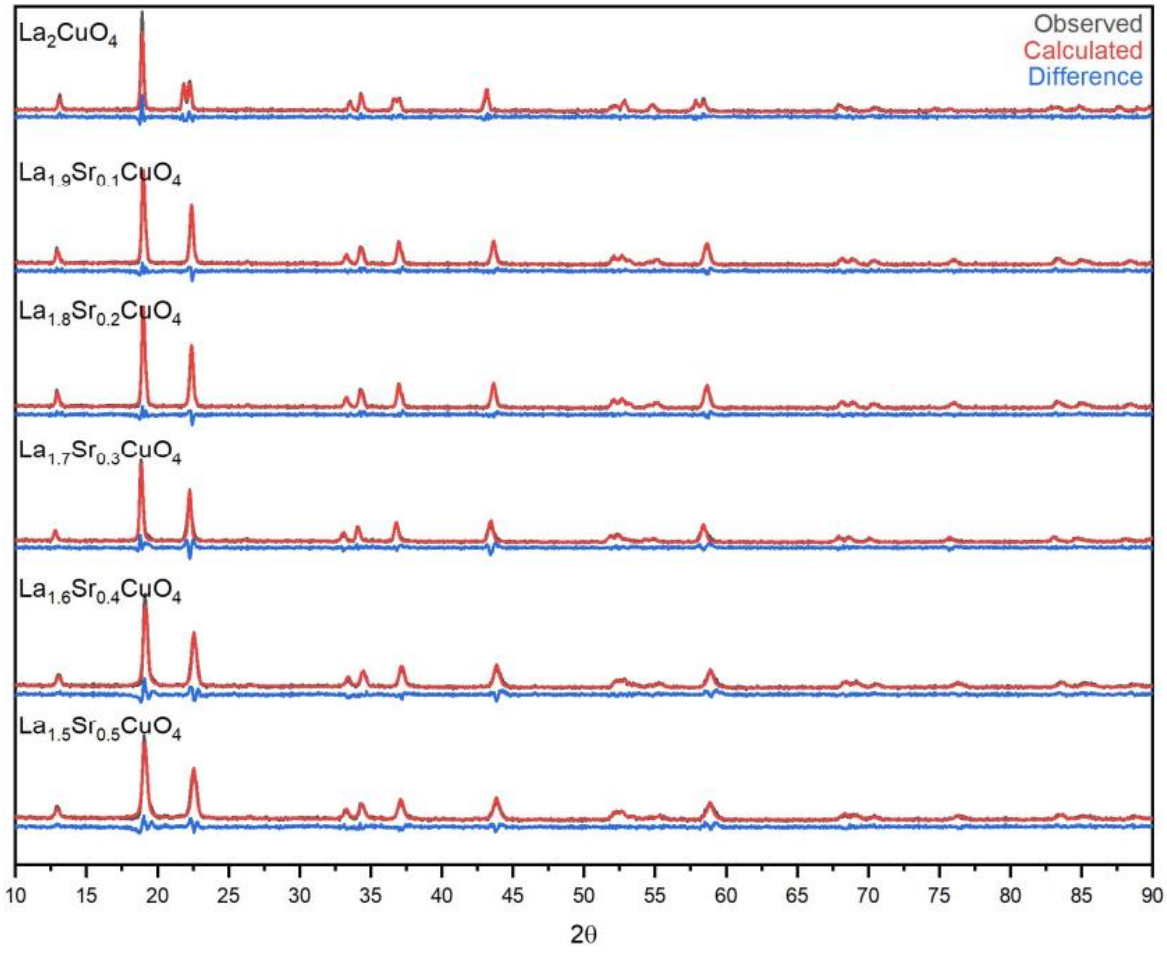

Figure 4.2: Rietveld refinements for $La_{2-x}Sr_xCuO_4$ phases with x = 0, 0.1, 0.2, 0.3, 0.4 and 0.5. Refinement of the powder diffraction patterns was performed using GSAS-2. The raw data (black) is shown alongside the fitting results (red) with the difference between the traces (blue) shown for each refinement.

In Chapter 3, factor group analysis of La_2CuO_4 predicted 15 Raman active vibrations for the *Cmce* space group, while there are only 4 are present for the *I4/mmm* structure.[110,188–191] At cryogenic temperatures (77 K), all 15 Raman active phonons can be observed for single crystal samples, but many of these vibrations disappear at room temperature.[190] Only two vibrations are consistently observed at room temperature for the *I4/mmm* phases, the A_{1g} 225 and A_{1g} 425 cm^{-1} peaks (Figure 4.3A). These peaks are also observed for the un-doped sample; however, additional peaks located at

ca. 504, 685, 882 and 1200 cm^{-1} are present due to the lowing of lattice symmetry from tetragonal to orthorhombic.

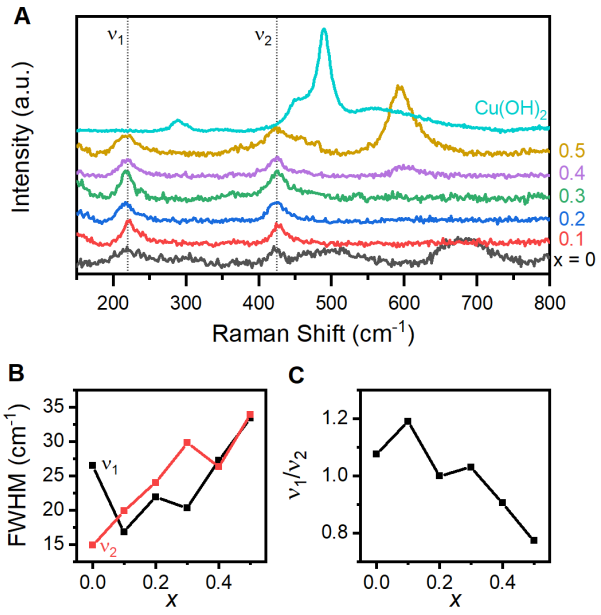

Figure 4.3: (A) Raman spectra for $La_{2-x}Sr_xCuO_4$ phases between x = 0 to 0.5 and $Cu(OH)_2$. (B) the dependence of FWHM on the degree of Sr-substitution for ν_1 and ν_2. (C) The intensity ratio of ν_1/ν_2 as a function of Sr-substitution.

For these Sr-substituted samples only the A_{1g} vibrations are observed, which is consistent with the formation of a lower symmetry tetragonal phase. Because the A_{1g} peaks are observed across the entire sample series these vibrations to assess structural changes in the perovskite and rocksalt layers. Assignment of the 225 and 425 cm^{-1} vibrations was based primarily on single crystal Raman studies, which attributed them to the La(Sr)-O vibration and Cu-O_{ax}-La(Sr) stretching mode. [190,192] These assignments remain the same for the orthorhombic and tetragonal unit cells. The full width at half maximum (FWHM) of both peaks increases substantially as Sr is substituted for La, a finding that is consistent with the introduction of lattice disorder (Figure 4.3B). The ν_1/ν_2 intensity ratio decreases in a roughly linear fashion as the concentration of Sr increases (Figure 4.3C). Such a result is expected, as the 225 cm^{-1} peak is based on the vibration of La ions.[110] Although no impurities are indicated by PXRD, an additional peak is observed at 591 cm^{-1} for the x = 0.4 and 0.5 samples (Figure 4.3A). The formation of this peak coincides with the onset of oxygen vacancy formation caused by the

introductions of large amounts of Sr.[187] This peak is also reminiscent of the T* RPO polymorph that was discussed in Chapter 1 (Figure 1.3E) .[193] To reiterate, the T* phase is partly defined by the absence of an apical oxygen on B-site octahedra, which yields a square pyramidal motif (Figure 1.3E).[3] Neutron diffraction patterns reported for the solid-state synthesis of ceramic $Nd_{2-x-y}Sr_xCe_y$-CuO_4 phases showed that this material crystallizes with the T* structure (x = 0.41, y = 0.27).[194] Raman spectra acquired from $Nd_{2-x-y}Sr_xCe_yCuO_4$ (x = 0.25, y = 0.4) that also possesses the T* structure exhibit strong Raman active vibrations at *ca.* 590 cm^{-1}.[193] The authors speculated that this vibration arises directly from defects or the lattice distortions they introduce. Such findings suggest that the $La_{1.6}Sr_{0.4}CuO_4$ and $La_{1.5}Sr_{0.5}CuO_4$ synthesized in this chapter possess a mixture of the T and T* structure that is difficult to observe by PXRD alone. Overall, the Raman spectra supports the formation of a higher symmetry unit cell in Sr-doped phases with increased disorder in the rocksalt and perovskite layers.

Table 4.1: Rietveld refinement results obtained for $La_{2-x}Sr_xCuO_4$ powders

x	***a***	***b***	***c***	***V***	U_{iso}**(La)**	U_{iso}**(Sr)**	U_{iso}**(Cu)**	R_{wp}
	Å	Å	Å	$Å^3$	$x10^{-2}$ Å	$x10^{-2}$ Å	$x10^{-2}$ Å	%
0	5.361 (0.001)	5.406 (0.001)	13.154 (0.011)	381.2 (0.1)	0.7270	-	1.475	13.78
0.1	3.782 (0.001)	3.782 (0.001)	13.218 (0.010)	188.9 (0.1)	1.313	1.149	1.806	10.94
0.2	3.771 (0.001)	3.771 (0.001)	13.217 (0.002)	188.0 (0.1)	9.650	7.310	2.347	13.34
0.3	3.789 (0.001)	3.789 (0.001)	13.240 (0.001)	190.1 (0.1)	1.497	1.910	1.901	13.32
0.4	3.773 (0.001)	3.773 (0.001)	13.193 (0.001)	187.8 (0.1)	2.502	4.720	2.679	12.76
0.5	3.772 (0.001)	3.772 (0.001)	13.214 (0.002)	188.0 (0.1)	2.376	1.050	2.874	12.39

4.2.2 Electrochemical Behaviour

Voltammetric characterization reveals that all $La_{2-x}Sr_xCuO_4$ phases react spontaneously with dissolved CO_2. Cyclic voltammograms (Figure 4.4A, C and Figure 4.5A) acquired in 0.1 M $KHCO_3$

electrolyte purged with N_2 gas show that all samples have irreversible cathodic current below 0.5 V vs RHE, with a small anodic peak located near ca. 0.7 V when the scan rate is slower than 10 mV s^{-1}. When the window examined is expanded to -0.8 V, where the exponential currents due to HER are visible, the observed redox behaviour appears to be maintained (Appendix B.1). Introducing CO_2 into the electrolyte results in the formation of a cathodic peak at 0.65 V and an anodic peak at 0.85 V (Figure 4.4B, D; 4.5A, B, and C). These peaks are observed at scan rates between 1 mV to 1 V s^{-1} and appear to have positions dependent on scan rate (ν; Figure 4.5B). La(III), Sr(II) and oxide anions are redox inert in the locations where these quasi reversible peaks appear. These peaks are also far too positive to yield products attributed to the initial electrochemical reduction of CO_2 such as formate or carbon monoxide.[195] Although the electrochemical reduction of carbonate and bicarbonate ions is possible[196–198], the lack of redox activity under N_2 purged conditions suggests otherwise. Bulk oxidation of Cu(II) to Cu(III) occurs at voltages near the onset of OER at 1.5 V so it is unlikely that this is the observed redox process.[133,178] The only reasonable assignment of this quasi-reversible process is the reduction of Cu(II) to Cu(I) on the cathodic scan, followed by oxidation back to Cu(II). This process is activated by the presence of CO_2 indicating that a chemical step must participate in the electrochemistry.

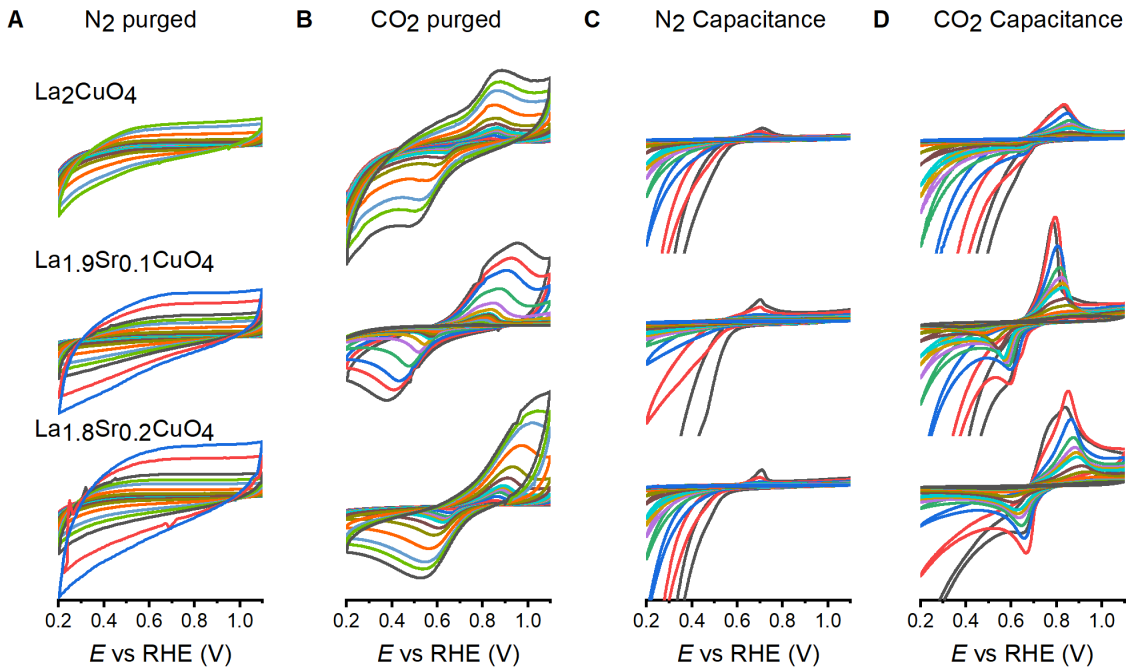

Figure 4.4: Cyclic voltammograms of $La_{2-x}Sr_xCuO_4$ for x = 0 to 0.2 under (A) N_2 and (B) CO_2 purged conditions in 0.1 $KHCO_3$ electrolyte. The same cyclic voltammogram data was normalized to the scan rate to highlight the changes to capacitance under (C) N_2 and (D) CO_2 purged conditions.

The effect of a chemical elementary step on electron-transfer kinetics can be described by the dimensionless parameter λ. This value is essentially a measure of competition between the reaction and the time constant of reaction as indicated by the dependence on the rate constant k and the scan rate ν.[199–202] For practical use in voltammetry, the ratio λ/k is used to measure this competition as is shown by Equation 4.1:

$$\frac{\lambda}{k} = \frac{RT}{Fv} \qquad (\mathbf{4.1})$$

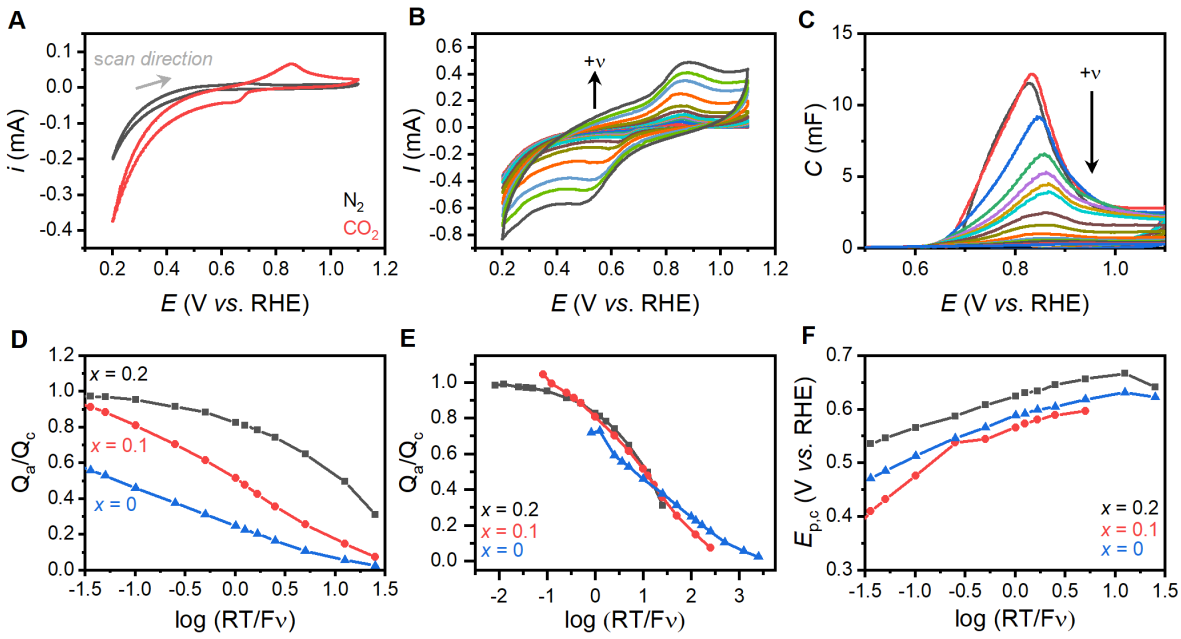

Figure 4.5: Voltammetric characterization of $La_{2-x}Sr_xCuO_4$ phases in 0.1 M $KHCO_3$. (A) Cyclic voltammograms of La_2CuO_4 under N_2 (black) and CO_2 (red) purged conditions with a 10 mV s^{-1} scan rate. (B) Variable scan rate experiment of La_2CuO_4 under CO_2 purged conditions with rates increasing from 1 mV s^{-1} to 1 V s^{-1}. (C) The capacitance plot of the anodic peak during the variable scan rate experiment. (D) The total anodic to cathodic charge transferred Q_a/Q_c for the variable scan rate data. (E) The ratio of charge passed after applying 10- and 100-fold corrections to the ordinate to highlight kinetic changes to the chemical step. (F) Cathodic peak position as a function of variable scan rate.

The electrochemical behaviour of this system is dependent on the scan-rate that controls the effect of chemical steps on electron transfer (Figure 4.5). Plotting the ratio of the anodic to cathodic charge passed (Q_a/Q_c) for CVs against the dimensionless parameter (λ/k) yields a plateau at low values of λ/k (Figure 4.5D). At high values for λ/k this plot approaches zero. This type of behaviour is characteristic of an EC_i mechanism where electron-transfer (E) precedes an irreversible chemical step (C_i).[199–203] This mechanism involves the consumption of the reduction product generated by the E step, by the chemical step. Such a process removes the product for oxidation on the reverse step causing the Q_a/Q_c ratio to approach zero at slower scan rates. We note that the change in Q_a/Q_c observed here is subtly different, arising due to simultaneous growth in Q_c and decrease in Q_a. This finding suggests that the mechanism is more complicated than a standard EC_i. Regardless, the

cathodic peak shifts relative to $E_{1/2}$ as the 1/k term increases (Figure 4.5F), a phenomenon that is characteristic of an EC_i mechanism and displayed by all $La_{2-x}Sr_xCuO_4$ samples. This allows us to assign the shift in Q_c/Q_a towards lower 1/k values with increasing Sr substitution to a decreased rate of reaction for the irreversible chemical step. Multiplying k by 10 for $La_{1.9}Sr_{0.1}CuO_4$ and by 100 for $La_{1.8}Sr_{0.2}CuO_4$ causes the data to overlap with the predicted model (Figure 4.5E). This provides further confidence that the rate of the C_i step decreases as more Sr is incorporated into the lattice.

4.2.3 Electron Transfer Kinetics

Staircase stepped potential electrochemical impedance spectroscopy (EIS) reveals electrochemically active surface sites in the $La_{2-x}Sr_xCuO_4$ that sensitive to the presence of solvated CO_2. Nyquist plots obtained from these EIS experiments (Figure 4.6A) reveals a lone semi-circular feature that can be modelled with a modified Randles circuit. The model consists of the solution resistance (R_s) in series with a parallel RC circuit that includes the charge transfer resistance across the interface (R_{CT}) and the space-charge capacitance (C_{sc}) of the electrochemical double layer (Appendix B.2). All samples examined have R_{CT} values of ca. 13 kΩ at 1.1 V and 600 Ω near 0.2 V under CO_2 purged conditions. The onset of a redox peak located at aligns with a sharp transition between these two values (Figure 4.6B). Mott-Schottky obtained from the C_{sc} of Nyquist fits indicate two sloped regions under CO_2 and N_2 (Figure 4.6C). These plots show negative slopes between 0.4 and 0.6 V that are characteristic of p-type semiconductors.[139] Between 0.6 and 0.8 V, a positive slope belonging to an n-type semiconductor is observed. Extrapolation of the linear fits to the x-axis yields the flat-band potential (V_{fb}). The position of the V_{fb} does not shift substantially between different samples or conditions. For the p-type region the slope of all samples conforms to 0.89 ± 0.1 V under CO_2 and 0.76 ± 0.15 V under N_2. The n-type region has V_{fb} of 0.52 ± 0.06 under CO_2 and 0.58 ± 0.11 V under N_2 purge. The charge carrier densities for the n-type slope increases from 1.4 to 3.7 x 10^8 mol cm^{-3} changing N_2 to CO_2. Plots of C_{sc}^2 vs potential (Figure 4.6D) possess peaks at ca. 0.6 V that increases under CO_2 purged conditions, behaviour that is aligned with a redox active surface state. The capacitive peak is superimposed over the accumulation of irreversible cathodic current observed in the CVs under N_2 purge. A similar observation is made for CO_2 where a cathodic peak emerges from irreversible cathodic currents. The EIS results highlight that the observable redox behaviour of the sample series originates from Cu surface sites. The concentration of these surface sites is magnified by the introduction of CO_2 into solution.

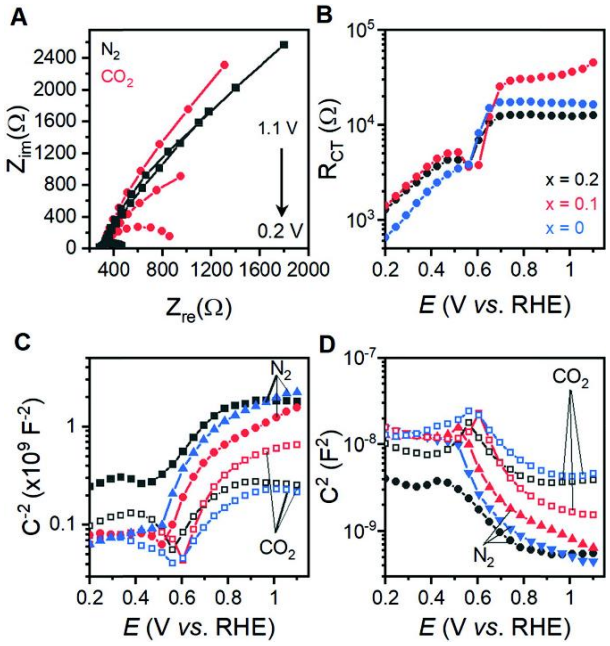

Figure 4.6: AC voltametric characterization of $La_{2-x}Sr_xCuO_4$ (x = 0 to 0.2). (A) sample Nyquist plots for La_2CuO_4 at 1.1 V, 0.6 and 0.2 V vs RHE under different purge conditions. (B) The charge transfer resistance, (C) C^{-2} and (D) C^2 extracted through Nyquist plot fitting as a function of voltage. Samples displayed include $La_{1.8}Sr_{0.2}CuO_4$ (black), $La_{1.9}Sr_{0.1}CuO_4$ (red) and La_2CuO_4 (blue). CO_2 purged conditions are shown as open shapes for panels (C) and (D). Panels (B) – (D) are displayed in semi-log format for ease of interpretation.

4.2.4 Spectroelectrochemistry

The evolution of species on $La_{2-x}Sr_xCuO_4$ surfaces during chronoamperometry was monitored by Fourier transform infrared spectroscopy (FTIR) configured in the attenuated total reflection geometry (Figure 4.7A, B and C). A series of these time-dependent spectroelectrochemical experiments reveals that electron-transfer elementary steps are accompanied by the conversion of CO_2 to surface bound carbonates with material dependent denticity. Experiments were performed at the extremes of voltametric characterization depicted in Figure 4.5A and B: 0.2 and 1.1 V. A single spectral baseline was acquired at OCV prior the start of each 30 min experiment, and subsequent spectra was acquired at 5 min intervals to create a time-series. These measurements were converted into absorbance

spectra, a data processing procedure that can result in positive peaks for accumulated products, or negative peaks for removed species. Spectroelectrochemical analysis of the Sr-free La_2CuO_4 sample (Figure 4.7A) yields two broad positive peaks at 1650 and 1540 cm^{-1} with additional sharp peaks located at 1470, 1369, and 1342 cm^{-1} at 0.2 V. Addition positive peaks at 3210, 1618, 1504, 1470, 1369, 1342 and 1014 cm^{-1} intensify when the potential is switched to 1.1 V with the growth of a negative peak at 3649 cm^{-1}. Purging the electrolyte with CO_2 results in changes to the infrared spectra. Chronoamperometry at 0.2 V introduces positive peaks at 3200, 1626, 1503, and 1365 cm^{-1} with negative peaks at 3570 and 1700 cm^{-1}. The peak at ca. 3600 cm^{-1} is attributed to O-H stretches as surface bound hydroxyls.[204] Peaks in the vicinity of 3200 cm^{-1} originate from interaction of O-H stretches with hydrogen bonds that are almost certainly with H_2O.[205–207] Peaks near 1470, 1365, 1014 have been assigned to solvated carbonate and bicarbonate anions due to their proximity to expected peaks at 1375 and 1430 cm^{-1} for carbonate[208] and 1000 and 1355 cm^{-1} for bicarbonate.[209] The position of these vibrations is consistent with FTIR-ATR measurements of 0.1, 0.5 and 1 M $KHCO_3$ buffer solutions that are expected to contain both species (Appendix B.3). Carbonate can bind to surfaces in either mono or bidentate modes. The monodentate mode yields peaks at 1370 and 1500 cm^{-1},[182,210,211] whereas bidentate carbonate has peaks around 1265 and 1610 cm^{-1}.[182,198,210,211] N_2 purged conditions appear to favour monodentate carbonate species on the surface, while CO_2 purged conditions tend to favor bidentate adsorption. Neither of the Sr-substituted phases stray significantly from the baseline FTIR spectrum under N_2 purged conditions (Figure 4.7B and C). CO_2 purged conditions seem to have comparable spectra to those for La_2CuO_4 at 1.1 V under N_2 purged conditions, with sole formation of monodentate carbonate on the surface. The potential, and time dependent FTIR-ATR experiments appears to support that carbonate and CO_2 adsorption mechanisms are different Sr-dependent processes.

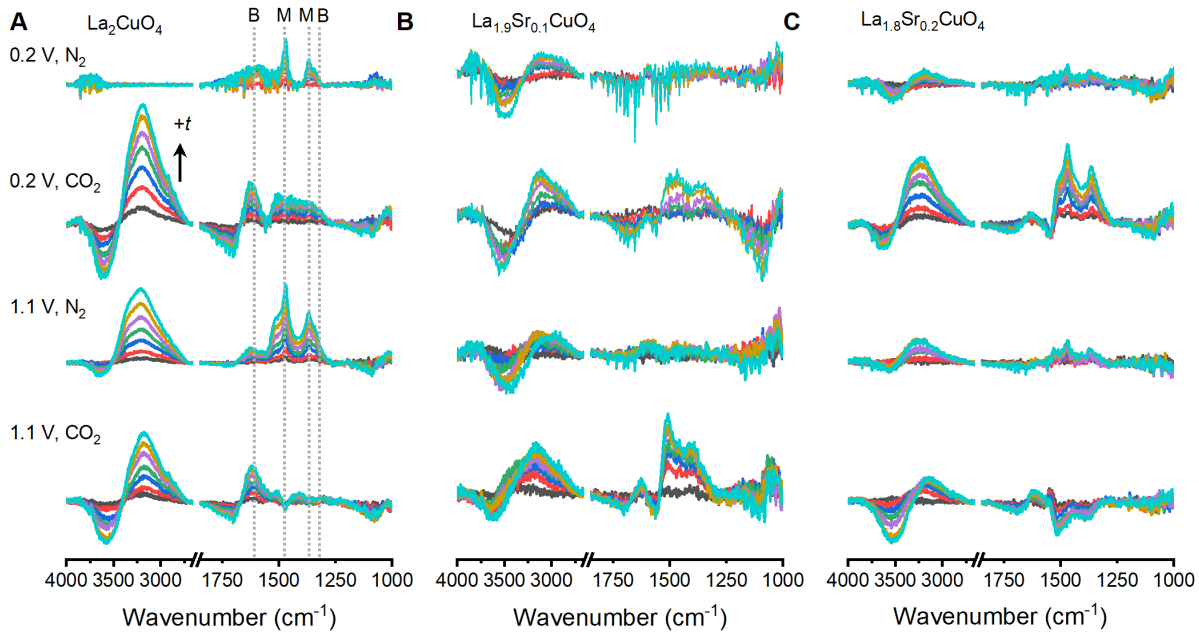

Figure 4.7: *In-situ* FTIR-ATR spectroelectrochemical measurements for chronoamperometric steps from 0.2 to 1.1 V vs RHE under N_2 and CO_2 purged conditions, respectively. Spectra acquisitions occurred every 5 min from 0 (black) to 30 (cyan) min for (A) La_2CuO_4, (B) $La_{1.9}Sr_{0.1}CuO_4$ and (C) $La_{1.8}Sr_{0.2}CuO_4$. A single spectrum was acquired at OCV immediately before each chronoamperometry experiment and was used as the background. Peak assignments for monodentate (M) and bidentate (B) carbonate binding modes are marked on panel (A).

4.3 Discussion

4.3.1 Mechanistic Discussion

Amorphization of LCO under cathodic biases is described by a three-step process that begins with bidentate carbonate bound to the surface that occurs through the reaction of CO_2 with oxygen vacancies. Cu(II) ions are known to undergo Jahn-Teller distortions that elongate the Cu-O_{ax} bond,[212,213] facilitating oxygen vacancy formation.[30,35,184,185,214] The observation of only monodentate carbonate vibrations on the surface of LCO when oxidizing and reducing voltages are used reveals carbonate ions from the electrolyte fill oxygen vacancies. The prevalence of bidentate carbonate as the primary binding mode under CO_2 purged conditions has substantially different geometry from the monodentate, requiring the interaction between two adjacent vacancies or a vacancy and an oxygen.

The former geometry is more likely, because it is directly supported by the disappearance of surface hydroxyls seen by FTIR (Figure 4.7). Reaction of CO_2 with the surface of the RPOs must occur spontaneously because bidentate adsorption is observed at both 0.2 and 1.1 V vs RHE. CO_2 adsorption increases the number of redox activated Cu sites as indicated by the growth of Q_a and Q_c. Electrochemical reduction of Cu(II) to Cu(I) will result in a d^{10} surface site which favors a tetrahedral coordination environment to an octahedral one. The bond distance mismatch between the oxygens in carbonate (2.2 Å) is much smaller than the distance between O_{ax}-O_{eq} (3.03 Å), O_{eq}-O_{eq} (2.68 Å), and O_{ax}-O_{ax} (3.81 Å) bond distances in LCO will introduce significant local strain and introduce instability. The EC_i mechanism observed in this work likely follows three steps: the electrochemical reduction of Cu(II) to Cu(I), followed by CO_2 adsorption and strain induced amorphization of the RPO structure. Increasing Q_c with slower scan rates results from the penetration of the amorphization process deeper into the bulk of the structure and phenomenon which was discussed in the previous chapter.[184] Oxidation of Cu(I) back to Cu(II) regenerates the d^9 state that prefers the octahedral environment, but this process must take place at the catalyst-electrolyte interface. A subsequent decrease in Q_a at slower scan rates is assigned to the partial healing of the structure.

4.3.2 Effect of Sr on CO_2 Adsorption

The results presented here demonstrate that Sr incorporation stabilizes the RPO lattice by inhibiting the reaction pathway that causes instability. Irreversible cathodic current appears for all $La_{2-x}Sr_xCuO_4$ samples, indicating instability, but the rate which the structure deteriorates in the presence of CO_2 is attenuated by several orders of magnitude (Figure 4.5E). *In-situ* FTIR ATR experiments do not detect surface bound carbonate species when N_2 is purged through the electrolyte indicating that the monodentate-bound carbonate is inactive for the parent phase (LCO). In addition, the reaction mechanism for CO_2 on LCO must change because the FTIR results show vibrations that arise solely from monodentate carbonate adsorption (Figure 4.7). Replacement of lanthanum for strontium forces the lattice to convert from the orthorhombic polymorph observed with LCO into a tetragonal lattice for LSCO. This transition arises from the tensile strain introduced from the mismatched atomic radii of La and Sr that causes the otherwise tilted Cu octahedra to align along the *c*-axis. The absence of octahedral tilt has consequences for oxygen vacancy population at the axial site, which is diminished in favor of equatorial site vacancies.[87,184,185,187] The observations shown here lead us to conclude that carbonate ions bind to Sr-containing samples through an alternate mechanism, where surface oxygen reacts with CO_2. A monodentate binding mode for carbonate species would relieve the strain felt by

the lattice allowing it to react with CO_2 without significant degradation. Aliovalent substitution there modulates the reaction mechanism between CO_2 and the surface, providing a useful dimension to control reactivity. Such a finding creates the basis to design RPOs for conditions relevant for electrocatalytic CO_2 reduction or for related reactions with small molecules.

4.3.3 Carbonate Formation and its Impact on the Stability of Related Phases

The formation of carbonates in metal oxides especially in the context of energy storage devices is a well-documented phenomenon that often has detrimental impacts on performance.[179] In anion exchange membranes the most prominent causes of performance deterioration is the formation of metal carbonates in addition to electrolyte effects. High temperature operating conditions often result in the formation of carbonates on the surface and the destruction of the parent phase to the detriment of oxygen mobility.[180,215,216] The effect of CO_2 on the perovskite structure at conditions relevant for SOFC was demonstrated on epitaxially grown $La_{0.6}Sr_{0.4}Co_{0.2}Fe_{0.8}O_{3-\delta}$ thin films.[180] Surface sensitive X-ray techniques revealed that annealing the perovskite films at 800°C in 30% CO_2 increased the rate of phase segregation relative to the conditions where CO_2 is absent. The phases detected on the surface of $La_{0.6}Sr_{0.4}Co_{0.2}Fe_{0.8}O_{3-\delta}$ films was $SrCO_3$. Deterioration of other perovskites in the presence of CO_2 has been observed in other compositions as well.[217–219] Structural deterioration via carbonate formation is attributed to multiple phenomena, such as the rate of diffusion of the alkali earth metals occupying the A-site and the basicity of the bonds in the lattice.[220] Regardless of the explanation given, materials high concentrations of alkali-earth metals such as Sr concentrations leads to enhanced segregation in the form of $SrCO_3$ on the sample surface which increasing the charge transfer resistance.[220] CO_2-induced instability is not unique to perovskites, but have also been observed in lanthanum nickelate RPOs.[221] Ellingham diagrams which depict the stability of materials as a function of temperature have been developed for La_2NiO_4 materials to help predict stability in CO_2 rich atmosphere.[221]

Our results contrast with much of the literature because Sr suppresses instability issues observed on other RPOs under a CO_2 atmosphere, which is the opposite of what is predicted at high temperature. This chapter demonstrated that Sr improved lattice stability by changing the denticity of carbonate adsorption. This reduced strain on the RPO structure as evident by lower amounts of irreversible current passed (Figure 4.5). Few papers study the formation of surface carbonates during the electrocatalytic reduction of CO_2 so a comprehensive comparison of carbonation mechanisms at low

temperature is not possible. However, several reports on cuprate oxides support the findings presented here, showing that CO_2 is primarily bound to Cu sites.[222,223] The authors also assert that oxygen vacancies bind CO_2 quite strongly which suggests that the mechanism of CO_2 adsorption described in section 4.3.2 has validity.

4.4 Conclusion

The spontaneous reaction of CO_2 with the surface of Cuprate-based RPOs was evaluated by using the $La_{2-x}Sr_xCuO_4$ family of materials. Structural characterization of the composition series shows that the unit cell of $La_{2-x}Sr_xCuO_4$ change from orthorhombic to tetragonal unit cell upon substitution of La for Sr. Cyclic voltammetry and EIS confirms the identity of a Cu(II) surface state that is reduced to Cu(I) at 0.6 V vs RHE. The accumulation of Cu(I) has consequences for the stability of the RPO structure causing the structure to degrade over time. Incorporation of Sr reduces the reaction rate responsible for instability by several orders of magnitude. *In-situ* FTIR reveals that carbonates are the sole surface species observed, with three distinct mechanisms for their formation. The structural instability of the orthorhombic *Cmce* structure arises from bidentate adsorption of carbonate that appears to coincide with the formation of oxide vacancies. Unlike the orthorhombic phase, the tetragonal unit cell binds carbonate exclusively in the monodentate configuration. The monodentate mode likely reduces the amount of strain felt by the system resulting in increased structural stability. Such observations provide insights into the interaction between CO_2 and the RPO structure, which could be extended to related systems.

4.5 Experimental details

4.5.1 Synthesis

A modified citrate–nitrate gel protocol was employed to synthesize a series of compounds based on the formula $La_{2-x}Sr_xCuO_4$, with x varied from 0 to 0.5 in steps of $x = 0.1$. Solutions containing 10 mM $Cu(NO_3)_2$ (ACS grade, Fischer Scientific) and a total of 20 mM of $La(NO_3)_3$ (99% purity, Alfa Aesar) and $Sr(CO_3)$ (99% purity, Alfa Aesar) with the appropriate relative stoichiometries were prepared in milliQ water (18.2 MΩ). Citric acid (99% purity, Alfa Aesar) was added to the solution to obtain 30 mM concentration, and the mixture was stirred until all precursors were dissolved. Vacuum distillation of the solution at 90 °C yielded a viscous dark blue liquid that was dried overnight at 120 °C. The resultant bright blue solid was ground with an agate mortar and pestle, heated at 350 °C to

drive initial combustion, and then calcined at 980 °C in a porcelain crucible for 12 h. All products were obtained as black polycrystalline solids, which were ground to a fine powder prior to analyses.

4.5.2 Powder X-ray Diffraction

X-ray diffraction experiments were performed on an Inel diffractometer equipped with a flat sample stage using a 2θ range of 10 to 120°. Powdered samples were plated onto an aluminum dish and run for 12 h. Unit cell parameters were extracted through Rietveld refinement of the diffraction data using the GSAS-2 software package. Fitted parameters include particle size, La and Cu thermal parameters, and fractional oxygen occupancy.

4.5.3 Raman Spectroscopy

Raman spectroscopy was carried out using 532 nm at 1% laser power with neutral density filters for powdered samples. Each spectrum was acquired over 480 s period. Data was analyzed using the Renishaw WiRE V5.2 software package and baseline subtracted using a polynomial baseline.

4.5.4 Electrochemical Measurements

Electrodes were prepared by drop casting 200 μL of an ethanol-based suspension containing $La_{2-x}Sr_xCuO_4$ (50 mg mL^{-1}) and 0.125% Nafion (from 5% suspension in 1-propanol and H_2O, Alfa Aesar) onto freshly polished (50 nm Al_2O_3, Metlab Corporation) wafers of glassy carbon (Hochtemperatur Werkstoffe GmbH, Germany). Electrodes were then mounted into a custom electrochemical cell made of high-density polyethylene, where a silicone O-ring masks the active surface area to 1.894 cm^{-2}. An electrical connection to the electrode was made by affixing copper tape to the rear of the electrode. Electrochemical measurements were acquired using a BioLogic SP300 potentiostat. The modified glassy carbon electrode served as the working electrode, a Hydroflex Reversible hydrogen electrode (RHE; Gaskatel GmbH, Germany) was used as the reference electrode and a platinum mesh as the counter electrode. Measurements used 0.1 M $KHCO_3$ (aq) deaerated with N_2. Voltammetry was performed at 5 mV s^{-1} unless otherwise stated. Potential-dependent EIS results were acquired between 1.1 to 0.2 V vs RHE in 45 mV increments for x = 0 to 0.2. The excitation pulse with a 10 mV amplitude was scanned at frequencies between 200 kHz and 1 Hz with 6 points per decade spacing. A 2-minute equilibration time was allowed before acquiring each measurement.

4.5.5 Spectroelectrochemistry

The VeeMax III Pike technologies reflectance accessory coupled to a Nicolet FTIR spectrometer. This accessory was equipped with a Germanium crystal (5500–600 cm^{-1}) with a 45° face for ATR reflectance. A “cup cell” with an O-ring sealing against the crystal was used. A three-electrode setup was used with a tube electrode with a 5 mm diameter circular face with catalyst pushed against the face of the crystal. A Ag/AgCl reference electrode and platinum mesh electrode was used. Prior to electrochemistry spectra were acquired at open circuit voltage under continuously purged conditions with the following settings: scans 64, resolution 4, gain 4, optical velocity 0.6329, DGTS TEC detector, 45° setting.

Chapter 5: The Impact of Cation Substitution on the Oxygen Reduction Reaction on $La_{2-x}Sr_xNi_{1-y}Fe_yO_4$

This chapter is reproduced in part with permission from John Wiley and Sons: A. W. H. Whittingham, X. Liu, and R. D. L. Smith, *ChemCatChem*, **2022**, e202101684. (DOI: cctc.202101684)

Contribution Statement: Research, synthesis, structural characterization, electrochemical experiments, data analysis and interpretation of the results was performed by A. W. H. Whittingham. X. Liu assisted with the analysis of $La_{2-x}Sr_xNi_{0.7}Fe_{0.3}O_4$ phases. Correlational analysis, interpretation and editing was done by R. D. L. Smith.

5.1 Introduction

Nickel containing substances are some of the most widely studied electrocatalytic systems thus far.[224–230] For example, Ni(Fe)OOH electrocatalysts have some of the highest OER activities reported so far with activities that rival commercially available IrO_2.[226] The effect is mostly electronic, and the exact reason is still being explored. In enzymes such as carbon monoxide dehydrogenase contain Ni and Fe sites within the active site[231] and can cooperatively participate to activate small molecules at high rates. Within the active site of this enzyme the oxygen of CO_2 binds to an oxophilic Fe while the carbon binds to an electron rich Ni atom.[232–235] RPOs are particularly interesting because their unit-cell is a composite of rocksalt and perovskite motifs with disparate properties. The juxtaposition of dissimilar neighbouring structures could allow for bifunctional activation of small molecules in a similar manner to enzymes. This effect has been observed in Sr_2RuO_4 for HER suggesting that biomimetic approaches could be viable for the activation of other small molecules.[236] The intersection of composition and bifunctional activation suggests that Ni-Fe based RPOs for could be powerful electrocatalysts.

As mentioned in previous chapters, the mixed conductivity of RPO electrodes often accompanies the formation of defects and lateral diffusion of oxygen through the rocksalt layer, introducing unique complexities to these catalyst systems.[35] Additionally, the structure and properties of RPOs are affected substantially by heteroatom substitution of the A and B-sites. Substitution can induce secondary effects such as lattice strain[237], changes to oxygen content[238] and phase impurities[239] can potentially affect the active site by modifying small molecule interactions. The structural instability of RPOs can also alter catalytic activity as was demonstrated in Chapters 3 and 4. Studies on nickelate

RPOs phases in particular reveals that their activity and stability is influenced by their surroundings and composition.[240] For example, under high temperature conditions with elevated gas partial pressures it was reveals that nickel alloy nanoparticles begin to form at the catalyst substrate interface.[241] A report in oxidizing environments reveals that higher order RPOs form reversibly and was a key component affecting ORR at elevated temperatures.[240,242] The contribution of the electrolyte pH was also demonstrated as factor affecting the instability of nickelate based RPOs.[243] A key reason for substituting heteroatoms is to modify the electronic structure of the B-site, particularly, by modifying the occupancy of the e_g electrons in the structure.[89] Using such an approach can drastically improve the catalytic activity, as was observed in $La_{0.5}Sr_{1.5}Ni_{1-y}Fe_yO_4$ where there is a change of mechanism from an adsorbate to a lattice oxygen mediated mechanism.[244] The reason for lattice-oxygen participation in the OER mechanism is thought to arise from the increased covalency between the B-site metals and lattice oxygen. In addition to altering the electronic structure heteroatoms could influence inductive effects and lattice distortions as well. The charge compensation mechanism introduced by the different valences of the substituents could also alter the oxidation states of Ni or Fe while simultaneously incorporating oxygen defects into the structure. Such charge compensation mechanisms were reported to affect selectivity and kinetics.[37] The ability to deconvolute the roles of structural-changes, defect variations up A and B-site behaviour in tuning the electrocatalytic activity will assist in the development of RPO catalysts.

This chapter demonstrates that electrocatalytic ORR on $La_{2-x}Sr_xNi_{1-y}Fe_yO_{4+\delta}$ is dictated by modifications of the RPO structure following substitution of Ni for Fe. Two composition series of $La_{2-x}Sr_xNi_{1-y}Fe_yO_{4+\delta}$ were synthesized. The first to examine the effect of Sr substitution at the A-site and the second to study the impact of Fe substitution on the B-site. The composition of Fe substituted samples was selected because it traverses a region in the $La_{2-x}Sr_xNi_{1-y}Fe_yO_{4+\delta}$ phase diagram where only solid solutions are expected.[245] Raman spectra and PXRD patterns of these two series reveal that A and B site substitutions alters the structure of the RPOs through different mechanism. Voltammetric experiments and rotating ring disc electrode analysis verifies the ORR capabilities of the RPOs and allows for the extraction of key electrochemical parameters to correlate with structural information. Correlation between structural and electrochemical parameters indicates that distortions due to Fe substitution controls the ORR activity between H_2O_2 and H_2O.

5.2 Results

5.2.1 Structural Characterization

Two intersecting series of RPOs based on the formula $La_{2-x}Sr_xNi_{1-y}Fe_yO_{4+\delta}$ were prepared to study the effects of A and B-site substitution on electrocatalytic ORR. All samples were synthesized according to a modified Pechini method[244] where the stoichiometry of series maintains a constant 1:1 ratio of La:Sr while varying the Fe stoichiometry from $y = 0$ to 0.5. The second series maintains a constant Fe composition of $y = 0.3$ while varying x from 0 to 1.2. The first composition series was selected to provide a vertical cross-section of the $La_{2-x}Sr_xNi_{1-y}Fe_yO_{4+\delta}$ phase diagram within composition ranges previously reported to yield solid solutions for both A and B site cations.[245] Rietveld refinements of the PXRD patterns (Figure 5.1A, and Appendix C.1) show that all solid solutions have diffraction patterns that can be fit to the space group *I4/mmm* (ICSD #234562) with an interstitial oxygen site to model oxygen hyperstoichiometry (Table 5.1).[245] The horizontal slice was fit in the same way as the solid solutions, and can be approximated with the *I4/mmm* space group, even with the impurity observed for the $x = 1.2$ composition (Figure 5.2A and B). This impurity is likely due to a Sr-rich phase observed in previous reports.[245]

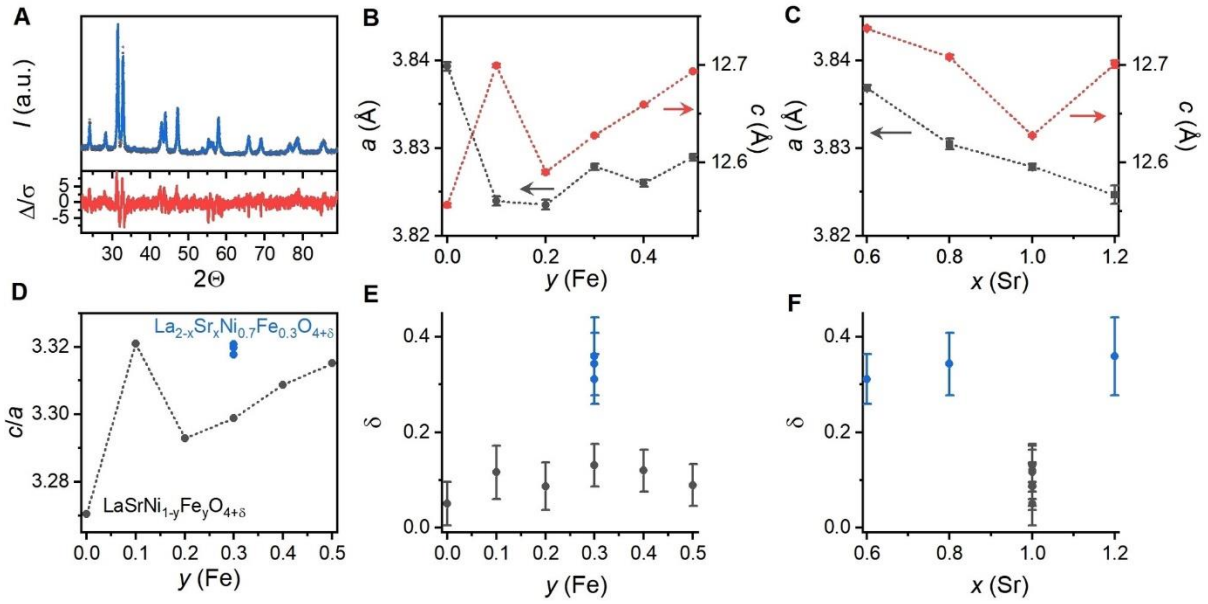

Figure 5.1: PXRD analysis of polycrystalline $La_{2-x}Sr_xNi_{1-y}Fe_yO_{4\pm\delta}$ samples. (A) A representative Rietveld refinement of $LaSrNi_{0.7}Fe_{0.3}O_4$ using the *I4/mmm* unit cell (ICSD# 234562). (B) The unit cell parameters for $LaSrNi_{1-y}Fe_yO_4$ and (C) $La_{2-x}Sr_xNi_{0.7}Fe_{0.3}O_4$. (D) The ratio of the unit

cell parameters *a* and *c* for all samples as a function of Fe composition. (E) Analysis of oxygen hyperstoichiometry tracked by Fe and (F) Sr concentration. Samples with varied Sr content are shown as blue circles, while samples with changing Fe content are depicted by black circles.

Table 5.1: Structural parameters for $La_{2-x}Sr_xNi_{1-y}Fe_yO_4$ phases.

x	***y***	***a***	***c***	***V***	**δ**	**R_{wp}**
(Sr)	**(Fe)**	**Å**	**Å**	**Å³**		**%**
1.0	0	3.839	12.550	369.8	0.023	15.35
		(0.001)	(0.002)	(0.1)	(0.022)	
1.0	0.1	3.824	12.701	371.6	0.055	15.32
		(0.001)	(0.002)	(0.1)	(0.027)	
1.0	0.2	3.824	12.588	367.8	0.046	13.98
		(0.001)	(0.002)	(0.2)	(0.025)	
1.0	0.3	3.828	12.627	370.0	0.037	12.51
		(0.001)	(0.001)	(0.1)	(0.022)	
1.0	0.4	3.826	12.659	370.6	0.035	11.65
		(0.001)	(0.001)	(0.1)	(0.022)	
1.0	0.5	3.829	16.694	372.2	0.022	11.27
		(0.001)	(0.002)	(0.1)	(0.023)	
0.6	0.3	3.837	12.738	187.5	0.624	15.02
		(0.001)	(0.001)	(0.2)	(0.104)	
0.8	0.3	3.831	12.709	186.5	0.687	17.72
		(0.001)	(0.002)	(0.2)	(0.132)	
1.2	0.3	3.825	12.701	185.8	0.718	20.56
		(0.001)	(0.004)	(0.2)	(0.164)	

Substitution of Sr and Fe induces different structural modifications on the unit cell. Introducing Fe into the lattice causes the unit cell parameters *a* and *c* to increase (Figure 5.1B), while Sr substitution causes both *a* and *c* to decrease. (Figure 5.1C). The compositions $LaSrNi_{0.9}Fe_{0.1}O_4$ and $LaSrNi_{0.7}Fe_{0.3}O_4$ disrupt smooth trends. Prior reports show a similar expansion in *a* and *c* for $La_{1.2}Sr_{0.8}Ni_{1-y}Fe_yO_4$ with a break in trends occurring at $y = 0.3$ and a compression of *a* and *c* following introduction of Sr ($La_{2-x}Sr_xNi_{0.8}Fe_{0.2}O_4$) with a break in trends at $x = 0.3$.[245] The B-site do not have a perfectly octahedral environment in the perovskite layer, as the $B\text{-}O_{ax}$ bond is longer than the $B\text{-}O_{eq}$. The change in these two bond lengths can be modelled according to the *c*/*a* ratio. The *c*/*a* ratio is stable at 3.32 for Sr-substituted phases but increases from 3.27 to 3.31 for Fe substituted phases (Figure 5.1D). Estimates of interstitial oxygen stoichiometry (δ) indicates a stable value of 0.1 $LaSrNi_{1-y}Fe_yO_{4+\delta}$ (Figure 5.1E) while $La_{2-x}Sr_xNi_{0.7}Fe_{0.3}O_{4+\delta}$ shows a higher value near 0.3 (Figure

5.1F). In a series of similar compositions, we know that like compositions reported in Chapter 3 and 4 that $La_{2-x}Sr_xNiO_4$ also has documented charge compensation behaviour.[246]

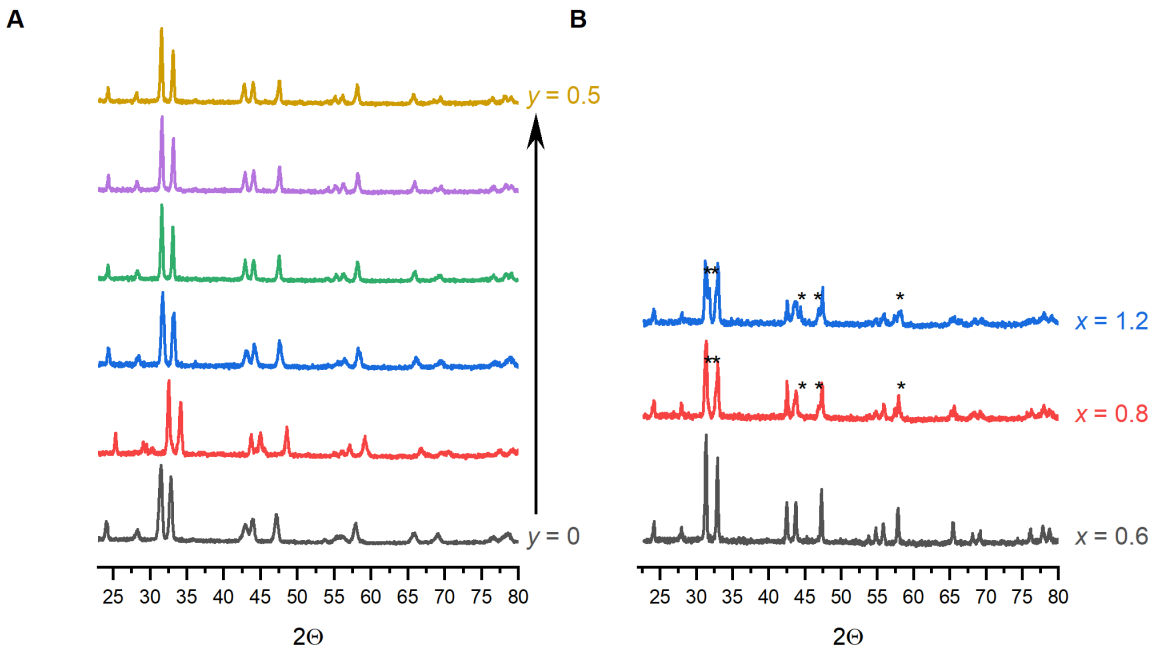

Figure 5.2: Powder X-ray diffraction patterns for (A) $LaSrNi_{1-y}Fe_yO_4$ in 0.1 increments of Fe and (B) $La_{2-x}Sr_xNi_{0.7}Fe_{0.3}O_4$ samples. Impurities are marked with an asterisk.

The structural trends shown in Figure 5.1 indicates the Fe substation primarily causes electronic compensation to occur. The structural modifications shown in Figure 5.1 suggests that increasing Fe relative to Ni induces electronic compensation mechanism, which is supported by lower oxygen content and systematic change in the *c*/*a* ratio indicates a change in bonding. The effect of Sr-substitution is clearer, yielding a consistent increase in volume. The lattice distortion and defects induced by Fe substitution are highlighted by Figure 5.3.

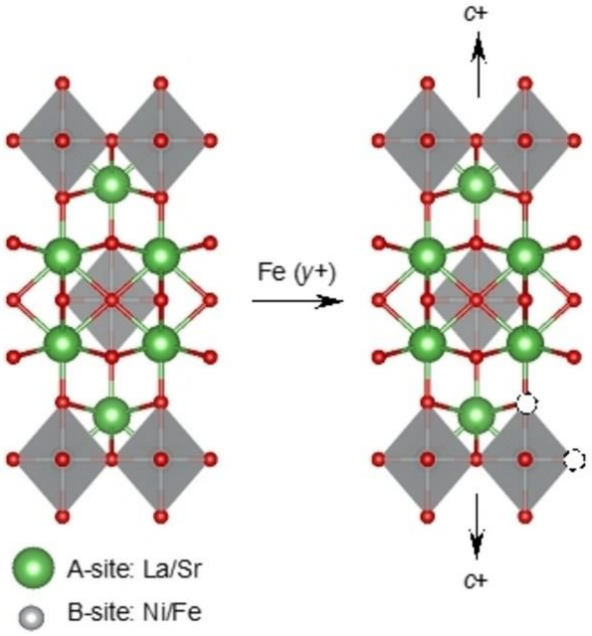

Figure 5.3: A graphical depiction of the $La_{2-x}Sr_xNi_{1-y}Fe_yO_{4\pm\delta}$ structure. Ni(Fe) octahedral sites are located at the center and vertices of the body centered unit cell. The structure shown is larger than a single unit-cell to capture the coordination environments of Ni(Fe) and La(Sr).

Changes to the morphology and position of Raman active vibrations provides additional support to Fe and Sr induced structural changes. The spectra acquired (Figure 5.4A) are very similar to those presented in Chapter 4, with a well-defined peak at 210 cm^{-1} and another multimodal vibration at 450 cm^{-1} with high-energy components. The two primary components are in line with previous assignments made for $La_{2-x}Sr_xCuO_4$ and are supported by reports on La_2NiO_4,[247] where the 210 cm^{-1} peak belongs to the A_{1g} (A-O) vibration of the rocksalt cations, and 440 cm^{-1} belongs to B-O_{ax} vibrations parallel to the unit cell's *c*-axis. In addition to both primary modes there are two components located at 350 cm^{-1} and 540 cm^{-1}. The former component belongs to a bending mode of B-O_{eq}-B sites in the lattice while the former has been described as a breathing mode.[248,249] The 610 cm^{-1} peak is not expected according to predictions made by factor group analysis, but similar features have been observed in $La_{2-x}Sr_xCuO_4$ phases and RPO polymorphs.[250] It appears as though this peak results from the distortion of neighbouring B-O octahedra by adjacent oxygen vacancies. Similar vibrations have also been observed for the T* structure of RPOs as well.[193] The convolution of these high energy vibrations reduces the certainty in assigning a firm location. For this reason, the A_{1g} vibrations at 210 and 440 cm^{-1} are used as the basis for structural analysis because their position can

be extracted with high confidence. Their change in position is consistent with a change in bond strength. For the solid solution compositions ($LaSrNi_{1-y}Fe_yO_4$) the peak location is consistently found at ca. 208 cm^{-1}, but red shifts by 8 cm^{-1} when the Sr composition is changed from x = 0.6 to 1.2 (Figure 5.4B and C). Replacement of La (III) for lower valence Sr (II) is expected to weaken this bond by decreasing the ionic character of the bond. The inverse of this effect is observed when Fe is introduced into the lattice, causing the A_{1g} (B-O_{ax}) to blue shift for the $LaSrNi_{1-y}Fe_yO_4$ phases (Figure 5.4B). This vibration is essentially static at 440 cm^{-1} for the Sr-varied compositions $La_{2-x}Sr_xNi_{0.7}Fe_{0.3}O_4$ (Figure 5.4C). Previous reports have shown that Ni (III) ions are Jahn-Teller active in $La_{2-x}Sr_xNiO_4$ as indicated by an increase in the *c*-axis unit cell parameter.[251] Addition of Fe (III) into this site should reduce the amount of Ni (III) resulting in a stronger B-O_{ax} bond. There is a difference in ionic radii between these two species however resulting in an expansion of the *c*-axis regardless (Figure 5.1B).[252] The breathing mode of the perovskite layer (540 cm^{-1}) appears to blue shift but its convolution with other components makes a definite assignments difficult (Appendix C.2). No clear shift in peak position is observed for the 350 cm^{-1} vibration (Appendix C.2). The peak at 210 cm^{-1} has consistent intensity and FWHM across both sets of samples allowing for its use as reference to normalize other components against its intensity. Normalization of the 450 and 610 cm^{-1} vibrations against the intensity of the 210 peak exhibits trends that track the unit cell parameters *a* and *c* (Figure 5.4D and E), including the anomalous behaviour observed for $LaSrNi_{0.9}Fe_{0.1}O_4$ and $LaSrNi_{0.7}Fe_{0.3}O_4$. These Raman spectra complement results obtained by Rietveld refinement of $LaSrNi_{1-y}Fe_yO_4$ and $La_{2-x}Sr_xNi_{0.7}Fe_{0.3}O_4$ samples, providing additional confidence in the structural changes observed.

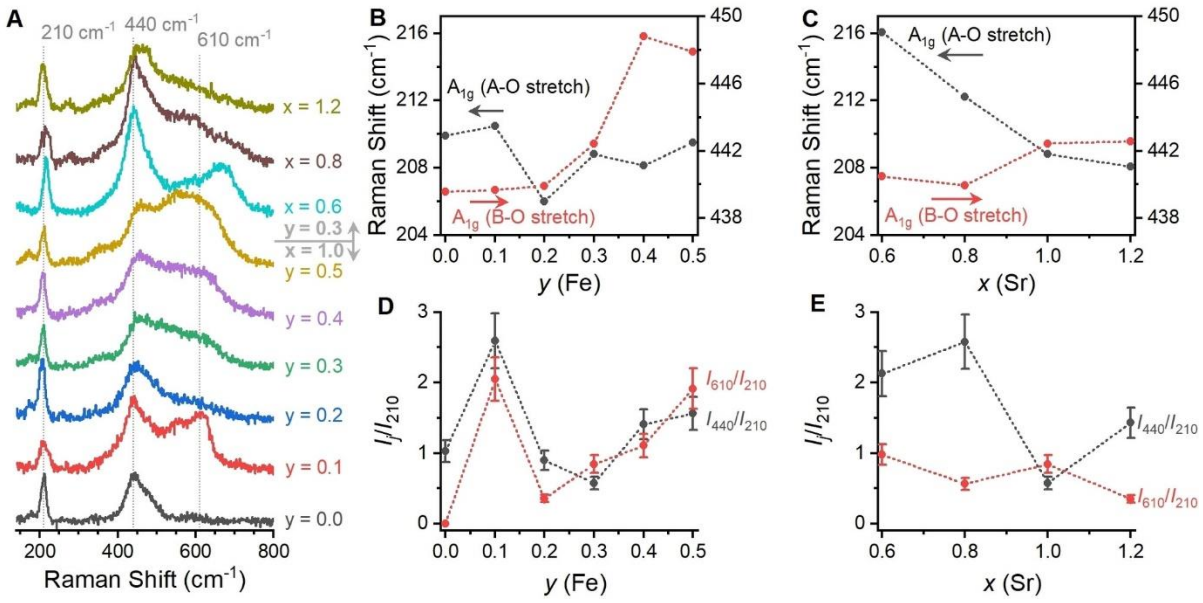

Figure 5.4: Raman spectra of $La_{2-x}Sr_xNi_{1-y}Fe_yO_{4\pm\delta}$ phases. (A) Raman spectra of all samples, the location of the A-O/B-O vibrations as a function of (B) Fe concentration and (C) Sr concentration. The relative areal intensity of the 440 and 610 cm^{-1} vibrations as a function of (D) Fe and (E) Sr concentration.

5.2.2 Electrochemistry

Cyclic voltammetry of the solid solutions under N_2 purged conditions reveals a broad, irreversible reduction process (Figure 5.5). Cathodically sweeping the potential from OCV, in the absence of O_2, reveals an irreversible, bimodal, cathodic process centered at ca. 0 V ($E_{p,\,c1}$) with catalytic current beyond -0.5 V that is characteristic of HER (Figure 5.5 and 5.6A). $E_{p,\,c1}$ shifts anodically and the peak current increases after the initial substitution with Fe (y = 0.1). For greater concentrations of Fe, this peak shifts cathodically and diminishes in size (Figure 5.6C). Purging the electrolyte with O_2 causes $E_{p,\,c1}$ to shift anodically by 500 mV and causes the peak to narrow. These redox active processes flatten into plateaus when linear sweep voltammograms are acquired under forced convection induced by RRDE electrodes. Such a change suggests that this process is mass transfer limited which is consistent with ORR. This feature is superimposed onto a secondary process that plateaus at 0 V (Figure 5.6B). The current measured at the Pt ring correlates with the current observed on the GC disc, passing through a plateau located near $E_{p,\,c1}$ before going to the next plateau near 0 V. Variation of Fe content appears to have minimal impact on the onset of ORR as all samples lie within 40 mV of

each other (Figure 5.6C). The current density of the plateaus exhibits different behaviour before and after y = 0.2 (Figure 5.6C). Addition of Fe between y = 0 to 0.2 causes the current density to decrease, while Fe contents at y = 0.3 and beyond causes the current density to increase again, reversing the trend. The Tafel slopes were obtained through linear fitting at the foot of the first plateau where $E_{p,c1}$ is located yielding a decrease in slope from 100 to 78 mV dec^{-1} after the initial introduction of Fe, followed by a steady increase to around 100 mV dec^{-1} and above (Figure 5.6D). Examination of the onset potential and current Sr-substituted phases yields similar results to the Fe-substituted phases with consistent values for the for all but the x = 1 sample that has a minimum current of *ca* 110 µA (Figure 5.6E). Tafel slopes of Sr-doped samples have consistent values of 80 mV dec^{-1} apart from the x = 1.0 sample (Figure 5.6F).

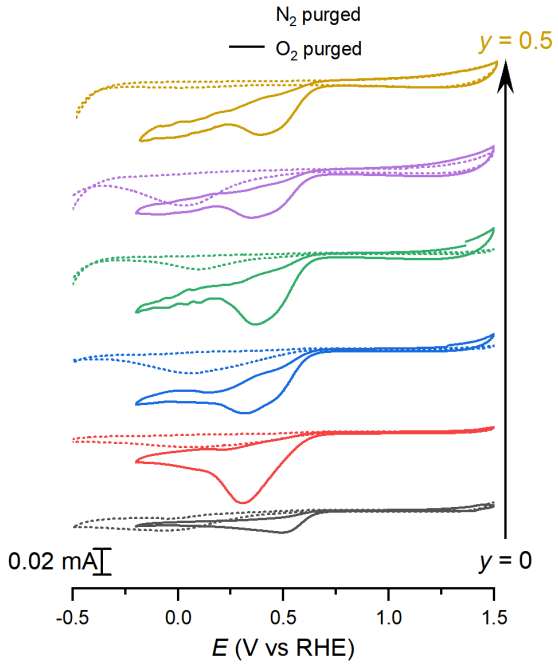

Figure 5.5: Cyclic voltammetry of $LaSrNi_{1-y}Fe_yO_4$ phases in 0.1 M KOH (aq) under O_2 (solid) and N_2 (dotted) purged conditions.

Measures of the ring and disc current allows for the estimation of ORR selectivity by calculating the number of electrons transferred for each electrochemical process observed by RRDE. In Chapter 1, two reaction pathways were provided for the reduction of O_2 in alkaline media. ORR can yield either peroxide via a two-electron transfer or water through a four-electron transfer reaction pathway. The Pt ring of the RRDE apparatus allows for the detection of ORR products with a bipotentiostat

that can detect the current originating from the oxidation of peroxides. At a potential of 1.5 V, the current due to OER is small enough that it can be negated and used as a measure of peroxide oxidation. Using these approximations, the number of electrons transferred at the disc (n_d) can be calculated by measuring the current observed on the disc (i_d) and comparing it with the current observed on the ring (i_r). The current observed at the ring is modified by the collection efficiency of the electrode (N) described by Equation 5.1.[253]

$$n_d = 4 * \left(\frac{i_d}{i_d + \frac{i_r}{N}} \right) \qquad (5.1)$$

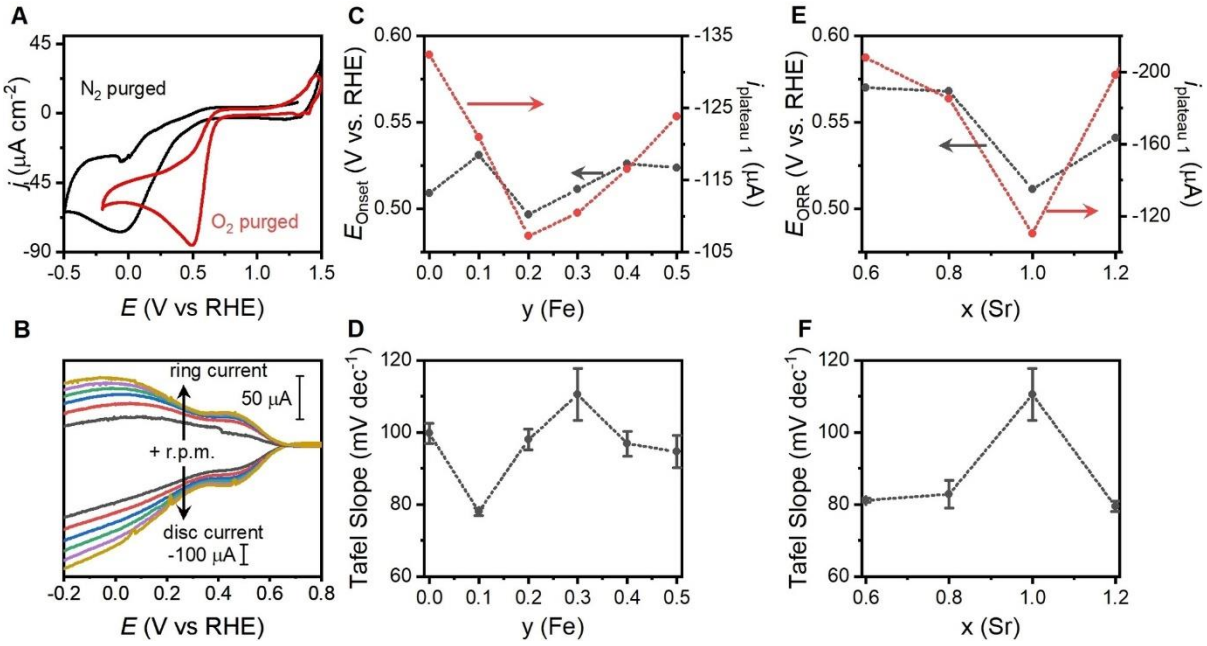

Figure 5.6: Voltammetry of $La_{2-x}Sr_xNi_{1-y}Fe_yO_{4\pm\delta}$ phases. (A) cyclic voltammetry of $LaSrNiO_4$ under O_2 (red) and N_2 (black) purged conditions, respectively. (B) RRDE linear sweep voltammetry under O_2 purged conditions. The rotation rates are varied between 500 (black) to 3000 RPM (yellow) with the ring current scaled to improve readability. (C) The onset potential and current as a function of Fe-content. (D) Tafel slopes as a function of Fe-content. (E) ORR onset potential and current measured at the first plateau. (F) Tafel slope as a function of Sr content.

Utilizing the above equation enables n_d to be interpreted as a function of catalyst composition and potential bias (Figure 5.7). The value of n_d is expected to yield a lower bound of two, for a reaction that is fully selective for peroxide or four for a reaction that exclusively yield water. Intermediate values are also expected, indicating a mixture of products of products obtained by two parallel reaction pathways. The n_d results span from 3.7 at the cathodic extremes of the $LaSrNi_{0.5}Fe_{0.5}O_4$ sample (Figure 5.7A) to 2.2 at moderate potentials for the Sr-deficient samples $La_{1.2}Sr_{0.8}Ni_{0.7}Fe_{0.3}O_4$ and $La_{1.4}Sr_{0.6}Ni_{0.7}Fe_{0.3}O_4$ (Figure 5.7B). Such findings indicate a near complete change in reaction selectivity from water to peroxides through modification of A and B-site composition. All samples yield stable n_d values across voltages where plateaus in current are located, but transitions between the regions between the two plateaus. All samples exhibit lower n_d values for the first plateau relative to the second indicating more peroxide is being produced. $LaSrNi_{1-y}Fe_yO_4$ phases show intermediate n_d values that are predominantly above 3 reflecting that ORR proceeds through a mechanism that favors water (hydroxide) as the primary product. $La_{2-x}Sr_xNi_{0.7}Fe_{0.3}O_4$ phases have n_d values primarily below 3, indicating that production of peroxides is favored. The trends in n_d plotted against Sr and Fe composition exist but are interrupted in a similar fashion to structural characterization methods (Figure 5.7C and D).

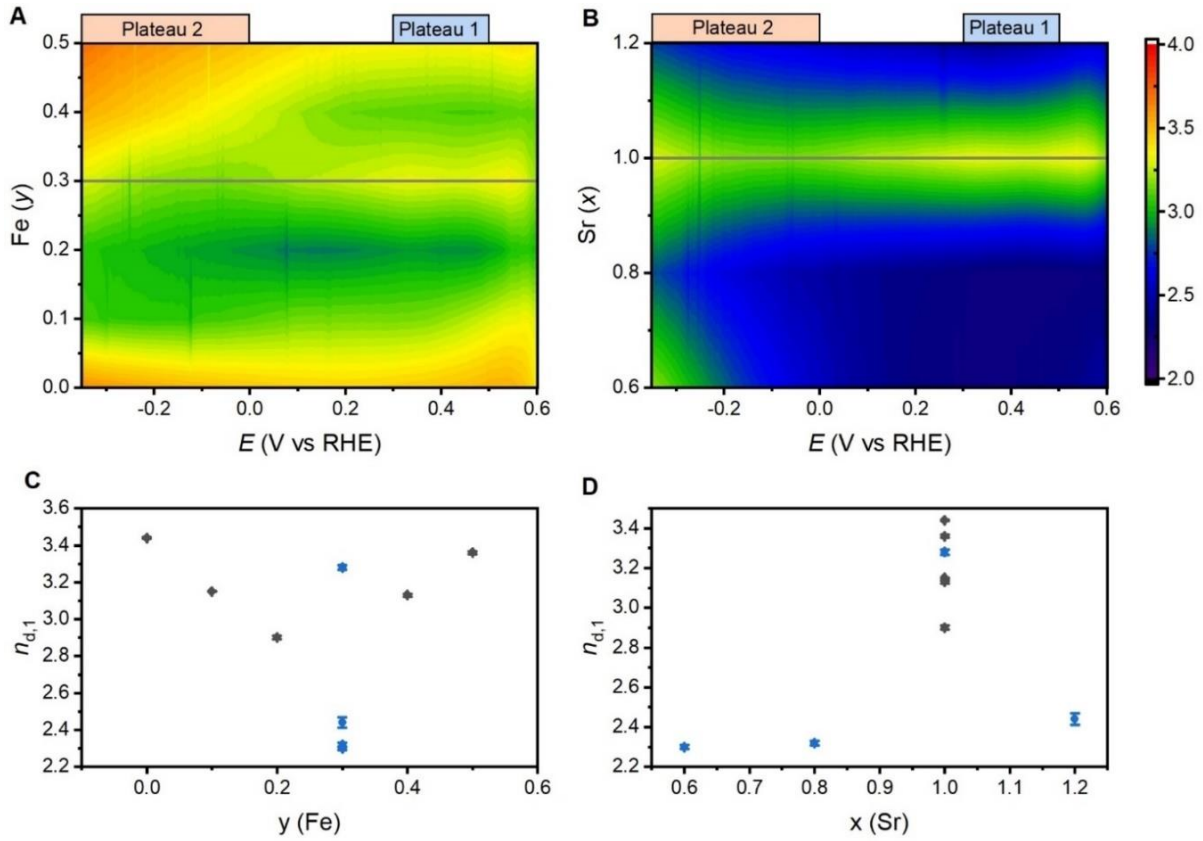

Figure 5.7: Average number of electrons transferred, n_d, during ORR as measured from RRDE hydrodynamic voltammetry. The variations to n_d as a function of (A) Fe content and (B) Sr content over a range of potentials. The average number of electrons transferred for the first plateau as a function of (C) Fe content and (D) Sr content. The horizontal line represents the compositions shared between the two samples.

5.2.3 Ex-situ Analysis

Ex-situ analysis of $LaSrNi_{1-y}Fe_yO_4$ samples reveal changes to the RPO structure over the course of ORR. After 30 minutes of electrolysis at -0.2 V under O_2 purged conditions, the powdered samples were analyzed by confocal Raman spectroscopy. Spectral changes are observed in all samples and typically include a shifting of peak energy or intensity (Figure 5.8A). Two major trends could be observed by monitoring spectral changes as Fe content is varied. The A_{1g} vibration resulting from the motion of La(Sr)-O reveals a 2.4 cm^{-1} blue shift for $LaSrNiO_4$ following ORR (Figure 5.8B). The Fe-dependent shift of the 210 cm^{-1} vibration following electrolysis demonstrates that ORR affects

La(Sr)-O bonds within the rocksalt layer. The shift of this vibration is attenuated as Fe is added, yielding only a 0.11 cm^{-1} redshift for $LaSrNi_{0.5}Fe_{0.5}O_4$. The intensity of the 610 cm^{-1} relative to the 210 cm^{-1} shows a volcano-like relationship with a maximum located at $LaSrNi_{0.8}Fe_{0.2}O_4$, while decreasing back to the original levels after addition of Fe (Figure 5.8C). Changes to the height of this peak are associated with B-site distortions induced by oxygen vacancies[250] supports that the defect density is changing during electrolysis. Such a volcano-like relationship suggests that variations in phase stability are predicted.

Convergent evidence obtained from several characterization methods provides insights into the relationships between structural modifications and the electrochemistry of $La_{2-x}Sr_xNi_{1-y}Fe_yO_4$ phases. The behaviour of the A_{1g} peak, which is associated with La-O vibrations in the rocksalt layer, correlates well with the unit cell *a* parameter for all samples (Figure 5.9A). The degree of change exhibited by lattice vibrations and *a* are different for Fe containing samples relative to Sr substituted samples suggesting that lateral distortions of the *a*/*b* plane proceed via different mechanisms. Additional evidence supporting a separate-mechanism hypothesis for A and B-site substituents is provided by the behaviour of the *c*/*a* ratio upon incorporation of Fe (Figure 5.9B). Substitution of Ni for Fe causes the *c*-axis to expand faster relative to the *a*/*b* plane. The *c*/*a* ratio correlates to the intensity of the 610 cm^{-1} (I_{610}) peak normalized against the 210 peak (I_{210}) for the $LaSrNi_{1-y}Fe_yO_4$ set of samples. Lengthening of the *c* relative to the *a*-axis after Fe doping appears to be partly caused by the introduction of oxygen vacancies.[250] A decrease of 440 vibration (I_{440}) normalized against the 210 cm^{-1} suggests that there is distortion about the Ni(Fe)-O_{ax} sites among the $LaSrNi_{1-y}Fe_yO_4$ set of samples. This change in spectra features is also correlated to the Tafel slopes observed for ORR (Figure 5.9C) implying that the Ni(Fe)-O_{ax} bond is linked to the rate determining step. A change of mechanism is also supported by differences between the average number of electrons transferred during ORR and the *a* unit cell dimension in $LaSrNi_{1-y}Fe_yO_4$ (Figure 5.9D). Sr substitution does not yield the same trend as the Fe substitution for the *c*/*a* ratio, number of electrons transferred or Tafel slope remaining relatively consistent for the entire series. This finding suggests that Fe is critical for tuning catalytic performance. Stability is also critical property that can be used to describe the observed electrocatalytic phenomenon as outlined in Chapter 3 and 4.[178,254] All $La_{2-x}Sr_xNi_{0.7}Fe_{0.3}O_4$ phases redshift in their 210 peak after 30 minutes of ORR electrolysis. The magnitude of this shift tracks the onset potential of ORR. The defect induced vibration at 610 cm^{-1} negatively correlates to the number of electrons transferred at the second plateau. These trends suggest that catalysts that heal

oxygen defects are more selective towards H_2O, while those that promote defects are more selective towards H_2O_2. To summarize, these findings suggest that the Ni(Fe)-O_{ax} bond is critical to ORR catalysis in these phases.

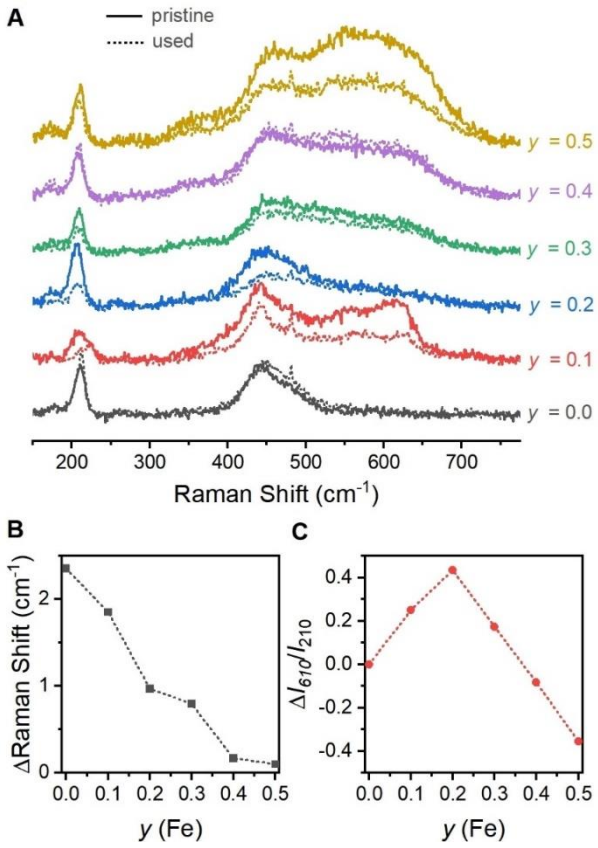

Figure 5.8: *Ex-situ* Raman spectroscopy of $LaSrNi_{1-y}Fe_yO_4$ after 30 minutes of chronoamperometry at -0.2 V vs RHE and 1500 RPM. (A) Raman spectra acquired for pristine phases (solid) and after chronoamperometry (dashed). (B) The change in position of the La-O (A_{1g}) vibration after electrolysis. (C) The change in relative intensity of the 610 cm^{-1} vibration after electrolysis.

5.3 Discussion

5.3.1 Correlation Analysis

Correlational analysis of PXRD, Raman spectra and electrochemical parameters for $La_{2-x}Sr_xNi_{1-y}Fe_yO_4$ phases provides evidence that the distortion of Ni(Fe)-O octahedra controls ORR selectivity.

Changing the composition of the A site by increasing the amount of Sr yields a simultaneous change in the *a* and *c* unit cell parameters leading to a constant *c*/*a* value (Figure 5.1D). Substitution of Ni for Fe results in an asymmetric expansion of *a* and *c* that increases the *c*/*a* ratio (Figure 5.1D). The different rates of *c*/*a* expansion also manifest in the A_{1g} vibration of the (La-O) which suggests that Fe addition does not expand the lateral plane efficiently (Figure 5.9A). The Fe induced distortion is accompanied by the formation of oxygen defects, as evident by the growth of the 610 cm^{-1} vibration (Figure 5.9B) and by a change in the disorder of the B-site coordination environment, seen by the relationship between the Tafel slope and the A_{1g} B-O vibration at 440 cm^{-1} (Figure 5.9C). The impact of B-site distortions, or the oxygen vacancies associated with them, on the observed electrocatalytic activity is evident by the change of selectivity experienced during ORR as the Fe content is varied. The selectivity change is reflected by the correlation between the number of electrons transferred (n_d) to the unit cell parameter *a* of the $LaSrNi_{1-y}Fe_yO_4$ series (Figure 5.9D). A change of Tafel slope is often associated with a change in rate determining step or mechanism of reaction.[55,255,256] Theoretically only three Tafel slopes are possible for accepted ORR mechanisms that include values of 120, 60 and 40 mV dec^{-1}.[255] These Tafel slopes reflect individual elementary steps, with 120 mV dec^{-1} reflecting a charge transfer limited process and the 60 mV dec^{-1} step reflecting O-O bond breaking as the RDS. The presence of Sr-rich impurities with a similar RPO structure (Figure 5.2B) seems to have little impact on the RDS as indicated by a constant Tafel slope of *ca.* 80 mV dec^{-1}. These impurities appear to have negligible consequences on the electrochemical properties measured indicating that the *I*4*/mmm* phase dominates the observed ORR activity.

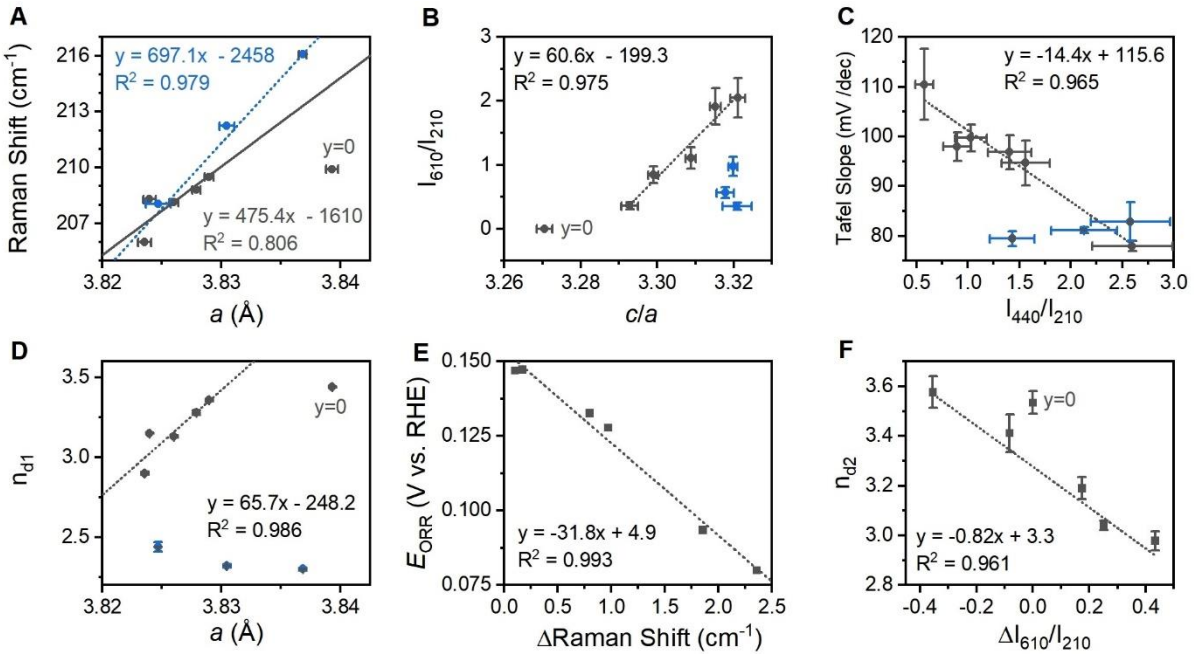

Figure 5.9: The correlation of structural and electrochemical parameters for $La_{2-x}Sr_xNi_{1-y}Fe_yO_{4\pm\delta}$. (A) The location of the A_{1g} La-O vibration as a function of the unit cell parameter *a*. (B) The relative intensity of the defect-based 610 cm^{-1} vibration relative to the unit cell distortion denoted by *c*/*a*. (C) Tafel slope of all phases as a function of the relative intensity of the A_{1g} Ni(Fe)-O vibration. (D) The average number of electrons transferred for the first plateau as a function of *a*. (E) The onset potential for ORR relative to the Raman shift of La-O after 30 minutes of electrolysis. (F) The number of electrons transferred measured at the second plateau as a function of the change to the defect induced vibration after 30 minutes of electrolysis. The 440 and 610 cm^{-1} are normalized against the La-O vibration due to its consistent behaviour across the sample series. Black circles represent the $LaSrNi_{1-y}Fe_yO_{4\pm\delta}$ samples and the blue circles represent $La_{2-x}Sr_xNi_{0.7}Fe_{0.3}O_{4\pm\delta}$. The linear regressions for $LaSrNi_{1-y}Fe_yO_{4\pm\delta}$ does not include $LaSrNiO_4$.

5.3.2 Fe-Induced Modification of Tafel slope and α

Ideal Tafel slopes rely on the assumption of completely symmetrical potential energy surfaces that is reflected by the empirical α parameter with a value of 0.5. The potential energy surfaces are often asymmetric resulting in deviations from the expected Tafel slopes in the literature. Plenty of non-standard Tafel slopes have been reported with values ranging from 70–90 mv dec^{-1} suggesting that the

α parameter deviates from 0.5.[255] The relationship between B-site disorder, Tafel slope, and the number of electrons transferred over the entire $LaSrNi_{1-y}Fe_yO_4$ sample series asserts that disruptions to the B-site coordination environment by Fe-substitution. The origins of composition dependent changes to the α parameter are not fully understood in the literature but have been proposed to result from distortions that modify the symmetry of potential energy surfaces. The impact of distortions has been outlined on studies of layered double hydroxide surfaces for OER[257–259] and be controllable through lattice strain.[88,246,260,261] This study outlined the use of lattice-incorporated redox inert ions to study the effect of tensile and compressive strain on electrocatalytic activity.[257] DFT calculations of the potential energy surface for the Al^{3+}, Ga^{3+}, Fe^{3+} showed that the potential energy surface could be broadened or narrowed changing the symmetry of the surface. Trivalent cations with atomic radii between Ni(IV) and Ni(II) causes the potential energy surface to broaden and shift reducing the activation barrier for OER by up to 1 eV for Fe(III). The result of this is a change in activation barrier caused a change in alpha from 0.53 to 0.45 which is accompanied by a Tafel slope decrease of approximately 40 mV dec^{-1}. We observe similar decreases upon substitution with Fe where the bond length change correlates to Tafel slope. The mechanism of the change is likely different though due to the ways the RPO structure can compensate for such distortions. The ability to systematically tune the Tafel slope through non-conventional values by simple compositional substitution identifies this family of materials, especially $LaSrNi_{1-y}Fe_yO_{4+\delta}$, as a candidate to establish a more robust understanding on the variation of the α parameter in heterogeneous electrocatalysis.

5.3.3 The Role of Defects

Correlational analysis provides additional evidence that the instability of defects for Ni(Fe) RPOs is associated with reaction mechanism. Changes in the intensity of the 610 cm^{-1} vibration following ORR suggests that oxygen vacancies are participants in the reaction mechanism. Oxygen vacancies have been frequently observed to participate in such reaction mechanisms.[262,263] These changes seem to indicate that the defect composition is a dependent on the mechanism of ORR for a specific composition. The general hypothesis proposed in Chapter 1 is that oxygen vacancies assist ORR by offering a novel unsaturated coordination environment with different adsorption properties for intermediates which dictate the reaction pathway taken. Oxygen reduction other phases such as spinels (Co_3O_4) have demonstrated quite clearly that these vacancies can change the reaction selectivity towards peroxide formation[262], so it is possible that oxides vacancies can activate O_2 in RPOs as well. The reaction pathway that results in the reduction of O_2 to H_2O yields a decrease in the

610 cm^{-1} vibration that is associated with oxygen vacancies that suggests that oxygen bond-breaking step leaves an adsorbed oxygen atom on the RPO surface. If the dominant reaction pathway involves the reduction of O_2 to H_2O_2 the defect-based vibration increases in intensity. The surface species on RPO phases are expected to follow a pseudo-steady state equilibrium, where the rate of individual elementary steps establishes the concentration of each species. Analysis of surface species equilibria is a significant challenge in performing rigorous mechanistic analysis of electrocatalytic reactions. The $LaSrNi_{1-y}Fe_yO_4$ system exhibits both increases and decreases in defect concentrations that highlight this catalyst family as a candidate for developing novel analysis techniques that allow for insight into kinetic and thermodynamic properties of reaction intermediates in heterogeneous electrocatalysis.

5.4 Conclusions

This chapter outlined a structural and electrochemical study of $LaSrNi_{1-y}Fe_yO_4$ and $La_{2-x}Sr_xNi_{0.7}Fe_{0.3}O_4$ indicates that Fe induced B-site distortions alters the electrocatalytic performance and selectivity. Correlation between the key parameters obtained from Raman spectroscopy and Rietveld refinements shows that substitution of La (III) for Sr (II) results in a concerted expansion of the unit cell dimensions, while substitution of Ni for Fe yields oxygen defects with the asymmetric expansion of the *c*-axis relative to the *a*-axis. Comparison of structural, spectroscopic, and electrochemical parameters for ORR across the sample sets reveals that the selectivity of electrocatalysis is dependent on Fe-induced expansion of the *a*-axis, while the addition of Sr does not affect selectivity. Changes to the RPO structure after electrolysis are observed by shifting of the 210 cm^{-1} La-O vibration and changes to the intensity of defect induced vibration. The intensity of the defect induced vibration predicts the change in selectivity, while the La-O vibration seems to predict onset potential. While no serious degradation to the RPO phases were observed a change in defect density is expected to alter both the reaction mechanism and selectivity during long term electrolysis. The results shown here provide a handle to identify the role of identify the role of different dopants in complex systems and reveal structural features that are useful predictors for electrocatalytic performance.

5.5 Experimental Details

5.5.1 Synthesis

Compounds were fabricated using a modified citrate-nitrate gel method based on the $LaSrNi_{1-y}Fe_yO_4$ formula, with the Fe content increases in increments of $y = 0.1$. A series of aqueous solutions were prepared with 5 mmol La(III), 5 mmol Sr(II), with an amount of Ni(II) and Fe(III) totaling 5 mmol. Appropriate amounts of $SrCO_3$ (99% purity, Alfa Aesar) and $Ni_4CO_3(OH)_6(H_2O)_4$ (99% purity, Sigma Aldrich) was weighed on an analytical balance, placed in a glass beaker, and wet with milli-Q H_2O (18.2 MΩ) and dissolved with dropwise addition of concentrated HNO_3. Once the carbonates were dissolved, pre-weighed amounts of $La(NO_3)_3$ and $Fe(NO_3)_3$ were added to the solution. Citric acid (99% purity, Alfa Aesar) and EDTA (99% purity, Alfa Aesar) in milli-Q H_2O were added and the pH of the solution was adjusted to 10 using NH_4OH. The solution was heated on a hotplate, which was set at 200 °C, until a dark brown gel formed. The gel was heated at 350 °C until combustion took place. Combusted powders were placed in a porcelain crucible and heated at 1000 °C for 24 h, with an intermediate regrinding step after 12 hr. All products retrieved were black polycrystalline powders.

5.5.2 Powder X-ray Diffraction

X-ray diffraction experiments was performed on an Inel diffractometer on an aluminum sample holder. Samples were run for 30 min each, and the structural parameters were extracted by Rietveld refinement of the diffraction patterns using the GSAS 2 software package.

5.5.3 Raman Spectroscopy

Raman spectroscopy was carried out on a Renishaw inVia Reflex Raman microscope using a 532 nm laser with a 2400 l/mm grating. Laser intensity was filetered to 1% maximum and spectra were recorded with a 400 s acquisition time. Data was processed using Renishaw WiRE 5.3 software package, unless stated otherwise. Data processing included polynomial baseline subtraction and peak fitting.

5.5.4 Electrochemical Characterization

Electrochemical measurements were taken on a BioLogic SP300 electrochemical workstation. Electrodes were prepared by drop casting two 10 μL aliquots of 10 mg ml^{-1} suspensions of $LaSrNi_{1-y}Fe_yO_4$ in 0.125% Nafion (from a 5% suspension containing isopropanol and H_2O, Alfa Aesar) onto

polished 5 mm diameter glassy carbon disks. The electrodes were analyzed in a three-electrode configuration, using a cup cell consisting of a beaker and a polyethylene cap to hold the electrodes in position. The catalyst-coated glassy carbon electrode was utilized as a working electrode, a Hydroflex reversible hydrogen electrode (RHE; Gaskatel GmbH, Germany) was used as a reference electrode and a platinum mesh as a counter electrode. The RHE electrode contains a compressed H_2 cartridge that maintains a local H_2 environment near a platinum electrode. The electrode is regularly compared against other RHE electrodes and an Ag/AgCl (sat'd KCl) electrode to ensure consistency. All measurements were acquired in 0.1 M KOH purged with either N_2 or O_2. Voltammetry was performed at a scan rate of 10 mV s^{-1}.

5.5.5 Rotating Ring Disc Electrode Voltammetry

Working electrodes were prepared by drop casting two, 10 μL aliquots of a 10 mg ml^{-1} suspensions of $LaSrNi_{1-y}Fe_yO_4$ in 0.125% Nafion (from a 5% suspension containing isopropanol and H_2O, Alfa Aesar), onto a 10 mm diameter glassy carbon disk electrode with an addition Pt counter electrode. Drop casting was performed in a manner that left the platinum ring clean. A Hydroflex reversible hydrogen electrode (RHE; Gaskatel GmbH, Germany) was used as a reference electrode and platinum foil was used as the counter electrode. Hydrodynamic measurements were acquired on a Metrohm Autolab electrochemical workstation, with the RRDE rotated at rates between 500 to 3000 RPM. All measurements were acquired at a scan rate of 10 mV s^{-1} in 0.1 M KOH purged with O_2. Linear sweep voltammetry was conducted from 1.1 V to -0.35 V vs RHE. The potential of the platinum ring was set to 1.5 V vs RHE for detection of hydrogen peroxide.

Chapter 6: An Investigation of Co-Induced Lattice Compression on the Electrocatalytic Performance of $La_{1.2}Sr_{0.8}Ni_{1-y}Co_yO_4$

A.W.H. Whittingham, M. Boke, R. D. L. Smith. **2022.** Manuscript in preparation. Tentative title: The Effect of Co-Induced Lattice Distortions on the Electrocatalytic Activity of $La_{1.2}Sr_{0.8}Ni_{1-y}Co_yO_4$.

Contribution Statement: Research, electrochemical experiments, *ex-situ* spectroscopy, data analysis, interpretation of the results was carried out by A. W. H. Whittingham. M. Boke synthesized the $La_{1.2}Sr_{0.8}Ni_{1-y}Co_yO_4$ powders, acquired Raman spectra, PXRD patterns and assisted with data processing. R. D. L. Smith assisted with editing and interpreting the results.

6.1 Introduction

Layered perovskites have received considerable attention as electrode materials where the activation and transport of oxygen atoms is necessary. Many groups have sought to synthesize and characterize their unique properties. Co-based RPOs with the K_2NiF_4 structure have been synthesized using conventional ceramic and citrate-nitrate gel methods for the following compositions: $La_{2-x}Sr_xCoO_4$,[264] $La_{2-x}A_xCoO_4$ (Sm^{3+}, Gd^{3+}, Dy^{3+}),[6] $Nd_{2-x}Sr_xNi_{1-y}Co_yO_4$,[265] $La_2Co_{1-y}Cu_yO_4$,[266] $La_2Ni_{1-y}Co_yO_4$,[267] $La_{2-x}Sr_xNi_{1-y}Co_yO_4$.[268] Several authors have noted that the range for forming a single phase is dependent on the identity and relative concentrations of the cations in the lattice.[265,268] For example, the phase diagram for the $La_{2-x}Sr_xNi_{1-y}Co_yO_4$ system revealed that solid solutions are predicted to form with the range x = 0.7 and 0.8 for all concentrations of Co.[268] Deviating from this range can yield a heterogenous mixture of Sr-rich and poor RPO phases. Lanthanum-based RPOs such as $La_2Ni_{1-y}Co_yO_4$ or $La_2Co_{1-y}Cu_yO_4$ have limited solubility Co(III) in the B-site because of charge imbalance, but sintering under an inert atmosphere can increase this solubility by reducing the need for charge compensation within the lattice.[266,267] In many materials Co exists in a mixture of oxidation states including Co(II), Co(III), and Co(IV) that can complicate synthesis by introducing these secondary phases along with Jahn-Teller distortions and size-mismatch strain.[264] In addition to structural modifications of the RPO structure, Co cations can exist in low, intermediate, and high spin state configurations that can completely alter the electronic or magnetic properties.[269]

The diversity of properties available to cobalt-based RPOs make them an attractive option for electrode materials catalyzing ORR and OER .[83,270–273] Cobalt perovskites are some of the most effective ORR and OER catalysts available with specific activities that rival noble and rare-earth

metals. Materials like $La_{1-x}Sr_xCo_{3+\delta}$ exemplify this with Tafel slopes as low as 31mV dec^{-1}, and specific activities as high as 28.4 mA cm^{-2}.[274] A Tafel slope of 58 mV dec^{-1} and specific activity of 1.2 mA cm^{-2} measured on commercially available IrO_2 highlights the efficiency $La_{1-x}Sr_xCoO_{3+\delta}$ electrocatalysts for OER.[274] Similar results have also be reported for other A-site substituted $LaCoO_3$ perovskites, such as $La_{1-x}Pr_xCoO_{3+\delta}$ which has OER onset 30 mV lower than IrO_2.[275] The fast kinetics of Co-oxides is often reflected by their position atop volcano plots constructed by plotting electrochemical parameters, such as overpotential, against thermodynamic or molecular orbital descriptors like e_g electron filling.[127] Bulk descriptors provide a insights into the origins of electrocatalytic activity of OER and ORR, but over reliance on these relationships may lead to broad generalizations about activity while neglecting nuanced changes to properties that can arise at low levels of heteroatom substitution. For example, several Co-based RPOs report that changing the oxidation state or substituent atoms can substantially change the electronic structure. Certain Co-RPO compositions can also result in phenomenon such as paramagnetism, and ferromagnetism.[276] Magnetic properties and changes to spin state could be of interest to OER and ORR because magnetic fields have been proposed to break scaling-relationships.[54] Fabrication of these RPOs at across a range of compositions could yield insights into the effect of structural distortions, electronic and magnetic properties on electrocatalysis.

The following chapter examines the effect of Co substitution on the, electrocatalytic performance, and stability of $La_{1.2}Sr_{0.8}Ni_{1-y}Co_yO_4$. A La:Sr ratio of 1.2:0.8 was selected because it was previously reported to exist as a solid solution with the K_2NiF_4 structure.[268] Characterization using PXRD and Raman spectroscopy reveals that Co substitution asymmetrically distorts the unit cell of $La_{1.2}Sr_{0.8}Ni_{1-y}Co_yO_4$ by altering B-site bonding. Multimodal Raman vibrations are observed, which highlight localized symmetry changes brought about by charge-ordering phenomenon. Hydrodynamic voltammetry confirms that the ORR and OER are catalyzed by these phases, but insulating behaviour is observed for several compositions. ORR is heavily influenced by small increments of Co substitution, yielding anomalous reaction selectivity. Anodic electrolysis of the cobaltate and nickelate phases indicates that two different structural degradation mechanisms exist for these RPOs. Correlation analysis reveals that the Tafel slopes for ORR are highly dependent on the degree of structural distortion along the *c*-axis, while OER seems to display an exponential dependency of Tafel slope on a defect related vibration.

6.2 Results

6.2.1 Structural Characterization by PXRD

A series of $La_{1.2}Sr_{0.8}Ni_{1-y}Co_yO_4$ RPO phases was fabricated using a modified citrate-nitrate gel method[244] and their crystal structure examined by PXRD (Figure 6.1). Rietveld refinement of the $La_{1.2}Sr_{0.8}NiO_4$ diffraction pattern is consistent with the *I4/mmm* space group, which is associated with the K_2NiF_4-type structure (Figure 6.2A). This crystal structure is maintained for all powders with the $La_{1.2}Sr_{0.8}Ni_{1-y}Co_yO_4$ formula (Appendix D.1).

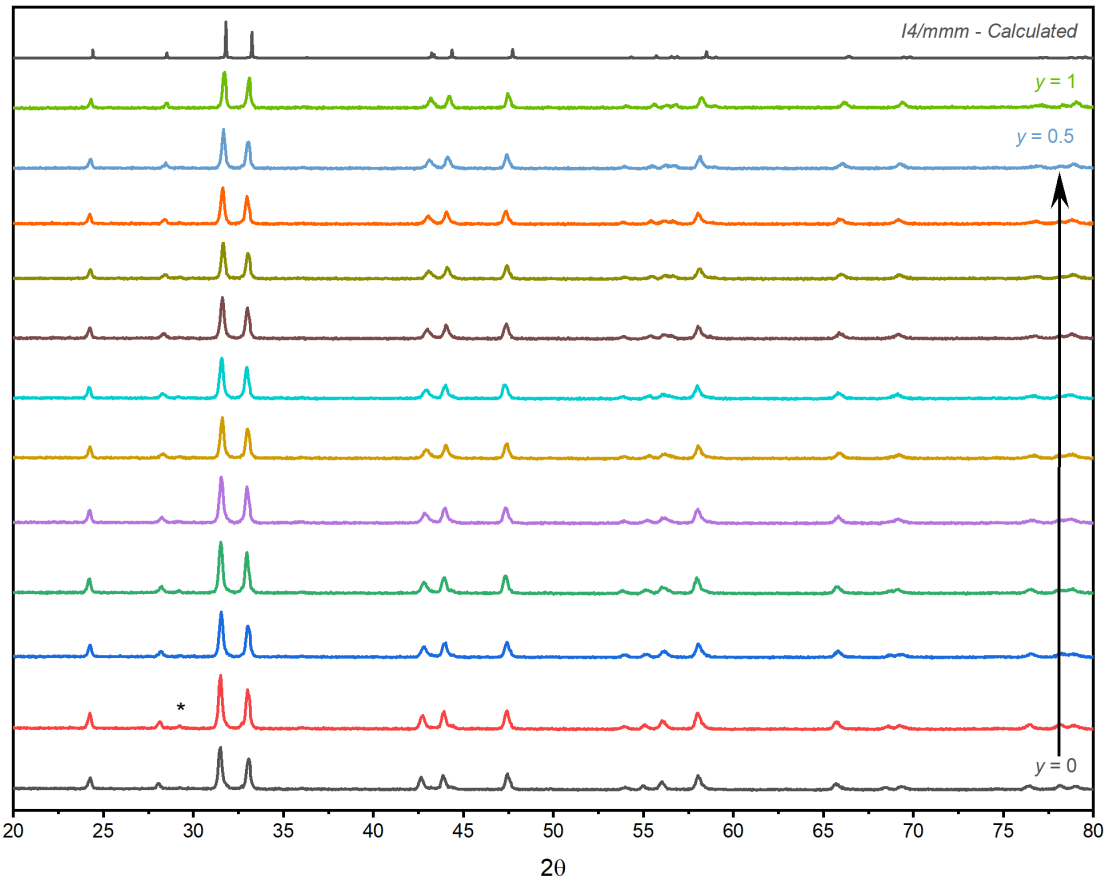

Figure 6.1: PXRD patterns of $La_{1.2}Sr_{0.8}Ni_{1-y}Co_yO_4$. PXRD patterns are presented in increments of y = 0.05, except for the pure Co-phase labelled as y = 1. A simulated *I*4/mmm diffraction pattern is provided for comparison (ICSD# 415838). A Sr-rich impurity marked with an asterisk.

Previous reports have shown that RPO phases with an *x*-value of 0.8 should form solid solutions for all ratios of Ni and Co.[268] PXRD of these phases show that compositions between $y = 0.05$ to 0.15 possess a minor impurity phase previously attributed to Sr-rich RPO phase (Figure 6.1). This impurity is also observed in other $La_{2-x}Sr_xNi_{1-y}Co_yO_4$ compositions (Appendix D.2). Rietveld refinements of these phases show that Co substitution compresses *c*-axis of the RPO structure from 12.68 to 12.54 Å as Co is increased from $y = 0$ to 0.5 (Figure 6.2B; Appendix Table D.1). For the pure Co-phase the *c*-axis is reduced further to 12.52 Å. The *a* unit cell parameter spans 3.83 ± 0.005 Å, beginning at 3.828 Å for the pure nickel phase and a maximum of 3.839 Å for $La_{1.2}Sr_{0.8}Ni_{0.7}Co_{0.3}O_4$. A minimum value of 3.825 Å is reached at $La_{1.2}Sr_{0.8}CoO_4$. The *a* and *c* unit cell parameters reported for $La_{1.9}Sr_{0.1}Ni_{1-y}Co_yO_4$ are 3.845 and 12.60 ± 0.05 Å respectively,[268] suggesting that the values shown here are realistic. In addition, Rietveld refinement of $Nd_{2-x}Sr_xNi_{1-y}Co_yO_4$ ($x = 1$, $y = 0.1 – 0.9$) powders depict a *c*-axis compression of 0.1 Å, which is comparable to the values reported here.[265] The trends in *a* and *c* are not as clean for other RPO phases presented in this dissertation, but the *c*/*a* ratio that which reflects the degree of distortion in the unit cell, exhibits an exponential decay as the Co composition is changed from $y = 0$ to $y = 1$ (Figure 6.2C).

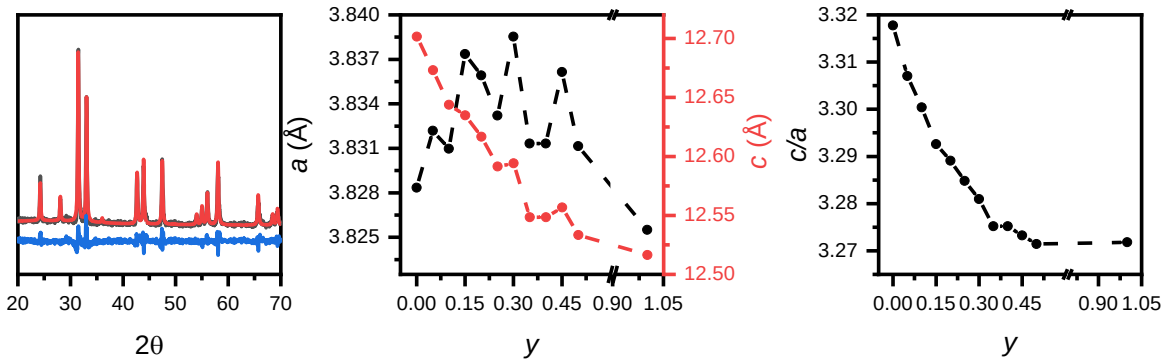

Figure 6.2:Rietveld refinement of (A) $La_{1.2}Sr_{0.8}CoO_4$ displayed alongside (B) the variation of the unit-cell parameters and (C) the *c*/*a* ration as a function of Co composition.

6.2.2 Analysis of Raman-Active Lattice Vibrations

Substitution of Ni for Co causes the Raman spectra of $La_{1.2}Sr_{0.8}Ni_{1-y}Co_yO_4$ to change substantially and shows significant differences relative to Raman spectra reported on similar RPO phases. As discussed in Chapters 4 and 5, factor group analysis predicts that RPO's with the *I*4/*mmm* space group should have a maximum of four Raman active vibrations: 2 A_{1g} and 2 E_g sets. The $La_{1.2}Sr_{0.8}NiO_4$ sample has

two vibrations visible at 210 and 450 cm^{-1}. Single crystal analysis of nickelate RPOs reported in previous studies assigns both vibrations to A_{1g} modes.[247–249] The $La_{1.2}Sr_{0.8}CoO_4$ phase differs, with 6 vibrations located at 210, 350, 450, 600 and 690 cm^{-1} (Figure 6.3A). All six vibrations are observed for any $La_{2-x}Sr_xNi_{1-y}Co_yO_4$ composition that contains Co (Figure 6.3A, Appendix D.3). In accordance with previous assignments, the 210 cm^{-1} peak arises from La(Sr)-O stretching in the rocksalt layer, while the 450 cm^{-1} is due to a symmetric Ni(Co)-O_{ax} stretch. The 600 cm^{-1} peak is a vibration is linked to the formation of oxygen defects. Previous reports determined that the 350 cm^{-1} peak is associated with B-O_{eq}-B vibrations.[248,249] Relative to the Fe doped phases, an additional peak is present at 690 cm^{-1} which is only observed in Co-containing phases. Studies on Sr_2CoO_4,[277] $LaCoO_3$,[278,279] and $La_{2-x}Sr_xCoO_4$[280] show a vibration near 700 cm^{-1} suggesting that it is not related to an impurity. Both the 210 and 450 cm^{-1} vibrations show composition-dependent trends. The La(Sr)-O vibration shifts in an approximately linear fashion from 214 to 226 cm^{-1} at a rate of about 0.4 cm^{-1} per each $y = 0.05$ increment of Co added (Figure 6.3B). The Ni(Co)-O_{ax} also blueshifts in a linear fashion from 439 to 469 cm^{-1} but at a faster rate of 1.5 cm^{-1} per $y = 0.05$ increment of Co added (Figure 6.3B). The relative intensities of the 450 and 690 cm^{-1} vibrations grow in a non-linear fashion as Co content is varied. Transitioning from $La_{1.2}Sr_{0.8}NiO_4$ to $La_{1.2}Sr_{0.8}Ni_{0.85}Co_{0.15}O_4$ causes the I_{450}/I_{210} ratio to increase from 2.01 to 5.96 in a non-linear fashion (Figure 6.3C). Subsequent increases in Co causes this ratio to oscillate by ±2 units before settling near a final baseline value of 4.37. The I_{690}/I_{210} ratio sharply increases from 0 to 85.9 between the pure nickel and $La_{1.2}Sr_{0.8}Ni_{0.6}Co_{0.4}O_4$ samples, but plateaus with subsequent increases to the Co concentration around (Figure 6.3C).

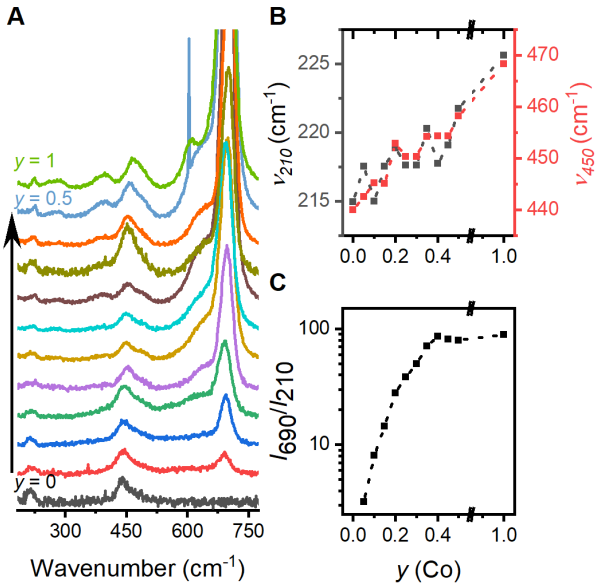

Figure 6.3: (A) Raman spectra of $La_{1.2}Sr_{0.8}Ni_{1-y}Co_yO_4$. (B) The position of the 210 cm^{-1} vibration and the 450 cm^{-1} vibration as a function of composition. (C) The relative intensity of the 450 and 690 cm^{-1} vibration normalized against the 210 cm^{-1} vibration.

6.2.3 Electrochemical Characterization

A series of voltammetric experiments were performed to identify B-site redox processes while extracting mechanistic information about the ORR activity of $La_{1.2}Sr_{0.8}Ni_{1-y}Co_yO_4$. Under N_2 purged conditions with $La_{1.2}Sr_{0.8}NiO_4$ two cathodic processes are observed located at 0.5 and 0 V vs RHE respectively (Figure 6.4A). These redox processes are like those observed in the previous chapter where the cathodic redox processes of $La_{2-x}Sr_xNi_{1-y}Fe_yO_4$ was examined**.** Purging with O_2 appears to preserve the location of these peaks, but increases the current observed by almost a factor of two. A cathodic process with two components is also observed near 0 V vs RHE for $La_{1.2}Sr_{0.8}CoO_4$ but disappears on subsequent cycles yield a relatively featureless CV (Figure 6.4B)**.** Purging the electrolyte with O_2 yields a CV that is almost identical to the measurement acquired under N_2 purged conditions. A series of RRDE experiments was conducted under hydrodynamic conditions to extract mechanistic information about ORR on $La_{1.2}Sr_{0.8}Ni_{1-y}Co_yO_4$ (Figure 6.4C). The linear sweep experiments are like those acquired in Chapter 5, showing the onset of ORR at *ca*. 0.55 V vs RHE with two plateaus near 0.4 and -0.2 V vs RHE. Obtaining plateaus during hydrodynamic voltammetry indicates that reduction of O_2 by the electrode is limited by mass transfer, a finding that is also

reflected by the current measured at the ring. The onset potential was determined by taking the first derivative of LSV curve and selecting peaks with the fastest rate of change. Onset potentials span 0.567 to 0.531 V vs RHE for $La_{1.2}Sr_{0.8}NiO_4$ and $La_{1.2}Sr_{0.8}Ni_{0.7}Co_{0.3}O_4$ respectively, but drift cathodically for Co-rich samples (Figure 6.4D). The onset potential measured after the first plateau is 0.196 V for $La_{1.2}Sr_{0.8}NiO_4$ but shifts cathodically by almost 100 mV after substitution with 0.1 equivalents of Co. Measurements taken with subsequent phases yield onset potentials near 0.12 ± 0.02 V vs RHE and appear to shift anodically to a final value of 0.142 V vs RHE. Tafel slopes measured near 0.55 V vs RHE increases steadily from 64.1 to 88.6 mV dec^{-1} going from $La_{1.2}Sr_{0.8}NiO_4$ to $La_{1.2}Sr_{0.8}Ni_{0.5}Co_{0.5}$ O_4 (Figure 6.4E). These Tafel slope values are do not reflect the expected values of 40, 60 and 120 mV dec^{-1} when an α value of 0.5 is assumed. The number of electrons transferred during ORR (*n*) was calculated using Equation 5.1 from Chapter 5 and presented as a function of applied potential (Figure 6.4F). As discussed in Section 1.3, ORR can follow one of two mechanistic pathways involving a series of proton and electron transfers. The first pathway involves the transfer of 4 electrons while the second pathway involves 2. Co-deficient samples generally yield *n* values near 2.5 to 2.8 e^- transferred during ORR. An anomalous increase to *n* was observed for $La_{1.2}Sr_{0.8}Ni_{0.65}Co_{0.35}O_4$ which has 3.25 e^- transferred during ORR across a wide range of potentials. The selectivity swings back towards peroxide for $La_{1.2}Sr_{0.8}Ni_{0.6}Co_{0.4}O_4$ and $La_{1.2}Sr_{0.8}Ni_{0.55}Co_{0.45}O_4$ yielding 2.51 and 2.82 e^- respectively. A final value of 3.46 e^- is obtained for $La_{1.2}Sr_{0.8}Ni_{0.5}Co_{0.5}O_4$ for the Co-substituted phases. The pure Co-phase, $La_{1.2}Sr_{0.8}CoO_4$, the number of electrons measured is 2.93.

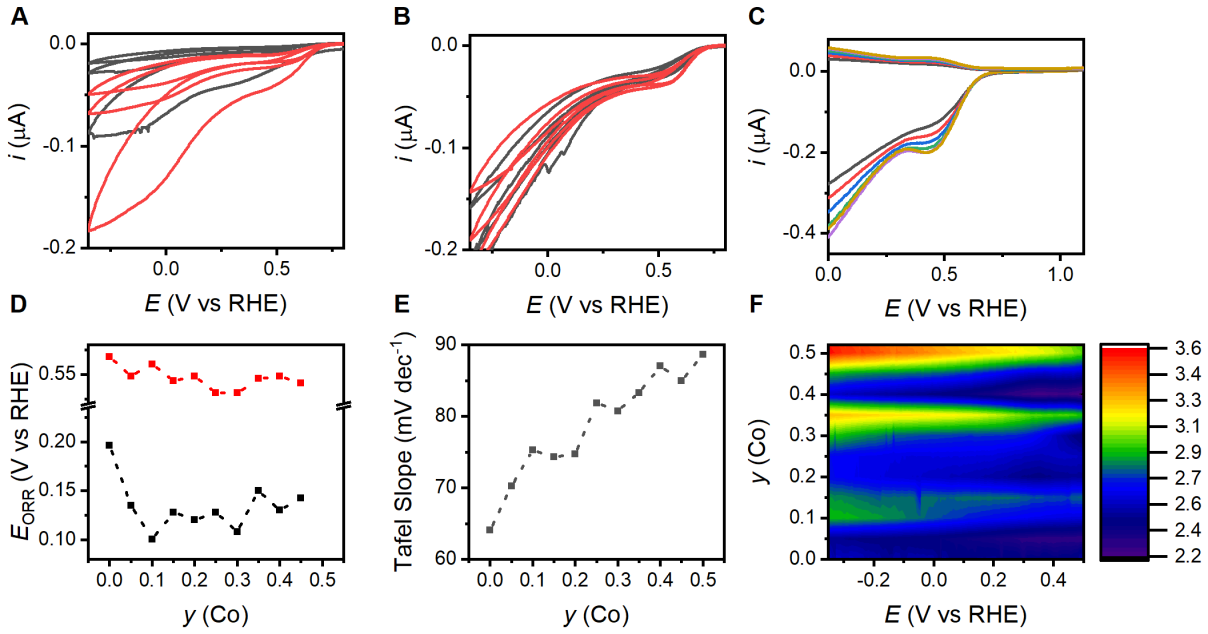

Figure 6.4: The cathodic electrochemistry of $La_{1.2}Sr_{0.8}Ni_{1-y}Co_yO_4$. (A) Cyclic voltammetry of $La_{1.2}Sr_{0.8}NiO_4$ and (B) $La_{1.2}Sr_{0.8}CoO_4$ under N_2 (black) and O_2 purged conditions (red) respectively. (C) Linear sweep voltammograms measured on the disc and ring from 500 to 3000 RPM in square route spacing. (D) Onset potentials of ORR taking before the two plateaus. (E) Tafel slopes as a function of composition and (F) a contour plot as of the number of electrons transferred (*n*) as a function composition and applied potential.

The OER activity of $La_{1.2}Sr_{0.8}Ni_{1-y}Co_yO_4$ was investigated using voltametric characterization. LSV experiments acquired at 3000 RPM (Figure 6.5A) reveal Tafel slopes are *ca.* 120 mV dec^{-1} for the lower concentrations of Co (y = 0 to 0.2), but increases towards 720 mV dec^{-1} for $La_{1.2}Sr_{0.8}Ni_{0.75}Co_{0.25}O_4$ (Figure 6.5B). These results are much larger than the maximum 120 mV dec^{-1} limit expected for the situation where the RDS is the initial electron transfer.[255] A value of 120 mV dec^{-1} assumes that the α parameter is equal to 0.5, but even increasing this value to 0.8 does not account for the observed behaviour. $La_{1.2}Sr_{0.8}NiO_4$, $La_{1.2}Sr_{0.8}Ni_{0.95}Co_{0.05}O_4$ and $La_{1.2}Sr_{0.8}Ni_{0.85}Co_{0.15}O_4$ have Tafel slopes of 132.1, 107.5 and 156.4 mV dec^{-1} that are approximately consistent with the 120 mV dec^{-1} RDS. All other phases have Tafel slopes greater than 200 mV dec^{-1} with $La_{1.2}Sr_{0.8}Ni_{0.75}Co_{0.25}O_4$ and $La_{1.2}Sr_{0.8}Ni_{0.55}Co_{0.45}O_4$ exhibiting anomalously large slopes of 720.1 and 496.4 mV dec^{-1}. Between 0 to 0.15 there is exponential current observed due to OER. Between 0.2 to 0.3 minimal current is observed despite an overpotential of 0.677 V at 1.9 V. This behaviour is

reminiscent of an electrical insulator. Between y = 0.35 to 0.4 some OER activity seems to be restored as indicated by some exponential current but exhibits insulating behaviour again for y = 0.45 and 0.5. The onset potential (Figure 6.5C), obtained by taking the first derivative of the LSVs, ranges from 1.59 V vs RHE for $La_{1.2}Sr_{0.8}CoO_4$ and 1.84 V vs RHE for $La_{1.2}Sr_{0.8}Ni_{0.65}Co_{0.35}O_4$. These onset potentials appear independent of composition, structure, and spectral features.

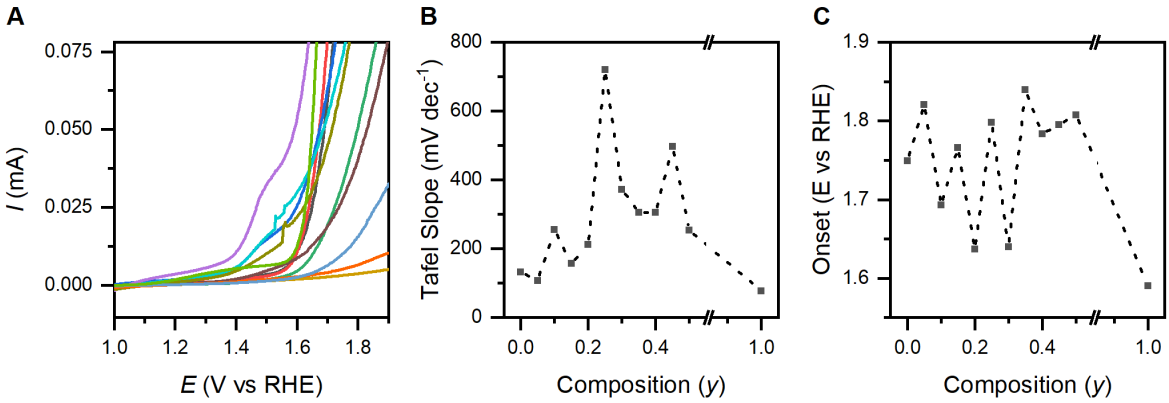

Figure 6.5: Anodic LSV experiments for $La_{1.2}Sr_{0.8}Ni_{1-y}Co_yO_4$. (A) Anodic sweeps for $La_{1.2}Sr_{0.8}Ni_{1-y}Co_yO_4$. (B) Tafel slope analysis and (C) the apparent onset potential for $La_{1.2}Sr_{0.8}Ni_{1-y}Co_yO_4$.

Ex-situ analysis of $La_{1.2}Sr_{0.8}NiO_4$ and $La_{1.2}Sr_{0.8}CoO_4$ reveals that prolonged electrolysis at anodic potentials induces vibrations associated with structural degradation. Samples subjected to 30 minutes of electrolysis at 1.9 V vs RHE and studied by confocal Raman spectroscopy show significant changes to Raman vibrations relative to the pristine phases. $La_{1.2}Sr_{0.8}NiO_4$ gains three additional peaks at 149, 179 and 1073 cm^{-1} which were previously assigned to $SrCO_3$ (Figure 6.6A).[281] The presence of Sr-enrichment on the surface is typically associated with A-site segregation and instability of the parent phase.[131] This coincided with the expected result that the relative intensity of the 210 cm^{-1} peak decreases when compared to the parent phase. The main A_{1g} vibration located near 439 cm^{-1} in the pristine phase blue-shifts to 446 cm^{-1} after electrolysis. Post-electrolysis $La_{1.2}Sr_{0.8}CoO_4$ changes colour from black to grey when observed by confocal microscopy suggesting a chemical change occurred to the bulk of the material. Electrolysis of $La_{1.2}Sr_{0.8}CoO_4$ also broadens and attenuates the intensity of the Raman active peaks between 120-750 cm^{-1} while introducing several high energy vibrations (Figure 6.6B). Broadening is so severe that the A_{1g} vibrations cannot be distinguished from the noise of the baseline preventing the comparison of relative intensities

between the pristine and conditioned phases. Despite degradation of the structure, no peaks consistent with $SrCO_3$ were observed. Additional vibrations are observed at 800, 948, and 1065 cm^{-1} which seems consistent with the high energy vibrations observed with the La_2CuO_4 phases in Chapter 3. Attempts to assign these vibrations varies in the literature, so they will remain unassigned to avoid unnecessary speculation. The only vibration that could be systematically analyzed from the pristine phase is the 698 cm^{-1} peak, which blue shifts to 707 cm^{-1}.

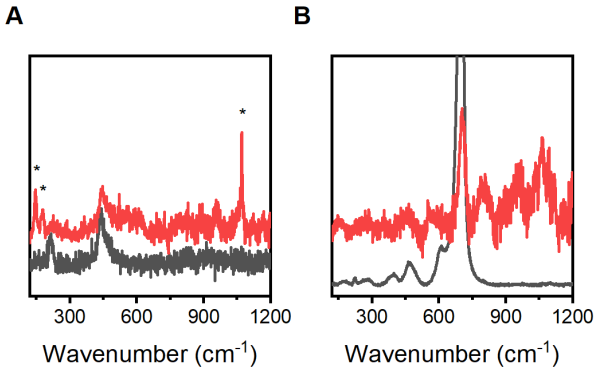

Figure 6.6: Ex-situ Raman of (A) $La_{1.2}Sr_{0.8}NiO_4$ and (B) $La_{1.2}Sr_{0.8}CoO_4$. Black lines are spectra acquired on the pristine phase, while the red lines are acquired from the surface after electrolysis.

6.3 Discussion

6.3.1 Correlation Analysis

Correlation analysis of PXRD, Raman, and electrochemical parameters indicate that Co-induced distortions provide distinct changes in electrocatalysis. The strongest correlations observed are with the compression of the *c*-axis and the anisotropic lattice distortion given by *c*/*a*. Distortions given by the *c*/*a* parameter approximately tracks the position of the 690 cm^{-1} peak shown in the Raman spectra (Figure 6.7A). Assignments of this peak varies across different studies. Polarized Raman spectra acquired on epitaxially grown $La_{1.5}Sr_{0.5}CoO_4$ films indicates that this vibration is an in-plane breathing mode Co octahedra.[282,283] This vibration was assigned as the simultaneous stretching of all four Co-O_{eq} bonds with A_g symmetry. The same vibration was also observed with Sr_2CoO_4 samples, but was assigned as an A_{1g} stretch of apical oxygens at B-site octahedra.[277]

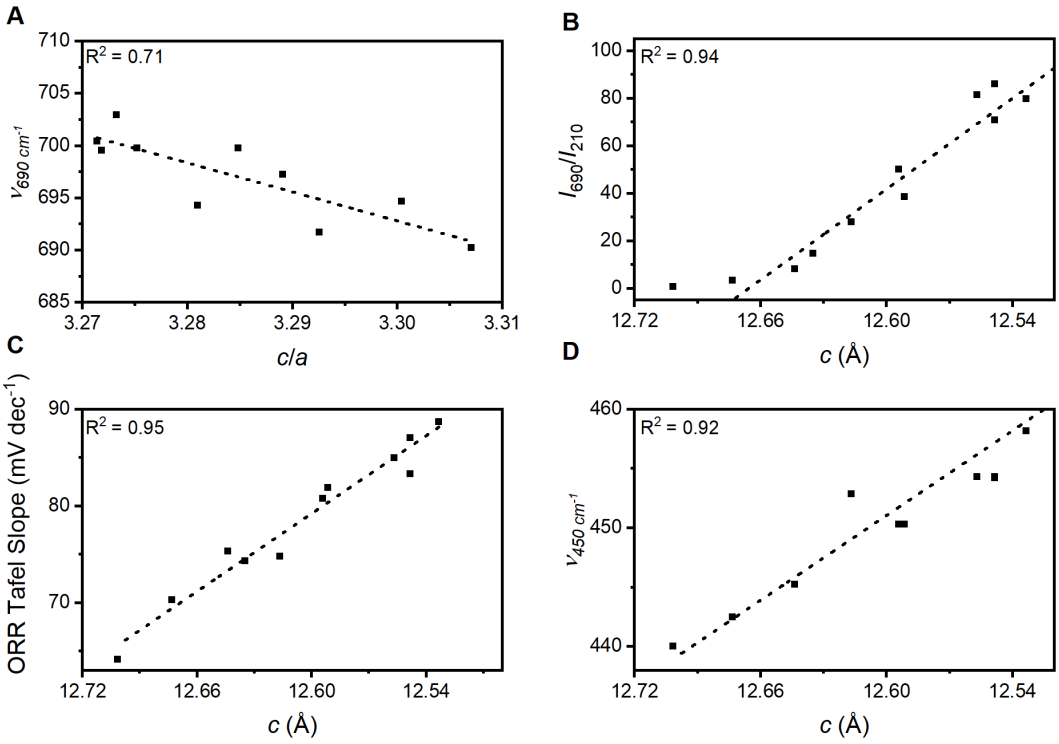

Figure 6.7: Analysis of correlations between the structural, spectroscopic and electrochemical parameters of $La_{1.2}Sr_{0.8}Ni_{1-y}Co_yO_4$. (A) Correlation between the 690 cm^{-1} vibration and the unit cell distortion *c*/*a*. (B) Correlation between the intensity of the 690 cm^{-1} vibration normalized against the 210 cm^{-1} La(Sr)-O vs the *c* unit cell parameter. (C) The 450 cm^{-1} vibration correlated against *c*. (D) ORR Tafel slope correlated with *c*.

This assignment contradicts several single crystal studies, so it will be disregarded in this chapter. The breathing mode is not predicted by factor group analysis of the *I*4/*mmm* unit cell, suggesting that there is a local distortion that reduces lattice symmetry and introduces the 690 cm^{-1} peak. Studies on cobaltate[282,283] and manganate[284] RPOs propose that the lowing of lattice symmetry arises from charge ordering of Co(II) and Co(III) within the lattice. Raman spectroscopy of $La_{0.5}Sr_{1.5}MnO_4$ single crystals suggest that ordering of Mn(III) and Mn(IV) in the "checkerboard" configuration lowers the lattice symmetry from the body centered *I*4/*mmm* to a primitive unit cell *P*4/*mmm*.[284] The lowering of symmetry activates the in-plane breathing mode which has A_g symmetry (Figure 6.8). Lowering of symmetry via this mechanism would be difficult to detect using PXRD because it relies on the

scattering of X-rays by electrons in the lattice. Ordering, and changes to oxidation state would still be detected as *I*4/*mmm* in the bulk structure while having *P*4/*mmm* local symmetry.

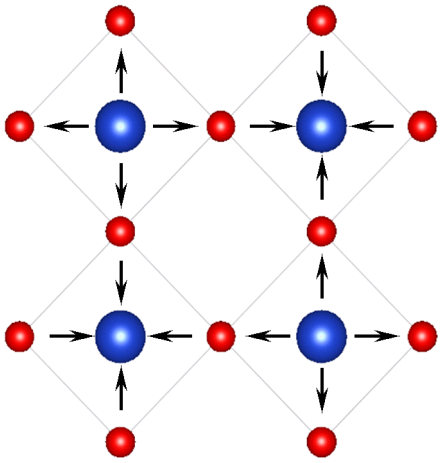

Figure 6.8: A cross section of the *a*/*b* plane showing checkerboard ordering of the A_g vibration.

It is counterintuitive that the energy of an A_g vibration involving oxygens in the *a*/*b* plane correlates so strongly with *c*-axis and *c*/*a* ratio. This finding suggests that compression of the axial oxygens around Co octahedra affects the bonding of oxygens at equatorial sites. This relationship is further reinforced by linear dependence of the I_{690}/I_{210} ratio on the length of the *c*-axis (Figure 6.7B). The A_{1g} vibration located at *ca.* 450 cm^{-1} also approximates the length of the *c*-axis which is expected because it involves symmetric stretching of Ni(Co)-O_{ax} octahedra (Figure 6.7C). However, weaker correlations between Tafel slopes and the I_{450}/I_{210} ratio are observed in comparison to $LaSrNi_{1-y}Fe_yO_4$ solid solutions.[285] This is likely due to additional components observed in Raman spectra of Co-containing phases which complicates the analysis of the 450 cm^{-1} vibration and introduces more uncertainty to Raman intensities. Regardless, the strong correlations amongst unit cell parameters, the position and relative intensity of Raman active vibrations suggests that they are a useful diagnostic tool for assessing the degree of distortion with these RPOs, especially along the *c*-axis.

Relationship between the electrocatalytic parameters and structural distortions are more complex than the utilization of spectroscopy alone. Among the samples that contain Ni, a strong, positive

correlation between the *c*-axis length and ORR Tafel slope was observed (Figure 6.7D). The $La_{1.2}Sr_{0.8}CoO_4$ sample does not fit this trend yielding a Tafel slope of 58.1 mV dec^{-1} that accompanies a *c*-axis parameter of 12.52 Å. To fit within the trend shown in Figure 6.7D a Tafel slope near 100 mV dec^{-1} would be required. This finding suggests that the observed electrocatalytic activity originates from activation of the Ni-O_{ax} rather than Co-O_{ax} bond during ORR. If analysis for phases with larger Co-contents was to continue it would be expected that we would anticipate the trend shown here to deviate from the linear trend as Co becomes the dominant electrocatalytic species. The selectivity of ORR, reflected by the number of electrons transferred and the Tafel slopes measured from ORR exhibit dependence on spectroscopic parameters. There is no strong correlation between the number of electrons transferred during ORR, structural or spectroscopic features. The strongest correlation observed is between I_{690}/I_{450} and *n*, yielding an R-value of 0.65 (Appendix D.4), but no clear conclusion can be drawn by this finding.

6.3.2 Oxygen Evolution and the Anodically-Induced Phase Changes of $La_{2-x}Sr_xNi_{1-y}Co_yO_4$

Voltammetric characterization of $La_{2-x}Sr_xNi_{1-y}Co_yO_4$ using anodic potentials yield OER activity that deviates significantly from expectations while introducing structural instability. A maximum Tafel slope of 120 mV dec^{-1} is traditionally expected when the RDS is the initial electron-transfer process.[255] Nickel rich compositions conform to this criterion with Tafel slopes spanning 107-156 mV dec^{-1}. For Co concentrations higher than $y = 0.15$ the Tafel slopes span 200-700 mV dec^{-1} indicating significant deviations from purely kinetic behaviour. Because the working electrode is under forced convection, it is unlikely that mass transfer is responsible for the large Tafel slopes observed. Tafel slopes greater than 120 mV dec^{-1} can also arise from insufficient conductivity, or kinetically inactive catalysts. Cyclic voltammetry indicates that several phases exhibit insulating qualities and could be responsible for deviations from ideal kinetic behaviour (Appendix D.5). Because these Tafel slopes are questionable, subsequent analysis will be limited to $La_{1.2}Sr_{0.8}NiO_4$ and $La_{1.2}Sr_{0.8}CoO_4$. *Ex-situ* analysis of both phases by Raman spectroscopy identified structural instability, albeit via different mechanisms for each phase. $SrCO_3$ was clearly identified as the primary degradation product of $La_{1.2}Sr_{0.8}NiO_4$ which like formed from the displacement of Sr atoms bulk of the RPO structure to the surface. SrO has been identified as a degradation product RPOs in other publications, and exposure of SrO to atmospheric conditions causes the rapid formation of carbonates in less than 30 minutes.[281] Attenuation of intensity and broadening of peaks in $La_{1.2}Sr_{0.8}CoO_4$ suggests the introduction of

disorder into the lattice via amorphization. Unlike the pure nickel phase, no $SrCO_3$ is observed indicating that the majority of Sr remains in the lattice. Oxidation of Co(III) to Co(IV) can occur at extreme anodic potentials in perovskites, but potentially introduce instability due to the size mismatch between the ionic radii of the two cations. The high energy vibrations identified at 800, 966 and 1063 cm^{-1} Have not been reported or assigned by for Co-containing RPOs. To avoid speculation, the nature of these vibrations will not be discussed.

The insulating behaviour observed by voltametric experiments has been reported in other Co containing perovskites and RPOs. Temperature dependent resistance measurements indicate that $ACoO_3$ perovskites are insulators at 300 K, but have metallic resistivity at temperature between 500 to 700 K.[286,287] Optical measures demonstrate that the $ACoO_3$ perovskites have band-gaps spanning 1 to 1.5 eV depending on the identity of the A-site cation (La, Pr, Nd, Sm, Eu, and Gd).[286] Band-gaps of this magnitude are often associated with semiconducting conductivity, but the high resistivity observed suggests that secondary interactions beyond structural distortions that inhibit the transfer of electrons.[288] The electronic structure and magnetic properties of $La_{2-x}A_xCoO_4$ has been extensively studied providing insights into the conductivity within these phases.[29,264,288–293] Insulating behaviour is observed across a broad range of x values, but resistivity begins to taper off near $x = 0.8 – 1$. This behaviour is frequently attributed to charge ordering and the spin-state of Co that can increase the activation barrier for electron transfer through imposition of spin-forbidden transitions.[288,294]

6.3.3 Comparison of Structural Correlations and ORR Activity with $La_{2-x}Sr_xNi_{1-y}Fe_yO_4$ Solid Solutions

In Chapter 5, Fe-induced structural distortions were analyzed using a combination of PXRD and Raman spectroscopy in a similar manner to this chapter. A major finding from this work was that Fe induces causes the *c*-axis to elongate faster than the *a/b* plane yielding a distortion that could be interpreted through utilization of the *c*/*a* ratio. Addition of Fe up to $y = 0.5$ yields an increase in the *c*/*a* parameter from 3.27 to 3.32. The opposite is observed for $La_{2-x}Sr_xNi_{1-y}Co_yO_4$ phases, where the unit cell compresses from 3.32 to 3.27 as Co content increases from $y = 0$ to 0.5. Assuming that the majority of Fe and Co are isovalent with an oxidation state of (III) it is unlikely that electronic effects cause these structural distortions. The A-site stoichiometry of $La_{1.2}Sr_{0.8}NiO_4$ suggests the majority of Ni is in the Ni(III) oxidation state. Ni(III) in a low-spin, octahedral coordination environment should have an ionic radius of 60 pm.[252] Co(III) is expected to be smaller than Ni(III), with an ionic radius of

54.5 pm in the low-spin octahedral environment.[252] Co(III) is smaller, and also, not expected to undergo an Jahn-Teller distortion like Ni(III). Therefore it is expected that Co(III) would induce a contraction of the lattice that is consistent with the *c*/*a* parameters reported in this chapter.

Even though the $La_{1.2}Sr_{0.8}Ni_{1-y}Co_yO_4$ and $LaSrNi_{1-y}Fe_yO_4$ systems are structurally similar, there is no-direct overlap amongst the parameters that correlate well. For example, the relative intensity of the 440 vibration, which describes the distortion of the Ni(Fe)-O_{ax} bonds, linearly correlates with the Tafel slope measured during ORR. In contrast, $La_{1.2}Sr_{0.8}Ni_{1-y}Co_yO_4$ shows weaker correlations between the relative intensity of the 450 cm^{-1} mode with the ORR Tafel slope. Compression along the *c*-axis is a stronger predictor of the ORR Tafel slope for the $La_{1.2}Sr_{0.8}Ni_{1-y}Co_yO_4$. It appears that the *c*/*a* ratio track the relative intensity of the 440 vibrations in $LaSrNi_{1-y}Fe_yO_4$, while in the $La_{1.2}Sr_{0.8}Ni_{1-y}Co_yO_4$, it does not. As discussed in Section 6.3.1, there is substantial overlap between the 450 cm^{-1} vibration and adjacent vibrational components in Co-containing samples. This clutter in the spectrum may interfere with the extraction of reliable I_{450}/I_{210} values that could be compared to $LaSrNi_{1-y}Fe_yO_4$ phases. Also, one system experiences tensile strain while the other experiences compressive strain. The blue-shifting of the 450 vibration indicates that the axial bond might also be involved in ORR in the system as well. This system is clearly complex.

Tafel slope analysis of $La_{2-x}Sr_xNi_{1-y}Co_yO_4$ during ORR clearly indicates that *c*-axis length dictates the energetics of the RDS (Figure 6.7D). Because the *c*-axis is directly related to the Ni(Co)-O_{ax} bond length it implies that this bond is also involved in the RDS. These results agree with those presented in Chapter 5 allowing for the similar conclusions to be drawn for the origins of ORR activity. To reiterate, this system appears to support that distorting B-site octahedra alters the α parameter causing Tafel slopes to deviate from standard values predicted in the literature. A Tafel slope of 64.1 mV dec^{-1} obtained from $La_{1.2}Sr_{0.8}NiO_4$ is close to the ideal slope of 60 mV dec^{-1} indicating that the RDS involves breaking of the O-O bond.[255] The progressive increase of the Tafel slope from 64.1 to 88.6 mV dec^{-1} indicates that the kinetics of the O-O bond breaking RDS is impeded by the shrinking of the Ni(Co)-O_{ax}. This appears to induce compressive strain along the *c*-axis which modifies the potential energy surface. This is similar to previous systems that were discussed in Chapter 5, particularly $Ni(OH)_2$.[257] Compressive strain moves the potential energy surface in such a way that increases the activation barrier by changing the symmetry of the potential energy surfaces between the oxidized and reduced states. Previous reports indicate that compressive strain decreases ORR kinetics in

Nd_2NiO_4 and reduces surface oxygen exchange kinetics by factor of two, bringing validity to the conclusions.[91]

6.4 Conclusion

This chapter investigated the effect of Co-induced structural distortions on the electrocatalytic activity of $La_{1.2}Sr_{0.8}Ni_{1-y}Co_yO_4$. Correlation analysis of diffraction and spectroscopic data indicates that increasing the Co concentration compresses the RPO structure along the *c*-axis while introducing checkerboard ordering within the *a*/*b* plane. Compression of the unit cell was found to directly impact the kinetics for the RDS of ORR while showing some influence on the reaction trajectory. The OER activity was impeded by the insulating nature of across several compositions, resulting in large, non-standard Tafel slopes. Prolonged electrolysis of the nickel and cobalt phase resulted in different decomposition products during the same period, suggesting that there are two different mechanisms for sample deterioration. The results shown here seem to confirm many of the trends shown in Chapter 5.

6.5 Experimental Details

6.5.1 Synthesis

Compounds were fabricated using a modified citrate-nitrate gel method based on the $La_{1.2}Sr_{0.8}Ni_{1-y}Co_yO_4$ formula in increments of y = 0.05. Solutions were prepared with 3 mmol La(III), 2 mmol Sr(II), with an amount of Ni(II)and Co(III) totaling 2.5 mmol. Appropriate amounts of $SrCO_3$ (99% purity, Alfa Aesar) and $Ni_4CO_3(OH)_6(H_2O)_4$ (99.9% purity, Sigma Aldrich) was wet with milli-Q H_2O and dissolved with dropwise addition of concentrated HNO_3. Once dissolved, $La(NO_3)_3(H_2O)_6$ (99.9% purity, Thermo Scientific) and $Co(NO_3)_2$ $(H_2O)_6$ (Alfa Aesar) were added to the solution. Citric acid (99% purity, Alfa Aesar) and EDTA (99% purity, Alfa Aesar) in milli-Q H_2O were added and the pH of the solution was adjusted to 10 using NH_4OH. The solution was heated on a hotplate set at 200 °C until a dark green gel formed. The gel was heated at 350 °C until combustion took place. Combusted powders were placed in a porcelain crucible and heated at 1000 °C for 24 h, with an intermediate regrinding step after 12 h. All products retrieved were black polycrystalline powders.

6.5.2 Powder X-ray Diffraction

X-ray diffraction experiments was performed on an Inel diffractometer with powdered samples mounted in an aluminum sample holder. Samples were run for 30 min each and the structural parameters were extracted by Rietveld refinement of the diffraction patterns using the GSAS 2 software package.

6.5.3 Raman Spectroscopy

Raman spectroscopy was carried out on a Renishaw inVia Reflex Raman microscope using a 532 nm laser with a 2400 l/mm grating. Laser intensity was filtered to 1% of the maximum intensity and spectra were recorded with a 400 s acquisition time. Data was processed using Renishaw WiRE 5.3 software package, which included polynomial baseline subtraction and peak fit.

6.5.4 Rotating Ring Disc Voltammetry

Two 7 μL aliquots of 10 mg ml^{-1} suspensions of $La_{1.2}Sr_{0.8}Ni_{1-y}Co_yO_4$ in 0.125% Nafion (from a 5% suspension containing isopropanol and H_2O, Alfa Aesar) were drop cast onto a 10 mm diameter glassy carbon disk electrode while leaving a platinum ring clean. A Hydroflex reversible hydrogen electrode (RHE; Gaskatel GmbH, Germany) was used as a reference electrode and platinum foil was used as the counter electrode. Hydrodynamic measurements were acquired on a Metrohm Autolab electrochemical workstation, with the RRDE rotated at rates between 500 to 3000 RPM. All measurements were acquired at a scan rate of 5 mV s^{-1} in 0.1 M KOH purged with O_2. Linear sweep voltammetry was conducted from 1.1 V to -0.35 V vs RHE. The potential of the platinum ring was set to 1.5 V vs RHE for detection of hydrogen peroxide.

Chapter 7: Summary and Concluding Remarks

This thesis provided an in-depth investigation on the electrochemically induced phase changes that governed phase changes amongst several RPO compositions, including $La_{2-x}Sr_xCuO_4$, $La_{2-x}Sr_xNi_{1-y}Fe_yO_4$ and $La_{2-x}Sr_xNi_{1-y}Co_yO_4$. PXRD and Raman spectroscopy identified composition-dependent distortions, amorphization, and changes to defect chemistry that occured after electrolysis. Whether these changes are beneficial or detrimental to the catalyst was dependent on the material and the reactions that took place on the electrode surface.

The electrochemical behaviour of the archetypical $La_2CuO_{4\pm\delta}$ phase was characterized using an array of techniques. Cyclic voltammetry at a variety of scan rates determined there was two Cu-based redox processes. Ex-situ analysis of La_2CuO_4 identified systematic changes to the unit cell parameters, Cu-O bond strength, and Cu oxidation state as the potential bias is varied. Application of extreme cathodic potentials resulted in the complete destruction of the RPO structure. These structural changes are consistent with defect formation and amorphization of the parent structure. Changes to the voltametric behaviour and product selectivity after electrolysis indicates that amorphization and defects affects small molecule interactions.

The investigation of cuprate-based RPOs was extended to the $La_{2-x}Sr_xCuO_4$ series. PXRD analysis of $La_{1.9}Sr_{0.1}CuO_4$, $La_{1.8}Sr_{0.2}CuO_4$, $La_{1.7}Sr_{0.3}CuO_4$, $La_{1.6}Sr_{0.4}CuO_4$, and $La_{1.5}Sr_{0.5}CuO_4$ confirmed that the addition of Sr forces the undoped La_2CuO_4 structure to adopt a unit cell with tetragonal symmetry. Voltammetric behaviour under CO_2-purged conditions revealed redox processes different than those observed under N_2. CO_2 was found to interact with all $La_{2-x}Sr_xCuO_4$ electrodes according to an EC_i mechanism with Sr reducing observed electrochemical phase changes. These phase changes were found to alter the binding mode between CO_2 and the surface.

A cross section of $La_{2-x}Sr_xNi_{1-y}Fe_yO_4$ revealed that their electrochemical activity is affected by the structural distortions of the A and B site. Incorporation of Fe into the lattice caused an asymmetric expansion of the *c* axis relative to the *a*. This impacted the onset potential and the selectivity of ORR reaction. Correlation analysis was a power tool for detecting changes to electrochemical activity. The investigation of B-site induced lattice distortions was continued by examining the $La_{1.2}Sr_{0.8}Ni_{1-y}Co_yO_4$ family of RPOs. X-ray diffraction and spectroscopy revealed that increasing the Co-concentration compressed the RPO structure along the *c*-axis. Compression of the unit-cell was shown to have an

impact on the RDS of the ORR reaction, but its impact on reaction selectivity remains unclear. Analysis of OER was complicated by the insulating properties and poor reaction kinetics across the sample series. Despite this, electrolysis at extreme anodic potentials revealed that these RPOs deteriorated by two different reaction mechanisms.

The findings presented in this thesis illustrated that RPOs have complicated structures that are sensitive to heteroatom substitution and electrolysis. Heteroatom substitution was shown to affect the unit cell dimensions of the RPO structure while confirming charge compensation mechanisms. Raman spectroscopy revealed that heteroatom substitution of the K_2NiF_4 structure introduced unexpected lattice vibrations that are similar to the T* polymorph and is a useful tool for analysis of defect concentration. The presence of secondary phases is seldom reported and could have implications for electrocatalysis. Data presented in Chapters 3, 4, 5 and 6 show that La_2CuO_4, $La_{2-x}Sr_xCuO_4$, $La_{2-x}Sr_xNi_{1-y}Fe_yO_4$ and $La_{1.2}Sr_{0.8}Ni_{1-y}Co_yO_4$ undergo some sort of lattice distortion or phase change after electrolysis. This could be as simple as the incorporation of defects that distort the unit cell, or phase segregation that can passivate the electrode. Changes to the RPO structure are seldom discussed, but can yield dramatic changes to reaction selectivity, as was shown in Chapter 3 and 5. These finding illustrated that strain, defects and phase segregation are important phenomenon to describe the electrocatalytic activity of RPOs.

References

(1) Ruddlesden, S. N.; Popper, P. New Compounds of the K_2NiF_4 Type. *Acta Crystallogr.* **1957**, *10* (8), 538–539.

(2) Xu, X.; Pan, Y.; Zhong, Y.; Ran, R.; Shao, Z. Ruddlesden–Popper Perovskites in Electrocatalysis. *Mater. Horiz.* **2020**, *7* (10), 2519–2565.

(3) Sharma, I. B.; Singh, D. Solid State Chemistry of Ruddlesden-Popper Type Complex Oxides. *Bull Mater Sci* **1998**, *21* (5), 363–374.

(4) Hong, Y.; Byeon, P.; Bak, J.; Heo, Y.; Kim, H.-S.; Bae, H. B.; Chung, S.-Y. Local-Electrostatics-Induced Oxygen Octahedral Distortion in Perovskite Oxides and Insight into the Structure of Ruddlesden–Popper Phases. *Nat. Commun.* **2021**, *12* (1), 5527.

(5) Takeda, Y.; Kanno, R.; Sakano, M.; Yamamoto, O.; Takano, M.; Bando, Y.; Akinaga, H.; Takita, K.; Goodenough, J. B. Crystal Chemistry and Physical Properties of $La_{2-x}Sr_xNiO_4$ ($0 \leq x \leq 1.6$). *Mater. Res. Bull.* **1990**, *25* (3), 293–306.

(6) James, M.; Tedesco, A.; Cassidy, D.; Colella, M.; Smythe, P. J. The Phase Diagram and Crystal Chemistry of Strontium-Doped Rare Earth Cobaltates: $Ln_{2-x}Sr_xCoO_{4+\delta}$ (Ln = La-Dy). *J. Alloys Compd.* **2006**, *419* (1), 201–207.

(7) Wang, H. H.; Geiser, U.; Thorn, R. J.; Carlson, K. D.; Beno, M. A.; Monaghan, M. R.; Allen, T. J.; Proksch, R. B.; Stupka, D. L. Synthesis, Structure, and Superconductivity of Single Crystals of High-T_c $La_{1.85}Sr_{0.15}CuO_4$, a Lanthanum Strontium Copper Oxide. *Inorg. Chem.* **1987**, *26* (8), 1190–1192.

(8) Lee, D.; Lee, H. N. Controlling Oxygen Mobility in Ruddlesden–Popper Oxides. *Materials* **2017**, *10* (4), 1–22.

(9) Amow, G.; Davidson, I. J.; Skinner, S. J. A Comparative Study of the Ruddlesden-Popper Series, $La_{n+1}Ni_nO_{3n+1}$ (N=1, 2 and 3), for Solid-Oxide Fuel-Cell Cathode Applications. *Solid State Ion.* **2006**, *177* (13), 1205–1210.

(10) Goldschmidt, V. M. Die Gesetze der Krystallochemie. *Sci. Nat.* **1926**, *14* (21), 477–485.

(11) Johnsson, M.; Lemmens, P. Crystallography and Chemistry of Perovskites. In *Handbook of Magnetism and Advanced Magnetic Materials*; John Wiley & Sons, Ltd, 2007.

(12) Abramov, Yu. A.; Tsirelson, V. G.; Zavodnik, V. E.; Ivanov, S. A.; D, B. I. The Chemical Bond and Atomic Displacements in $SrTiO_3$ from X-Ray Diffraction Analysis. *Acta Crystallogr. B* **1995**, *51* (6), 942–951.

(13) Ali, R.; Yashima, M. Space Group and Crystal Structure of the Perovskite $CaTiO_3$ from 296 to 1720 K. *J. Solid State Chem.* **2005**, *178* (9), 2867–2872.

(14) Lehnert, H.; Boysen, H.; Schneider, J.; Frey, F.; Hohlwein, D.; Radaelli, P.; Ehrenberg, H. A Powder Diffraction Study of the Phase Transition in $LaAlO_3$. *Z. Kristallogr.* **2000**, *215* (9), 536–541.

(15) Takeda, Y.; Kanamura, F.; Shimada, M.; Koizumi, M. The Crystal Structure of $BaNiO_3$. *Acta Crystallogr. B* **1976**, *32* (8), 2464–2466.

(16) Yamada, K.; Kudo, E.; Endoh, Y.; Tsuda, K.; Tanaka, M.; Kokusho, K.; Asano, H.; Izumi, F.; Oda, M.; Hidaka, Y.; Suzuki, M.; Murakami, T. Determination of Space Group and Refinement of Structure Parameters for $La_2CuO_{4-\delta}$ Crystals. *Jpn. J. Appl. Phys.* **1988**, *27* (7R), 1132–1137.

(17) Le Toquin, R.; Paulus, W.; Cousson, A.; Dhalenne, G.; Revcolevschi, A. Interstitial and Apical Oxygen Order–Disorder in $La_2CoO_{4+\delta}$ Observed by Single-Crystal Neutron and X-Ray Diffraction. *Phys. B: Condens. Matter* **2004**, *350* (1), E269–E272.

(18) Marin, C.; Henry, J. Y.; Boucherle, J. X. Structural Neutron Diffraction Study of a $Nd_2CuO_{4-\delta}$ Single Crystal. *Solid State Commun.* **1993**, *86* (7), 425–430.
(19) Mukherjee, K.; Hayamizu, Y.; Kim, C. S.; Kolchina, L. M.; Mazo, G. N.; Istomin, S. Ya.; Bishop, S. R.; Tuller, H. L. Praseodymium Cuprate Thin Film Cathodes for Intermediate Temperature Solid Oxide Fuel Cells: Roles of Doping, Orientation, and Crystal Structure. *ACS Appl. Mater. Interfaces* **2016**, *8* (50), 34295–34302.
(20) Hyatt, N. C.; Gray, L.; Gameson, I.; Edwards, P. P.; Hull, S. High-Pressure Neutron Diffraction Study of the Quasi-One-Dimensional Cuprate Sr_2CuO_3. *Phys. Rev. B* **2004**, *70* (21), 214101.
(21) Pikalova, E. Yu.; Sadykov, V. A.; Filonova, E. A.; Eremeev, N. F.; Sadovskaya, E. M.; Pikalov, S. M.; Bogdanovich, N. M.; Lyagaeva, J. G.; Kolchugin, A. A.; Vedmid', L. B.; Ishchenko, A. V.; Goncharov, V. B. Structure, Oxygen Transport Properties and Electrode Performance of Ca-Substituted Nd_2NiO_4. *Solid State Ion.* **2019**, *335*, 53–60.
(22) Gilev, A. R.; Kiselev, E. A.; Zakharov, D. M.; Cherepanov, V. A. Effect of Calcium and Copper/Iron Co-Doping on Defect-Induced Properties of La_2NiO_4-Based Materials. *J. Alloys Compd.* **2018**, *753*, 491–501.
(23) Makhnach, L. V.; Pankov, V. V.; Strobel, P. High-Temperature Oxygen Non-Stoichiometry, Conductivity and Structure in Strontium-Rich Nickelates $La_{2-x}Sr_xNiO_{4-\delta}$ (x = 1 and 1.4). *Mater. Chem. Phys.* **2008**, *111* (1), 125–130.
(24) West, A. R. *Solid State Chemistry and Its Applications*, 2nd ed.; Wiley, 2014.
(25) Kanai, H.; Mizusaki, J.; Tagawa, H.; Hoshiyama, S.; Hirano, K.; Fujita, K.; Tezuka, M.; Hashimoto, T. Defect Chemistry of $La_{2-x}Sr_xCuO_4$: Oxygen Nonstoichiometry and Thermodynamic Stability. *J. Solid State Chem.* **1997**, *131* (1), 150–159.
(26) Alyoshin, V. A.; Romanova, I. P.; Mikhailova, D.; Oswald, S.; Senyshyn, A.; Ehrenberg, H. Oxygen Nonstoichiometry of Tetragonal $La_{2-x}Sr_xCuO_{4-\delta}$ (x = 0.15-1.2) and in Situ XPS Studies at Elevated Temperatures. *J. Phys. Chem. A* **2010**, *114* (51), 13362–13369.
(27) Teske, K.; Ullmann, H.; Trofimenko, N. Thermal Analysis of Transition Metal and Rare Earth Oxide System-Gas Interactions by a Solid Electrolyte-Based Coulometric Technique. *J. Therm. Anal. Calorim.* **1997**, *49* (3), 1211–1220.
(28) Munnings, C. N.; Skinner, S. J.; Amow, G.; Whitfield, P. S.; Davidson, I. J. Oxygen Transport in the $La_2Ni_{1-x}Co_xO_{4+\delta}$ System. *Solid State Ion.* **2005**, *176* (23), 1895–1901.
(29) Vashook, V. V.; Ullmann, H.; Olshevskaya, O. P.; Kulik, V. P.; Lukashevich, V. E.; Kokhanovskij, L. V. Composition and Electrical Conductivity of Some Cobaltates of the Type $La_{2-x}Sr_xCoO_{4.5-x/2\pm\delta}$. *Solid State Ion.* **2000**, *138* (1), 99–104.
(30) Xie, W.; Lee, Y.-L.; Shao-Horn, Y.; Morgan, D. Oxygen Point Defect Chemistry in Ruddlesden-Popper Oxides $(La_{1-x}Sr_x)_2MO_{4\pm\delta}$ (M = Co, Ni, Cu). *J. Phys. Chem. Lett.* **2016**, *7* (10), 1939–1944.
(31) Bassat, J.-M.; Odier, P.; Villesuzanne, A.; Marin, C.; Pouchard, M. Anisotropic Ionic Transport Properties in $La_2NiO_{4+\delta}$ Single Crystals. *Solid State Ion.* **2004**, *167* (3), 341–347.
(32) Burriel, M.; Garcia, G.; Santiso, J.; Kilner, J. A.; Chater, R. J.; Skinner, S. J. Anisotropic Oxygen Diffusion Properties in Epitaxial Thin Films of $La_2NiO_{4+\delta}$. *J. Mater. Chem.* **2008**, *18* (4), 416–422.
(33) Bassat, J.-M.; Burriel, M.; Wahyudi, O.; Castaing, R.; Ceretti, M.; Veber, P.; Weill, I.; Villesuzanne, A.; Grenier, J.-C.; Paulus, W.; Kilner, J. A. Anisotropic Oxygen Diffusion Properties in $Pr_2NiO_{4+\delta}$ and $Nd_2NiO_{4+\delta}$ Single Crystals. *J. Phys. Chem. C* **2013**, *117* (50), 26466–26472.

(34) Zhang, L.; Yao, F.; Meng, J.; Zhang, W.; Wang, H.; Liu, X.; Meng, J.; Zhang, H. Oxygen Migration and Proton Diffusivity in Transition-Metal (Mn, Fe, Co, and Cu) Doped Ruddlesden–Popper Oxides. *J. Mater. Chem. A* **2019**, *7* (31), 18558–18567.
(35) Gu, X.-K.; Nikolla, E. Design of Ruddlesden–Popper Oxides with Optimal Surface Oxygen Exchange Properties for Oxygen Reduction and Evolution. *ACS Catal.* **2017**, *7* (9), 5912–5920.
(36) Huan, D.; Wang, Z.; Wang, Z.; Peng, R.; Xia, C.; Lu, Y. High-Performanced Cathode with a Two-Layered R–P Structure for Intermediate Temperature Solid Oxide Fuel Cells. *ACS Appl. Mater. Interfaces* **2016**, *8* (7), 4592–4599.
(37) Tomkiewicz, A. C.; Tamimi, M.; Huq, A.; McIntosh, S. Oxygen Transport Pathways in Ruddlesden–Popper Structured Oxides Revealed via in Situ Neutron Diffraction. *J. Mater. Chem. A* **2015**, *3* (43), 21864–21874.
(38) Huan, D.; Zhang, L.; Zhu, K.; Li, X.; Shi, N.; Yang, Y.; Xia, C.; Xie, Y.; Peng, R. Oxygen Vacancy-Engineered Cobalt-Free Ruddlesden-Popper Cathode with Excellent CO_2 Tolerance for Solid Oxide Fuel Cells. *J. Power Sources* **2021**, *497*, 229872.
(39) Akbay, T.; Staykov, A.; Druce, J.; Téllez, H.; Ishihara, T.; Kilner, J. A. The Interaction of Molecular Oxygen on LaO Terminated Surfaces of La_2NiO_4. *J. Mater. Chem. A* **2016**, *4* (34), 13113–13124.
(40) Chou, F. C.; Cho, J. H.; Johnston, D. C. Synthesis, Characterization, and Superconducting and Magnetic Properties of Electrochemically Oxidized $La_2CuO_{4+\delta}$ and $La_{2-x}Sr_xCuO_{4+\delta}$ ($0.01 \leq x \leq 0.33$, $0.01 \leq \delta \leq 0.36$). *Phys. C: Supercond. Appl.* **1992**, *197* (3–4), 303–314.
(41) Blakeslee, P.; Birgeneau, R.; Chou, F.; Christianson, R.; Kastner, M.; Lee, Y.; Wells, B. Electrochemistry and Staging in $La_2CuO_{4+\delta}$. *Phys. Rev. B* **1998**, *57* (21), 13915–13921.
(42) Oda, Y.; Yamada, M.; Ochiai, H.; Asayama, K.; Kohara, T.; Yamada, Y.; Koga, K.; Kashiwai, S.; Motoyama, M. Superconducting Properties of $La_2CuO_{4+\delta}$ Annealed in High Pressure Oxygen Gas. *Solid State Commun.* **1990**, *73* (10), 725–728.
(43) Nirala, G.; Yadav, D.; Upadhyay, S. Ruddlesden-Popper Phase A_2BO_4 Oxides: Recent Studies on Structure, Electrical, Dielectric, and Optical Properties. *J. Adv. Ceram.* **2020**, *9* (2), 129–148.
(44) Sukumar, M.; John Kennedy, L.; Judith Vijaya, J.; Al-Najar, B.; Bououdina, M. Facile Microwave Assisted Combustion Synthesis, Structural, Optical and Magnetic Properties of $La_{2-x}Sr_xCuO_4$ ($0 \leq x \leq 0.5$) Perovskite Nanostructures. *J. Magn. Magn. Mater* **2018**, *465*, 48–57.
(45) Balachandran, P. V.; Rondinelli, J. M. Massive Band Gap Variation in Layered Oxides through Cation Ordering. *Nat. Commun.* **2015**, *6* (1), 6191.
(46) Das, A.; Xhafa, E.; Nikolla, E. Electro- and Thermal-Catalysis by Layered, First Series Ruddlesden-Popper Oxides. *Catal. Today* **2016**, *277*, 214–226.
(47) Ding, P.; Li, W.; Zhao, H.; Wu, C.; Zhao, L.; Dong, B.; Wang, S. Review on Ruddlesden–Popper Perovskites as Cathode for Solid Oxide Fuel Cells. *J. Phys. Mater.* **2021**, *4* (2), 022002.
(48) Lasia, A. Mechanism and Kinetics of the Hydrogen Evolution Reaction. *Int. J. Hydrog. Energy* **2019**, *44* (36), 19484–19518.
(49) Zhu, D. D.; Liu, J. L.; Qiao, S. Z. Recent Advances in Inorganic Heterogeneous Electrocatalysts for Reduction of Carbon Dioxide. *Adv. Mater.* **2016**, *28* (18), 3423–3452.
(50) Sun, Z.; Ma, T.; Tao, H.; Fan, Q.; Han, B. Fundamentals and Challenges of Electrochemical CO_2 Reduction Using Two-Dimensional Materials. *Chem* **2017**, *3* (4), 560–587.

(51) Lu, Q.; Jiao, F. Electrochemical CO_2 Reduction: Electrocatalyst, Reaction Mechanism, and Process Engineering. *Nano Energy* **2016**, *29*, 439–456.
(52) Garza, A. J.; Bell, A. T.; Head-Gordon, M. Mechanism of CO_2 Reduction at Copper Surfaces: Pathways to C_2 Products. *ACS Catal.* **2018**, *8* (2), 1490–1499.
(53) Li, Y.; Sun, Q. Recent Advances in Breaking Scaling Relations for Effective Electrochemical Conversion of CO_2. *Adv. Energy Mater.* **2016**, *6* (17), 1600463.
(54) Pérez-Ramírez, J.; López, N. Strategies to Break Linear Scaling Relationships. *Nat. Catal.* **2019**, *2* (11), 971–976.
(55) Bockris, J. O.; Otagawa, T. Mechanism of Oxygen Evolution on Perovskites. *J. Phys. Chem.* **1983**, *87* (15), 2960–2971.
(56) Nurlaela, E.; Shinagawa, T.; Qureshi, M.; Dhawale, D. S.; Takanabe, K. Temperature Dependence of Electrocatalytic and Photocatalytic Oxygen Evolution Reaction Rates Using NiFe Oxide. *ACS Catal.* **2016**, *6* (3), 1713–1722.
(57) Huan, Y.; Chen, S.; Zeng, R.; Wei, T.; Dong, D.; Hu, X.; Huang, Y. Intrinsic Effects of Ruddlesden-Popper-Based Bifunctional Catalysts for High-Temperature Oxygen Reduction and Evolution. *Adv. Energy Mater.* **2019**, *9* (29), 1901573.
(58) Ascolani-Yael, J.; Montenegro-Hernández, A.; Garcés, D.; Liu, Q.; Wang, H.; Yakal-Kremski, K.; Barnett, S.; Mogni, L. The Oxygen Reduction Reaction in Solid Oxide Fuel Cells: From Kinetic Parameters Measurements to Electrode Design. *J. Phys. Energy* **2020**, *2* (4), 042004.
(59) Gu, X.-K.; Samira, S.; Nikolla, E. Oxygen Sponges for Electrocatalysis: Oxygen Reduction/Evolution on Nonstoichiometric, Mixed Metal Oxides. *Chem. Mater.* **2018**, *30* (9), 2860–2872.
(60) Adler, S. B.; Lane, J. A.; Steele, B. C. H. Electrode Kinetics of Porous Mixed-Conducting Oxygen Electrodes. *J. Electrochem. Soc* **1996**, *143* (11), 3554–3564.
(61) Yang, G.; El Loubani, M.; Hill, D.; Keum, J. K.; Lee, D. Control of Crystallographic Orientation in Ruddlesden-Popper for Fast Oxygen Reduction. *Catal. Today* **2022**. Article ASAP.
(62) Burriel, M.; Téllez, H.; Chater, R. J.; Castaing, R.; Veber, P.; Zaghrioui, M.; Ishihara, T.; Kilner, J. A.; Bassat, J.-M. Influence of Crystal Orientation and Annealing on the Oxygen Diffusion and Surface Exchange of $La_2NiO_{4+\delta}$. *J. Phys. Chem. C* **2016**, *120* (32), 17927–17938.
(63) Carneiro, J. S. A.; Brocca, R. A.; Lucena, M. L. R. S.; Nikolla, E. Optimizing Cathode Materials for Intermediate-Temperature Solid Oxide Fuel Cells (SOFCs): Oxygen Reduction on Nanostructured Lanthanum Nickelate Oxides. *Appl. Catal. B.* **2017**, *200*, 106–113.
(64) Nikonov, A. V.; Kuterbekov, K. A.; Bekmyrza, K. Z.; Pavzderin, N. B. A Brief Review of Conductivity and Thermal Expansion of Perovskite-Related Oxides for SOFC Cathode. *Eurasian J. Phys. Funct. Mater.* **2018**, *2* (3), 274–292.
(65) Mahato, N.; Banerjee, A.; Gupta, A.; Omar, S.; Balani, K. Progress in Material Selection for Solid Oxide Fuel Cell Technology: A Review. *Prog. Mater. Sci* **2015**, *72*, 141–337.
(66) Chen, Y.; Téllez, H.; Burriel, M.; Yang, F.; Tsvetkov, N.; Cai, Z.; McComb, D. W.; Kilner, J. A.; Yildiz, B. Segregated Chemistry and Structure on (001) and (100) Surfaces of $(La_{1-x}Sr_x)_2CoO_4$ Override the Crystal Anisotropy in Oxygen Exchange Kinetics. *Chem. Mater.* **2015**, *27* (15), 5436–5450.
(67) Lee, W.; Han, J. W.; Chen, Y.; Cai, Z.; Yildiz, B. Cation Size Mismatch and Charge Interactions Drive Dopant Segregation at the Surfaces of Manganite Perovskites. *J. Am. Chem. Soc.* **2013**, *135* (21), 7909–7925.

(68) Huber, A.-K.; Falk, M.; Rohnke, M.; Luerßen, B.; Gregoratti, L.; Amati, M.; Janek, J. In Situ Study of Electrochemical Activation and Surface Segregation of the SOFC Electrode Material $La_{0.75}Sr_{0.25}Cr_{0.5}Mn_{0.5}O_{3\pm\delta}$. *Phys. Chem. Chem. Phys.* **2012**, *14* (2), 751–758.
(69) Xu, Z.; Li, Y.; Wan, Y.; Zhang, S.; Xia, C. Nickel Enriched Ruddlesden-Popper Type Lanthanum Strontium Manganite as Electrode for Symmetrical Solid Oxide Fuel Cell. *J. Power Sources* **2019**, *425*, 153–161.
(70) Islam, Q. A.; Paydar, S.; Akbar, N.; Zhu, B.; Wu, Y. Nanoparticle Exsolution in Perovskite Oxide and Its Sustainable Electrochemical Energy Systems. *J. Power Sources* **2021**, *492*, 229626.
(71) Chung, Y. S.; Kim, T.; Shin, T. H.; Yoon, H.; Park, S.; Sammes, N. M.; Kim, W. B.; Chung, J. S. In Situ Preparation of a $La_{1.2}Sr_{0.8}Mn_{0.4}Fe_{0.6}O_4$ Ruddlesden–Popper Phase with Exsolved Fe Nanoparticles as an Anode for SOFCs. *J. Mater. Chem. A* **2017**, *5* (14), 6437–6446.
(72) Vecino-Mantilla, S.; Gauthier-Maradei, P.; Huvé, M.; Serra, J. M.; Roussel, P.; Gauthier, G. H. Nickel Exsolution-Driven Phase Transformation from an n = 2 to an n = 1 Ruddlesden-Popper Manganite for Methane Steam Reforming Reaction in SOFC Conditions. *ChemCatChem* **2019**, *11* (18), 4631–4641.
(73) Park, S.; Kim, Y.; Han, H.; Chung, Y. S.; Yoon, W.; Choi, J.; Kim, W. B. In Situ Exsolved Co Nanoparticles on Ruddlesden-Popper Material as Highly Active Catalyst for CO_2 Electrolysis to CO. *Appl. Catal. B.* **2019**, *248*, 147–156.
(74) Fu, L.; Zhou, J.; Yang, J.; Lian, Z.; Wang, J.; Cheng, Y.; Wu, K. Exsolution of Cu Nanoparticles in $(LaSr)_{0.9}Fe_{0.9}Cu_{0.1}O_4$ Ruddlesden-Popper Oxide as Symmetrical Electrode for Solid Oxide Cells. *Appl. Surf. Sci.* **2020**, *511*, 145525.
(75) Wang, Z.; Yin, Y.-M.; Yu, Y.; Song, Y.; Ma, Z.-F.; Yin, J. Roles of FeNi Nanoparticles and $SrLaFeO_4$ Substrate in the Performance and Reliability of a Composite Anode Prepared through in-Situ Exsolution for Intermediate Temperature Solid Oxide Fuel Cells. *Int. J. Hydrog. Energy* **2018**, *43* (22), 10440–10447.
(76) Lv, H.; Lin, L.; Zhang, X.; Song, Y.; Matsumoto, H.; Zeng, C.; Ta, N.; Liu, W.; Gao, D.; Wang, G.; Bao, X. In Situ Investigation of Reversible Exsolution/Dissolution of CoFe Alloy Nanoparticles in a Co-Doped $Sr_2Fe_{1.5}Mo_{0.5}O_{6-\delta}$ Cathode for CO_2 Electrolysis. *Adv. Mater.* **2020**, *32* (6), 1906193.
(77) Kim, K. J.; Rath, M. K.; Kwak, H. H.; Kim, H. J.; Han, J. W.; Hong, S.-T.; Lee, K. T. A Highly Active and Redox-Stable $SrGdNi_{0.2}Mn_{0.8}O_{4\pm\delta}$ Anode with in Situ Exsolution of Nanocatalysts. *ACS Catal.* **2019**, *9* (2), 1172–1182.
(78) Kim, C.; Bui, J. C.; Luo, X.; Cooper, J. K.; Kusoglu, A.; Weber, A. Z.; Bell, A. T. Tailored Catalyst Microenvironments for CO_2 Electroreduction to Multicarbon Products on Copper Using Bilayer Ionomer Coatings. *Nat. Energy* **2021**, *6* (11), 1026–1034.
(79) Rabiee, H.; Ge, L.; Zhang, X.; Hu, S.; Li, M.; Yuan, Z. Gas Diffusion Electrodes (GDEs) for Electrochemical Reduction of Carbon Dioxide, Carbon Monoxide, and Dinitrogen to Value-Added Products: A Review. *Energy Environ. Sci.* **2021**, *14* (4), 1959–2008.
(80) Inprasit, T.; Wongkasemjit, S.; Skinner, S. J.; Burriel, M.; Limthongkul, P. Effect of Sr Substituted $La_{2-x}Sr_xNiO_{4+\delta}$ (x = 0, 0.2, 0.4, 0.6, and 0.8) on Oxygen Stoichiometry and Oxygen Transport Properties. *RSC Adv.* **2015**, *5* (4), 2486–2492.
(81) Lee, D.; Lee, Y.-L.; Grimaud, A.; Hong, W. T.; Biegalski, M. D.; Morgan, D.; Shao-Horn, Y. Strontium Influence on the Oxygen Electrocatalysis of $La_{2-x}Sr_xNiO_{4\pm\delta}$ ($0.0 \leq x_{Sr} \leq 1.0$) Thin Films. *J. Mater. Chem. A* **2014**, *2* (18), 6480–6487.
(82) Opila, E. J.; Tuller, H. L.; Wuensch, B. J.; Maier, J. Oxygen Tracer Diffusion in $La_{2-x}Sr_xCuO_{4-y}$ Single Crystals. *J. Am. Ceram. Soc.* **1993**, *76* (9), 2363–2369.

(83) Samira, S.; Camayang, J. C. A.; Nacy, A. M.; Diaz, M.; Meira, S. M.; Nikolla, E. Electrochemical Oxygen Reduction on Layered Mixed Metal Oxides: Effect of B-Site Substitution. *J. Electroanal. Chem* **2019**, *833*, 490–497.
(84) Wang, X.; Gao, X. J.; Qin, L.; Wang, C.; Song, L.; Zhou, Y.-N.; Zhu, G.; Cao, W.; Lin, S.; Zhou, L.; Wang, K.; Zhang, H.; Jin, Z.; Wang, P.; Gao, X.; Wei, H. E_g Occupancy as an Effective Descriptor for the Catalytic Activity of Perovskite Oxide-Based Peroxidase Mimics. *Nat. Commun.* **2019**, *10* (1), 704.
(85) Suntivich Jin; May Kevin J.; Gasteiger Hubert A.; Goodenough John B.; Shao-Horn Yang. A Perovskite Oxide Optimized for Oxygen Evolution Catalysis from Molecular Orbital Principles. *Science* **2011**, *334* (6061), 1383–1385.
(86) Yu, J.; Sunarso, J.; Zhu, Y.; Xu, X.; Ran, R.; Zhou, W.; Shao, Z. Activity and Stability of Ruddlesden–Popper-Type $La_{n+1}Ni_nO_{3n+1}$ (n = 1, 2, 3, and ∞) Electrocatalysts for Oxygen Reduction and Evolution Reactions in Alkaline Media. *Eur. J. Chem.* **2016**, *22* (8), 2719–2727.
(87) Lee, Y.-L.; Lee, D.; Wang, X. R.; Lee, H. N.; Morgan, D.; Shao-Horn, Y. Kinetics of Oxygen Surface Exchange on Epitaxial Ruddlesden–Popper Phases and Correlations to First-Principles Descriptors. *J. Phys. Chem. Lett.* **2016**, *7* (2), 244–249.
(88) Benson, E. E.; Ha, M.-A.; Gregg, Brian. A.; van de Lagemaat, J.; Neale, N. R.; Svedruzic, D. Dynamic Tuning of a Thin Film Electrocatalyst by Tensile Strain. *Sci. Rep.* **2019**, *9* (1), 15906.
(89) Li, X.; Huan, D.; Shi, N.; Yang, Y.; Wan, Y.; Xia, C.; Peng, R.; Lu, Y. Defects Evolution of Ca Doped $La_2NiO_{4+\delta}$ and Its Impact on Cathode Performance in Proton-Conducting Solid Oxide Fuel Cells. *Int. J. Hydrogen Economy* **2020**, *45* (35), 17736–17744.
(90) Chattot, R.; Bordet, P.; Martens, I.; Drnec, J.; Dubau, L.; Maillard, F. Building Practical Descriptors for Defect Engineering of Electrocatalytic Materials. *ACS Catal.* **2020**, *10* (16), 9046–9056.
(91) Tsvetkov, N.; Lu, Q.; Chen, Y.; Yildiz, B. Accelerated Oxygen Exchange Kinetics on $Nd_2NiO_{4+\delta}$ Thin Films with Tensile Strain along c-Axis. *ACS Nano* **2015**, *9* (2), 1613–1621.
(92) Lee, D.; Grimaud, A.; Crumlin, E. J.; Mezghani, K.; Habib, M. A.; Feng, Z.; Hong, W. T.; Biegalski, M. D.; Christen, H. M.; Shao-Horn, Y. Strain Influence on the Oxygen Electrocatalysis of the (100)-Oriented Epitaxial $La_2NiO_{4+\delta}$ Thin Films at Elevated Temperatures. *J. Phys. Chem. C* **2013**, *117* (37), 18789–18795.
(93) Suntivich, J.; Gasteiger, H. A.; Yabuuchi, N.; Nakanishi, H.; Goodenough, J. B.; Shao-Horn, Y. Design Principles for Oxygen-Reduction Activity on Perovskite Oxide Catalysts for Fuel Cells and Metal–Air Batteries. *Nat. Chem.* **2011**, *3* (7), 546–550.
(94) Lee, Y.-L.; Kleis, J.; Rossmeisl, J.; Shao-Horn, Y.; Morgan, D. Prediction of Solid Oxide Fuel Cell Cathode Activity with First-Principles Descriptors. *Energy Environ. Sci.* **2011**, *4* (10), 3966–3970.
(95) Tao, H. B.; Fang, L.; Chen, J.; Yang, H. B.; Gao, J.; Miao, J.; Chen, S.; Liu, B. Identification of Surface Reactivity Descriptor for Transition Metal Oxides in Oxygen Evolution Reaction. *J. Am. Chem. Soc.* **2016**, *138* (31), 9978–9985.
(96) Wang, B.; Zhang, F. Main Descriptors To Correlate Structures with the Performances of Electrocatalysts. *Angew. Chem. Int. Ed.* **2022**, *61* (4), e202111026.
(97) Calle-Vallejo, F.; Martínez, J. I.; García-Lastra, J. M.; Sautet, P.; Loffreda, D. Fast Prediction of Adsorption Properties for Platinum Nanocatalysts with Generalized Coordination Numbers. *Angew. Chem. Int. Ed.* **2014**, *53* (32), 8316–8319.

(98) Wu, D.; Dong, C.; Zhan, H.; Du, X.-W. Bond-Energy-Integrated Descriptor for Oxygen Electrocatalysis of Transition Metal Oxides. *J. Phys. Chem. Lett.* **2018**, *9* (12), 3387–3391.
(99) Ma, X.; Xin, H. Orbitalwise Coordination Number for Predicting Adsorption Properties of Metal Nanocatalysts. *Phys. Rev. Lett.* **2017**, *118* (3), 036101.
(100) Zhu, Y.; Tahini, H. A.; Hu, Z.; Yin, Y.; Lin, Q.; Sun, H.; Zhong, Y.; Chen, Y.; Zhang, F.; Lin, H.-J.; Chen, C.-T.; Zhou, W.; Zhang, X.; Smith, S. C.; Shao, Z.; Wang, H. Boosting Oxygen Evolution Reaction by Activation of Lattice-Oxygen Sites in Layered Ruddlesden-Popper Oxide. *EcoMat* **2020**, *2* (2), e12021.
(101) Deganello, F.; Marcì, G.; Deganello, G. Citrate–Nitrate Auto-Combustion Synthesis of Perovskite-Type Nanopowders: A Systematic Approach. *J. Eur. Ceram. Soc.* **2009**, *29* (3), 439–450.
(102) Doménech-Carbó, M. T.; Osete-Cortina, L. Another Beauty of Analytical Chemistry: Chemical Analysis of Inorganic Pigments of Art and Archaeological Objects. *ChemTexts* **2016**, *2* (3), 14.
(103) Toby, B. H.; Von Dreele, R. B. GSAS-II: The Genesis of a Modern Open-Source All Purpose Crystallography Software Package. *J. Appl. Crystallogr.* **2013**, *46* (2), 544–549.
(104) Su, D. S.; Zhang, B.; Schlögl, R. Electron Microscopy of Solid Catalysts—Transforming from a Challenge to a Toolbox. *Chem. Rev.* **2015**, *115* (8), 2818–2882.
(105) Franken, L. E.; Grünewald, K.; Boekema, E. J.; Stuart, M. C. A. A Technical Introduction to Transmission Electron Microscopy for Soft-Matter: Imaging, Possibilities, Choices, and Technical Developments. *Small* **2020**, *16* (14), 1906198.
(106) Oswald, S. X-Ray Photoelectron Spectroscopy in Analysis of Surfaces. In *Encyclopedia of Analytical Chemistry*; John Wiley & Sons, Ltd, 2013.
(107) Greczynski, G.; Hultman, L. X-Ray Photoelectron Spectroscopy: Towards Reliable Binding Energy Referencing. *Prog. Mater. Sci* **2020**, *107*, 100591.
(108) Thomas, S.; Thomas, Raju; Zachariah, A.; Mishra, R. *Spectroscopic Methods for Nanomaterials Characterization*, 1st ed.; Elsevier, 2017.
(109) Dieing, T.; Hollricher, O.; Toporski, J. *Confocal Raman Microscopy*, 2nd ed.; Springer, 2010.
(110) Denisov, V. N.; Mavrin, B. N.; Podobedov, V. B.; Bykov, A. B.; Goncharov, A. F.; Zibrov, I. P.; Mel'nikov, O. K. Raman Scattering in $La_{2-x}Sr_xCuO_4$ Single Crystals. *Phys. Lett. A* **1989**, *140* (3), 141–146.
(111) Neumann, C.; Reichardt, S.; Venezuela, P.; Drögeler, M.; Banszerus, L.; Schmitz, M.; Watanabe, K.; Taniguchi, T.; Mauri, F.; Beschoten, B.; Rotkin, S. V.; Stampfer, C. Raman Spectroscopy as Probe of Nanometre-Scale Strain Variations in Graphene. *Nat. Commun.* **2015**, *6* (1), 8429.
(112) Loridant, S. Raman Spectroscopy as a Powerful Tool to Characterize Ceria-Based Catalysts. *Catal. Today* **2021**, *373*, 98–111.
(113) Beams, R.; Gustavo Cançado, L.; Novotny, L. Raman Characterization of Defects and Dopants in Graphene. *J. Condens. Matter Phys.* **2015**, *27* (8), 083002.
(114) Teng, Q. *Structural Biology Practical NMR Applications*, 2nd ed.; Springer, 2005.
(115) Gottlieb, H. E.; Kotlyar, V.; Nudelman, A. NMR Chemical Shifts of Common Laboratory Solvents as Trace Impurities. *J. Org. Chem.* **1997**, *62* (21), 7512–7515.
(116) Bharti, S. K.; Roy, R. Quantitative ^{1}H NMR Spectroscopy. *Trends Anal. Chem.* **2012**, *35*, 5–26.
(117) Wang, J. *Analytical Electrochemistry*, 3rd ed..; Wiley-VCH, 2006.

(118) Choi, W.; Shin, H.-C.; Kim, J. M.; Choi, J.-Y.; Yoon, W.-S. Modeling and Applications of Electrochemical Impedance Spectroscopy (EIS) for Lithium-Ion Batteries. *J. Electrochem. Sci. Technol.* **2020**, *11* (1), 1–13.
(119) Hankin, A.; Bedoya-Lora, F. E.; Alexander, J. C.; Regoutz, A.; Kelsall, G. H. Flat Band Potential Determination: Avoiding the Pitfalls. *J. Mater. Chem. A* **2019**, *7* (45), 26162–26176.
(120) Bard, A. J.; Faulkner, L. R. *Electrochemical Methods Fundamentals and Applications*, 2nd ed.; John Wiley & Sons, 2001.
(121) Du, C.; Tan, Q.; Yin, G.; Zhang, J. 5 - Rotating Disk Electrode Method. In *Rotating Electrode Methods and Oxygen Reduction Electrocatalysts*; Xing, W., Yin, G., Zhang, J., Eds.; Elsevier, 2014; pp 171–198.
(122) Levich, V. G. *Physicochemical Hydrodynamics*; Prentice-Hall, 1962.
(123) Treimer, S.; Tang, A.; Johnson, D. C. A Consideration of the Application of Koutecký-Levich Plots in the Diagnoses of Charge-Transfer Mechanisms at Rotated Disk Electrodes. *Electroanalysis* **2002**, *14* (3), 165–171.
(124) Lee, S.-J.; Pyun, S.-I.; Lee, S.-K.; Kang, S.-J. L. Fundamentals of Rotating Disc and Ring–Disc Electrode Techniques and Their Applications to Study of the Oxygen Reduction Mechanism at Pt/C Electrode for Fuel Cells. *Isr. J. Chem.* **2008**, *48* (3–4), 215–228.
(125) He, J.; Johnson, N. J. J.; Huang, A.; Berlinguette, C. P. Electrocatalytic Alloys for CO_2 Reduction. *ChemSusChem* **2018**, *11* (1), 48–57.
(126) Gewirth, A. A.; Varnell, J. A.; Diascro, A. M. Nonprecious Metal Catalysts for Oxygen Reduction in Heterogeneous Aqueous Systems. *Chem. Rev.* **2018**, *118* (5), 2313–2339.
(127) Hwang, J.; Rao, R. R.; Giordano, L.; Katayama, Y.; Yu, Y.; Shao-Horn, Y. Perovskites in Catalysis and Electrocatalysis. *Science* **2017**, *358*, 751–756.
(128) May, K. J.; Carlton, C. E.; Stoerzinger, K. A.; Risch, M.; Suntivich, J.; Lee, Y.-L.; Grimaud, A.; Shao-Horn, Y. Influence of Oxygen Evolution during Water Oxidation on the Surface of Perovskite Oxide Catalysts. *J. Phys. Chem. Lett* **2012**, *3*, 3264–3270.
(129) Risch, M.; Grimaud, A.; May, K. J.; Stoerzinger, K. A.; Chen, T. J.; Mansour, A. N.; Shao-Horn, Y. Structural Changes of Cobalt-Based Perovskites upon Water Oxidation Investigated by EXAFS. *J. Phys. Chem. C* **2013**, *117*, 8628–8635.
(130) Bergmann, A.; Martinez-Moreno, E.; Teschner, D.; Chernev, P.; Gliech, M.; De Araújo, J. F.; Reier, T.; Dau, H.; Strasser, P. Reversible Amorphization and the Catalytically Active State of Crystalline Co_3O_4 during Oxygen Evolution. *Nat. Commun.* **2015**, *6*, 1–9.
(131) Feng, Z.; Yacoby, Y.; Gadre, M. J.; Lee, Y.-L.; Hong, W. T.; Zhou, H.; Biegalski, M. D.; Christen, H. M.; Adler, S. B.; Morgan, D.; Shao-Horn, Y. Anomalous Interface and Surface Strontium Segregation in $(La_{1-y}Sr_y)_2CoO_{4\pm\delta}/La_{1-x}Sr_xCoO_{3-\delta}$ Heterostructured Thin Films. *J. Phys. Chem. Lett.* **2014**, *5* (6), 1027–1034.
(132) Kuai, C.; Xu, Z.; Xi, C.; Hu, A.; Yang, Z.; Zhang, Y.; Sun, C.-J.; Li, L.; Sokaras, D.; Dong, C.; Qiao, S.-Z.; Du, X.-W.; Lin, F. Phase Segregation Reversibility in Mixed-Metal Hydroxide Water Oxidation Catalysts. *Nat. Catal.* **2020**, *3* (9), 743–753.
(133) Grenier, J.-C.; Wattiaux, A.; Lagueyte, N.; Park, J. C.; Marquestaut, E.; Etourneau, J.; Pouchard, M. A New Superconductor Obtained by Electrochemical Oxidation of La_2CuO_4. *Phys. C: Supercond. Appl* **1991**, *173*, 139–144.
(134) Jorgensen, J. D.; Dabrowski, B.; Pei, S.; Hinks, D. G.; Soderholm, L.; Morosin, B.; Schirber, J. E.; Venturini, E. L.; Ginley, D. S. Superconducting Phase of $La_2CuO_{4+\delta}$. A Superconducting Composition Resulting from Phase Separation. *Phys. Rev. B* **1988**, *38* (16), 11337–11344.

(135) Kremer, R. K.; Sigmund, E.; Hizhnyakov, V.; Hentsch, F.; Simon, A. I.; Miiller, K. A.; Mehring, M. Original Contributions Percolative Phase Separation in $La_2CuO_{4+\delta}$ and $La_{2-x}Sr_xCuO_4$. *Z. Phys. B: Condens. Matter* **1992**, *86*, 319–324.
(136) Cava, R. J.; Siegrist, T.; Hessen, B.; Krajewski, J. J.; Peck, W. F.; Batlogg, B.; Takagi, H.; Waszczak, J. V.; Schneemeyer, L. F.; Zandbergen, H. W. A New Homologous Series of Lanthanum Copper Oxides. *J. Solid State Chem.* **1991**, *94* (1), 170–184.
(137) Grenier, J. C.; Wattiaux, A.; Monroux, C.; Pouchard, M.; Locquet, J. P. Electrochemical Oxygen Insertion into La_2CuO_4-Related Compounds. *Phys. C: Supercond. Appl* **1994**, *235–240*, 79–82.
(138) Sanchez, R. D.; Torresi, R. M.; Rettori, C.; Oseroff, S.; Fisk, Z. Electrochemical Intercalation of O^{2-} in La_2CuO_4 Single Crystals. *Electrochim. Acta* **1995**, *40* (2), 209–212.
(139) Lahmar, H.; Trari, M. Photocatalytic Generation of Hydrogen under Visible Light on La_2CuO_4. *Bull. Mater. Sci.* **2015**, *38* (4), 1043–1048.
(140) Li, Q.; Zhao, H.; Huo, L.; Sun, L.; Cheng, X.; Grenier, J. C. Electrode Properties of Sr Doped La_2CuO_4 as New Cathode Material for Intermediate-Temperature SOFCs. *Electrochem. Commun.* **2007**, *9* (7), 1508–1512.
(141) Schwartz, M.; Cook, R. L.; Kehae, V. M.; Macduff, R. C.; Patel, J.; Sammells, A. F. Carbon Dioxide Reduction to Alcohols Using Perovskite-Type Electrocatalysts. *J. Electrochem. Soc.* **1993**, *140*, 614–618.
(142) Mignard, D.; Barik, R. C.; Bharadwaj, A. S.; Pritchard, C. L.; Ragnoli, M.; Cecconi, F.; Miller, H.; Yellowlees, L. J. Revisiting Strontium-Doped Lanthanum Cuprate Perovskite for the Electrochemical Reduction of CO_2. *J. CO2 Util.* **2014**, *5*, 53–59.
(143) Magnone, E.; Cerisola, G.; Ferretti, M.; Barbucci, A. Electrochemical Investigation of Oxygen Intercalation into $La_2CuO_{4+\delta}$ Phases. *J. Solid State Chem.* **1999**, *144* (1), 8–15.
(144) Radaelli, P. G.; Jorgensen, J. D.; Schultz, A. J.; Hunter, B. A.; Wagner, J. L.; Chou, F. C.; Johnston, D. C. Structure of the Superconducting $La_2CuO_{4+\delta}$ Phases ($\delta = 0.08, 0.12$) Prepared by Electrochemical Oxidation. *Phys. Rev. B* **1993**, *48* (1), 499–510.
(145) Chaillout, C.; Marezio, M.; Cheong, S. W.; Fisk, Z.; Lehmann, M. S.; Marezio, M.; Morosin, B.; Schirber, J. E. The Crystal Structure of Superconducting $La_2CuO_{4.032}$ by Neutron Diffraction. *Phys. Scr.* **1989**, *1989* (T29), 97–99.
(146) Kajitani, T.; Onozuka, T.; Yamaguchi, Y.; Hirabayashi, M.; Yasukiko, S. Displacement Waves in $La_2CuO_{4-\delta}$ and $La_{1.85}Sr_{0.15}CuO_{4-\delta}$. *Jpn. J. Appl. Phys.* **1987**, *26*, 1877.
(147) Chaillout, C.; Chenavas, J.; Cheong, S. W.; Fisk, Z.; Marezio, M.; Morosin, B.; Schirber, J. E. Two-Phase Structural Refinement of $La_2CuO_{4.032}$ at 15 K. *Phys. C: Supercond. Appl* **1990**, *170* (1–2), 87–94.
(148) Yamada, K.; Kudo, E.; Endoh, Y.; Tsuda, K.; Tanaka, M.; Kokusho, K.; Asano, H.; Izumi, F.; Oda, M.; Hidaka, Y.; Suzuki, M.; Murakami, T. Determination of Space Group and Refinement of Structure Parameters for $La_2CuO_{4-\delta}$ Crystals. *Jpn. J. Appl. Phys.* **1988**, *27*, 1132.
(149) Burns, G.; Dacol, F. H. Anomalous Raman Spectra from La_2CuO_4. *Phys. Rev. B* **1990**, *41* (7), 4747–4748.
(150) Grande, B.; Müller-Buschbaum, Hk.; Schweizer, M. Über Oxocuprate. XV Zur Kristallstruktur von Seltenerdmetalloxocupraten: La_2CuO_4, Gd_2CuO_4. *Z. Anorg. Allg. Chem.* **1977**, *428* (1), 120–124.
(151) Lagueyte, N.; Weill, F.; Wattiaux, A.; Grenier, J. C. Observation of Superstructures in $La_2CuO_{4.09}$. *Eur. J. Solid State Inorg. Chem.* **1993**, *30* (9), 859–869.

(152) Chen, L.; Dong, C.; Che, G.; Zhou, F.; Huang, Y.; Zhao, Z. A New Metastable Phase with T_c of 32K in $La_2CuO_{4+\delta}$ System. *IEEE Trans. Appl. Supercond.* **2001**, *11* (1), 3403–3406.
(153) Sheptyakov, D. V.; Pomjakushin, V. Yu.; Balagurov, A. M.; Zakharov, A. A.; Chaillout-Bougerol, C.; McIntyre, G. J. Structure of Non-Phase-Separated $La_2CuO_{4.03}$ Studied by Single-Crystal Neutron Diffraction. *Phys. C: Supercond. Appl.* **1999**, *321*, 103–107.
(154) Izumi, F.; Kim, Y.-I.; Takayama-Muromachi, E.; Kamiyama, T. Neutron Powder Diffraction Study of Phase Separation in $La_2CuO_{4+\delta}$ Oxidized in $KMnO_4$ Solutions. *Phys. C: Supercond. Appl.* **1994**, *240* (94), 841–842.
(155) Tuilier, M. H.; Chevalier, B.; Tressaud, A.; Brisson, C.; Soubeyroux, J. L.; Etourneau, J. EXAFS Study at the La LIII X-Ray Absorption Edge of Superconducting Materials Obtained by Fluorination of $La_{2-X}Sr_xCuO_4$ Oxides ($0 \leq x \leq 0.15$). *Phys. C: Supercond. Appl.* **1992**, *200* (1–2), 113–121.
(156) Maksimow, A. I.; Misochko, O. V.; Tartakovsky, I. T.; Timofeev, V. B.; Remeika, J. P.; Copper, A. S.; Fisk, Z. Raman Scattering in Single Crystal La_2CuO_4. *Solid State Commun.* **1988**, *66* (10), 1077–1078.
(157) Biesinger, M. C. Advanced Analysis of Copper X-Ray Photoelectron Spectra. *Surf. Interface Anal.* **2017**, *49* (13), 1325–1334.
(158) Vasquez, R. P.; Jung, C. U.; Kim, J. Y.; Park, M.-S.; Kim, H.-J.; Lee, S.-I. X-Ray Photoemission Study of the Infinite-Layer Cuprate Superconductor $Sr_{0.9}La_{0.1}CuO_2$. *J. Phys.: Condens. Matter* **2001**, *13*, 7977–7985.
(159) Vasquez, R. Intrinsic Photoemission Signals, Surface Preparation, and Surface Stability of High Temperature Superconductors. *J. Electron Spec. Rel. Phen.* **1994**, *66*, 209–222.
(160) Wang, J.; Cheng, C.; Huang, B.; Cao, J.; Li, L.; Shao, Q.; Zhang, L.; Huang, X. Grain-Boundary-Engineered La_2CuO_4 Perovskite Nanobamboos for Efficient CO_2 Reduction Reaction. *Nano Lett.* **2021**, *21* (2), 980–987.
(161) Zhu, J.; Wang, Y.; Zhi, A.; Chen, Z.; Shi, L.; Zhang, Z.; Zhang, Y.; Zhu, Y.; Qiu, X.; Tian, X.; Bai, X.; Zhang, Y.; Zhu, Y. Cation-Deficiency-Dependent CO_2 Electroreduction over Copper-Based Ruddlesden–Popper Perovskite Oxides. *Angew. Chem. Int. Ed.* **2022**, *61* (3), e202111670.
(162) Chen, S.; Su, Y.; Deng, P.; Qi, R.; Zhu, J.; Chen, J.; Wang, Z.; Zhou, L.; Guo, X.; Xia, B. Y. Highly Selective Carbon Dioxide Electroreduction on Structure-Evolved Copper Perovskite Oxide toward Methane Production. *ACS Catal.* **2020**, *10* (8), 4640–4646.
(163) Moura de Salles Pupo, M.; Kortlever, R. Electrolyte Effects on the Electrochemical Reduction of CO_2. *ChemPhysChem* **2019**, *20* (22), 2926–2935.
(164) König, M.; Vaes, J.; Klemm, E.; Pant, D. Solvents and Supporting Electrolytes in the Electrocatalytic Reduction of CO_2. *iScience* **2019**, *19*, 135–160.
(165) Ahn, S. T.; Abu-Baker, I.; Palmore, G. T. R. Electroreduction of CO_2 on Polycrystalline Copper: Effect of Temperature on Product Selectivity. *Catal. Today* **2017**, *288*, 24–29.
(166) Lu, Q.; Rosen, J.; Zhou, Y.; Hutchings, G. S.; Kimmel, Y. C.; Chen, J. G.; Jiao, F. A Selective and Efficient Electrocatalyst for Carbon Dioxide Reduction. *Nat. Commun.* **2014**, *5* (1), 3242.
(167) Mistry, H.; Reske, R.; Zeng, Z.; Zhao, Z.-J.; Greeley, J.; Strasser, P.; Cuenya, B. R. Exceptional Size-Dependent Activity Enhancement in the Electroreduction of CO_2 over Au Nanoparticles. *J. Am. Chem. Soc.* **2014**, *136* (47), 16473–16476.
(168) Kang, M. P. L.; Kolb, M. J.; Calle-Vallejo, F.; Yeo, B. S. The Role of Undercoordinated Sites on Zinc Electrodes for CO_2 Reduction to CO. *Adv. Funct. Mater.* **2022**, *32* (23), 2111597.

(169) Guo, R.-H.; Liu, C.-F.; Wei, T.-C.; Hu, C.-C. Electrochemical Behavior of CO_2 Reduction on Palladium Nanoparticles: Dependence of Adsorbed CO on Electrode Potential. *Electrochem. commun.* **2017**, *80*, 24–28.
(170) Won, D. H.; Choi, C. H.; Chung, J.; Chung, M. W.; Kim, E.-H.; Woo, S. I. Rational Design of a Hierarchical Tin Dendrite Electrode for Efficient Electrochemical Reduction of CO_2. *ChemSusChem* **2015**, *8* (18), 3092–3098.
(171) Zhu, Q.; Ma, J.; Kang, X.; Sun, X.; Liu, H.; Hu, J.; Liu, Z.; Han, B. Efficient Reduction of CO_2 into Formic Acid on a Lead or Tin Electrode Using an Ionic Liquid Catholyte Mixture. *Angew. Chem. Int. Ed.* **2016**, *55* (31), 9012–9016.
(172) Yang, F.; Elnabawy, A. O.; Schimmenti, R.; Song, P.; Wang, J.; Peng, Z.; Yao, S.; Deng, R.; Song, S.; Lin, Y.; Mavrikakis, M.; Xu, W. Bismuthene for Highly Efficient Carbon Dioxide Electroreduction Reaction. *Nat. Commun.* **2020**, *11* (1), 1088.
(173) Hori, Y. Electrochemical CO_2 Reduction on Metal Electrodes. In *Modern Aspects of Electrochemistry*; Vayenas, C. G., White, R. E., Gamboa-Aldeco, M. E., Eds.; Springer New York, 2008;pp 89–189.
(174) Peterson, A. A.; Nørskov, J. K. Activity Descriptors for CO_2 Electroreduction to Methane on Transition-Metal Catalysts. *J. Phys. Chem. Lett.* **2012**, *3* (2), 251–258.
(175) Kortlever, R.; Shen, J.; Schouten, K. J. P.; Calle-Vallejo, F.; Koper, M. T. M. Catalysts and Reaction Pathways for the Electrochemical Reduction of Carbon Dioxide. *J. Phys. Chem. Lett.* **2015**, *6* (20), 4073–4082.
(176) Heidary, N.; Ly, K. H.; Kornienko, N. Probing CO_2 Conversion Chemistry on Nanostructured Surfaces with Operando Vibrational Spectroscopy. *Nano Lett.* **2019**, *19* (8), 4817–4826.
(177) Shan, W.; Liu, R.; Zhao, H.; He, Z.; Lai, Y.; Li, S.; He, G.; Liu, J. In Situ Surface-Enhanced Raman Spectroscopic Evidence on the Origin of Selectivity in CO_2 Electrocatalytic Reduction. *ACS Nano* **2020**, *14* (9), 11363–11372.
(178) Whittingham, A. W. H.; Smith, R. D. L. Electrochemically Induced Phase Changes in La_2CuO_4 During Cathodic Electrocatalysis. *ChemElectroChem* **2019**, *6* (19), 5116–5123.
(179) Ramaswamy, N.; Mukerjee, S. Alkaline Anion-Exchange Membrane Fuel Cells: Challenges in Electrocatalysis and Interfacial Charge Transfer. *Chem. Rev.* **2019**, *119* (23), 11945–11979.
(180) Yu, Y.; Luo, H.; Cetin, D.; Lin, X.; Ludwig, K.; Pal, U.; Gopalan, S.; Basu, S. Effect of Atmospheric CO_2 on Surface Segregation and Phase Formation in $La_{0.6}Sr_{0.4}Co_{0.2}Fe_{0.8}O_{3-\delta}$ Thin Films. *Appl. Surf. Sci.* **2014**, *323*, 71–77.
(181) Davis, J.; Yu, Y.; Cetin, D.; Ludwig, K.; Pal, U.; Gopalan, S.; Basu, S. Surface Segregation and Phase Formation in Thin Films of SOFC Cathode Materials. In *TMS 2014: 143rd Annual Meeting & Exhibition*; Springer International Publishing: Cham, 2016; pp 675–682.
(182) Baruch, M. F.; Pander III, J. E.; White, J. L.; Bocarsly, A. B. Mechanistic Insights into the Reduction of CO_2 on Tin Electrodes Using in Situ ATR-IR Spectroscopy. *ACS Catal.* **2015**, *5* (5), 3148–3156.
(183) Lander, G. H.; Brown, P. J.; Stassis, C.; Gopalan, P.; Spalek, J.; Honig, G. Magnetic and Structural Study of $La_{1.8}Sr_{0.2}NiO_4$. *Phys. Rev. B* **1991**, *43* (1), 448–456.
(184) Opila, E. J.; Tuller, H. L.; Wuensch, B. J.; Maier, J. Oxygen Tracer Diffusion in $La_{2-x}Sr_xCuO_{4-y}$ Single Crystals. *J. Am. Ceram. Soc.* **1993**, *76* (9), 2363–2369.
(185) Opila, E. J.; Tuller, H. L. Thermogravimetric Analysis and Defect Models of the Oxygen Nonstoichiometry in $La_{2-x}Sr_xCuO_{4-y}$. *J. Am. Ceram. Soc.* **1994**, *77* (10), 2727–2737.
(186) Mazo, G. N.; Savvin, S. N. The Molecular Dynamics Study of Oxygen Mobility in $La_{2-x}Sr_xCuO_{4-\delta}$. *Solid State Ion.* **2004**, *175* (1–4), 371–374.

(187) Alyoshin, V. A.; Romanova, I. P.; Mikhailova, D.; Oswald, S.; Senyshyn, A.; Ehrenberg, H. Oxygen Nonstoichiometry of Tetragonal $La_{2-x}Sr_xCuO_{4-\delta}$ (x = 0.15-1.2) and in Situ XPS Studies at Elevated Temperatures. *J. Phys. Chem. A* **2010**, *114* (51), 13362–13369.
(188) Katsufuji, T.; Tokura, Y. Symmetry-Dependent Electronic Raman Scattering in $La_{2-x}Sr_xCuO_4$: Evidence for Doping-Induced Change in k-Space Anisotropy of Charge Dynamics. *Phys. Rev. B* **1993**, *48* (21), 131–134.
(189) Copic, M.; Mihailovic, D.; Zgonik, M.; Prester, M.; Biljakovic, K.; Orel, B.; Brnicevic, N. Raman and Infrared Study of Lattice Vibrations in the High-T_c Ceramic Superconductor $La_{2-x}Sr_xCuO_4$. *Solid State Commun.* **1987**, *64* (3), 297–300.
(190) Sugai, S. Phonon Raman Scattering in $(La_{1-x}Sr_x)_2CuO_4$ Single Crystals. *Phys. Rev. B* **1989**, *39* (7), 4306–4315.
(191) Pickett, W. E.; Cohen, R. E.; Krakauer, H. Lattice Instabilities, Isotope Effect, and High-T_c Superconductivity in $La_{2-x}Ba_xCuO_4$. *Phys. Rev. Lett.* **1991**, *67* (2), 228–231.
(192) Ogita, N.; Udagawa, M.; Kojima, K.; Obhayashi, K. Infrared and Raman Study of $(La_{1-x}Sr_x)NiO_4$ and $La_2Ni_{1-x}Cu_xO_4$. *J. Phys. Soc. Jpn* **1988**, *57* (11), 3932–3940.
(193) Litvinchuk, A. P.; Cardona, M. Optical Phonons in T*-Structure $Nd_{2-x-y}Ce_xSr_yCuO_4$. *Phys. Rev. B* **1991**, *43* (16), 60–65.
(194) Sawa, H.; Suzuki, S.; Watanabe, M.; Akimitsu, J.; Matsubara, H.; Watabe, H.; Uchida, S.; Kokusho, K.; Asano, H.; Izumi, F.; Takayama-Muromachi, E. Unusually Simple Crystal Structure of an Nd–Ce–Sr–Cu–O Superconductor. *Nature* **1989**, *337* (6205), 347–348.
(195) Chaplin, R. P. S.; Wragg, A. A. Effects of Process Conditions and Electrode Material on Reaction Pathways for Carbon Dioxide Electroreduction with Particular Reference to Formate Formation. *J. Appl. Electrochem.* **2003**, *33* (52), 1107–1123.
(196) Imhof, R.; Novák, P. In Situ Investigation of the Electrochemical Reduction of Carbonate Electrolyte Solutions at Graphite Electrodes. *J. Electrochem. Soc* **1998**, *145* (4), 1081–1087.
(197) Kortlever, R.; Tan, K. H.; Kwon, Y.; Koper, M. T. M. Electrochemical Carbon Dioxide and Bicarbonate Reduction on Copper in Weakly Alkaline Media. *J. Solid State Electrochem* **2013**, *17* (7), 1843–1849.
(198) Zhu, S.; Jiang, B.; Cai, W.; Shao, M. Direct Observation on Reaction Intermediates and the Role of Bicarbonate Anions in CO_2 Electrochemical Reduction Reaction on Cu Surfaces. *J. Am. Chem. Soc.* **2017**, *139*, 15664–15667.
(199) Savéant, J.-M. *Elements of Molecular and Biomolecular Electrochemistry: An Electrochemical Approach to Electron Transfer Chemistry*, 2nd ed.; John Wiley & Sons, Inc., 2006.
(200) Costentin, C.; Savéant, J. M. Concepts and Tools for Mechanism and Selectivity Analysis in Synthetic Organic Electrochemistry. *Proceedings of the National Academy of Sciences of the United States of America* **2019**, *166* (23), 11147–11152.
(201) Amatore, C.; Gareil, M.; Savéant, J.-M. Kinetics of the Protonation of Anthracene Anion Radical by Phenol in Dimethylformamide. *J. Electroanal. Chem* **1984**, *176*, 377–382.
(202) Amatore, C.; Lexa, D.; Savéant, J. M. ECE Reaction Pathways in the Electrochemical Reduction of Dicyanocobalamin: Kinetics of Ligand Substitution in Vitamin B12r Cyanocob(II)Alamin. *J. Electroanal. Chem.* **1980**, *111*, 81–89.
(203) Savéant, J. M.; Vianello, E. Potential-Sweep Voltammetry: General Theory of Chemical Polarization. *Electrochim. Acta* **1967**, *12* (6), 629–646.
(204) Cavani, F.; Triforo, F.; Caccari, A. Hydrotalcite-Type Anionic Clays: Preparation, Properties and Applications. *Catal. Today* **1991**, *11*, 173–301.

(205) Barique, M. A.; Tsuchida, E.; Ohira, A.; Tashiro, K. Effect of Elevated Temperatures on the States of Water and Their Correlation with the Proton Conductivity of Nafion. *ACS Omega* **2018**, *3*, 349–360.
(206) Chen, Z. Y.; Persson, D.; Nazarov, A.; Zakipour, S.; Thierry, D.; Leygraf, C. In Situ Studies of the Effect of CO_2 on the Initial NaCl-Induced Atmospheric Corrosion of Copper. *J. Electrochem. Soc* **2005**, *152* (9), 342–351.
(207) Hahn, F.; Floner, D.; Beden, B.; Lamy, C. In Situ Investigation of the Behaviour of a Nickel Electrode in Alkaline Solution by UV-VIS and IR Reflectance Spectroscopies. *Electrochim. Acta* **1987**, *32* (11), 1631–1636.
(208) Davis, A. R.; Oliver, B. G. A Vibrational-Spectroscopic Study of the Species Present in the CO_2-H_2O System. *J. Solution Chem* **1972**, *1* (4), 329–339.
(209) Dobson, K. D.; Mcquillan, A. J. An Infrared Spectroscopic Study of Carbonate Adsorption to Zirconium Dioxide Sol - Gel Films from Aqueous Solutions. *Langmuir* **1997**, *7463* (15), 3392–3396.
(210) Pander III, J. E.; Baruch, M. F.; Bocarsly, A. B. Probing the Mechanism of Aqueous CO_2 Reduction on Post-Transition Metal Electrodes Using ATR-IR Spectroelectrochemistry. *ACS Catal.* **2016**, *6* (11), 7824–7833.
(211) Gao, L.; Sun, G.; Kawi, S. A Study on Methanol Steam Reforming to CO_2 and H_2 over the La_2CuO_4 Nanofiber Catalyst. *J. Solid State Chem.* **2008**, *181*, 7–13.
(212) Halcrow, M. A. Jahn–Teller Distortions in Transition Metal Compounds, and Their Importance in Functional Molecular and Inorganic Materials. *Chem. Soc. Rev.* **2013**, *42* (4), 1784–1795.
(213) Lufaso, M. W.; Woodward, P. M. Jahn-Teller Distortions, Cation Ordering and Octahedral Tilting in Perovskites. *Acta Crystallogr. B* **2004**, *60* (1), 10–20.
(214) Kanai, H.; Mizusaki, J.; Tagawa, H.; Hoshiyama, S.; Hirano, K.; Fujita, K.; Tezuka, M.; Hashimoto, T. Defect Chemistry of $La_{2-x}Sr_xCuO_4$: Oxygen Nonstoichiometry and Thermodynamic Stability. *J. Solid State Chem.* **1997**, *159* (131), 150–159.
(215) Almar, L.; Störmer, H.; Meffert, M.; Szász, J.; Wankmüller, F.; Gerthsen, D.; Ivers-Tiffée, E. Improved Phase Stability and CO_2 Poisoning Robustness of Y-Doped $Ba_{0.5}Sr_{0.5}Co_{0.8}Fe_{0.2}O_{3-\delta}$ SOFC Cathodes at Intermediate Temperatures. *ACS Appl. Energy Mater.* **2018**, *1* (3), 1316–1327.
(216) Rehman, A. U.; Li, M.; Knibbe, R.; Khan, M. S.; Peterson, V. K.; Brand, H. E. A.; Li, Z.; Zhou, W.; Zhu, Z. Enhancing Oxygen Reduction Reaction Activity and CO_2 Tolerance of Cathode for Low-Temperature Solid Oxide Fuel Cells by in Situ Formation of Carbonates. *ACS Appl. Mater. Interfaces* **2019**, *11* (30), 26909–26919.
(217) Heinsaar, A.; Kivi, I.; Möller, P.; Kooser, K.; Käämbre, T.; Aruväli, J.; Nurk, G.; Lust, E. Influence of Carbon Dioxide and Humidity on the Stability of $(La_{0.6}Sr_{0.4})_{0.99}Co_{1-x}Ti_xO_{3-\delta}$ Cathode. *J. Electrochem. Soc* **2022**, *169* (1), 014514.
(218) Yan, A.; Yang, M.; Hou, Z.; Dong, Y.; Cheng, M. Investigation of $Ba_{1-x}Sr_xCo_{0.8}Fe_{0.2}O_{3-\delta}$ as Cathodes for Low-Temperature Solid Oxide Fuel Cells Both in the Absence and Presence of CO_2. *J. Power Sources* **2008**, *185* (1), 76–84.
(219) Pellegrinelli, C.; Huang, Y.-L.; Wachsman, E. D. Effect of H_2O and CO_2 on LSCF-GDC Composite Cathodes. *ECS Trans* **2019**, *91* (1), 665–680.
(220) Li, J.; Gao, Z.; Min, H.; Li, M.; Lu, Y.; Wang, X.; Ding, X. Enabled Fast Cathode Kinetics for Intermediate-Temperature Solid Oxide Fuel Cell with Improved CO_2 Poisoning Robustness: La_2NiO_4 Surfaced-Modified $SrCo_{0.8}Nb_{0.1}Ta_{0.1}O_{3-\delta}$ Composite. *J. Power Sources* **2021**, *506*, 230057.

(221) Klande, T.; Efimov, K.; Cusenza, S.; Becker, K.-D.; Feldhoff, A. Effect of Doping, Microstructure, and CO_2 on $La_2NiO_{4+\delta}$-Based Oxygen-Transporting Materials. *J. Solid State Chem.* **2011**, *184* (12), 3310–3318.
(222) Yao, X.; Guo, Y.; Liu, B.; Wang, P.; Sun, J.; Li, W.; Zhao, C. Syngas Production from Electrochemical CO_2 Reduction on Copper Oxide Electrodes in Aqueous Solution. *ChemElectroChem* **2021**, *8* (3), 592–602.
(223) Baiano, C.; Schiavo, E.; Gerbaldi, C.; Bella, F.; Meligrana, G.; Talarico, G.; Maddalena, P.; Pavone, M.; Muñoz-García, A. B. Role of Surface Defects in CO_2 Adsorption and Activation on $CuFeO_2$ Delafossite Oxide. *Mol. Catal.* **2020**, *496*, 111181.
(224) Wang, A.; Zhao, Z.; Hu, D.; Niu, J.; Zhang, M.; Yan, K.; Lu, G. Tuning the Oxygen Evolution Reaction on a Nickel-Iron Alloy via Active Straining. *Nanoscale* **2019**, *11*, 426.
(225) Diaz-Morales, O.; Ferrus-Suspedra, D.; Koper, M. T. M. The Importance of Nickel Oxyhydroxide Deprotonation on Its Activity towards Electrochemical Water Oxidation. *Chem. Sci.* **2016**, *7* (4), 2639–2645.
(226) Enman, L. J.; Burke, M. S.; Batchellor, A. S.; Boettcher, S. W. Effects of Intentionally Incorporated Metal Cations on the Oxygen Evolution Electrocatalytic Activity of Nickel (Oxy)Hydroxide in Alkaline Media. *ACS Catal.* **2016**, *6*, 2416–2423.
(227) Smith, R. D. L.; Pasquini, C.; Loos, S.; Chernev, P.; Klingan, K.; Kubella, P.; Mohammadi, M. R.; González-Flores, D.; Dau, H. Geometric Distortions in Nickel (Oxy)Hydroxide Electrocatalysts by Redox Inactive Iron Ions. *Energy Environ. Sci* **2018**, *11*, 2476–2485.
(228) Garcia, A. C.; Touzalin, T.; Nieuwland, C.; Perini, N.; Koper, M. T. M. Enhancement of Oxygen Evolution Activity of Nickel Oxyhydroxide by Electrolyte Alkali Cations. *Angew. Chem. Int. Ed.* **2019**, *58* (37), 12999–13003.
(229) Smith, R. D. L.; Sherbo, R. S.; Dettelbach, K. E.; Berlinguette, C. P. On How Experimental Conditions Affect the Electrochemical Response of Disordered Nickel Oxyhydroxide Films. *Chem. Mater.* **2016**, *28*, 5635–5642.
(230) Xue, X.; Yu, F.; Peng, B.; Wang, G.; Lv, Y.; Chen, L.; Yao, Y.; Dai, B.; Shi, Y.; Guo, X. One-Step Synthesis of Nickel-Iron Layered Double Hydroxides with Tungstate Acid Anions: Via Flash Nano-Precipitation for the Oxygen Evolution Reaction. *Sustain. Energy Fuels* **2019**, *3* (1), 237–244.
(231) Dobbek Holger; Svetlitchnyi Vitali; Gremer Lothar; Huber Robert; Meyer Ortwin. Crystal Structure of a Carbon Monoxide Dehydrogenase Reveals a [Ni-4Fe-5S] Cluster. *Science* **2001**, *293* (5533), 1281–1285.
(232) Piontek, S.; Siegmund, D.; Smialkowski, M.; Sinev, I.; Cuenya, R.; Apfel, U. Bio-Inspired Design: Bulk Iron–Nickel Sulfide Allows for Efficient Solvent-Dependent CO_2 Reduction. *Chem. Sci.* **2019**, *10* (4), 1075–1081.
(233) Jeoung, J.-H.; Dobbek, H. Carbon Dioxide Activation at the Ni,Fe-Cluster of Anaerobic Carbon Monoxide Dehydrogenase. *Science* **2007**, *318*, 1461–1464.
(234) Appel, A. M.; Bercaw, J. E.; Bocarsly, A. B.; Dobbek, H.; DuBois, D. L.; Dupuis, M.; Ferry, J. G.; Fujita, E.; Hille, R.; Kenis, P. J. A.; Kerfeld, C. A.; Morris, R. H.; Peden, C. H. F.; Portis, A. R.; Ragsdale, S. W.; Rauchfuss, T. B.; Reek, J. N. H.; Seefeldt, L. C.; Thauer, R. K.; Waldrop, G. L. Frontiers , Opportunities , and Challenges in Biochemical and Chemical Catalysis of CO_2 Fixation. *Chem. Rev.* **2012**, *113*, 6621–6658.
(235) Hansen, H. A.; Varley, J. B.; Peterson, A. A. Understanding Trends in the Electrocatalytic Activity of Metals and Enzymes for CO_2 Reduction to CO. *J. Phys. Chem. Lett.* **2013**, *4*, 388–392.

(236) Zhu, Y.; Tahini, H. A.; Hu, Z.; Dai, J.; Chen, Y.; Sun, H.; Zhou, W.; Liu, M.; Smith, S. C.; Wang, H.; Shao, Z. Unusual Synergistic Effect in Layered Ruddlesden−Popper Oxide Enables Ultrafast Hydrogen Evolution. *Nat. Commun.* **2019**, *10* (1), 1–9.
(237) Meyer, T. L.; Jacobs, R.; Lee, D.; Jiang, L.; Freeland, J. W.; Sohn, C.; Egami, T.; Morgan, D.; Lee, H. N. Strain Control of Oxygen Kinetics in the Ruddlesden-Popper Oxide $La_{1.85}Sr_{0.15}CuO_4$. *Nat. Commun.* **2018**, *9* (1), 92.
(238) Niemczyk, A.; Stępień, A.; Cichy, K.; Dąbrowa, J.; Zhang, Z.; Gędziorowski, B.; Zheng, K.; Zhao, H.; Świerczek, K. Modification of Ruddlesden-Popper-Type $Nd_{2-x}Ni_{0.75}Cu_{0.2}M_{0.05}O_{4\pm\delta}$ by the Nd-Site Cationic Deficiency and Doping with Sc, Ga or In: Crystal Structure, Oxygen Content, Transport Properties and Oxygen Permeability. *J. Solid. State. Chem.* **2021**, *296*, 121982.
(239) Han, N.; Guo, X.; Cheng, J.; Liu, P.; Zhang, S.; Huang, S.; Rowles, M. R.; Fransaer, J.; Liu, S. Inhibiting in Situ Phase Transition in Ruddlesden-Popper Perovskite via Tailoring Bond Hybridization and Its Application in Oxygen Permeation. *Matter* **2021**, *4* (5), 1720–1734.
(240) Tsai, C.-Y.; McGilvery, C. M.; Aguadero, A.; Skinner, S. J. Phase Evolution and Reactivity of $Pr_2NiO_{4+\delta}$ and $Ce_{0.9}Gd_{0.1}O_{2-\delta}$ Composites under Solid Oxide Cell Sintering and Operation Temperatures. *Int. J. Hydrogen Economy* **2019**, *44* (59), 31458–31465.
(241) Li, H.; Song, Y.; Xu, M.; Wang, W.; Ran, R.; Zhou, W.; Shao, Z. Exsolved Alloy Nanoparticles Decorated Ruddlesden–Popper Perovskite as Sulfur-Tolerant Anodes for Solid Oxide Fuel Cells. *Energy Fuels* **2020**, *34* (9), 11449–11457.
(242) Xue, J.; Schulz, A.; Wang, H.; Feldhoff, A. The Phase Stability of the Ruddlesden-Popper Type Oxide $(Pr_{0.9}La_{0.1})_{2.0}Ni_{0.74}Cu_{0.21}Ga_{0.05}O_{4+\delta}$ in an Oxidizing Environment. *J. Membr. Sci.* **2016**, *497*, 357–364.
(243) Yang, C.; Batuk, M.; Jacquet, Q.; Rousse, G.; Yin, W.; Zhang, L.; Hadermann, J.; Abakumov, A. M.; Cibin, G.; Chadwick, A.; Tarascon, J.-M.; Grimaud, A. Revealing pH-Dependent Activities and Surface Instabilities for Ni-Based Electrocatalysts during the Oxygen Evolution Reaction. *ACS Energy Lett.* **2018**, *3* (12), 2884–2890.
(244) Forslund, R. P.; Hardin, W. G.; Rong, X.; Abakumov, A. M.; Filimonov, D.; Alexander, C. T.; Mefford, J. T.; Iyer, H.; Kolpak, A. M.; Johnston, K. P.; Stevenson, K. J. Exceptional Electrocatalytic Oxygen Evolution via Tunable Charge Transfer Interactions in $La_{0.5}Sr_{1.5}Ni_{1-x}Fe_xO_{4\pm\delta}$ Ruddlesden-Popper Oxides. *Nat. Commun.* **2018**, *9* (1), 3150.
(245) Gilev, A. R.; Kiselev, E. A.; Cherepanov, V. A. Homogeneity Range, Oxygen Nonstoichiometry, Thermal Expansion and Transport Properties of $La_{2-x}Sr_xNi_{1-y}Fe_yO_{4+\delta}$. *RSC Adv.* **2016**, *6* (77), 72905–72917.
(246) Aguadero, A.; Escudero, M. J.; Pérez, M.; Alonso, J. A.; Pomjakushin, V.; Daza, L. Effect of Sr Content on the Crystal Structure and Electrical Properties of the System $La_{2-x}Sr_xNiO_{4+\delta}$ ($0 \leq x \leq 1$). *Dalton Trans.* **2006**, No. 36, 4377–4383.
(247) Blumberg, G.; Klein, M. V.; Cheong, S.-W. Charge and Spin Dynamics of an Ordered Stripe Phase in $La_{12/3}Sr_{1/3}NiO_4$ Investigated by Raman Spectroscopy. *Phys. Rev. Lett.* **1998**, *80* (3), 564–567.
(248) Yamamoto, K.; Katsufuji, T.; Tanabe, T.; Tokura, Y. Raman Scattering of the Charge-Spin Stripes in $La_{1.67}Sr_{0.33}NiO_4$. *Phys. Rev. Lett.* **1998**, *80* (7), 1493–1496.
(249) Pashkevich, Yu. G.; Blinkin, V. A.; Gnezdilov, V. P.; Tsapenko, V. V.; Eremenko, V. V.; Lemmens, P.; Fischer, M.; Grove, M.; Güntherodt, G.; Degiorgi, L.; Wachter, P.; Tranquada, J. M.; Buttrey, D. J. Stripe Conductivity in $La_{1.775}Sr_{0.225}NiO_4$. *Phys. Rev. Lett.* **2000**, *84* (17), 3919–3922.

(250) Kim, G.; Christiani, G.; Logvenov, G.; Choi, S.; Kim, H.-H.; Minola, M.; Keimer, B. Selective Formation of Apical Oxygen Vacancies in $La_{2-x}Sr_xCuO_4$. *Phys. Rev. Materials* **2017**, *1* (5), 054801.
(251) Gopalakrishnan, J.; Colsmann, G.; Reuter, B. Studies on the $La_{2-x}NiO_4$ ($0 \leq x \leq 1$) System. *J. Solid. State. Chem.* **1977**, *22*, 145–149.
(252) Shannon, R. D. Revised Effective Ionic Radii and Systematic Studies of Interatomic Distances in Halides and Chalcogenides. *Acta Cryst* **1976**, *32*, 751–767.
(253) Zhou, R.; Zheng, Y.; Jaroniec, M.; Qiao, S.-Z. Determination of the Electron Transfer Number for the Oxygen Reduction Reaction: From Theory to Experiment. *ACS Catal.* **2016**, *6* (7), 4720–4728.
(254) Whittingham, A. W. H.; Lau, J.; Smith, R. D. L. Mechanistic Insights into the Spontaneous Reaction Between CO_2 and $La_{2-x}Sr_xCuO_4$. *Can. J. Chem.* **2021**, *99*, 773–779.
(255) Shinagawa, T.; Garcia-Esparza, A. T.; Takanabe, K. Insight on Tafel Slopes from a Microkinetic Analysis of Aqueous Electrocatalysis for Energy Conversion. *Sci. Rep.* **2015**, *5*, 13801.
(256) Alsaç, E. P.; Bodappa, N.; Whittingham, A. W. H.; de Lazzari, A.; Smith, R. D. L. Structure-Property Correlations for Analysis of Heterogeneous Electrocatalysts. *Chem. Phys. Rev.* **2021**, *2* (3), 031306.
(257) Alsaç, E. P.; Whittingham, A.; Liu, Y.; Smith, R. D. L. Probing the Role of Internalized Geometric Strain on Heterogeneous Electrocatalysis. *Chem. Mater.* **2019**, *31*, 7522–7530.
(258) Yang, H.; Long, Y.; Zhu, Y.; Zhao, Z.; Ma, P.; Jin, J.; Ma, J. Crystal Lattice Distortion in Ultrathin $Co(OH)_2$ Nanosheets Inducing Elongated Co–OOH Bonds for Highly Efficient Oxygen Evolution Reaction. *Green Chem.* **2017**, *19* (24), 5809–5817.
(259) Zhuang, L.; Jia, Y.; He, T.; Du, A.; Yan, X.; Ge, L.; Zhu, Z.; Yao, X. Tuning Oxygen Vacancies in Two-Dimensional Iron-Cobalt Oxide Nanosheets through Hydrogenation for Enhanced Oxygen Evolution Activity. *Nano Res.* **2018**, *11* (6), 3509–3518.
(260) Lankauf, K.; Mroziński, A.; Błaszczak, P.; Górnicka, K.; Ignaczak, J.; Łapiński, M.; Karczewski, J.; Cempura, G.; Jasiński, P.; Molin, S. The Effect of Fe on Chemical Stability and Oxygen Evolution Performance of High Surface Area $SrTi_{x-1}Fe_xO_{3-\delta}$ Mixed Ionic-Electronic Conductors in Alkaline Media. *Int. J. Hydrogen Economy* **2021**, *46* (56), 28575–28590.
(261) Rajić, V.; Stojković Simatović, I.; Veselinović, L.; Čavor, J. B.; Novaković, M.; Popović, M.; Škapin, S. D.; Mojović, M.; Stojadinović, S.; Rac, V.; Častvan, I. J.; Marković, S. Bifunctional Catalytic Activity of $Zn_{1-x}Fe_xO$ toward the OER/ORR: Seeking an Optimal Stoichiometry. *Phys. Chem. Chem. Phys.* **2020**, *22* (38), 22078–22095.
(262) Li, Z.; Zhang, Y.; Feng, Y.; Cheng, C.-Q.; Qiu, K.-W.; Dong, C.-K.; Liu, H.; Du, X.-W. Co_3O_4 Nanoparticles with Ultrasmall Size and Abundant Oxygen Vacancies for Boosting Oxygen Involved Reactions. *Adv. Funct. Mater.* **2019**, *29* (36), 1903444.
(263) Zhao, S.; Wang, Y.; Dong, J.; He, C.-T.; Yin, H.; An, P.; Zhao, K.; Zhang, X.; Gao, C.; Zhang, L.; Lv, J.; Wang, J.; Zhang, J.; Khattak, A. M.; Khan, N. A.; Wei, Z.; Zhang, J.; Liu, S.; Zhao, H.; Tang, Z. Ultrathin Metal–Organic Framework Nanosheets for Electrocatalytic Oxygen Evolution. *Nat. Energy* **2016**, *1* (12), 16184.
(264) Ghorbani-Moghadam, T.; Kompany, A.; Bagheri-Mohagheghi, M. M.; Abrishami, M. E. Cobalt Spin States Investigation of Ruddlesden-Popper $La_{2-x}Sr_xCoO_4$, Using X-Ray Diffraction and Infrared Spectroscopy. *J. Magn. Magn. Mater* **2018**, *465*, 768–774.

(265) Chaker, H.; Raies, I.; Chouket, A.; Roisnel, T.; Ben Hassen, R. Chemical and Physical Characterizations of the n = 1 Ruddlesden–Popper Phases: $Nd_{2-y}Sr_yNi_{1-x}Co_xO_{4\pm\delta}$ (y = 1 and $0.1 \leq x \leq 0.9$). *Ionics* **2017**, *23* (9), 2229–2240.
(266) Lappas, A.; Prassides, K. Oxygen-Defect Geometry in Oxygen-Rich $La_2Co_xCu_{1-x}O_{4+\delta}$ Layered Oxides. *J. Solid State Chem.* **1994**, *108* (1), 56–67.
(267) Skinner, S. J.; Amow, G. Structural Observations on $La_2(Ni,Co)O_{4\pm\delta}$ Phases Determined from in Situ Neutron Powder Diffraction. *J. Solid State Chem.* **2007**, *180*, 1977–1983.
(268) Aksenova, T. V.; Bannykh, L. A.; Cherepanov, V. A. PHASE EQUILIBRIA AND CRYSTAL STRUCTURE OF COMPLEX OXIDES IN THE La–Sr–Co–Ni–O SYSTEM. *J. Struct. Chem.* **2003**, *44* (2), 282–285.
(269) Subías, G.; Blasco, J.; Lafuerza, S.; Cuartero, V.; Sánchez, M. C.; Boada, R.; Díaz-Moreno, S.; Fauth, F.; García, J. Relation among Oxygen Stoichiometry, Structure, and Co Valence and Spin State in Single-Layer $La_{2-x}A_xCoO_{4\pm\delta}$ (A = Ca, Sr) Perovskites. *Inorg. Chem.* **2020**, *59* (21), 15757–15771.
(270) Vibhu, V.; Vinke, I. C.; Eichel, R. A.; de Haart, L. G. J. Cobalt Substituted $Pr_2Ni_{1-x}Co_xO_{4+\delta}$ (x = 0, 0.1, 0.2) Oxygen Electrodes: Impact on Electrochemical Performance and Durability of Solid Oxide Electrolysis Cells. *J. Power Sources* **2021**, *482*, 228909.
(271) Kuterbekov, K. A.; Bekmyrza, K. Z.; Aidarbekov, N. K.; Nikonov, A. V.; Pavzderin, N. B.; Khrustov, V. R.; Semenova, I. V.; Medvedev, A. I.; Gyrdasova, O. I. Effect of the Cobalt Content on Properties of $La_2Ni_{1-x}Co_xO_{4+\delta}$. *Solid State Ion.* **2021**, *363*, 115594.
(272) Cao, Y.; Gu, H.; Chen, H.; Zheng, Y.; Zhou, M.; Guo, L. Preparation and Characterization of $Nd_{2-x}Sr_xCoO_{4+\delta}$ Cathodes for Intermediate-Temperature Solid Oxide Fuel Cell. *Int. J. Hydrogen Economy* **2010**, *35* (11), 5594–5600.
(273) Ferkhi, M.; Rekaik, M.; Khaled, A.; Cassir, M.; Pireaux, J. Neodymium Nickelate $Nd_{2-x}Sr_xNi_{1-y}Co_yO_{4\pm\delta}$ (x and Y=0 or 0.05) as Cathode Materials for the Oxygen Reduction Reaction. *Electrochim. Acta* **2017**, *229*, 281–290.
(274) Mefford, J. T.; Rong, X.; Abakumov, A. M.; Hardin, W. G.; Dai, S.; Kolpak, A. M.; Johnston, K. P.; Stevenson, K. J. Water Electrolysis on $La_{1-x}Sr_xCoO_{3-\delta}$ Perovskite Electrocatalysts. *Nat. Commun.* **2016**, *7*, 11053.
(275) Xie, R.; Nie, Z.; Hu, X.; Yu, Y.; Aruta, C.; Yang, N. Pr-Doped $LaCoO_3$ toward Stable and Efficient Oxygen Evolution Reaction. *ACS Appl. Energy Mater.* **2021**, *4* (9), 9057–9065.
(276) Mukherjee, S.; Mukherjee, R.; Banerjee, S.; Ranganathan, R.; Kumar, U. Glassy Behavior in the Layered Perovskites $La_{2-x}Sr_xCoO_4$ ($1.1 \leq x \leq 1.3$). *J. Magn. Magn. Mater* **2012**, *324* (6), 928–933.
(277) Pandey, P. K.; Choudhary, R. J.; Mishra, D. K.; Sathe, V. G.; Phase, D. M. Signature of Spin-Phonon Coupling in Sr_2CoO_4 Thin Film: A Raman Spectroscopic Study. *Appl. Phys. Lett.* **2013**, *102* (14), 142401.
(278) Hong, W. T.; Gadre, M.; Lee, Y.-L.; Biegalski, M. D.; Christen, H. M.; Morgan, D.; Shao-Horn, Y. Tuning the Spin State in $LaCoO_3$ Thin Films for Enhanced High-Temperature Oxygen Electrocatalysis. *J. Phys. Chem. Lett.* **2013**, *4* (15), 2493–2499.
(279) Orlovskaya, N.; Steinmetz, D.; Yarmolenko, S.; Pai, D.; Sankar, J.; Goodenough, J. Detection of Temperature- and Stress-Induced Modifications of $LaCoO_3$ by Micro-Raman Spectroscopy. *Phys. Rev. B* **2005**, *72* (1), 014122.
(280) Dong, S. T.; Sun, N.; Zhang, B. B.; Zhang, F.; Yao, S. H.; Zhou, J.; Zhang, S. T.; Gu, Z. B.; Chen, Y. B.; Chen, Y. F. Crystal Growth, Structure, and Dielectric Properties of Layered Cobaltates $La_{2-x}Sr_xCoO_4$ (x = 0.4, 0.5, and 0.6) Single Crystal. *Mater. Res. Bull.* **2015**, *61*, 352–356.

(281) Hong, J.; Heo, S. J.; Singh, P. Water Mediated Growth of Oriented Single Crystalline $SrCO_3$ Nanorod Arrays on Strontium Compounds. *Sci. Rep.* **2021**, *11* (1), 3368.
(282) Okimoto, Y.; Egawa, T.; Fukaya, R.; Matsubara, Y.; Yamada, Y.; Yamaya, N.; Ishikawa, T.; Onda, K.; Koshihara, S.; Taniguchi, H.; Itoh, M.; Isayama, A.; Sasagawa, T. Ultrafast Real Space Dynamics of Photoexcited State in a Layered Perovskite-Type Spin Crossover Oxide $La_{1.5}Sr_{0.5}CoO_4$. *J. Phys. Soc. Jpn.* **2013**, *82* (7), 074721.
(283) Fukaya, R.; Yamaya, N.; Ishikawa, T.; Koshihara, S.; Okimoto, Y.; Onda, K.; Isayama, A.; Sasagawa, T.; Horigane, K. Picosecond Dynamics in Layered Cobalt Perovskites Studied by Time-Resolved Raman Spectroscopy. *Comptes Rendus. Physique* **2021**, *22* (S2), 95–102.
(284) Yamamoto, K.; Kimura, T.; Ishikawa, T.; Katsufuji, T.; Tokura, Y. Raman Spectroscopy of the Charge-Orbital Ordering in Layered Manganites. *Phys. Rev. B* **2000**, *61* (21), 14706–14715.
(285) Whittingham, A. W. H.; Xinran, L.; Smith, R. D. L. How Cation Substitutions Affect the Oxygen Reduction Reaction on $La_{2-x}Sr_xNi_{1-y}Fe_yO_{4+\delta}$. *ChemCatChem* **2022**, *14*, e202101684.
(286) Yamaguchi, S.; Okimoto, Y.; Tokura, Y. Bandwidth Dependence of Insulator-Metal Transitions in Perovskite Cobalt Oxides. *Phys. Rev. B* **1996**, *54* (16), R11022–R11025.
(287) Yan, J.-Q.; Zhou, J.-S.; Goodenough, J. B. Bond-Length Fluctuations and the Spin-State Transition in $LCoO_3$ (L= La, Pr, and Nd). *Phys. Rev. B* **2004**, *69* (13), 134409.
(288) Chang, C. F.; Hu, Z.; Wu, H.; Burnus, T.; Hollmann, N.; Benomar, M.; Lorenz, T.; Tanaka, A.; Lin, H.-J.; Hsieh, H. H.; Chen, C. T.; Tjeng, L. H. Spin Blockade, Orbital Occupation, and Charge Ordering in $La_{1.5}Sr_{0.5}CoO_4$. *Phys. Rev. Lett.* **2009**, *102* (11), 116401.
(289) Cwik, M.; Benomar, M.; Finger, T.; Sidis, Y.; Senff, D.; Reuther, M.; Lorenz, T.; Braden, M. Magnetic Correlations in $La_{2-x}Sr_xCoO_4$ Studied by Neutron Scattering: Possible Evidence for Stripe Phases. *Phys. Rev. Lett.* **2009**, *102* (5), 057201.
(290) Horigane, K.; Nakao, H.; Kousaka, Y.; Murata, T.; Noda, Y.; Murakami, Y.; Akimitsu, J. Crystal Structure and Charge-Ordering in $La_{1.5}Ca_{0.5}CoO_4$ Studied by Neutron and Resonant X-Ray Scattering. *J. Phys. Soc. Jpn* **2008**, *77* (4), 4–9.
(291) Okamoto, J.; Chainani, A.; Chen, Z. Y.; Huang, H. Y.; Singh, A.; Sasagawa, T.; Khomskii, D. I.; Fujimori, A.; Chen, C. T.; Huang, D. J. Evolution of Valence- and Spin-Specific Local Distortions in $La_{2-x}Sr_xCoO_4$. *Phys. Rev. B* **2021**, *104* (5), 054417.
(292) Hollmann, N.; Haverkort, M. W.; Benomar, M.; Cwik, M.; Braden, M.; Lorenz, T. Evidence for a Temperature-Induced Spin-State Transition of Co^{3+} in $La_{2-x}Sr_xCoO_4$. *Phys. Rev. B* **2011**, *83* (17), 174435.
(293) Guo, H.; Schmidt, W.; Tjeng, L. H.; Komarek, A. C. Charge Correlations in Cobaltates $La_{2-x}Sr_xCoO_4$. *Phys. Status Solidi RRL* **2015**, *9* (10), 580–582.
(294) Wu, H. Metal-Insulator Transition in $Sr_{2-x}La_xCoO_4$ Driven by Spin-State Transition. *Phys. Rev. B* **2012**, *86* (7), 1–5.

Appendices

Appendix A

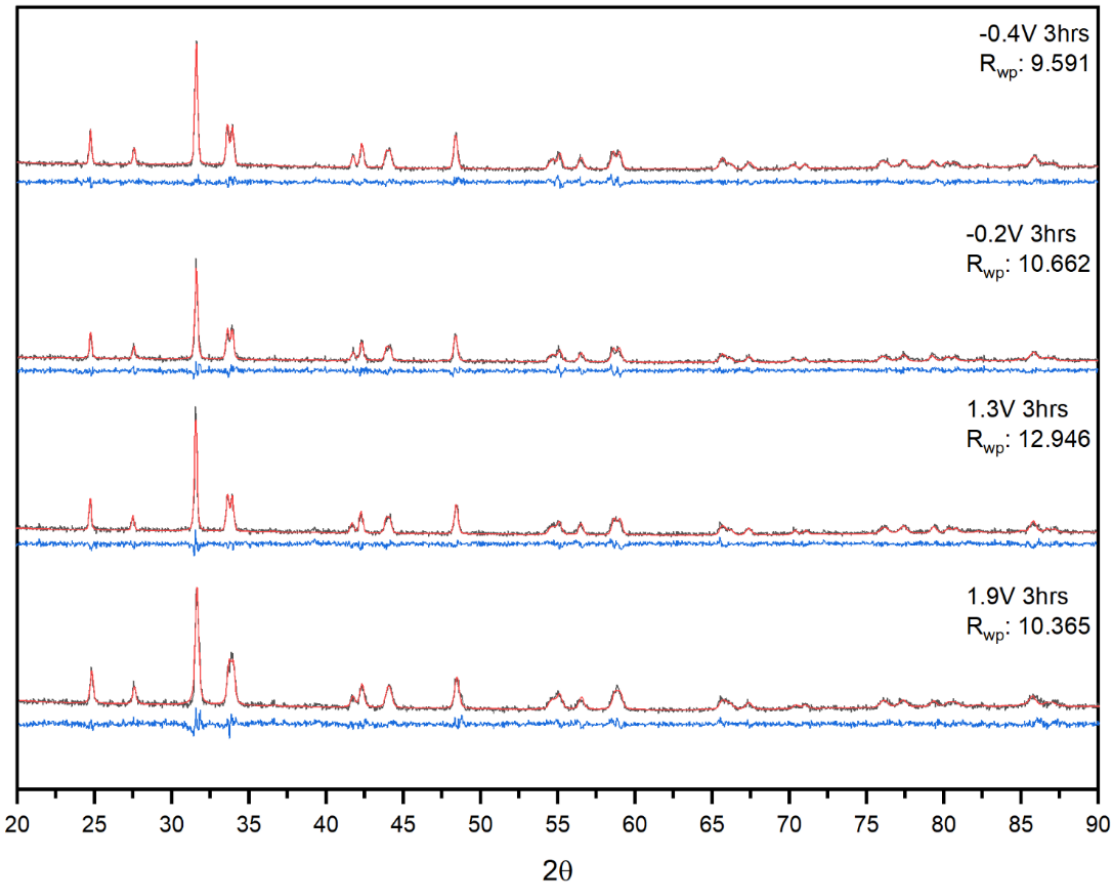

Appendix A.1: PXRD patterns of electrochemically conditioned La_2CuO_4. Refinement of the powder diffraction patterns was performed using GSAS-2. The raw data (black) is shown alongside the fitting results (red) with the difference between the traces (blue) shown for each refinement.

Appendix Table A.1: A summary of literature sources used to construct the calibration curve in Figure 3.2C reporting unit cell parameters, and oxygen non-stoichiometry.

δ	*a* (Å)	*b* (Å)	*c* (Å)	CIF file (ICSD)	Space Group	Reference
-0.12	5.36	5.393	13.181	65864	cmca	146
-0.05	5.353	13.14	5.4012	65380	cmmm	146
-0.04	5.35	13.148	5.398	69286	cmca	148
-0.03	5.3535	13.1441	5.4003	65270	cmca	139
-0.02	5.3548	13.1529	5.4006	65268	cmca	139
0	5.37	5.406	13.15	-	-	149
0	5.3578	5.4048	13.1531	-	-	150
0.03	5.3609	5.3827	13.1841	-	cmca	148
0.03	5.362	13.169	5.4	89196	cmca	151
0.05	5.35	5.398	13.148	-	cmca	148
0.055	5.3532	5.3806	13.1964	-	-	150
0.0625	5.3485	5.3896	13.2146	-	-	150
0.084	5.3416	5.4102	13.2198	-	-	150
0.086	5.3236	5.4033	13.1835	73485	bmab	152
0.09	5.34	5.34	13.23	41494	fmmm	144
0.11	5.3408	5.4043	13.2188	-	fmmm	153
0.137	5.3347	5.4268	13.2324	-	-	150
0.138	5.341	5.403	13.219	-	-	152
0.138	5.3412	5.4033	13.2191	73486	bmab	152
0.178	5.328	5.427	13.194	-	bmab	154
0.186	5.333	5.43	13.222	-	bmab	155

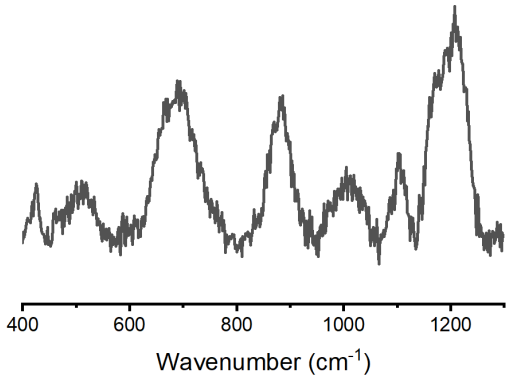

Appendix A.2: The Raman spectrum of La_2CuO_4 between 400 and 1300 cm^{-1}.

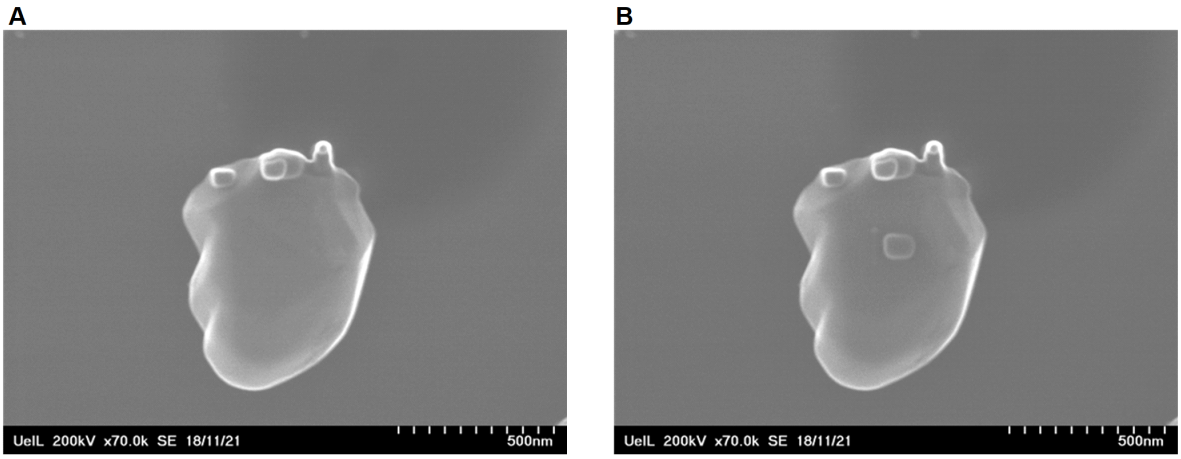

Appendix A.3: SEM image of Cu-metal growth on La_2CuO_4 after high magnification. (A) La_2CuO_4 particle before and (B) after focusing on the center of the particle.

Appendix B

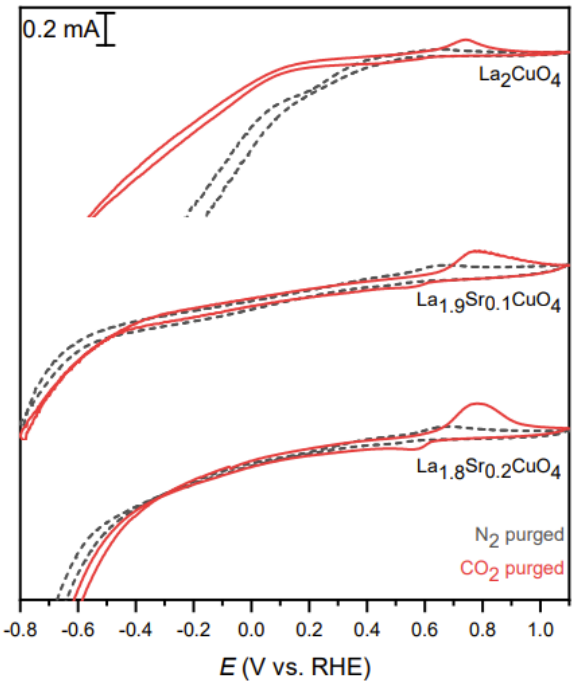

Appendix B.1: Cyclic voltammetry of $La_{2-x}Sr_xCuO_4$ phases under N_2 and CO_2 purged conditions in 0.1 M $KHCO_3$.

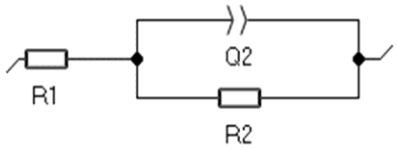

Appendix B.2: The modified Randle Circuit used to model the Nyquist data. R1 and R2 refer to the solution resistance and charge transfer resistance respectively. Q2 is a constant phase element.

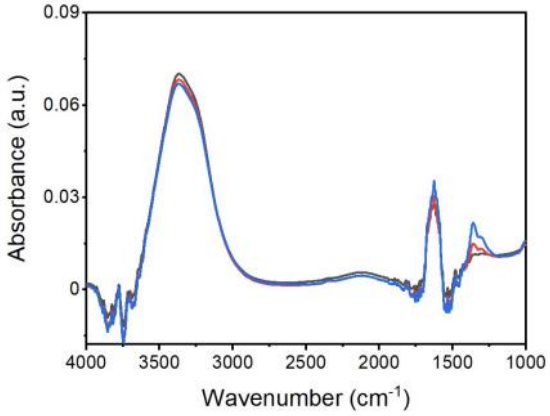

Appendix B.3: FTIR-ATR absorbance spectrum of 0.1, 0.5 and 1 M $KHCO_3$.

Appendix C

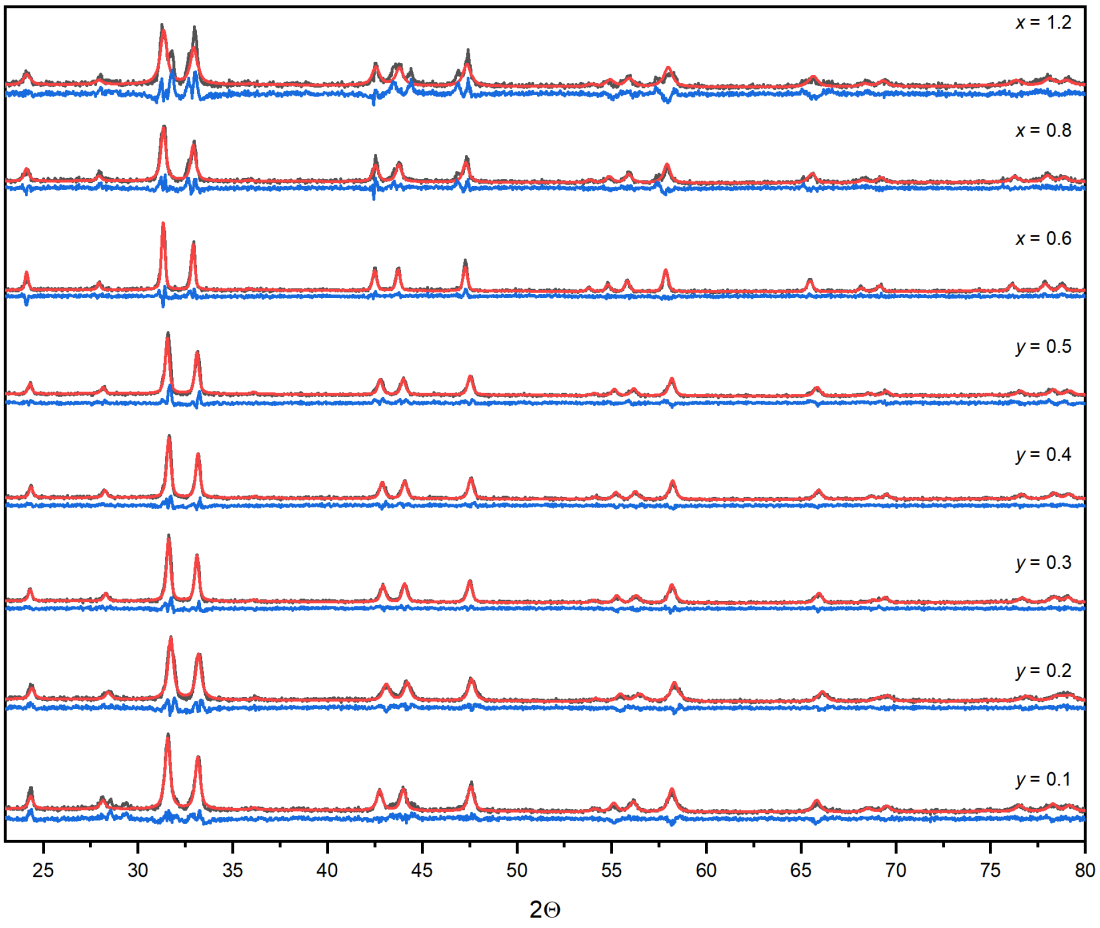

Appendix C.1: Rietveld refinements of $La_{2-x}Sr_xNi_{1-y}Fe_yO_4$. Refinement of the powder diffraction patterns was performed using GSAS-2. The raw data (black) is shown alongside the fitting results (red) with the difference between the traces (blue) shown for each refinement.

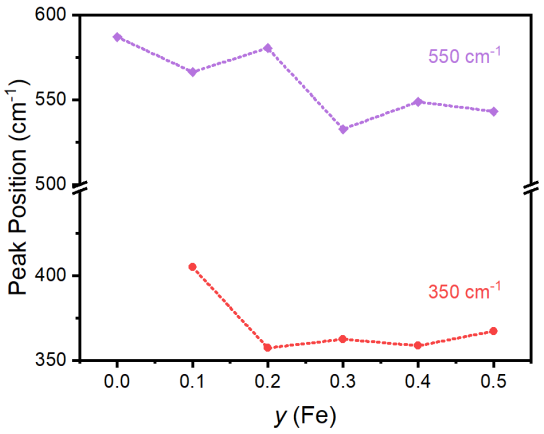

Appendix C.2: Position of the 550 and 350 cm^{-1} spectra components in the $LaSrNi_{1-y}Fe_yO_4$ system.

Appendix Table C.1: Summary of Renishaw peak fit results for $La_{2-x}Sr_xNi_{1-y}Fe_yO_4$ vibrations.

		A_{1g} (La-based)			A_{1g} (O-based)		
y (Fe)	*x*(Sr)	Center	FWHM	Height	Center	FWHM	Height
0	1	209.9	15.29	910	439.5	44.65	938
0.1	1	210.4	25.27	545	439.6	42.48	1415
0.2	1	205.9	17.30	1140	439.9	64.75	1024
0.3	1	208.8	14.24	798	442.4	58.23	459
0.4	1	208.1	15.59	822	448.8	74.07	1156
0.5	1	209.5	15.86	1080	447.9	66.31	1687
0.3	0.6	216.0	16.47	1485	440.4	66.50	2702
0.3	0.8	212.2	32.24	1463	439.9	42.65	1782
0.3	1.2	208.0	19.58	840.3	442.5	71.23	981.2

Appendix D

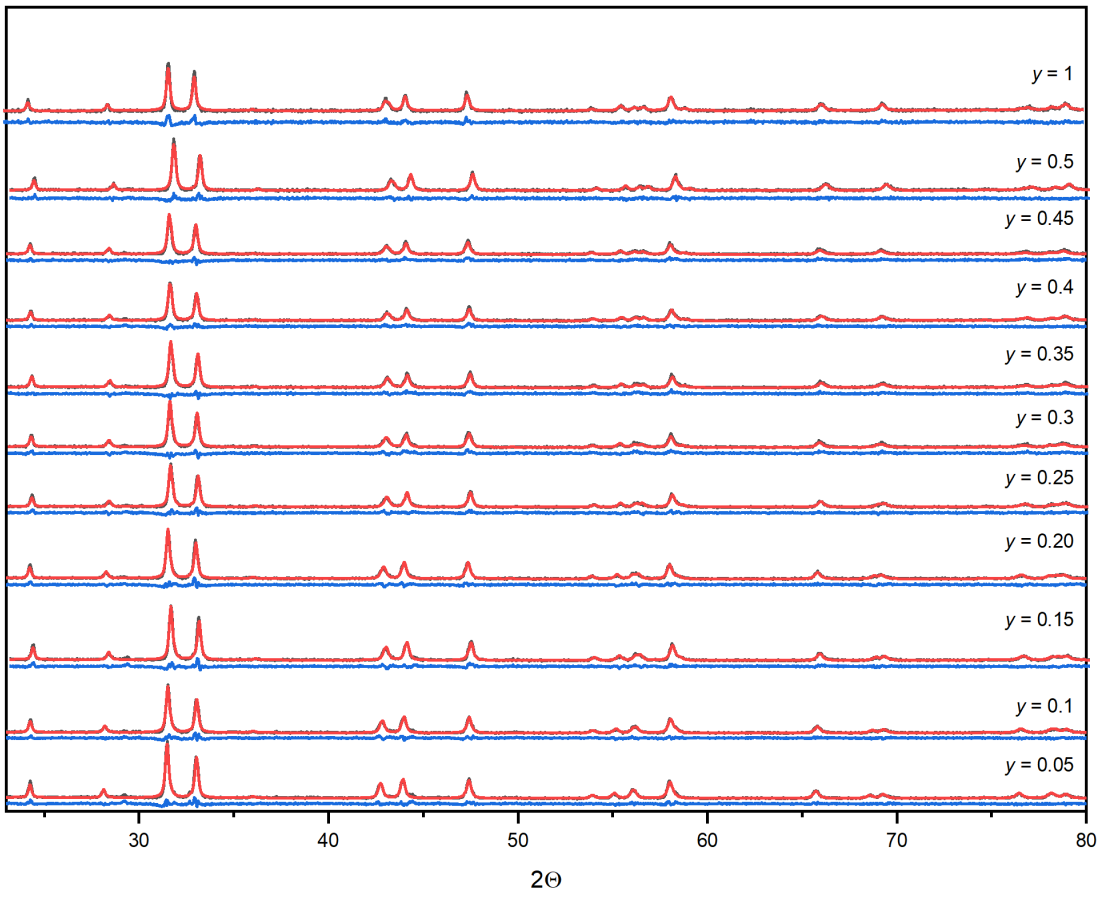

Appendix D.1: Rietveld refinements of $La_{1.2}Sr_{0.8}Ni_{1-y}Co_yO_4$. Refinement of the powder diffraction patterns was performed using GSAS-2. The raw data (black) is shown alongside the fitting results (red) with the difference between the traces (blue) shown for each refinement.

Appendix Table D.1: Unit cell parameters of $La_{1.2}Sr_{0.8}Ni_{1-y}Co_yO_4$.

x (Sr)	*y* (Co)	*a* Å	*c* Å	*V* Å^3	*c/a*	R_{wp} %
0.8	0	3.828 (0.001)	12.702 (0.001)	186.1 (0.1)	3.317	10.73
0.8	0.05	3.832 (0.001)	12.673 (0.001)	186.1 (0.1)	3.307	8.738
0.8	0.10	3.831 (0.001)	12.644 (0.001)	185.5 (0.1)	3.300	8.347
0.8	0.15	3.837 (0.001)	12.635 (0.001)	186.0 (0.1)	3.292	8.289
0.8	0.20	3.835 (0.001)	12.617 (0.001)	185.6 (0.1)	3.289	8.009
0.8	0.25	3.833 (0.001)	12.591 (0.001)	185.0 (0.1)	3.284	8.155
0.8	0.30	3.838 (0.001)	12.594 (0.001)	185.5 (0.1)	3.280	8.519
0.8	0.35	3.831 (0.001)	12.558 (0.001)	184.2 (0.1)	3.275	8.151
0.8	0.40	3.831 (0.001)	12.562 (0.001)	184.2 (0.1)	3.275	7.273
0.8	0.45	3.836 (0.001)	12.556 (0.001)	184.7 (0.1)	3.273	8.209
0.8	0.50	3.831 (0.001)	12.533 (0.001)	183.9 (0.1)	3.271	7.141
0.8	1.00	3.825 (0.001)	12.516 (0.001)	183.1 (0.1)	3.271	6.796

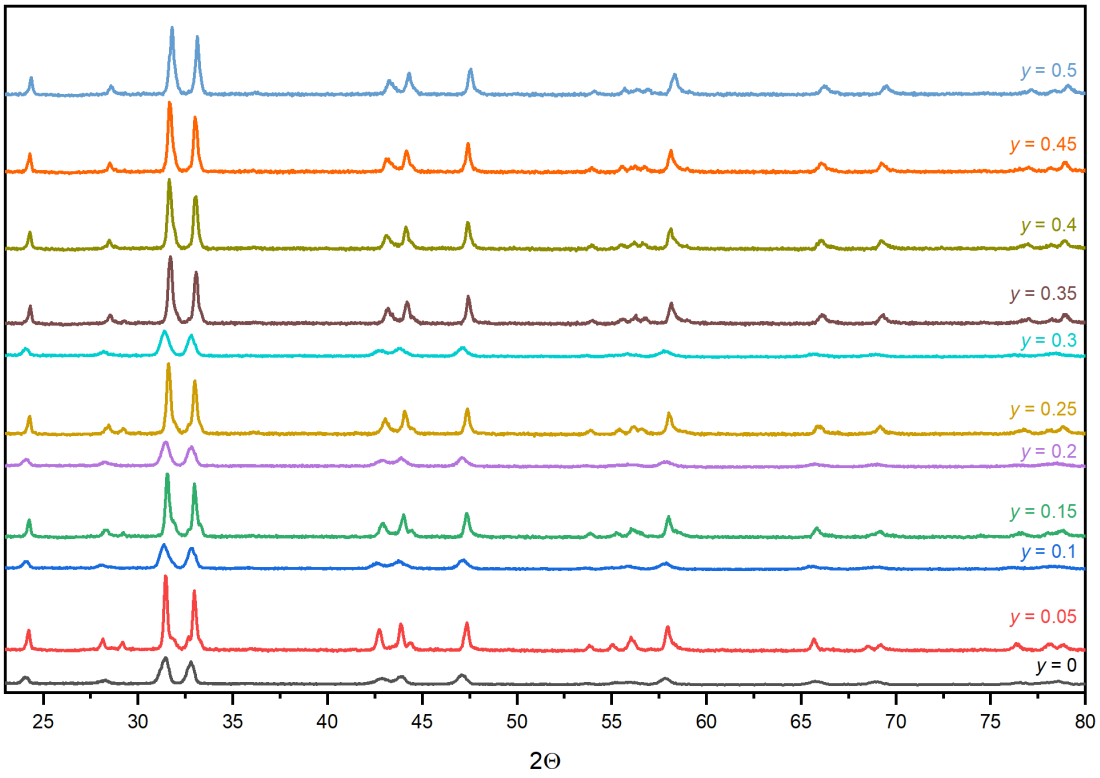

Appendix D.2: PXRD patterns of $LaSrNi_{1-y}Co_yO_4$.

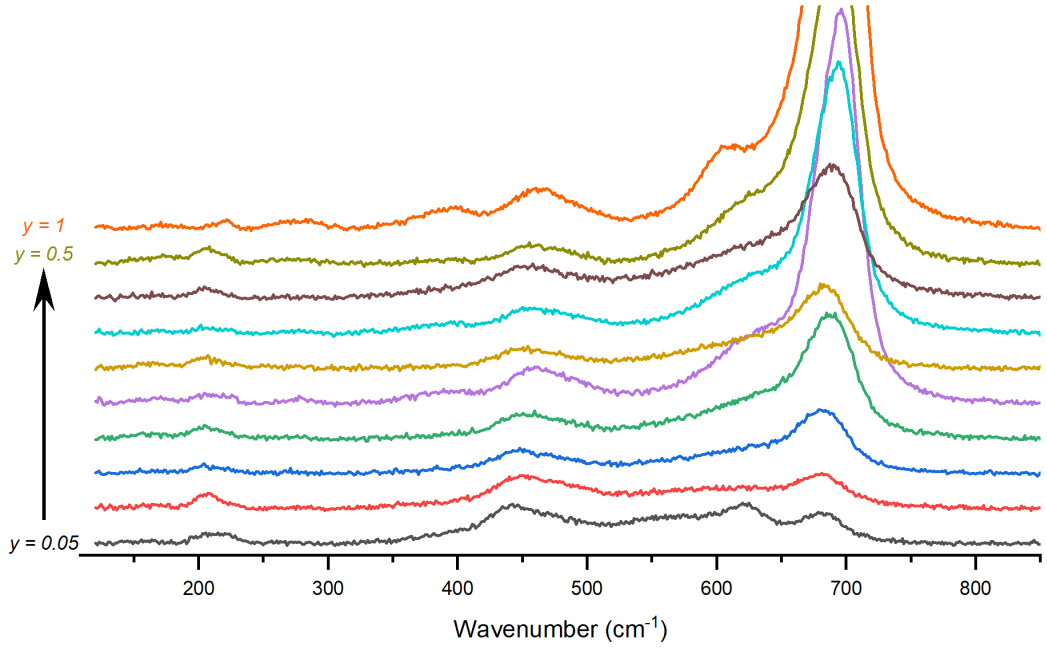

Appendix D.3: Raman Spectroscopy of $LaSrNi_{1-y}Co_yO_4$.

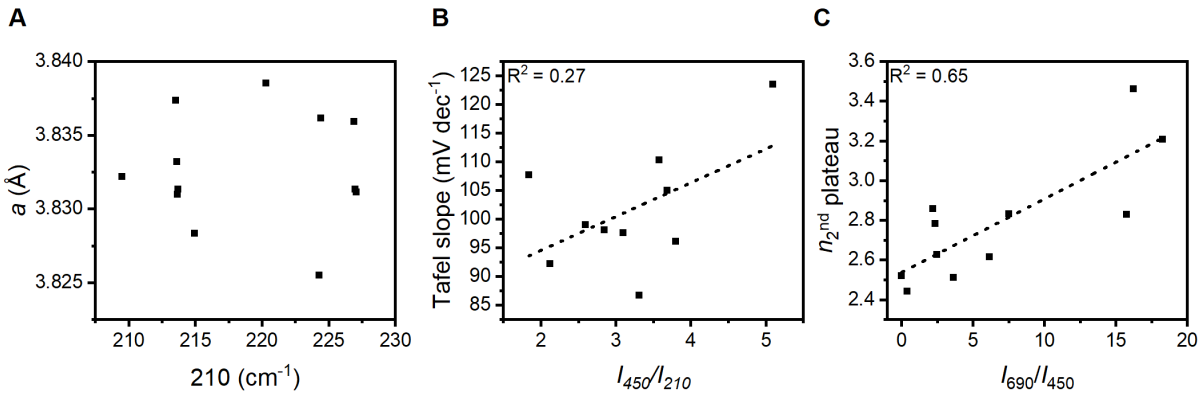

Appendix D.4: Correlation analysis for $La_{1.2}Sr_{0.8}Ni_{1-y}Co_yO_4$. (A) No correlation is observed between the unit cell parameter *a* and the 210 cm^{-1} vibration. (B) A weak, linear correlation observed between the normalized intensity of the 450 cm^{-1} vibration and the ORR Tafel slope. (C) Correlation between the number of electrons transferred at the second plateau against the I_{690}:I_{450} ratio.

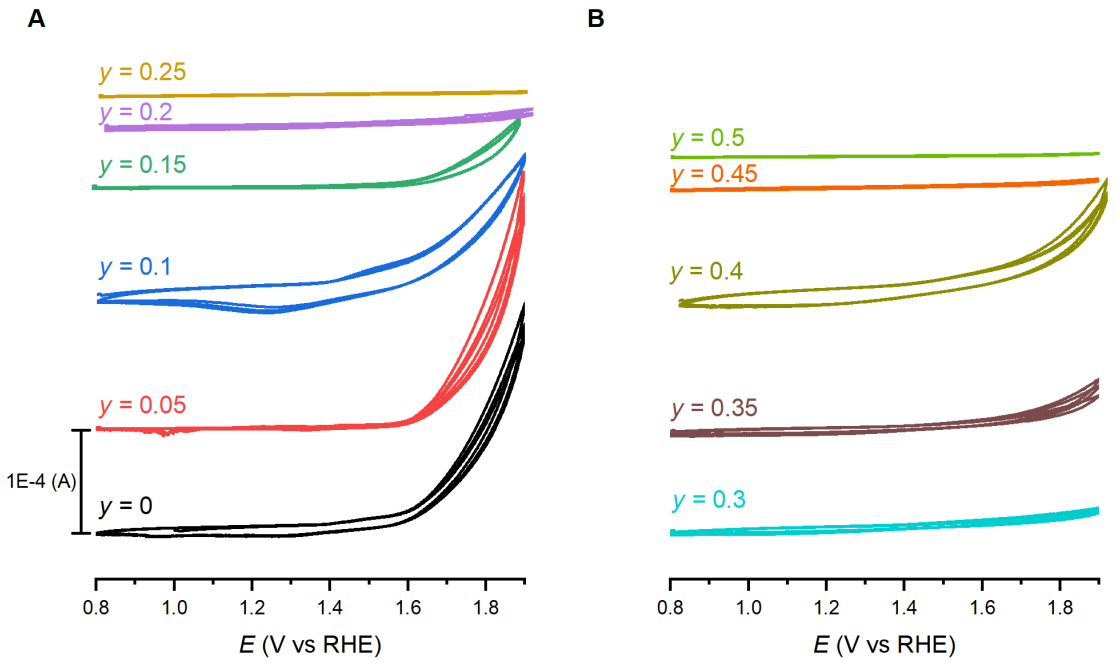

Appendix D.5: Anodic Cyclic voltammetry of $La_{1.2}Sr_{0.8}Ni_{1-y}Co_yO_4$ under N_2 purged conditions. Three cycles were acquired for each CV.